

1-1-2012

# Optimal Control of Vapor Extraction of Heavy Oil

Hameed Muhamad  
*Ryerson University*

Follow this and additional works at: <http://digitalcommons.ryerson.ca/dissertations>



Part of the [Petroleum Engineering Commons](#)

---

## Recommended Citation

Muhamad, Hameed, "Optimal Control of Vapor Extraction of Heavy Oil" (2012). *Theses and dissertations*. Paper 1427.

This Dissertation is brought to you for free and open access by Digital Commons @ Ryerson. It has been accepted for inclusion in Theses and dissertations by an authorized administrator of Digital Commons @ Ryerson. For more information, please contact [bcameron@ryerson.ca](mailto:bcameron@ryerson.ca).

# **OPTIMAL CONTROL OF VAPOR EXTRACTION OF HEAVY OIL**

by

**Hameed Muhamad**

B.Sc. in Chemical Engineering, University of Technology, Baghdad, 1992

M.A.Sc. in Chemical Engineering, Ryerson University, Toronto, 2008

A dissertation presented to

**Ryerson University**

in partial fulfillment of the  
requirements for the degree of

**Doctor of Philosophy**

in the program of

**Chemical Engineering**

Toronto, Ontario, Canada, 2012

©Hameed Muhamad 2012

**Author's Declaration**

I hereby declare that I am the sole author of this dissertation. This is a true copy of the dissertation, including any required final revisions, as accepted by my examiners.

I authorize Ryerson University to lend this dissertation to other institutions or individuals for the purpose of scholarly research

I further authorize Ryerson University to reproduce this dissertation by photocopying or by other means, in total or in part, at the request of other institutions or individuals for the purpose of scholarly research.

I understand that my dissertation may be made electronically available to the public.

# **OPTIMAL CONTROL OF VAPOR EXTRACTION OF HEAVY OIL**

**Doctor of Philosophy**

**2012**

**Hameed Muhamad**

**Chemical Engineering**

**Ryerson University**

## **Abstract**

Vapor extraction (Vapex) process is an emerging technology for viscous oil recovery that has gained much attention in the oil industry. However, the oil production rates in Vapex are too low to make it attractive for field implementation. Although several researchers have investigated several aspects of Vapex, there are few reported attempts to enhance oil production in Vapex. This research aims to enhance the same using solvent injection pressure versus time as a control function. For this purpose, the necessary conditions for maximum heavy oil production are derived based on a detailed mass transfer model of the Vapex experiment carried out in this work. These conditions are then used to develop an optimal control algorithm to determine the optimal solvent injection pressure policies to maximize oil production in Vapex. The optimal policies successfully generate 20–35% increase in experimental oil production with propane and butane as pure solvents, and heavy oil of 14,500 mPa·s viscosity in lab scale reservoirs of 25 and 45 cm heights, and 204 Darcy permeability. The accuracy of optimal control is experimentally validated. The results show that the experimental oil production values from the optimal policies are within  $\pm 5\%$  of those predicted by the optimal control algorithm.

## **Acknowledgements**

I am extremely indebted to my supervisor Professor Simant R. Upreti for his excellent supervision and inspiration throughout the thesis work. From his instruction, I learned the arts and skills of a researcher and more importantly the way of thought.

My special thanks go to Professor Ali Lohi for giving me an opportunity to work on this research and for his support with meaningful discussions, invaluable advices and rich ideas.

I would like to extend my deepest gratitude to Professor Huu Doan for continuous support, encouragement and guidance throughout this work.

I appreciate the indisputable support that I received from the mechanical workshop team Mr. Ali Hemmati and Mr. Daniel Boothe during the lab setup. I also appreciate the support I received from the electrical lab supervisor, Mr. Tondar Tajrobehkar.

I would like to extend my sincere thanks to everyone provided me help, support and courage throughout this study in every possible way.

Finally and most importantly, this thesis is dedicated to my mother, my dearest daughters, my son and loving wife whose continuous backing and encouragement made this possible

# Table of Contents

Author's declaration	ii
Abstract	iii
Acknowledgments	iv
Table of Contents	v
List of Tables	ix
List of Figures	xi
List of Appendices	xiii
Nomenclature	xv

<b>Chapter 1: Introduction</b>	<b>1</b>
1.1 Crude Oil Classification	1
1.2 Heavy Crude Oil	3
1.3 Heavy Oil Reserves	3
1.3.1 World and Canadian Heavy Oil Resources	3
1.3.2 Canadian Heavy Oil Belt Resources	5
1.4 Existing EOR Processes in Canada for Heavy Oil Recovery	5
1.4.1 Open Pit or Surface Mining	6
1.4.2 Well Production	8
1.4.2.1 Cold Heavy Oil Production with Sand (CHOPS)	8
1.4.2.2 Cyclic Steam Stimulation (CSS) and Steam Flood	9
1.4.2.3 Steam Assisted Gravity Drainage (SAGD)	10
1.5 Technologies in Development	13
1.5.1 Hybrid Solvent and Steam Processes	13
1.5.2 In Situ Combustion	13
1.6 Introduction to Vapex	14
 <b>Chapter 2: Literature Review</b>	 <b>17</b>
2.1 Idea of Vapex Process	17
2.2 Fluid Flow in Vapex Process	18

2.3 Experimental Methods in Vapex	18
2.4 Effect of Petro Physical Properties on Vapex Performance	22
2.5 Effect of Asphaltene Deposition and Precipitation on Vapex Performance	24
2.6 Optimization of Vapex	26
2.7 Mass Transfer Mechanism in Vapex	27
2.7.1 Diffusion of Solvent Gases in Heavy Oil	27
2.7.2 Dispersion of Solvent Gases in Heavy Oil and Bitumen	29
2.8 Operating Pressure in Vapex	32
2.9 Optimal Control	33
2.9.1 Optimal Control and Optimization	33
2.10 Objectives of Current Study	34
2.11 Structure of the Dissertation	34
<b>Chapter 3: Experimental Setups and Procedures</b>	<b>37</b>
3.1 Main Experimental Setups	37
3.1.1 VapexSetups	38
3.1.1.1 Experimental Procedure	42
3.1.2 Interfacial Solvent Concentration Setup	44
3.1.2.1 Experimental Procedure	45
3.2 Heavy Oil Properties	47
3.3 Glass Beads Properties	49
3.4 The Physical Model Preparation	49
3.5 Constant Temperature	52
3.6 Live Oil Viscosity	53
3.7 Solvent Gas Solubility and Live Oil Density	54
3.8 Permeability Measurement	55
3.9 Experimental Error	57
<b>Chapter 4: Optimal Control of Vapex</b>	<b>59</b>
4.1 Mass Transfer Model	60
4.2 Initial and Boundary Conditions	64

4.3 Optimal Control Analysis	65
4.4 Necessary Conditions for the Optimum	67
4.5 Adjoint Equations	73
4.6 Optimal Control Algorithm	74
4.6.1 The Gradient Improvement Method	75
4.6.2 Implementation of the Improvement Method	76
4.7 Integration of Continuity and Adjoint Equations	76
4.7.1 Discretized Mathematical Model	79
4.7.2 The Adjoint Equations	82
4.8 The Optimal Control Algorithm	86
<b>Chapter 5: Results and Discussion</b>	<b>89</b>
5.1 Live Oil Production	90
5.1.1 Oil Production Rate with Different Permeabilities	91
5.1.2 Oil Production Rate with Different Model Heights	93
5.1.3 Oil Production Rate at Different Uniform Pressures	94
5.2 Live Oil Properties	97
5.2.1 Live Oil Density	98
5.2.2 Live Oil Viscosity	98
5.2.3 Solubility of Solvent in Produced Oil	100
5.2.4 Correlation of Pressure with Solvent Interfacial Concentration	100
5.3 Proof of Concept for Enhancement of Vapex by Variation of Solvent Injection Pressure	101
5.3.1 Effect of Pressure Variations	102
5.3.2 Effect of Pressure Variation with Different Medium Permeabilities	104
5.3.3 Effect of Pressure Variation with Different Physical Model Heights	106
5.4 Steps to Formalize the Concept	109
5.4.1 Determination of Concentration-Dependent Dispersion Coefficient	109
5.5 Optimal Control Policy for Solvent Injection	112
5.5.1 Optimal Control Policy for Solvent Concentration	112
5.5.2 Optimal Solvent Injection Pressure	115



5.6 Validation of Optimal Control Policy	117
5.6.1 Accuracy of Optimal Control	117
5.6.2 Enhanced Oil Recovery	118
5.6.3 Summary	120
<b>Chapter 6: Conclusions and Recommendations</b>	<b>121</b>
6.1 Conclusions	121
6.2 Recommendations	123
<b>Appendix A: Sample of Porous Medium Permeability Calculation</b>	<b>125</b>
<b>Appendix B: Sample of Live Oil Viscosity Calculation</b>	<b>127</b>
<b>Appendix C: Solubility and Live Oil Density Calculation</b>	<b>129</b>
<b>Appendix D: Derivations of Necessary Conditions</b>	<b>131</b>
<b>Appendix E: Finding Adjoint Equations</b>	<b>135</b>
<b>Appendix F: Finding the Jacobians for the state and adjoint equations</b>	<b>141</b>
<b>Appendix G: Recorded Mass of the Physical Model versus Time</b>	<b>153</b>
<b>Appendix H: Average Live Oil Density for Various Physical Models</b>	<b>159</b>
<b>Appendix I: Determination of Concentration-Dependent Dispersion Coefficient</b>	<b>161</b>
<b>Appendix J: Validation of Optimal Control Policy for Solvent Injection Pressure</b>	<b>173</b>
<b>References</b>	<b>183</b>

## List of Tables

Table 1.1 Molecular composition of crude oil	2
Table 0.2 Alberta bitumen deposits — in place volumes billion m <sup>3</sup>	12
Table 2.1 Characteristics of the experimental studies carried out for Vapex	20
Table 2.2 Different correlations for diffusivity estimation	29
Table 3.1 Pressure versus interfacial concentration for propane and butane	46
Table 3.2 Properties of the heavy oil	48
Table 3.3 Specifications of the glass beads	49
Table 3.4 Permeability of the glass beads	57
Table 3.5 Instrument specifications used during Vapex study	57
Table 5.1 Average live oil density for various physical models	98
Table 5.2 Average live oil viscosity for various physical models	99
Table 5.3 Solvent mass fraction in produced oil for various physical models	100
Table 5.4 Simulation model parameters (204 D and 25 cm)	113
Table 5.5 Validation experiments for different physical models and solvent gas	119



## List of Figures

Figure 1.1 Global crude oil reserves by country	4
Figure 1.2 Surface mining process	7
Figure 1.3 Side view of SAGD process	11
Figure 1.4 Vapor extraction (Vapex) process	14
Figure 1.5 Schematic of vapor extraction (Vapex )	15
Figure 2.1 Differential element of the physical model	31
Figure 3.1 Schematic diagram of the Vapex experimental setup	40
Figure 3.2 Picture of the Vapex experimental setup	41
Figure 3.3 Schematic of solvent–heavy oil system for the measurement of interfacial solvent concentration	45
Figure 3.4 Picture of solvent–heavy oil system for the measurement of interfacial solvent concentration	47
Figure 3.5 Viscosity of heavy oil versus temperature	48
Figure 3.6 (a) Picture of heavy oil and glass beads	50
Figure 3.6 (b) Picture of heating the sample	51
Figure 3.6 (c) Picture of mixing glass beads with the oil	51
Figure 3.7 Temperature for a couple of typical Vapex experiments	52
Figure 3.8 Picture of the Viscosity Measuring Unit	54
Figure 4.1 Packed cylindrical medium with its differential element and the arrangement of grid points	63
Figure 4.2 Cylindrical model and node distribution	78
Figure 4.3 The optimal control algorithm	87
Figure 5.1 Recorded mass of the physical model with time for permeability 204 D	90
Figure 5.2 Oil production versus time	91
Figure 5.3 Oil production versus time at different permeabilities	92
Figure 5.4 Variation of production rate with model permeability	93
Figure 5.5 Oil production versus experimental time for butane	94
Figure 5.6 Oil production versus time	95
Figure 5.7 Variation of production rate with model different pressure	96
Figure 5.8 Oil production versus time at different constant injection pressures	97

Figure 5.9 Live oil viscosity versus propane mass fraction	99
Figure 5.10 Variation of propane mass fraction with different constant pressure	101
Figure 5.11 Pressure versus time with long 8 min pulses, and short 3 min pulses	103
Figure 5.12 Oil production versus time	103
Figure 5.13 Oil production versus time	104
Figure 5.14 Oil production versus time	105
Figure 5.15 Oil production versus time	106
Figure 5.16 Oil production versus time	107
Figure 5.17 Oil production versus time	107
Figure 5.18 Dispersion coefficient function of propane in heavy oil	110
Figure 5.19 Error versus iteration number	111
Figure 5.20 Experimental and calculated mass of live oil produced with time	111
Figure 5.21 The interfacial solvent concentration $\omega_{\text{int}}(t)$ at different iterations of the optimal control algorithm	114
Figure 5.22 Objective functional versus iteration number	115
Figure 5.23 Optimal interfacial propane concentration versus time (25 cm model height, 204 Darcy permeability)	116
Figure 5.24 Solvent injection pressure corresponding to the optimal $\omega_{\text{int}}(t)$ in Figure 5.23	116
Figure 5.25 Load cell reading of oil production versus time	118
Figure 5.26 Experimental and the predicted masses of produced oil	119
Figure 5.27 Experimental mass of produced oil for different physical models	120

## List of Appendices

<b>Appendix A:</b> Sample of Porous Medium Permeability Calculation	125
<b>Appendix B:</b> Sample of Live Oil Viscosity Calculation	127
<b>Appendix C:</b> Solubility and Live Oil Density Calculation	129
<b>Appendix D:</b> Derivations of Necessary Conditions	131
<b>Appendix E:</b> Finding Adjoint Equations	135
<b>Appendix F:</b> Finding the Jacobians for the state and adjoint equations	141
<b>Appendix G:</b> Recorded Mass of the Physical Model versus Time	153
<b>Appendix H:</b> Average Live Oil Density for Various Physical Models	159
<b>Appendix I:</b> Determination of Concentration-Dependent Dispersion Coefficient	161
<b>Appendix J:</b> Validation of Optimal Control Policy for Solvent Injection Pressure	173



## Nomenclature

$A$	area, $m^2$
$D(\omega)$	dispersion coefficient of solvent in medium, $m^2/s$
$D_p$	diameter of the particle, $m$
$g$	gravity, $m/s^2$
$I$	objective functional defined by Equation
$J$	augmented objective functional defined by Equation
$J_f$	dispersive flux of solvent in the medium along the radial direction, $kg/m^2 \cdot s$
$K$	permeability of the medium, $D$
$K_r$	relative permeability of the medium
$m_c$	calculated mass of the produced live oil, $kg$
$m_e$	experimental mass of the produced live oil, $kg$
$P$	Pressure, $kPa$
$r$	distance along the radial direction, $m$
$R$	radius of cylindrical medium, $m$
$S$	surface area, $m^2$
$T$	final Time, $min$
$t$	time, $min$
$u$	interstitial velocity, $m/s$
$V$	volume of a finite element in the medium, $m^3$
$v$	Darcy velocity, $m/s$
$z$	distance along the vertical direction, $m$
$Z$	bitumen height in the medium at a given $r$ and $t$ , $m$
$Z_0$	initial height, $m$



## Greek Symbols

$\varphi$	porosity of the medium
$\lambda_1, \lambda_2$	adjoint variables
$\mu$	viscosity of the live oil, cP
$\mu_0$	viscosity coefficient of the live oil, kg/m·s
$\rho$	density of the live oil, kg/m <sup>3</sup>
$\omega$	mass fraction of solvent in bitumen
$\omega_{\text{int}}$	mass fraction of solvent at the solvent–heavy oil interface

## Abbreviations

BFGS	Broyden-Fletcher-Goldfarb-Shanno Method
BOPD	Barrels of Oil Per Day
CHOPS	Cold Heavy Oil Production with Sand
CSS	Cyclic Steam Stimulation
EOR	Enhanced Oil Recovery
NEB	National Energy Board
OOIP	Original Oil In Place
SAGD	Steam Assisted Gravity Drainage
SOR	Steam-to-Oil Ratios
Vapex	Vapor extraction

# 1

# Introduction

This chapter provides the background information on crude oil classification, heavy crude oil properties, heavy oil reservoirs, Canadian heavy oil resources, and heavy oil recovery processes including vapor extraction or Vapex.

## **1.1 Crude Oil Classification**

Petroleum or crude oil is a naturally occurring flammable liquid consisting of a complex mixture of hydrocarbons of various molecular weights and other liquid organic compounds that are found in geologic formations beneath the Earth's surface. A fossil fuel, petroleum was formed when large quantities of dead organisms, usually zooplankton and algae, were buried underneath sedimentary rock and undergo intense heat and pressure.

In its strictest sense, petroleum includes only crude oil, but in common usage it includes all liquid, gaseous, and solid (e.g., paraffin) hydrocarbons. Under surface pressure and temperature conditions, lighter hydrocarbons methane, ethane, propane and butane occur as gases, while pentane and heavier ones are in the form of liquids or solids. However, in an underground oil

reservoir, the proportions of gas, liquid, and solid depend on subsurface conditions and on the phase diagram of the petroleum mixture.

The hydrocarbons in crude oil are mostly alkanes, cycloalkanes and various aromatic hydrocarbons while the other organic compounds contain nitrogen, oxygen and sulfur, and trace amounts of metals such as iron, nickel, copper and vanadium. Table 1.1 shows that the molecular composition of crude oil varies widely from formation to formation but the proportion of chemical elements varies over fairly narrow limits as follows (Speight, 1999).

**Table 1.1:** Molecular composition of crude oil

Composition by weight	
Element	Percent range
Carbon	83 to 87%
Hydrogen	10 to 14%
Nitrogen	0.1 to 2%
Oxygen	0.05 to 1.5%
Sulfur	0.05 to 6.0%
Metals	< 0.1%

The petroleum industry generally classifies crude oil by the geographic production location (e.g. West Texas Intermediate, Brent, or Oman), its API gravity (an oil industry measure of density), and its sulfur content. Crude oil may be considered light if it has low density, or heavy if it has high density. It may be referred to as sweet if it contains relatively little sulfur or sour if it contains substantial amounts of sulfur.

The geographic location is important because it affects transportation costs of crude oil to the refinery. Light crude oil is more desirable than heavy oil since it produces a higher yield of petrol, while sweet oil commands a higher price than sour oil because it has fewer environmental problems and requires less refining to meet sulfur standards imposed on fuels in consuming countries.

## **1.2 Heavy Crude Oil**

Heavy crude oil or extra heavy crude oil is any type of crude oil that does not flow easily. It is referred to as “heavy” because its density or specific gravity is higher than that of light crude oil. Heavy crude oil has been defined as any liquid petroleum with an API gravity less than 20°. Physical properties that differ between heavy crudes lighter grades include higher viscosity and specific gravity as well as heavier molecular composition. Extra heavy oil is defined with a gravity of less than 10° API (i.e. with density greater than 1000 kg/m<sup>3</sup>), and a reservoir viscosity of no more than 10,000 cP (Attanasi and Meyer, 2010). With a specific gravity of greater than unity, extra heavy crude is present as a dense non-aqueous phase liquid in ambient conditions.

Heavy crude oil is closely related to natural bitumen from oil sands. Some petroleum geologists categorize bitumen from oil sands as extra heavy crude oil due to the density of less than 10 °API. Other classifications label this as bitumen differing it from extra-heavy oil. These oils differ in the degree by which they have been degraded from the original crude oil by bacteria and erosion. Often, bitumen is present as a solid and does not flow at ambient conditions. The largest reserves of heavy crude oil in the world are located north of the Orinoco river in Venezuela, the same amount as the conventional oil reserves of Saudi Arabia, but 30 or more countries are known to have reserves (Talwani, 2002).

## **1.3 Heavy Oil Reserves**

Heavy Oil is an up and coming energy resource that is aggressively being sought after as the world’s energy demand increases. As technology continues to improve, this once costly energy source is quickly becoming a more viable alternative.

### **1.3.1 World and Canadian Heavy Oil Resources**

Petroleum is the world’s primary energy source and is a key factor in the continued development of world economies. The deflection of conventional oil resources all around the world has become a serious source of concern for industry and government and is a reason to think about other energy alternatives. On the other hand there are huge and virtually untouched reserves of

heavy oil and bitumen deposits in the globe especially in Canada and Venezuela, which are almost six times of total conventional resources.

Figure 1.1 compares of Canadian oil reserves with other oil-rich countries. In Canada, the estimated original oil in place (OOIP) is more than 400 billion m<sup>3</sup> (2.5 trillion barrels) approximately twice that of the total conventional oil reserves in the Middle East (ERCB, 1989).

In Canada, Alberta's in-place oil sands reserves are about 1.7 trillion bbl. More than 175 billion bbl is recoverable with current technology. With technical advances, about 315 billion bbl could be recovered. However, the main difficulty in the oil recovery from these vast reserves is their immobility under reservoir conditions due to their high viscosity (10<sup>4</sup>–10<sup>6</sup>cP or even higher) (Das and Butler, 1996).

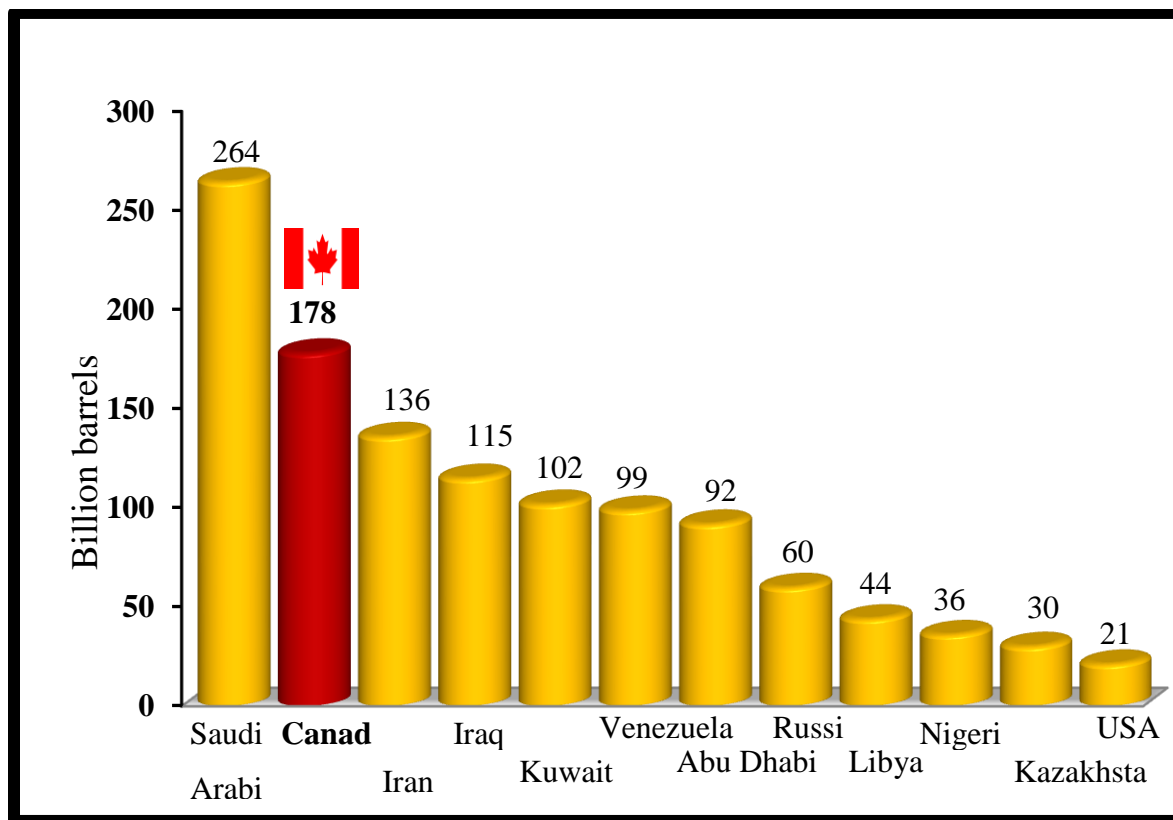


**Figure 0.1** Global crude oil reserves by country (CAPP, 2008)

The world heavy oil resource is about  $12 \times 10^{12}$  bbl. Apparently, there is more than twice as much resource available in <20°API oil as in conventional oil >20°API. Heavy oil resources are found through the world, but Canada and Venezuela are singularly endowed. The two countries

appear to share 35-40% of the world resources of  $<20^\circ\text{API}$  heavy oil, approximately  $2.5 \times 10^{12}$  bbl in the Canadian heavy oil belt and oil sands regions, and  $1.5 \times 10^{12}$  bbl in the Venezuelan Faja del Orinoco tar sands belt.

To put the available heavy oil resources into an understandable context, its size in Canada alone is so large about  $(350-400 \times 10^9 \text{ m}^3)$ , more than 20% of the World total) that, at a stable combined US and Canadian consumption rate (about  $1.2 \times 10^9 \text{ m}^3/\text{year}$ ), there is enough heavy oil in Canada to meet 100% of the demand for over 100 years if the overall extraction efficiency is about 30%. In the best strata, the new extraction technologies in Canada are already approaching, and in some cases exceeding, this recovery ratio of 30%. Oil sands mines approach 85% extraction (ERCB Report 2011).

### **1.3.2 Canadian Heavy Oil Belt Resources**

The National Energy Board (NEB) report on Conventional Heavy Oil resources of the Western Canada Sedimentary Basin has identified  $50 \times 10^9 \text{ m}^3$  ( $\sim 350 \times 10^9$  bbl) of heavy oil in place in the heavy oil belt. This is about 15% of the total  $<20^\circ\text{API}$  resource in Alberta, exclusive of the ill-defined Carbonate Triangle. They estimate that 21% of this  $\sim 74 \times 10^9$  bbl, can be recovered with current technology. This is 1000 days of supply for the entire world at current consumption rates. Given Canada's light population, it is of huge economic importance, with a current commodity value somewhat below CAN\$  $3 \times 10^{12}$  at a world price of US\$ 25.00. Given the technological progress that is ongoing, referring to the 59% probability estimate of Canadian industry engineers, the NEB estimate of technologically accessible reserves in the heavy oil belt is conservative, perhaps by a factor of two.

### **1.4 Existing EOR Processes in Canada for Heavy Oil Recovery**

The recovery of heavy oil and bitumen is difficult, as 90% of these reserves lie deep inside the earth crust and are not easily recoverable owing to their high viscosity and immobility. The objective of recovery process is to reduce the viscosity, or equivalently to increase the mobility of heavy oil and bitumen. This objective is achieved by providing additional energy to heavy oil

and bitumen reserves (Upreti et al., 2007). The production methods widely adapted in Canada for heavy oil production can be classified as:

1. Open pit or Surface Mining
2. Well Production

#### **1.4.1 Open Pit or Surface Mining**

Surface mining is a type of mining used to extract bitumen accumulations that are close to the surface. This process involves digging up the oil sand then transporting it to a treatment facility where it will be subjected to steam or hot water treatment and centrifuging to separate the bitumen from the sand.

In open-pit mining, trees and other vegetation are first removed; then the overburden is excavated and either used to build retaining dykes for ponds or stockpiled for later land reclamation. Large shovels and trucks are used to load and transport the unconsolidated oil sands from the mine face to an ore crusher. After being crushed into 12 inch or smaller chunks, the ore is slurred with water in a cyclo-feeder. The slurry is sent by pipeline to a central processing facility for upgrading. The bitumen, sand and water mixtures create emulsions which are extremely difficult to separate, and the process of separating oil from the sand particles begins during hydro transport. This process is continued in the primary separation vessel (PSV) at the central facility. Bitumen froth (60% bitumen, 30% water, 10% fine solids) is removed from the PSV and then is either processed with naphtha or paraffinic solvents to remove water and fine solids. The paraffinic solvent process results in bitumen with less than 0.1% water and fines remaining. Clean sand from the PSV is removed and stockpiled. A combination of mixed bitumen and water, fine particles and clay (fine tailings) is transported to a holding pond.

If the resource lies within 50 to 75 m of the surface, then open-pit mining is the only commercial production method. Approximately 10% of the heavy oil and bitumen in Western Canada can be recovered by this method (Oil Sands Technology Roadmap, Alberta 2004). A typical picture of this process is shown below in Figure 1.2. There are large oil sand resources near Fort McMurray, Alberta, currently being mined.

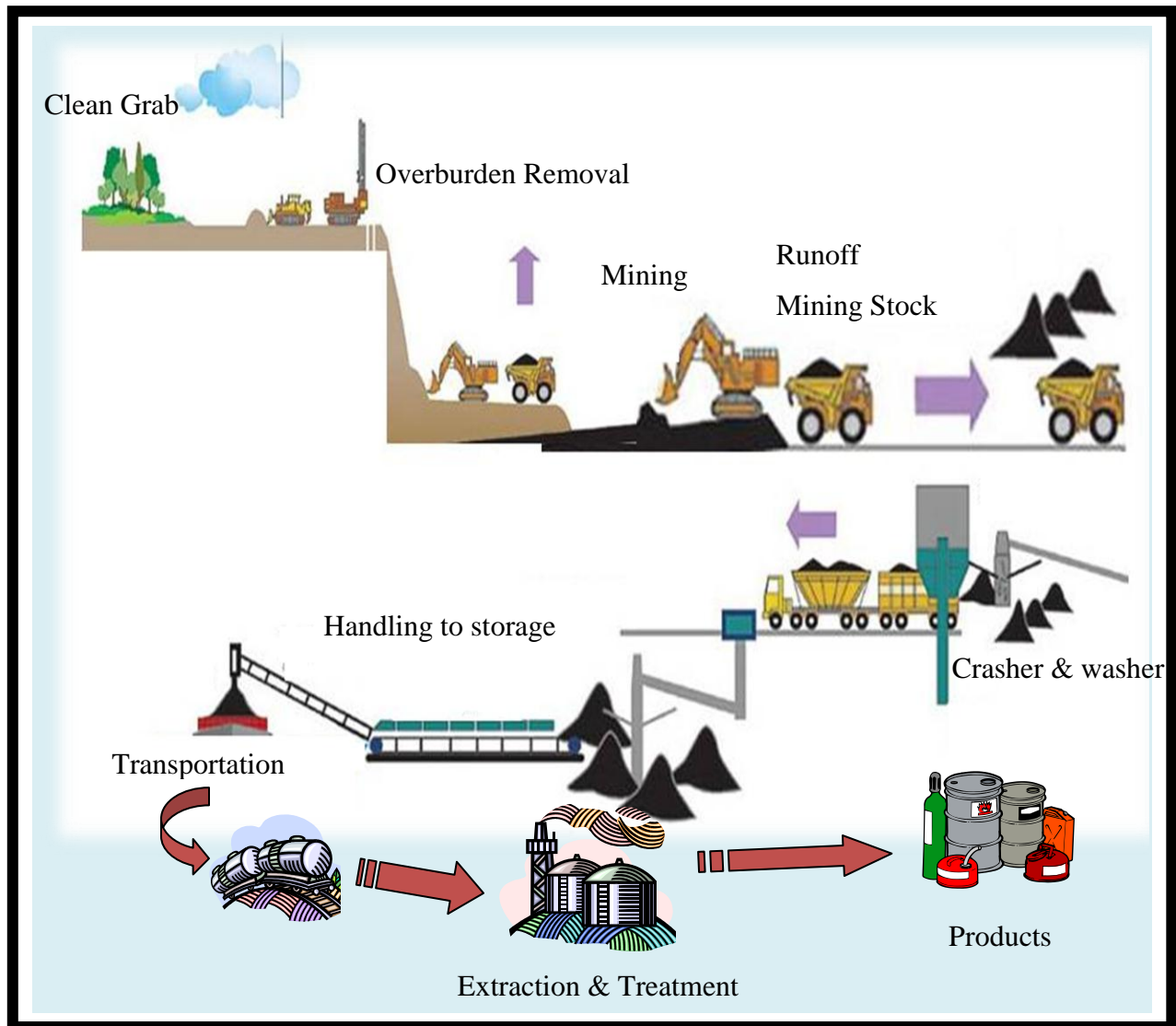


**Figure 1.2** Surface mining process

Mining of Canadian oil sands produced 0.552 million bbl/day in 2005, and will grow to 2.27 million bbl/day by 2020. By comparison, subsurface production of Canadian heavy oil was 0.438 million bbl/day in 2005, and will grow to 1.724 million bbl/day by 2020 (Canadian Association of Petroleum Producers: Canadian Crude Oil Production and Supply Forecast 2006-2020). Hence, mining will produce a significant portion of Canada's heavy oil production for the foreseeable future.



Surface mining of bitumen has been operating commercially for over 40 years and is now a mature technology. The main challenges for the surface mining process are minimizing the environmental impact, land reclamation, and forest restoration. For every cubic meter of synthetic crude produced, 6 cubic meters of sand and 1.5 cubic meters of fine tailings must be transported (Oil Sands Technology Roadmap, Alberta Chamber of Resources 2004). Stockpiled overburden, sand, and tailing ponds can occupy a significant area of the mine, and may have to be moved to access oil sands beneath them.

## **1.4.2 Well Production**

There are a variety of production methods for resources that are too deep for open-pit mining. A brief description of these methods is given below:

### **1.4.2.1 Cold Heavy Oil Production with Sand (CHOPS)**

CHOPS (Cold Heavy Oil Production with Sand) is widely used as a “primary” production approach in unconsolidated sandstones; thousands of wells in Canada are now stably producing oil in this manner.

CHOPS wells are vertical or slightly deviated wells; they are cased and perforated, and a down hole pump is deployed to create an aggressive pressure differential between formation and wellbore pressures. This causes natural gas to break out of solution from the heavy oil, resulting in “foamy oil.” Gas bubbles evolving at the wormhole-sand interface destabilize sand grains and the expanding gas helps move the mixture through the wormholes. Gravity drive on the unconsolidated sands also provides energy for production. At the start-up of production, up to 10% sand by volume is produced along with oil, water, and gas. Sand production eventually falls to under 2% during the well lifetime. The recovery factor for CHOPS wells is low, typically less than 10%. Hence, the well must be drilled, completed, and operated as economically as possible.

CHOPS is used for thin subsurface oil sands (typically 1 to 7 m thick) in Canada, provided the oil sand is unconsolidated and provided the heavy oil contains sufficient solution gas to power the production process (Dusseault B. M., 2002).. To have any natural gas in solution, the oil sand

must be at least a few hundred meters deep. For example, there are a large number of CHOPS wells located near Lloydminster, Alberta. In fact, today CHOPS is the only commercial method for exploiting these thin oil sands. CHOPS wells (by definition) require sand production. Foamy oil production may occur without sand production in other areas. Alternatively, oil maybe produced with sand, but without solution gas in still other areas.

It is believed that CHOPS production occurs with the formation of “wormholes” tunnels that may extend some distance into the formation. There are no current methods for predicting the distribution, location, length, or diameter of wormholes, and there are very limited means of measuring them once formed. Surface seismic may give an indication of their distribution and density. Hence, there is considerable uncertainty about the behavior of CHOPS wells.

#### **1.4.2.2 Cyclic Steam Stimulation (CSS) and Steam Flood**

There are three phases in CSS. First, high-temperature, high-pressure steam is injected for up to one month. Second, the formation is allowed to “soak” for one or two weeks to allow the heat to diffuse and lower the heavy oil viscosity. Third, heavy oil is pumped out of the well until production falls to uneconomic rates, which may take up to one year. Then the cycle is repeated, as many as 15 times, until production can no longer be recovered. Artificial lift is required to bring the heavy oil to surface. Typical recovery factors for CSS are 20% to 35% with steam-to-oil ratios (SOR) of 3 to 5.22.

CSS is often the preferred method for production in heavy oil reservoirs that can contain high-pressure steam without fracturing the overburden. In Canada, the minimum depth for applying CSS is 300 m even though there are some limited locations in other areas where steam injection has been successful at depths between 200 and 300 m. CSS works best when there are thick pay zones (>10 m) with high porosity sands (>30%). Shale layers that reduce vertical permeability are not a problem for vertical wells that penetrate thick pay zones. However, good horizontal permeability (>1 Darcy) is important for production. Recently, CSS has been applied to wells with multilateral horizontal legs.

Steam floods may follow CSS. While CSS produces the heavy oil around a single wellbore, steam flood recovers the heavy oil between wells. For example, a five-spot pattern with four producing wells surrounding a central steam injection well is a common configuration. The well spacing can be less than 2 acres for a field in steam flood. The steam heats the oil to lower its viscosity and provides pressure to drive the heavy oil toward the producing wells. In most steam flood operations, all of the wells are steam-stimulated at the beginning of the flood.

In a sense, CSS is always the beginning phase of a steam flood. In some cases, even the steam flood injection wells are put on production for one or two CSS cycles to help increase initial project production and pay-out the high steam flood capital and operating costs. Technical challenges for CSS and steam flood are primarily related to reducing the cost of steam, which is generated in most locations using natural gas (Lim, et al., 2004).

#### **1.4.2.3 Steam Assisted Gravity Drainage (SAGD)**

In SAGD, two wells with horizontal sections are drilled with one well directly above the other well (see Figure 1.3). The two wells maintain a constant vertical separation of typically 5 m, but 3 to 7 m could be used depending on the oil viscosity. The horizontal sections are typically 500 to 1,500 m long, and are completed with slotted liners to reduce sand production and increase oil productivity. In the start-up phase, steam is injected in both wells to reduce the heavy oil's viscosity. In the production phase, steam is injected in the upper well and heavy oil is produced from the lower well.

Ideally, a steam chamber is formed above the injection well, but does not breakthrough to the lower well. Heat travels by convection of the steam to the edge of the steam chamber, where the steam releases its heat of vaporization to the heavy oil and formation, and condenses into water. The heated oil and hot water drain into the producing well. Because gravity provides the drive rather than steam pressure, the steam injection pressure is lower than that for CSS or steam flood (Roopa and Dawe, 2007).

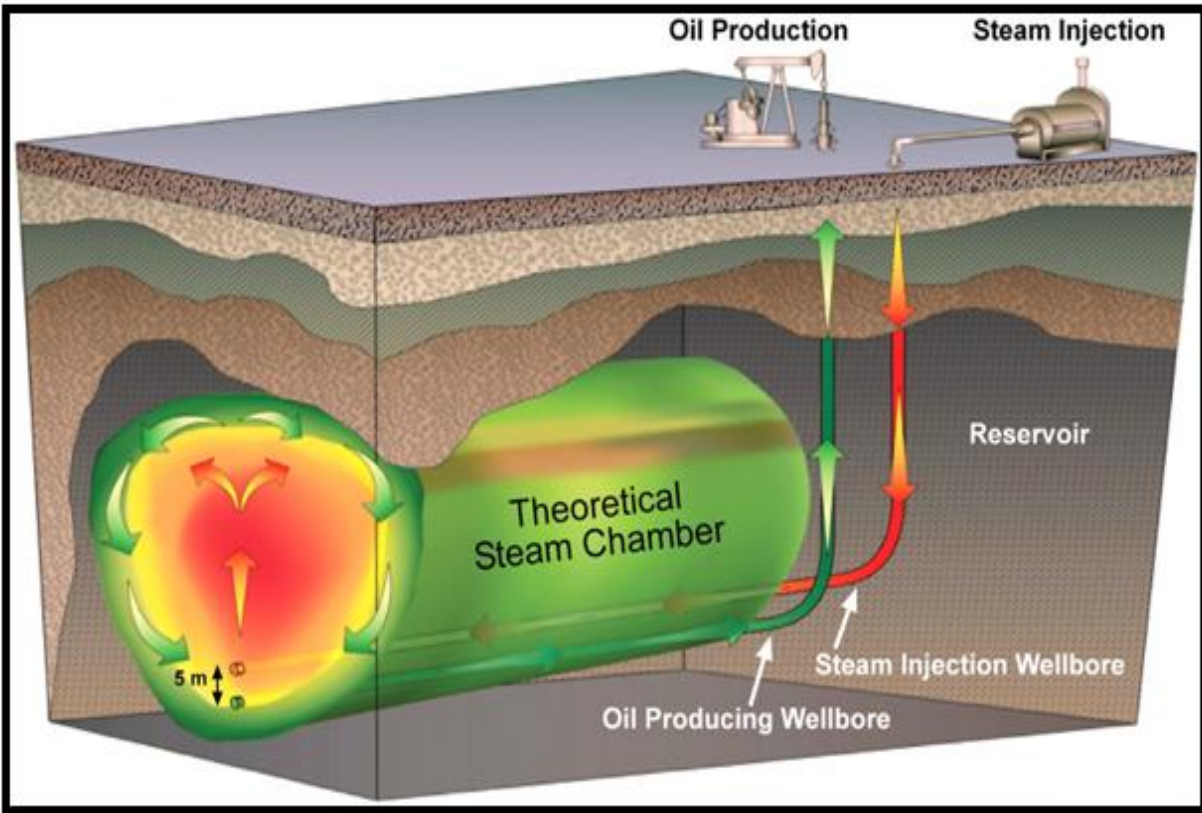


**Figure 1.3** Side view of SAGD process (The Geological Society)

Artificial lift is required to move the viscous oil to surface. Gas lift is the least expensive approach; progressive cavity pumps and electric submersible pumps are more effective, but must survive high temperatures. Production from a pair of SAGD wells is anticipated to last from 7 to 12 years with a relatively constant output over that time. A SAGD well can produce from 500BOPD up to several thousand BOPD. Recovery factors of 50% to 70% are theoretically predicted for SAGD, with SOR values in the range of 2 to 3 (Canada's Oil Sands, 2004). For SAGD to be effective the heavy oil zone must be at least 10 m thick; preferably it is thicker. The formation must have good vertical and horizontal permeabilities; if there are shale layers, the steam chamber cannot form properly. Hence, evaluation of the vertical permeability is important before using SAGD to develop a resource. Gas zones above the heavy oil, or water zones below, may result in heat loss and higher energy costs.

SAGD is a more recent development than CSS or steam floods. SAGD is expanding rapidly in western Canada due to its ability to produce heavy oil from formations too shallow for

conventional steam injection methods. Because SAGD wells operate at lower steam pressures than CSS or steam flood wells, less overburden steam containment is required. SAGD wells can exploit formations from 100 m to a few hundred meters deep. Table 1.2 shows currently used recovery techniques for different oil fields in Alberta.

**Table 0.2:** Alberta bitumen deposits – in place volumes billion m<sup>3</sup> (AEUB, 2005)

Deposit Type	Athabasca	Cold Lake	Peace River	Total	Percent
Thermal Processes	66.8	7.5	8.6	82.9	30.7
Surface Mining	9.4	0.0	0.0	9.4	3.5
Cold Production	2.0	21.0	0.06	23.1	8.6
Total Accessible deposits	78.2	28.5	8.7	115.4	42.8
Deposits with no recovery factors					
Bitumen in Carbonate formation	60.8	0.0	10.3	71.1	26.4
Too thin for thermal recovery Processes	60.4	3.4	1.3	65.1	24.1
Deposits with clay barriers	5.8	0.0	0.0	5.8	2.1
Too deep for surface mining but too shallow for SAGD	4.4	0.0	0.0	4.4	1.6
Deposits with Tar	2.2	0.0	0.0	2.2	0.8
Others	5.7	0.0	0.2	5.9	2.2
Total deposits with no recovery Factors	139.3	3.4	11.8	154.5	57.2
Total Deposits	217.5	31.9	20.5	269.9	100.0

## **1.5 Technologies in Development**

There are several technologies in research, development, or pilot phase that are not yet commercialized.

### **1.5.1 Hybrid Solvent and Steam Processes**

These processes combine solvent with SAGD, to reduce the energy requirements, increase production rates, and oil recovery. In addition, capital investment, CO<sub>2</sub> emission, water and natural gas usage may be reduced. The solvent when mixed with the heavy oil reduces the viscosity and may even provide some in situ upgrading. Pilot testing is underway in a few locations in Canada. High cost and recovery of solvent are critical for success (Nasr and Ayodele, 2006).

### **1.5.2 In-Situ Combustion**

In this process down hole combustion of heavy oil is used to provide the heat to mobilize the heavy oil, and provide some in situ upgrading. This process is also known as fire flooding. Either dry air or air mixed with water can be injected into the reservoir. Ideally, the fire propagates uniformly from the air injection well to the producing well, moving oil and combustion gases ahead of the front. The coke remaining behind the moved oil provides the fuel. Temperatures in the thin combustion zone may reach several hundred degrees centigrade, so that the formation and completion hardware can be severely stressed.

The fire front can be difficult to control, and may propagate in a haphazard manner resulting in premature breakthrough to a producing well. There is a danger of a ruptured well with hot gases escaping to the surface. The produced fluid may contain an oil-water emulsion that is difficult to break. As with output from many heavy oil projects, it may also contain heavy-metal compounds that are difficult to remove in the refinery. In situ combustion eliminates the need for natural gas to generate steam, but significant energy is still required to compress and pump air into the formation.

## 1.6 Introduction to Vapex

Vapor Extraction (Vapex) of Heavy Oil and Bitumen is a promising recovery technology that involves the injection of gaseous solvents into the reservoir (Das, 1997). A solvent dissolves in the high viscosity oil. As a result, the viscous oil gets diluted and drains to the horizontal production well by gravity. The schematic of a typical Vapex process is shown in Figure 1.4. Vapex is a non thermal method in which a light hydrocarbon acts as mobilizing agent instead of steam in SAGD.

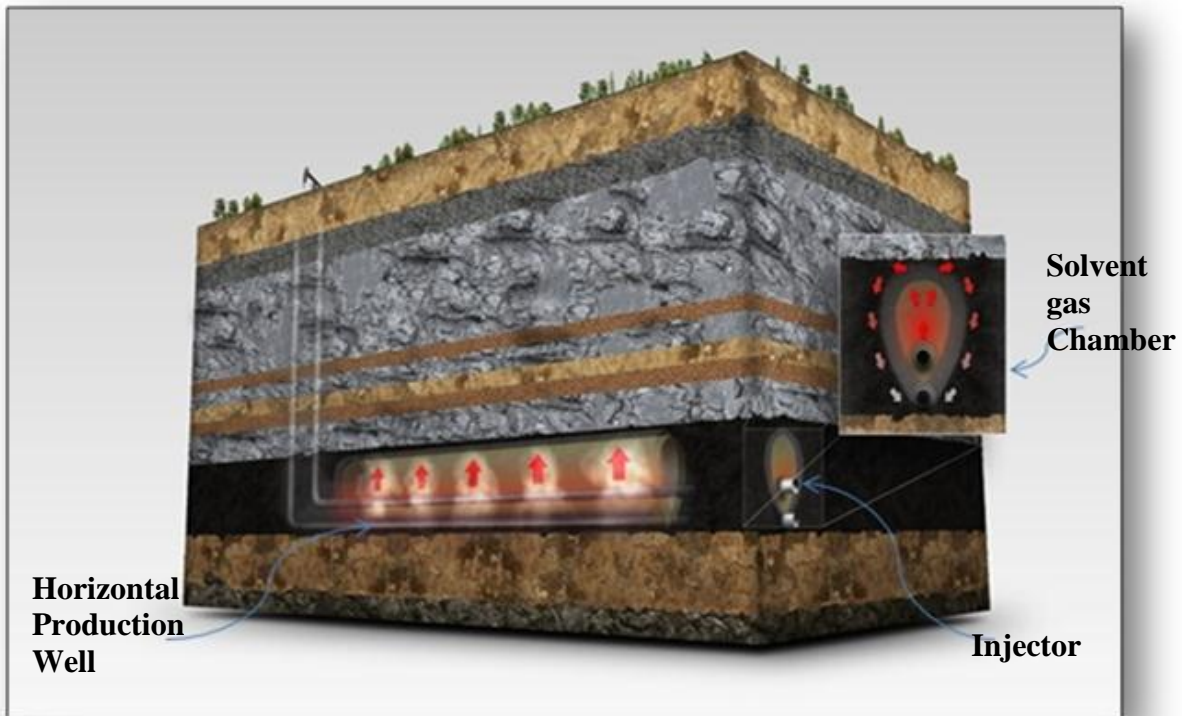


**Figure 1.4** Vapor extraction (Vapex) process

The performance of Vapex process is directly related to the amount of solvent dissolving into the bitumen. The more area of contact between solvent vapor and the crude ensures the higher rate of mass transfer of solvent and higher recovery (Das and Butler, 1996).

Figure 1.5 shows the Vapex chamber formed during Vapex. Das (1998) has described the different mechanisms involved in the Vapex process in detail. The predominant mechanism for

Vapex process is the diffusion of solvent into the heavy oil and bitumen. Production rates are directly related to viscosity reduction, which in turn depends on the amount of solvent dissolved in the oil. Mixing of the solvent with heavy oil and bitumen is slow because it occurs only when solvent diffuses through the pores. Compared to SAGD, the heating of reservoirs is much faster because heat can be carried through at relatively high thermal conductivity of rock as well as in the pores (Butler and Yee, 2002), thus thermal diffusion is much faster than the molecular diffusion required for solvent mixing. Therefore, it is generally expected that Vapex production rates will be much lower than those in a steam process.

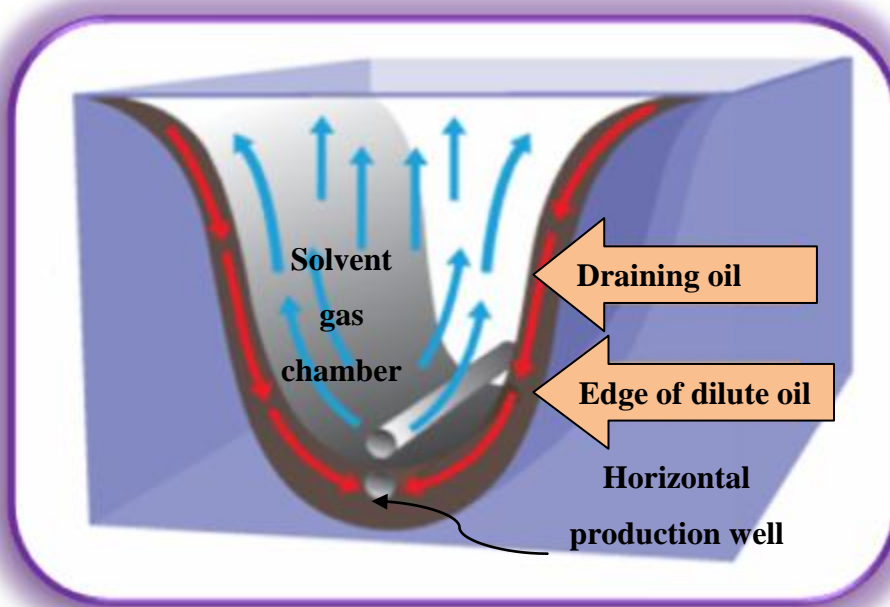


**Figure 1.5** Schematic of vapor extraction (Vapex)

Solvent selection is a critical economic factor in Vapex. The ideal solvent depends on reservoir characteristics such as temperature, pressure and bitumen properties. It is important that the solvent remains in the gas phase to minimize the amount of solvent required to fill evacuated pore spaces. Moreover the diffusivity of gas-liquid is higher than liquid-liquid. The advantage of this process is that natural gas is not required to produce steam, thus providing a savings on energy usage. Vapex process uses only 3% of the energy required by steam processes (Das, 1998). In addition to its superior energy efficiency, this process has many advantages, notably



the absence of costly water treatment installations. Vapex also does some partial upgrading of bitumen to oil right in the formation (Karmaker and Maini, 2003). Moreover, Vapex does away with the emission of large quantities of greenhouse gases inherent in steam generation. Das (2002) estimated that Vapex process produces 80% less green house gas emission than steam assisted gravity drainage process. The main perceived drawback of Vapex is the low drainage rates predicted for real reservoirs compared with drainage rates given by SAGD process. This has hampered the field implementation of the process.

Vapex offers an alternative process to recover bitumen from reservoirs that are not amenable to thermal processes such as reservoirs with bottom water and/or high water saturation, vertical fractures, low porosity and low thermal conductivity. The important factors influencing Vapex are viscosity of heavy oil and bitumen, diffusion of solvent into heavy oil and bitumen, dispersion of solvent with heavy oil and bitumen, deasphalting of heavy oil and bitumen, solvent selection for Vapex, permeability of reservoir and geological factors of reservoir.

The main drawback of the Vapex process is the lower oil production rates compared to SAGD process. The oil production rate is governed by the dispersion phenomenon, which is a combination of molecular diffusion and convective mixing. Thus, the knowledge of dispersion of solvents in heavy oil and bitumen is crucial to optimize the oil production rates.

# 2

## Literature Review

The Vapex process was first developed by Butler and Mokrys (1989) as a solvent analogue to steam assisted gravity drainage (SAGD). Since invention, this process has been the subject of interest of many heavy oil researchers during the last two decades. Below is presented a brief literature survey that focuses on the laboratory-scale advances and the field experiences.

### **2.1 Idea of Vapex Process**

The basic idea for the Vapex process was first introduced by Allen in (1974). He came up with a new technique of injecting hydrocarbon solvents such as butane and propane instead of steam in Cyclic Steam Stimulation process (Allen, 1974; and Allen et al., 1976). After the initial establishments he further enhanced the idea by injecting the blend gaseous phase to overcome the reservoir pressure constraint. He injected the hydrocarbon solvent along with a carrier gas (Allen, 1977).

Butler and Mokrys (1989) further developed the idea of solvent injection and gravity drainage. They modified the Allen's concept by injecting the solvent or their blends in heavy oil reservoir

but with similar well configuration as of SAGD. They named this process “Vapex”. Since then, this process has been the primary focus of interest for many researchers as well as oil industry.

During a typical Vapex process, the hydrocarbon solvent is injected via a horizontal injector well and the oil is produced from a second horizontal well that is parallel placed beneath the injection well. The driving mechanism behind the oil extraction is reduction in the heavy oil viscosity at the solvent oil interface due to vapor diffusion and dilution. This reduced viscosity oil drains towards the production well due to gravity.

## **2.2 Fluid Flow in Vapex Process**

The injection of solvent through the injection well creates a solvent chamber similar to steam chamber as in SAGD. The solvent chamber (Figure 1.5) rises towards the top of the reservoir and expands towards the reservoir boundaries. At the chamber boundaries the solvent in its vapor state comes in contact with the reservoir oil. Due to highest solvent concentration in the vapor chamber and minimum solvent concentration in the oil there presents huge concentration gradient. Due to this, solvent starts to diffuse or dilute into the oil. Azin et al. (2008); Muhamad et al., (2012) discovered that the oil recovery with propane is improved by increasing the injection pressure up to the dew point pressure. Moreover, Vapex is more effective with pure solvent compared to the use of solvent mixtures.

## **2.3 Experimental Methods in Vapex**

Experimental techniques to visualize the performance of Vapex can be divided into the following two classes:

1. Experiments performed in Hele-Shaw Cell.
2. Experiments performed in sand pack models.

The Hele-Shaw cell has been used to study the rate of interface advancement in Vapex for a two dimension system, as well as to understand the growth of vapor chamber. The Hele-Shaw cell consists of two parallel glass plates separated by a uniform gap. The gap between the plates is used to set the permeability of the cell. The cell cavity is formed by sealing three edges of the two parallel glass plates. The cell cavity is then placed in a pressure vessel. The gap between the

plates is filled with heavy oil or bitumen, and the solvent gas is injected to the cell. Gas comes into contact with the oil from the unsealed portion of the cell.

Butler and Mokrys (1989, 1991), Mokrys and Butler (1993), and Das and Butler (1994) performed set of experiments in vertical Hele-Shaw cell using heavy oil and different solvents to investigate different aspects of Vapex process. It was found that experiments performed in Hele-Shaw cell do not represent a real system to investigate the pore scale phenomenon.

The sand packed models has been used to simulate actual porous media. Different geometries of cylindrical and rectangular models filled with porous media have been under investigation. Glass beads with different sizes, or sand with different permeability is used to simulate the permeability of the media. It has been observed that in porous media the process occurs approximately ten times faster than predicted on Hele-Shaw cell results. Butler and Mokrys (1993), Jiang and Butler (1996), Jiang (1997), Butler and Mokrys (1998), Jin (1999), Butler and Jiang (2000), Oduntan et al., (2001), Karmaker and Maini (2003), Yazdani and Maini (2004), and El-Haj (2007) performed such experiments. Table (2.1) from Upreti et al. (2007) lists some of the characteristics of the experimental studies carried out for Vapex.

**Table 0.1:** Characteristics of the experimental studies carried out for Vapex  
(Upreti et al., 2007).

<b>Reservoir Model</b>	<b>Solvent</b>	<b>Heavy oil and Bitumen</b>	<b>Temp °C</b>	<b>Pressure MPa</b>	<b>Permeability Darcy</b>
Scaled and Packed with 1mm glass beads	Hot water and propane mixture, ethane and propane	Tangleflags oil	20-70	0.89-1.55	1150
Scaled and packed with 1mm glass beads	Propane, propane and steam mixtures	Tangleflags North heavy oil	20-26 with propane, 185 with mixture	.708-.984 with propane, 1.1 with mixture	830
Scaled and packed with 1mm glass beads	Butane	Piece River Bitumen, Lloydminster oil	21-22	0.23	20-30,30-50, 50-70 mesh Ottawa sand
Two dimensional multi layer	Butane	Tangleflags Northfield Lloydminster	21-23	0.21-0.23	43.5-217
Packed with silica sand	Ethane	Cold Lake Bitumen	20-33	0.83-4	80-110
Scaled and packed with 1mm glass beads	Propane	Tangleflags Heavy oil, Peace River Bitumen	20-23	0.8-1	20-30 30-50,50-70 mesh Ottawa sand

**Table 0.1:** Characteristics of the experimental studies carried out for Vapex.  
(Upreti et al., 2007).

<b>Reservoir Model</b>	<b>Solvent</b>	<b>Heavy oil and Bitumen</b>	<b>Temp °C</b>	<b>Pressure MPa</b>	<b>Permeability Darcy</b>
Packed with 20-30 mesh Ottawa sand	Propane, butane and mixture with non condensable gas	Atlee Buffalo Oil	21–27	0.31–2.2	220
Angled rectangle micro models	Butane	Peace River	19–22	0.21–0.23	55-192
Packed with 20-30 mesh Ottawa sand	Propane, butane and mixture with non condensable gas	Atlee Buffalo Oil	21–27	0.31–2.2	220
Hele-Shaw cell	Propane	Dover and Penny Bitumen	10–23	Below dew point	
Angled rectangle micro models	Butane	Peace River	19–22	0.21–0.23	55–192
Annular Model packed with glass beads	CO2 propane, methane propane	Oil viscosity 3.3 pa.s at 24 °C	23–24.9	1.82-4.23	648
Rectangular and packed model	n-butane	Oil viscosity 18.5 pa.s at 15 °C	15	0.17	223–648
Rectangular sand packed model	Methane propane	Oil viscosity of 40 Pa.s at 10 °C	10,19	1.2	2-8

## **2.4 Effect of Petro Physical Properties on Vapex Performance**

Jiang (1997) studied the effect of reservoir homogeneity and heterogeneity both homogenous and heterogeneous reservoir packed model and Tangle flags, Peace River and Atlee Buffalo heavy crudes with butane and propane as solvents. He investigated the effects of well spacing, well configurations, permeability, temperature, viscosity of original oil and solvent injection rates on the Vapex performance. He found that the effect of reservoir heterogeneity is more important when a continuous low-permeability layer or shale is present.

Butler and Mokrys (1998) investigated the effect of aquifers on Vapex process by performing the experiments Peace River and Lloydminster heavy and using propane as injected solvent. They concluded that the presence of aquifers helps in mixing the solvent more effectively and efficiently and results in increased process performance.

Butler and Jiang (2000) studied the effect of major petro physical parameters like well spacing and configurations on the performance of Vapex process. They discovered that wider lateral well spacing allow higher production rate but with a compromise on the injection and production wells communication time.

Yazdani and Maini (2005) investigated the effect of drainage height and grain size on production rates in the Vapex process. The primary objective of their work was to develop an improved scale up method for Vapex process using physical model experiments carried out with different model sizes. The authors proposed a new correlation for scaling up the experimental data to field cases. As per the correlation the height dependency of the convective dispersion contribution (which can be the dominant mass transfer mechanism in Vapex process) to be higher order than previously reported in the literature. The authors concluded that stabilized oil production rates in Vapex process is a function of drainage height to the power of 1.1 to 1.3 instead of square function as reported by the Butker and Mokry's (1989) model.

Azin et al (2007) studied the effect of fractures on the Vapex performance. They used a rectangular physical model to evaluate the effect of vertical and horizontal fractures on Vapex performance. They concluded that the availability of the fractures in the reservoir increases the solvent oil contact area that improves the cross flow of solvent and oil between the fracture and the matrix. Consequently increases the area for solvent diffusion into the reservoir fluid.

Rahnema et al. (2007) investigated the well configuration and the lateral spacing in reservoirs containing gas cap. Based upon the experimental data, they developed a numerical model and utilized it to simulate a two dimensional sand-packed reservoir. They concluded that optimum well location for injection well was near oil and gas contact. Moreover, they showed that the lateral spacing between production and injection wells has a negligible effect on the ultimate oil recovery.

Moghadam et al. (2007) examined the effects of varying permeability on Vapex performance using pure propane as injected solvent. They showed that at permeability range up to 100 Darcies the heavy oil production rate is dependent on the square root of permeability.

Zeng et al. (2008) investigated a tee-well pattern that enhanced the oil flow rate two to ten times over the classical Vapex process. They proposed a well pattern consisted of additional horizontal injectors, perpendicular to the injector and the producer in classical Vapex, which were placed in the top-most region of the reservoir. In this pattern, the heavy oil was solvent contacted and diluted in both axial planes.

Yazdani and Maini (2010) designed an experimental set-up and performed a series of PVT experiments for Frog Lake heavy oil using butane as a solvent. From the experiments they measured the mixture density, dissolved solvent mass fraction, and mixture viscosity at different saturation pressures at a constant temperature. They used the experimental data to tune the Peng Robinson EOS for their particular heavy oil and solvent system. The results showed that a two component model would predict the experimental data and is sufficient to be used in the



numerical simulation of Vapex process. The authors also concluded that many of the available viscosity correlations in the literature are not suitable for the heavy oil systems with necessary adjustments.

Fatemi and Bahonar (2010) evaluated the effects of fractures geometrical properties on Vapex performance. They studied the fracture orientation, the fracture length, the fracture discontinuity in both the far well region and the upper well region, and the vertical fracture location. They also assessed the effects of horizontal and vertical fracture dispersion in various density, dispersion scheme and networking on the performance of the Vapex process. In their work, a fracture's discontinuity effect has been scrutinized in the presence of parallel-piped networked fractures. This confirmed the results in the case of either vertical or horizontal fractured matrices. They found that the Vapex process enhanced the performance in the case of longer vertical fractures, shorter horizontal fractures, lower horizontal fracture dispersion, and lower vertical fracture discontinuity.

Alkindi et al. (2010) assessed the role of reservoir thickness on the drainage rates during a Vapex process. They found that drainage rates had a higher than square root dependency on the height of the standard analytical model of Butler-Mokrys.

## **2.5 Effect of Asphaltene Precipitation on Vapex Performance**

Asphaltene precipitation is the most important physical phenomena occurring during the Vapex process. At the solvent oil interface, when solvent diffuses in the oil it changes its phase from vapor to liquid. Due to this phase change there is alteration in the temperature, pressure and concentration at the contact point. Due to these three parameters change the process of asphaltene precipitation takes place. After the asphaltene precipitation occurs, the produced heavy oil is in-situ deasphalted and thus has a lower viscosity, more mobility and better quality. On the other hand, deposited asphaltenes may change the matrix wettability to oil wet and thus decrease its permeability. Moreover, the precipitated asphaltenes may plug some small pores of the reservoir formation and thus reduce its permeability.

Nghiem et al. (2000) discussed the results of phase behavior calculations and compositional simulation of asphaltene precipitation in the Vapex process. They used a sand packed model saturated with Athabasca heavy oil and propane as a solvent. The authors concluded that deasphalting can affect the viscosity of solvent diluted oil. In situ de-asphalting reduces the oil viscosity and leads to higher production, but the precipitated asphaltenes also plug the formation pores and cause severe damage to the permeability.

Frauenfeld et al. (2004) investigated a bottom water Vapex process and they reported that no significant asphaltene precipitation and upgrading were noted. However, they predicted that by increasing the solvent loading, it might be possible to initiate asphaltene precipitation and thus further reduce oil viscosity.

Luo and Gu (2005) assessed the respective and synergistic effects of solvent concentration on heavy oil viscosity by measuring the solvent concentration in heavy oil samples. The result showed that solvent dissolution played a dominant role in heavy oil viscosity reduction. When the equilibrium propane concentration is high enough, the heavy oil-propane system had extremely low viscosity. They compared the effect of asphaltene removal and solvent dissolution on reduction the heavy oil viscosity and they found that the effect of asphaltene removal was negligible.

Haghighat and Maini (2008) studied the role of asphaltene precipitation in Vapex process. They studied experimentally whether the beneficial effects of asphaltene precipitation will outweigh any formation damage. They showed that the oil produced at higher injection pressures was substantially upgraded but the viscosity reduction by asphaltene precipitation did not lead to higher rates of production. In other hand, the effect of viscosity reduction was negated by the accompanying damage to formation permeability.

Kok et al. (2008) compared the asphaltene precipitation during propane and butane injection and revealed that propane gave better results than butane. Ardali et al. (2009) used low permeability

sand packed models in both dry and non-dry systems and they assessed the performance of Vapex process when asphaltene precipitation/deposition occurred. They observed that adsorption of asphaltenes had decreased in non-dry systems. Movement of precipitated asphaltene and less adsorption in non-dry experiments resulted in more stable Vapex processes while in dry experiments higher adsorption of asphaltenes resulted in plugging of low permeability porous medium.

Pourabdollah et al. (2010) investigated the effect of matrix permeability and vapor dew point on the movement of deposited asphaltenes in this process. Moreover, the distribution of asphaltenes, resins, residual hydrocarbons, and metal chelates was determined. They measured the asphaltene resin, and vanadium chelates in residual hydrocarbon of swept zone. According to the results of their experiments with high permeable matrices close to the solvent dew point, the precipitated streaks moved faster than other conditions. Distributions of measures substances showed a reduction in their interfacial concentration from the vapor injection to the oil production ports. But the distribution of dissolved vanadium chelate in asphaltene and resin precipitated followed a reverse pattern.

## **2.6 Optimization of Vpaex**

Kok et al. (2008) used a Hele Shaw cell model filled with light crude oil with API gravity of 26° API. They used butane and propane as a solvents and injected the fluids at three injection rates of (20, 40, and 80 ml/min). They found that for both the solvent, the recovery rates increased with injection rates. Instantaneous asphaltene rate showed fluctuated performance with propane solvent, while the butane showed almost constant degree of asphaltene precipitation.

In the Vapex process, the solvent vapor chamber has to be maintained at pressures lower than the solvent vapor pressure to prevent the extracted region from being filled with liquid. Das and Butler (1995) studied the potential for injecting a non-condensable carrier gas along with the solvent to increase the operating pressure. To achieve the maximum solubility, they proposed to inject a leaching liquid solvent to be vaporized and carried to the bitumen interface by the carrier

gas. They named this technique as the BUTEX process. Karmaker and Maini (2003) briefly discussed the effect of reservoir aquifer, gas cap reservoir, well configuration, process operation, the heavy oil viscosity and temperature as well as the solvent injection scheme and well spacing in the Vapex process. Glass beads with different sizes, or sand with different permeability is used to simulate the permeability of the media. The results show that much higher oil rates in field processes are possible compared to those predicted by previous investigators based on the results from Hele-Shaw cell experiments and the available scale-up procedure.

## **2.7 Mass Transfer Mechanism in Vapex**

The performance of Vapex is directly related to the amount of solvent dissolving into the heavy oil. Solvent transfers into the heavy oil by the transport mechanism of dispersion. Dispersion is a combination of molecular diffusion and convective dispersion. More detail will provide for diffusion and dispersion of the solvent-heavy oil in the following sections.

### **2.7.1 Diffusion of Solvent Gases in Heavy Oil**

Three distinct stages are involved in the molecular diffusion phenomena of an injected gas into heavy oil. First, the gas moves towards the oil-gas interface, then the gas penetrates the interface, and finally the penetrated gas diffuses in the oil body. The accurate diffusion data for solvent-heavy oil systems are necessary to determine the amount of gas required, the extent of heavy oil reserves, the required time and the rate of oil production (Aconcha et al., 2008 ).

The molecular diffusion coefficient is not a constant. It varies with temperature, concentration and pressure. In most of the published literature on molecular diffusion measurements in hydrocarbons, the calculations are based on the assumption that the diffusion is constant over the concentration range used in the experiments. However, Oballa and Butler (1989) studied the diffusion process in toluene-bitumen system and found that the overall diffusion coefficients were strongly dependent on the concentration of the solute.

James 2009 investigated the mass transfer mechanism during the solvent recovery of heavy oil. The author designed the experiments to capture the rate of solvent mass transfer into the bitumen

by measuring the bitumen swelling and the butane uptake independently. The author developed a mathematical model to predict the bitumen swelling using a concentration dependent diffusivity. Using the non-linear regression function in Matlab and independently validating the results using the solvent uptake the authors the diffusivity of butane in heavy oil at 25°C to be  $D_{sb} = 4.78 \times 10^{-6} \omega_s + 4.91 \times 10^{-6} \text{ cm}^2/\text{s}$  where  $\omega_s$  is the solvent mass fraction.

Das and Butler (1996) obtained empirical correlations for the diffusion coefficients of propane and butane in bitumen. The diffusivity showed a strong dependence on viscosity. The dependence of diffusivity on viscosity and the dependence of viscosity on solvent concentration imply that diffusivity in heavy oil is a function of solvent concentration.

Upreti and Mehrotra (2000) obtained similar results as the concentration profiles for the sorption of carbon dioxide in Athabasca bitumen indicated that the diffusivity is concentration dependent. Table (2.2) indicates some of the available correlations for diffusivity estimation.

**Table 2.2** Different correlations for diffusivity estimation

Reference	Gas	Bitumen	Diffusivity Correlation
Hayduk& Cheng, 1971	Variety of solvents	11 different solute	$D = \alpha\mu^{-\beta}$
Hiss &Cussler, 1973			$D = \alpha\mu^{-2/3}$
Hayduk et al., 1973	Propane	Peace River	$D = 0.0591 \times 10^{-9} \mu^{-0.545}$ $D \text{ (m}^2\text{/s); } \mu \text{ (Ps)}$
Hayduk&Minhas, 1982	Propane	Peace River	$D = 13.3 \times 10^{-8} T^{1.47} V_a^{0.71} \mu^{(10.2/V_a - 0.791)}$ $D \text{ (cm}^2\text{/s); } \mu \text{ (cP)}$
Das and Butler, 1996	Propane	Peace River	$D = 1.306 \times 10^{-9} \mu^{-0.46}$ $D \text{ (m}^2\text{/s); } \mu \text{ (Ps)}$
Das and Butler, 1996	Butane	Peace River	$D = 4.131 \times 10^{-9} \mu^{-0.46}$ $D \text{ (m}^2\text{/s); } \mu \text{ (Ps)}$
Upreti and Mehrotra, 2002	CO <sub>2</sub> , CH <sub>4</sub> C <sub>2</sub> H <sub>6</sub> , N <sub>2</sub>	Athabasca bitumen	$\ln D = d_0 + d_1(T + 273.15)$ $D \text{ (m}^2\text{/s)}$

### 2.7.2 Dispersion of Solvent Gases in Heavy Oil and Bitumen

For a Vapex process the dispersion of solvent in porous media can be explained as a combined effect of molecular diffusion, convective motion, surface renewal, viscosity reduction and gravity drainage. In the extraction of heavy oil and bitumen using vaporized gases, as the gas diffuses into oil, it swells and gets diluted and drains under the action of gravity. As the oil drains the covered surface of heavy oil gets exposed to gas. That is how oil surface renewal takes place along with gas diffusion.

Kapadia et al. (2006) developed and simulated a mathematical model to determine gas dispersion during the vapor extraction of Cold Lake bitumen from a rectangular block of homogeneous porous medium using butane. The gas dispersion and heavy oil and bitumen viscosity were considered to be dependent on concentration. The dispersion coefficient was found to be four orders of magnitude higher than reported molecular diffusion.

El-Haj et al. (2009) studied the butane dispersion in the Vapex process using butane solvent at the dew point pressure, Athabasca bitumen and sand packed cylindrical model with different permeabilities. They developed a mathematical model for solvent transfer into the matrix and determined the concentration-dependent dispersion coefficient of butane optimally by matching the experimental live oil production with the model-predicted one. The results were obtained for three different permeabilities. They minimized the root-mean-squared fractional error between the experimental and the calculated production to determine the optimum interfacial mass fraction and dispersion coefficient of butane. The dispersion coefficients were determined to be  $9.8 \times 10^{-8} \text{ m}^2/\text{s}$ ,  $9.5 \times 10^{-8} \text{ m}^2/\text{s}$  and  $9.4 \times 10^{-8} \text{ m}^2/\text{s}$  for 110, 157 and 180 Darcy permeabilities, respectively. The dispersion coefficients were three orders of magnitude higher than the molecular diffusion of butane in the heavy oil.

Abukhalifeh et al. (2010) developed a technique to determine the concentration-dependent dispersion coefficient of a propane as a solvent in the Vapex process via a mass transfer model and a computational algorithm to compute the solvent dispersion as a function of its concentration in heavy oil. Figure 2.1 presents the differential element of the physical model. The unsteady state mass balance for solvent propane over a differential element of the medium was derived. Equation (2.1) described the mass balance of the mass transfer model that applied to the physical model. Based upon their experimentally results, they showed that dispersion of propane was a unimodal function of its concentration in bitumen.

$$\frac{d}{dt}(V\phi\rho\omega) = (vA\rho\omega)_{z+\Delta z} - (vA\rho\omega)_z + (J_f S\phi)_{r+\Delta r} - (J_f S\phi)_r \quad (2.1)$$

where  $V = 2\pi r \Delta r \Delta z$  the volume of the element,  $A = 2\pi r \Delta r$  is the area transverse to the live oil velocity  $v$  in the vertical direction, and  $S = 2\pi r \Delta z$  is the area transverse to the dispersive flux  $J_f$  in the radial direction. The final equation of the mass transfer model was given by

$$\frac{\partial \omega}{\partial t} = \frac{1}{r} \left[ D \left( \frac{\partial \omega}{\partial r} \right) + r D \left( \frac{\partial^2 \omega}{\partial r^2} \right) + r \left( \frac{\partial D}{\partial \omega} \right) \left( \frac{\partial \omega}{\partial r} \right)^2 \right] - \frac{1}{\phi} \left[ v \left( \frac{\partial \omega}{\partial z} \right) + \omega \left( \frac{\partial v}{\partial \omega} \right) \left( \frac{\partial \omega}{\partial z} \right) \right] \quad (2.2)$$

where  $\omega(t, r, z)$  is the mass fraction of solvent in bitumen, which is a function of time, radius, and height of the porous medium where  $D$  is the undetermined concentration-dependent dispersion coefficient;  $v$  is the Darcy velocity of the live oil

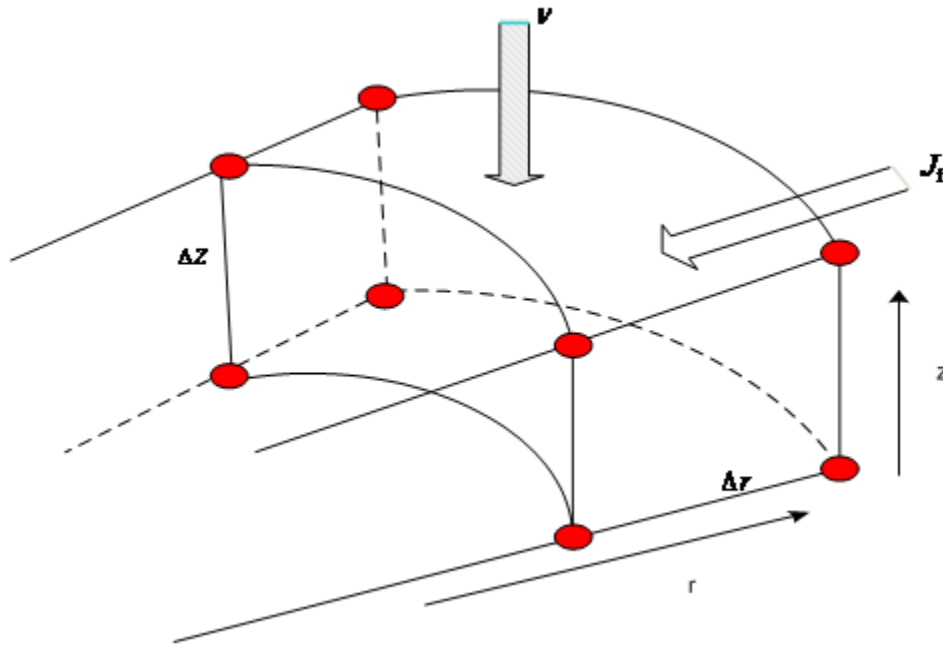


**Figure 2.1** Differential element of the physical model (Abukhalifeh et al., 2010)



## 2.8 Operating Pressure in Vapex

The operating pressure stands for the solvent injection pressure during Vapex. This pressure is a crucial factor that affects the heavy oil production rate in the Vapex process because the solvent state is strongly dependent on the operating pressure. As one of the major factors for asphaltene precipitation, the operating pressure influences oil production rate significantly. Most researchers (Butler and Mokrys, 1991; Das and Butler, 1998; Butler and Jiang, 2000; Boustani and Maini, 2001) conducted their experiments at an operating pressure close to the solvent injection pressure, under which a higher oil production rate might be obtained. The detailed effect of the operating pressure on heavy oil production rate in the Vapex process has been studied by Das and Butler (1995). They tested two different pressures of 779 and 434 kPa by using butane as an extraction solvent and nitrogen as a carrier gas to increase the operating pressure. Their results showed that the operating pressure did not have a significant effect on the oil production rate if a gas mixture was used to extract heavy oil.

Furthermore, Butler and Jiang (2000) studied the effect of an operating pressure on the heavy oil production rate in the Vapex process. Two experimental tests were conducted at the operating pressure of 2,140 and 1,360 kPa and temperature of 27°C with propane and butane as an extracting solvent mixture, respectively. Their results showed that for the first four hours, two experiments gave almost the same oil production rate, which is due to the initial connection between the injector and producer. During the solvent chamber spreading phase, experiment at lower operating pressure gave a higher oil production rate than that at higher operating pressure. An average oil production rate during the entire experiment was reduced by approximately 8% at an increased operating pressure. It was probably because less gaseous solvent is available at the increased operating pressure due to phase change so that the amount of solvent dissolved into heavy oil becomes less.

It has to be kept in mind that the above studies did not consider the variation of solvent injection pressure with time as a means to influence oil production in Vapex. Providing a proof-of-concept for this approach, formalizing it, and validating it to enhance oil production in Vapex is the novel contribution of the present study.

## 2.9 Optimal Control

An optimal control is a function that optimizes the performance of a system changing with time, space, or any other independent variable (Upreti, 2012). Optimal Control is a superset of optimization that deals with the determination control functions for a given system that will maximize or minimize a specific performance criterion subject to constraints describing the system dynamics (Ray, 1981).

Optimal Control is different than that the classical process control, which is generally a trial and error process in which various methods of analysis are used iteratively to determine the design parameters of an “acceptable” system. Acceptable performance is generally defined in terms of time and frequency domain criteria such as rise time, settling time, peak overshoot, gain and phase margin, and bandwidth. Radically different performance criteria must be satisfied, however, by the complex, dynamic systems required to meet the demands of modern day technology.

For example, consider a well-mixed batch reactor with chemical species A and B reacting to form a product C. The reactivities are dependent on the reactor temperature. Such a system is described by species material balances, or equation of change. They are differential equations with time as the independent variable. An optimal control problem for this system is to find the reactor temperature versus time function, the application of which maximizes the product concentration at the final time. That function is the optimal control among all possible control functions (Upreti, 2012).

### 2.9.1 Optimal Control and Optimization

Optimal Control is the optimization of an objective functional subject to the equations of change in a system, and additional constraints, if any. Because of this fact, Optimal Control is also known as dynamic or trajectory optimization. The salient feature of Optimal Control is that it uses functions as optimization parameters. A control function used in optimal control is made of a number of values, one for each value of the independent variable. That number is infinity if at least a portion of the function is continuous. Hence, from the standpoint of traditional

optimization, Optimal Control is equivalent to multi-parameter optimization. With a significantly greater number of parameters available to optimize in general, optimal control unleashes an infinite region to search for optimal solutions otherwise out of reach of traditional optimization (Upreti, 2012).

The literature survey presented above briefly discussed the efforts done by different researchers in the last two decades to understand the transport mechanism in Vapex as well as recognize important parameters to increase the performance. Although Vapex researchers have been trying to investigate the effect of important parameters such as solvent injection rates, injection pressure, oil viscosity, and pressure on oil production, no one has applied Optimal Control for this purpose. In this work, we apply Optimal Control to determine the optimal solvent injection pressure versus time policy, which maximizes oil production in Vapex.

## **2.10 Objectives of Current Study**

The objectives of this study are as follows:

1. To prove experimentally that oil production in Vapex can be increased by suitably varying solvent injection pressure with time, i.e. by utilizing solvent pressure versus time as a control function.
2. To utilize the theory of Optimal Control to determine optimal solvent injection pressure versus time function (or policy) to maximize oil production in Vapex.
3. To experimentally validate the optimal policy determined in the last step for different solvents in Vapex.

## **2.11 Structure of the Dissertation**

This dissertation is organized in seven Chapters.

**Chapter 1** provides a brief background of heavy oil, recovery methods, heavy oil reserves, oil recovery processes, and Vapex.

**Chapter 2** provides a literature review on Vapex. The topics include the concept of Vapex, experimental methods, effect of petro-physical properties on Vapex performance, effect of

asphaltene deposition and precipitation on Vapex, optimization of Vapex, mass transfer in Vapex, operating pressure in Vapex, and a brief introduction to Optimal Control leading to the objectives of the present study.

**Chapter 3** provides the details of setups used to run the proof-of-concept experiments. The experiments employ two different heights of the physical reservoir models, three different permeabilities, and different pressures.

**Chapter 4** presents Optimal Control of Vapex. The optimal control problem is formulated. The necessary conditions are derived for the maximum of the oil production. An optimal control algorithm is developed to determine optimal solvent injection pressure versus time policy to maximize oil production in Vapex.

**Chapter 5** presents the results of proof-of-concept experiments. Next, it provides the optimal solvent injection pressure versus time policies obtained from the optimal control algorithm. The results of the validation experiments are included in the end.

**Chapter 6** summarizes the contributions of this research. The future work and recommendations are presented in this final chapter.



# 3

## Experimental Setups and Procedures

This chapter describes experimental setups and procedures used to perform different experiments in this study. The generated experimental data were used to calculate the live oil viscosity, density, cumulative production rate, solubility of solvent gas in heavy oil and maximum interfacial solvent concentration as function of injection pressures. The details of experimental permeability determination are also incorporated.

### **3.1 Main Experimental Setups**

The main experimental setups were designed and built in this study are

1. Vapex setup
2. Interfacial concentration setup

#### **Vapex Setup**

The Vapex setup was used to perform

- i) the following proof-of-concept experiments:
  - a. Oil production using constant injection pressure of pure solvents.
  - b. Oil production using the temporal variation of solvent injection pressure was varied to examine the effect on oil production injection.

These experiments were used to realize the possibility of positive reinforcement of varying solvent injection pressure on oil production in Vapex.

- ii) the validation of the optimal solvent injection pressure versus time policies determined from the optimal control algorithm.

## **Interfacial Concentration Setup**

This setup was used to correlate the injection pressure of a solvent to its concentration at the solvent-oil interface during Vapex. This evaluation was required to map the optimal interfacial solvent concentration versus time obtained from the optimal control algorithm to solvent injection pressure versus time policy.

The details of the experimental setups and procedures are as follows.

### **3.1.1 Vapex Setup**

The schematic of the Vapex setup used in this work is shown in Figure 3.1. This setup was used to perform Vapex experiments in order to study the production rates of the live oil and measured the required data to calculate the dispersion coefficient of solvent gas into the heavy oil as well as variation of injection pressure to enhance oil production rate in Vapex process. The picture of the experimental setup is shown in Figure 3.2. The experiments were performed using two electronically regulated proportional valves (Model, PV101-10V, Omega Engineering, Inc. Canada) to control pressure.

The setup consists of a cylindrical pressure vessel of 15 cm internal diameter and 80 cm height with the arrangement of a load cell (LC, capacity: 4500 g, LSB200, JR S-Beam , provided by FUTAK advance sensor technology. INC., Irvine, CA, USA), and monitoring instruments for

temperature of the vessel, pressure inside the vessel, temperature of the sample and temperature of water bath. Proportional control valves are placed in the butane gas line and the other is attached to the pressure vessel. The pressure inside the vessel is either kept constant or temporally varied. The vessel is placed inside a temperature-controlled water bath. The temperature controller is designed to maintain the temperature within  $\pm 0.5$  °C of the set point.

In a given experiment, oil saturated porous medium with glass beads of known size was packed in one of the cylindrical models comprising of a stainless steel wire mesh and attached to the load cell hook, fitted on the top flange of the pressure vessel. The load cell was used to record the weight change in the sample model resulted from dispersive action of the solvent gas that dilute the heavy oil.

All the temperature sensors, pressure transducers, flow meter of input gas, load cell, and two pressure valves were connected to a data acquisition system (DAS), which was connected to a computer.



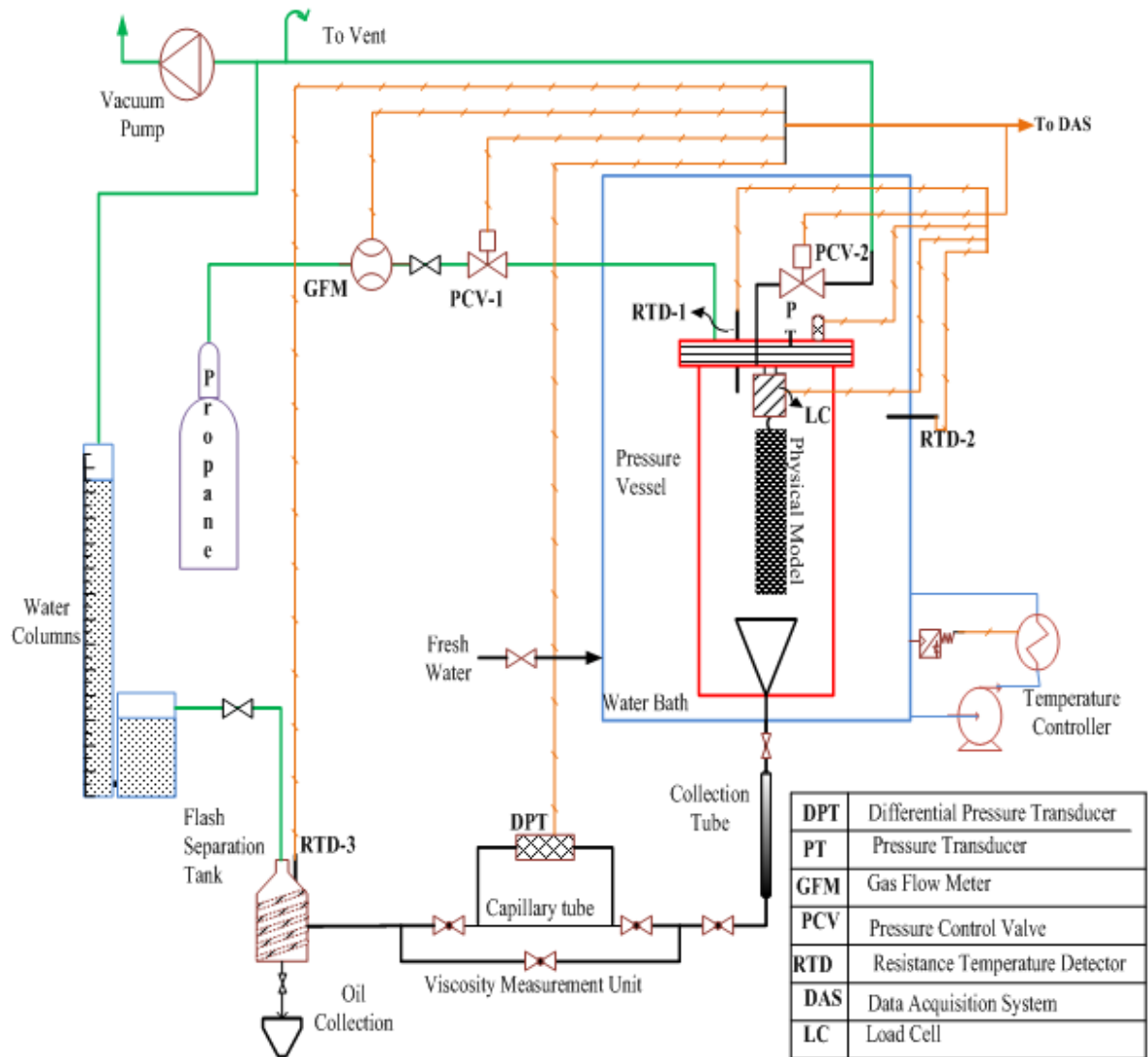


**Figure 3.1:** Schematic diagram of the Vapex experimental setup

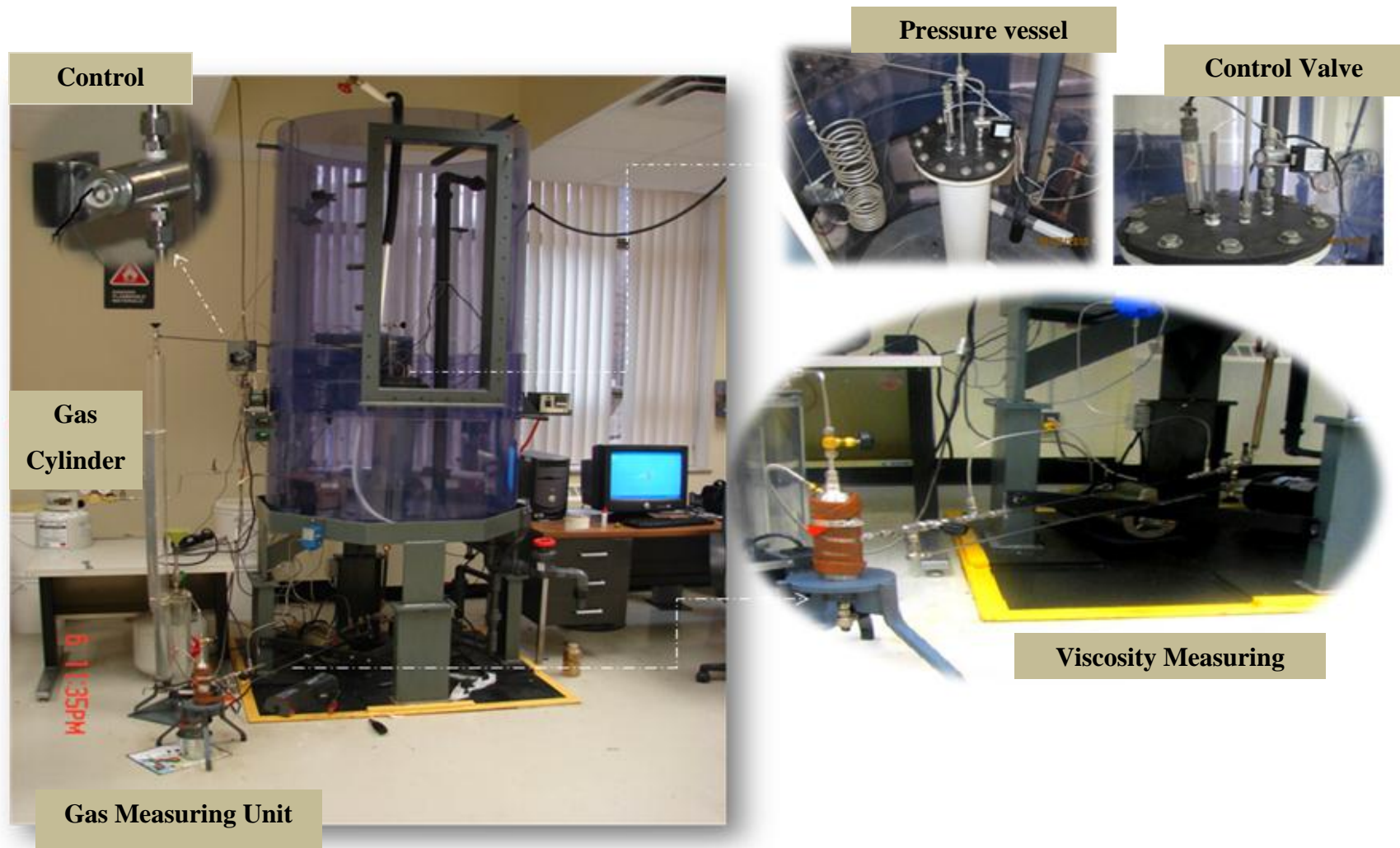


**Figure 3.2** Picture of the Vapex experimental setup

LabView version 7.1 software provided by National instruments was used for graphical user interface and online monitoring of all input and output data of the setup. Research grade butane and propane with purity of 99.99% (MEGS specialty gases Inc., Montreal, Quebec) were used as solvents at laboratory ambient temperature, which varied between 21°C and 22°C, for all experiments.

To collect the produced oil, a small carbon steel funnel at the vessel bottom was used. The funnel collected the diluted drain oil and directed it towards the collection tube calibrated to 25 cm<sup>3</sup>. The collection tube was connected to a stainless steel capillary tube of length 50 cm with an internal inside diameter of 0.1016 cm. The capillary tube was used to measure the viscosity of live oil. A differential pressure transducer was connected to both ends of the capillary tube. Through the capillary tube, oil was directed to a stainless steel flash tank with holding capacity of 300 cm<sup>3</sup>.

The flash tank was wrapped with an electrical heating tape (HTWC 101, heat tape with controller) and a controller to maintain the temperature of the live oil. Flash separation tank was used to remove the dissolved solvent gas from the produced live oil.

### **3.1.1.1 Experimental Procedure**

Before starting an experiment, the vessel was pressurized with air and leak-tested for no detectible pressure decay for 12 h. The physical model was vertically suspended inside the pressure vessel from the load cell (see Figure 3.1). After sealing the vessel, the leak test was performed again for a short period of time to ensure proper sealing of the vessel. Air was purged from the entire setup by applying vacuum close to -15 mm Hg (gauge) using a vacuum pump. To ensure complete displacement of dead air, the entire system was flushed with solvent gas for 15 min and vacuumed again. Butane or propane close to the dew point pressure corresponding to room temperature (21°C) was injected from the top port into the vessel exposing the physical model from all around. Resistance temperature detectors were used to measure the temperature of physical sample, solvent gas, flash tank, and water bath. Research grade butane or propane of purity 99.99% were used individually in the experiments. The flow of solvent gas to the pressure vessel was monitored by a flow meter (Model No: FMA-1605, Maximum Pressure 125 psia).

The injection pressure was controlled through two pressure control valves installed on the setup. With solvent gas absorption, the heavy oil in the exposed external pores of the porous physical model became less viscous and began to drain into a collection tube as live oil. The load cell recorded a decrease in the mass of the physical model every minute as the production continued.

The concentration of solvent gas at the interface where oil and gas are in contact is the maximum concentration of gas in the oil medium. When the oil viscosity was reduced to a certain point, diluted oil now stated as live oil started to drain out of physical model by gravity, and accumulated in the funnel placed at the bottom of the pressure vessel. The valve was opened to direct the diluted oil towards the calibrated collection tube. The flash separation tank was wrapped with a flexible heating tape with temperature controller to maintain the temperature inside the separator at 60°C or higher. The liberated butane was allowed to enter a graduated gas measuring column from the port located on the top flash tank. The gas measuring column was initially filled with water. The liberated volume of solvent gas was determined by calculating the volume of the space occupied by the removed water.

The produced solvent gas-free oil or “dead oil” was collected in a beaker placed on a weighing balance after each flashing by opening valve located below the flash tank. The live oil production was recorded online every 5 seconds with data acquisition system from the load cell, which exhibited reduction in the weight of the model.

Before starting each experiment, the load cell was calibrated to the desired mark, and its behaviour was closely observed during the leak test as well as gas filling process. After a certain amount of live oil had been collected in the collection tube (almost 17 cm<sup>3</sup>), the live oil was directed towards the capillary tube, and then to the flash tank for determining the required parameters (i.e density, viscosity, and solubility) for dispersion coefficient and optimal control problem calculations.

At the end of an experiment, the solvent gas feed was shut. The experimental setup was vented, flushed with air, and vented again. The production of live oil with time was recorded.

### 3.1.2 Interfacial Solvent Concentration Setup

This experimental setup primarily comprised of a high-pressure vessel, syringe pump, water bath, data acquisition system, capillary tubes for oil sample collection and high accuracy scale. This experimental setup was designed to determine a functional relationship between the solvent injection pressure ( $P$ ) and interfacial solvent concentration ( $\omega_{\text{int}}$ ) at the solvent-oil interface, i.e.

$$P = P(\omega_{\text{int}}) \quad (3.1)$$

Knowing the above relation, we can obtain solvent pressure injection policy from optimal interfacial solvent concentration. It may be noted that the optimal control algorithm provides optimal mass fraction of solvent at the solvent-heavy oil interface [ $\omega_{\text{int}}(t)$ ] as a function of time, which needs to be mapped to the policy  $P(t)$  using Equation (3.1). Experiments with different injection pressures were performed in the setup whose schematic is shown in Figure 3.3 and the maximum solvent concentration for each pressure was measured.

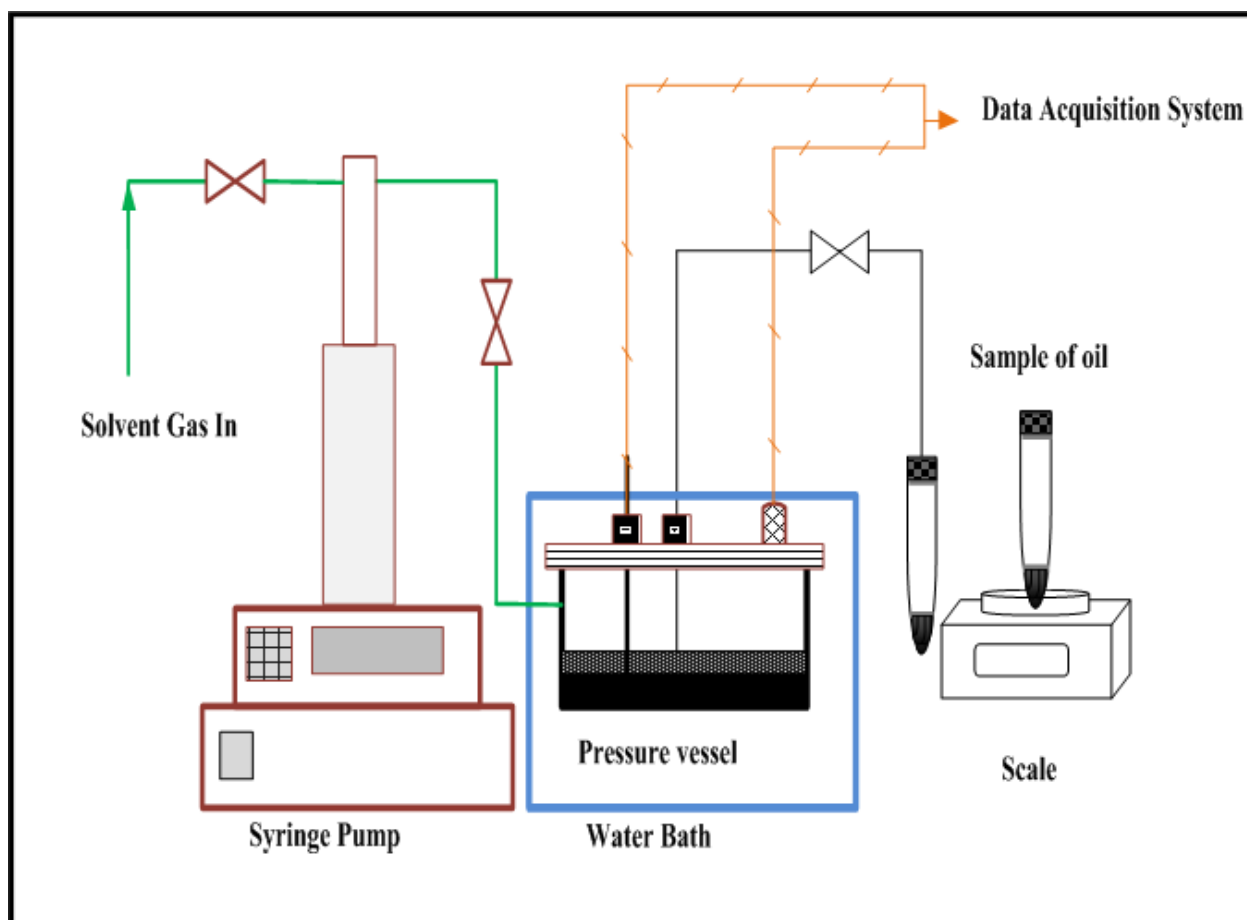


**Figure 3.3** Schematic of solvent–heavy oil system for the measurement of interfacial solvent concentration

### 3.1.2.1 Experimental Procedure

The pressure vessel was placed in a water bath held at a constant temperature, and was filled with about 25 grams of heavy oil. The top end of the vessel was connected to syringe pump and a capillary tube that was used to take the oil sample from the top most layers. Propane or butane gas was injected to the vessel through the syringe pump at a constant pressure for at least 8 hours at 21°C. The concentration of solvent present in the surface was determined as follows.

Through capillary lines the diluted oil sample was taken from the top layer very close to the heavy oil surface (about one millimeter) into a sealed collection tube (see Figure 3.4). The sealed sample tube was weighed for oil with solvent. Then this tube was open to atmosphere and warmed around 60°C to release the dissolved and residual propane in the oil. After flushing the solvent gas out the tube with oil (only) was weighed. From the mass balance, gas mass fraction in the oil was calculated. The experiments were performed at different injection pressures. The solvent concentration thus obtained is the interfacial concentration used in this study. Table 3.1 shows the interfacial concentration of propane and butane at different pressures.

**Table 3.1** Pressure versus interfacial concentration for propane and butane, 21°C, 14,500 mPa·s viscosity

<b>Propane Pressure(kPa)</b>	<b>Propane mass fraction( <math>\omega_{\text{int}}</math> )</b>	<b>Butane Pressure(kPa)</b>	<b>Butane mass fraction( <math>\omega_{\text{int}}</math> )</b>
413.7	0.26	91.01	0.22
482.6	0.45	97.9	0.34
551.6	0.54	101.3	0.37
620.5	0.68	104.8	0.49
689.5	0.77	111.69	0.61

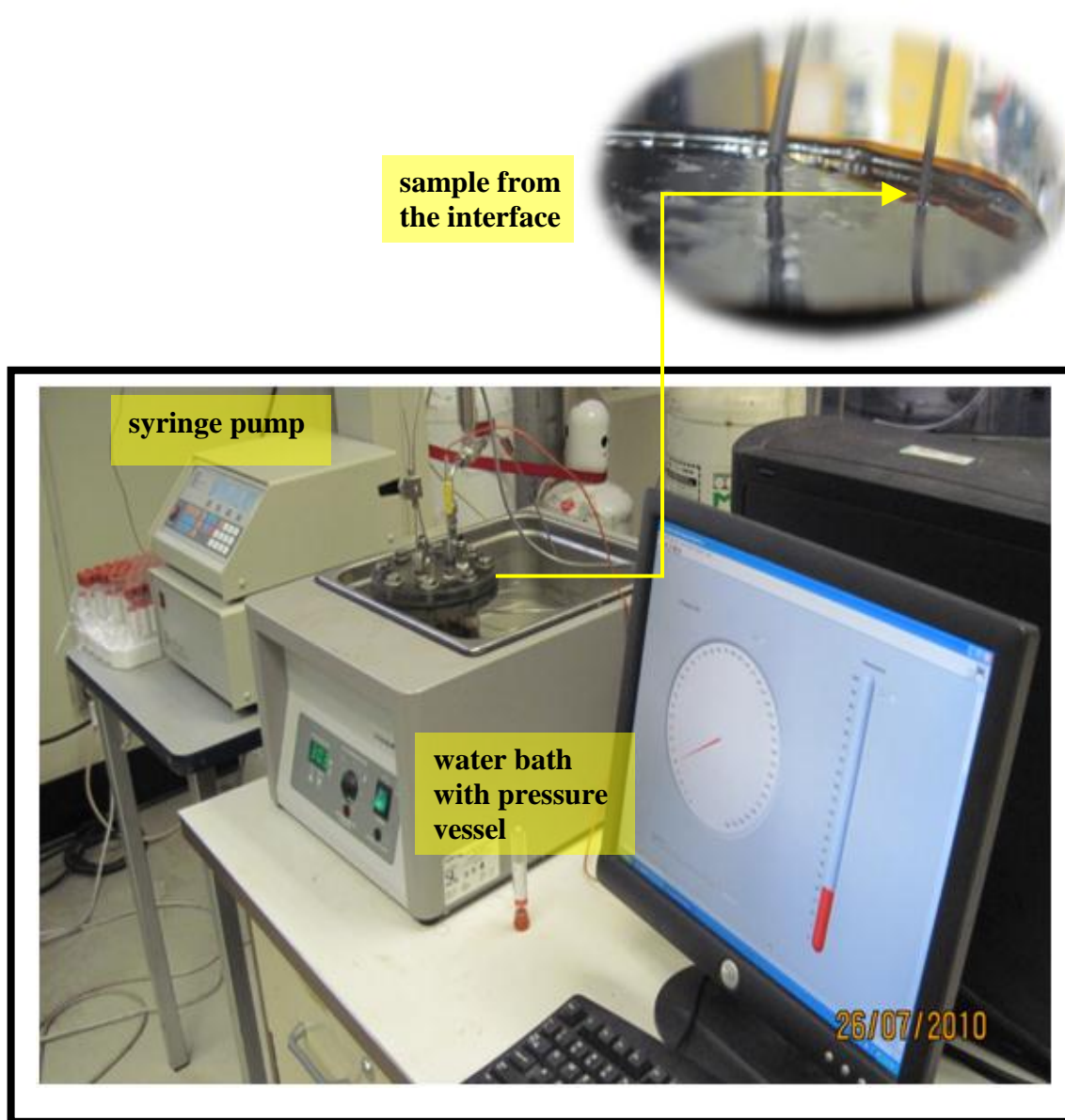


**Figure 3.4** Picture of solvent–heavy oil system for the measurement of interfacial solvent concentration

### 3.2 Heavy Oil Properties

The heavy oil used in this study was obtained from Saskatchewan Research Council (SRC), Regina. The viscosity of heavy oil was determined by using Bohlin Viscometer. A small amount of oil (10 grams) was placed in the cone and plate arrangement of the viscometer. The viscosity



of the heavy oil was determined at different temperatures starting from 20°C to 40°C. The viscosity of the oil at the experimental temperature was found to be 14,500 mPa·s. Figure 3.5 shows viscosity of heavy oil versus temperature. The heavy oil density, molecular weight, and SARA (wt %) are shown in Table 3.2.

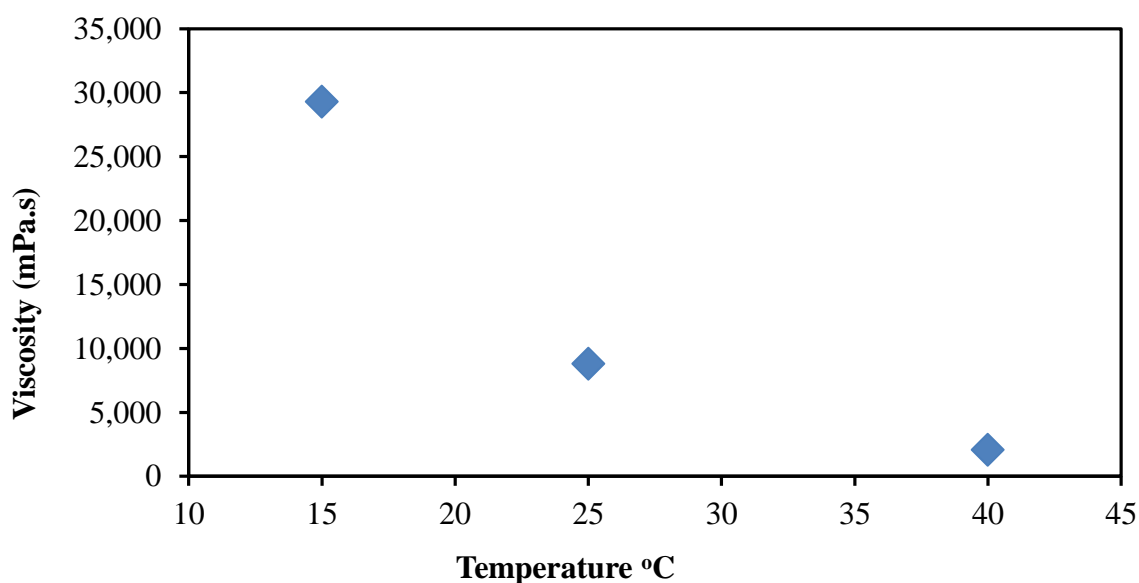


**Figure 3.5** Viscosity of heavy oil versus temperature

**Table 3.2** Properties of the heavy oil

Heavy Oil Properties	(°C)	(kg/m <sup>3</sup> )
Density (kg/m <sup>3</sup> ) at °C	15	984
	25	977
	40	968
Mol Weight (kg/kmol)	496	
SARA (wt %)		
Saturates	29	
Aromatics	31	
Resins	22	
Asphaltenes	14	

### 3.3 Glass Beads Properties

The packing material used in this experiment to simulate a reservoir was a simulated mixture of heavy oil and glass beads. The latter were obtained from Flex-O-Lite (supplied by Ritchey Supply Ltd.). Glass beads are manufactured from high-grad optical crown glass, lead free, soda lime type with a minimum silica content of 67 % (free silica content, 0%). The specific gravity of this media is approximately 2.5 g/cm<sup>3</sup>. Specifications of the glass beads are shown in Table 3.3.

**Table 3.3** Specifications of the glass beads

<b>Glass beads type</b>	<b>U.S Screen</b>	<b>Size range (mm)</b>	<b>U.S sieve size Min 95 % pass</b>	<b>U.S sieve size Max 10 % pass</b>	<b>Min % true spheres</b>
<b>BT 3</b>	20-30	0.840-0.594	20	30	65
<b>BT 4</b>	30-40	0.594-0.419	30	40	65
<b>BT 5</b>	40-60	0.419-0.248	40	60	75
<b>BT 6</b>	40-70	0.248-0.210	40	70	70

### 3.4 The Physical Model Preparation

Knowing the density of the glass beads and density of the heavy oil, the porosity of the physical model was calculated to be 0.38. Porosity was measured by taking a known volume of glass beads and heavy oil saturated mixture and placing it in water filled graduated cylinder. Taking the volume of the water displaced, porosity was calculated as:

$$\phi = \frac{V_{oil}}{V_{displaced\ water}} \quad (3.2)$$

where  $V_{oil}$  is volume of oil, and  $V_{displacedwater}$  is the total volume. The physical model was prepared very carefully to avoid any air trapping within mixture of heavy oil and glass beads. A known amount of heavy oil was collected in a pan, which was placed in a temperature controlled heater. The heavy oil was heated for at least 30 minutes at  $70^{\circ}\text{C}$  for a sufficient reduction in oil viscosity to promote glass beads mixing. Four different sizes of glass beads with different permeabilities were used to pack homogeneous physical models. Glass beads were gradually added to the heated heavy oil to ensure proper mixing without trapping air bubbles. After allowing the beads to settle down by gravity another layer was added to the oil surface. The same procedure was repeated until there was no more room for the beads. It took about 5-6 hours to prepare a physical model. Figures 3.6 a, b, c show the pictures of the steps to prepare physical model for experiments.

The saturated mixture of the heavy oil and glass beads was packed in a different cylindrical wire meshes with inside radius 3 cm and lengths of 25 and 45 cm. The cylindrical physical model thus prepared carried heavy oil saturated with glass beads. Each physical model was weighed, and left at room temperature for one day to reach thermal equilibrium prior to an experiment.



**Figure 3.6.a** Picture of heavy oil and glass beads



**Figure 3.6.b** Picture of heating the sample



**Figure 3.6.c** Picture of mixing glass beads with the oil

### 3.5 Constant Temperature

Constant temperature during the experiment was maintained through the big vessel (of 200 cm height, 150 cm diameter) made of PVC, used as water bath (Figure 3.1). Once the leak test for pressure vessel was done with air, water bath was filled with fresh water by opening the valve of the source water. The experiment water bath temperature was set at 21.4 °C after filling the water bath. Hot water was circulated in the water bath. Once uniform set point temperature was attained in about 4 hours, the physical model was suspended inside the pressure vessel for the Vapex experiments.

Figure 3.7 present the temperature of the pressure vessel for two different runs throughout the experiment (25 cm physical model height and 204 Darcy permeability physical model). The temperatures lie between  $\pm 0.5$  °C of the set point which indicates a relatively good temperature control.

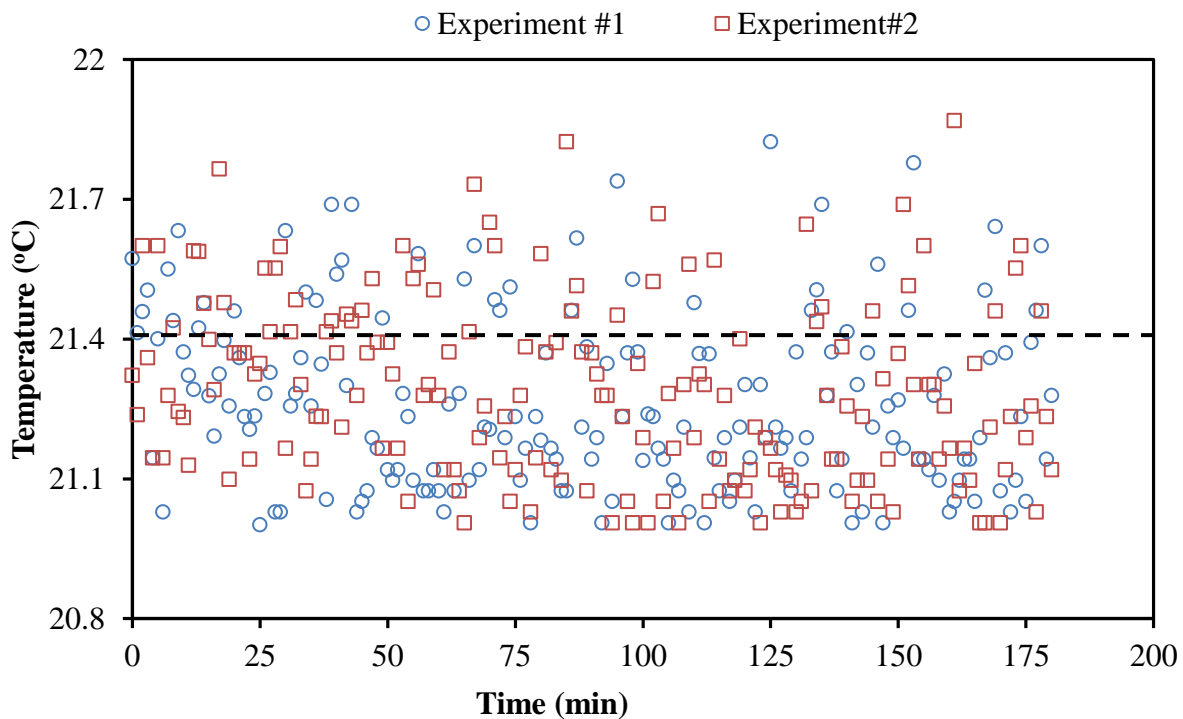


**Figure 3.7** Temperature for a couple of typical Vapex experiments

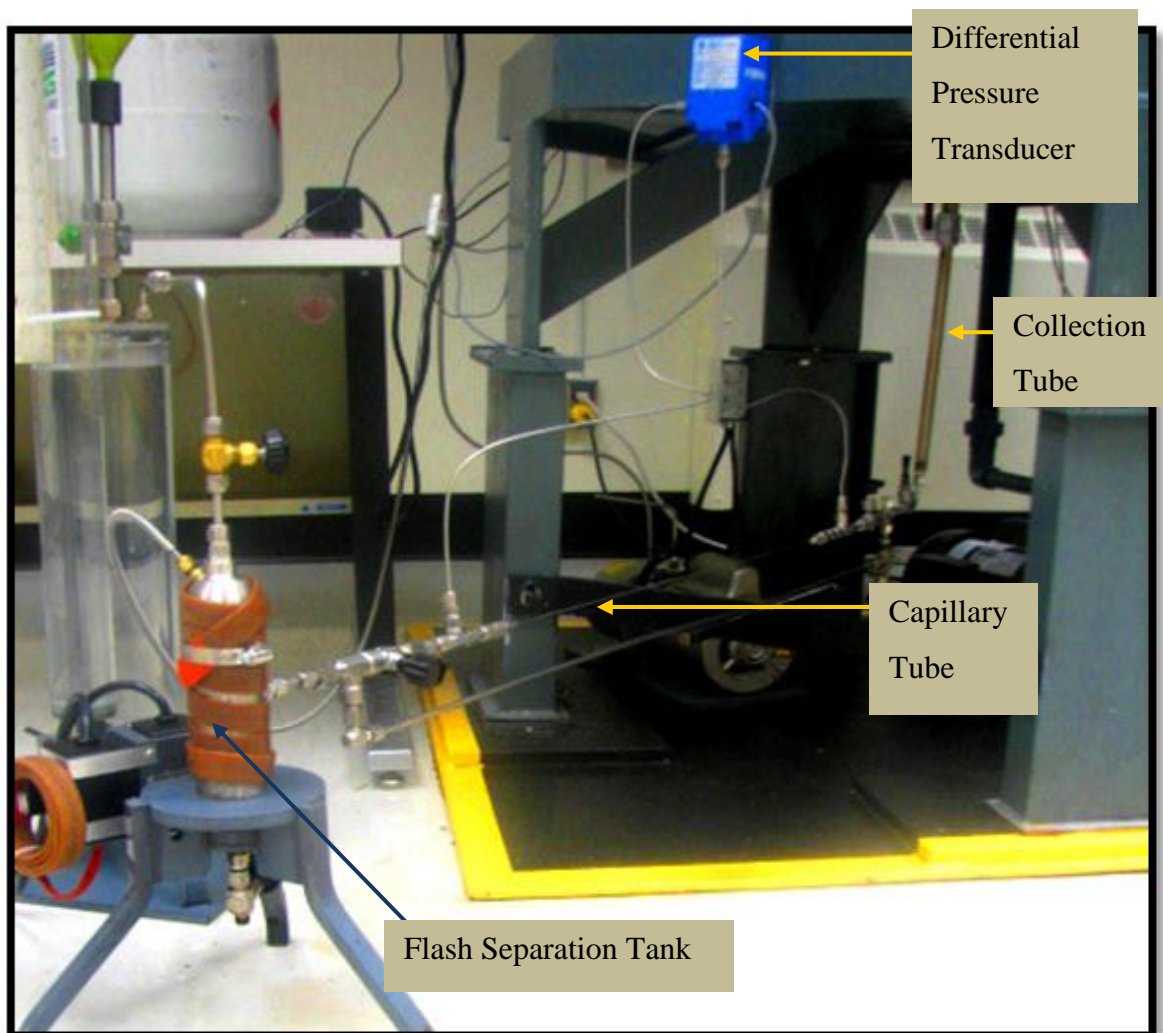
### 3.6 Live Oil Viscosity

Figure (3.8) shows picture of the experimental setup used for live oil viscosity determination. The setup comprises of a collection tube, capillary tube, pressure transducer, and needle valve. After the collection tube was filled with produced live oil, the live oil was allowed to flow through a viscosity measuring unit via a stainless steel tube of 12 mm outside diameter, and 2 mm thickness. The viscosity was determined by passing the live oil through a capillary tube of 0.1016 cm diameter and 50 cm length. A pressure transducer was connected at both sides of tube to measure pressure drop across the tube.

To make the live oil flow from the calibrated collection tube, the valve situated between the funnel and calibrated collection tube was opened. The flow rate of live oil was determined by measuring the time required by known volume of live oil to pass through the collection tube. The viscosity of live oil was determined by using the Hagen-Poiseuille equation.

$$Q = \frac{\pi d^4 \Delta P}{128 \mu L} \quad (3.3)$$

with known the diameter of the capillary tube ( $d$ ), ( $\Delta P$ ) across the tube, length of the capillary tube ( $L$ ) and flow of live oil across the tube ( $Q$ ). A sample calculation is shown in Appendix B.



**Figure 3.8** Picture of the viscosity measuring unit

### 3.7 Solvent Gas Solubility and Live Oil Density

In this experimental work, butane and propane were used separately as solvents. The collected live oil was periodically flashed inside a stainless steel flash separation tank (300 cm<sup>3</sup> capacity) wrapped with a flexible electrical heating tap. The temperature of the tank was kept around 60°C. The amounts of (i) absorbed gas transferring the liberated gas to gas measuring column initially filled with water, and (ii) residual gas free oil (dead oil) were measured. The flashed liberated solvent gas was allowed to collect into a transparent gas-measuring column (3000 cm<sup>3</sup>) for volume measurement.

The mass of the solvent gas was determined as follows. A known amount of live oil was transferred to flash tank through capillary tube by controlling the amount of oil by using the valve located before the flash tank. Temperature of flash tank was maintained at 70°C to ensure proper flashing of the gas. The flashed gas was diverted to the first water column. Wherein the water was displaced resulting in a rise of the water level in second water column. After some time (10-15 min) differential pressure reading approached zero with no more displacement in the second water column. The displaced volume of water determined the gas volume. The valve on the top of first column was opened to vent the gas, and net amount of dead oil was collected by opening the valve at the bottom of the flash tank.

Knowing the amount of propane or butane ( $C_3H_8$  or  $C_4H_{10}$ ), dissolved in oil, the solvent gas-free oil (dead oil) weight, and the volume of the live oil, the solubility of gas was determined as well as the live oil density using the following formulas:

$$\omega = \frac{m_{\text{gas}}}{m_{\text{gas}} + m_{\text{oil}}} \quad (3.4)$$

$$\rho = \frac{m_{\text{gas}} + m_{\text{oil}}}{V_{\text{live oil}}} \quad (3.5)$$

where  $\omega$  weight fraction of solvent gas,  $m_{\text{gas}}$  is weight of liberated solvent gas,  $m_{\text{oil}}$  is the weight of dead oil,  $\rho$  is the live oil density, and  $V_{\text{live oil}}$  is the volume of live oil.

A sample of propane solubility and live oil density calculations is presented in Appendix C.

### 3.8 Permeability Measurement

We prepared physical model of different permeabilities to study the permeability effect on production rate. Different glass beads sizes (industrial name BT3, BT4, BT5 and BT6) were used. The packing material simulating a reservoir was glass beads obtained from (Flex-O-Lite Ltd., St. Louis, United States).



To measure the permeability of the porous media consisting of heavy oil and glass beads mixture, a horizontal cylindrical physical model of 4 cm diameter and 26 cm length was used. The cylinder had two ports; one for air inlet and one for discharge air with a screen placed at the two sides to avoid any glass beads passage. Two pressure gauges at both ends of the cylinder were used to measure the air pressure drop across the media when air was passed through it. The airflow rate was measured by a flow meter at the outlet. Darcy law for single-phase steady state flow was used to calculate the permeability ( $K$ ) of the glass beads packing as follows (Dullien, 1992).

$$K = \frac{P_2 \times u_2 \times \mu_{air} \times L}{P_m \times \Delta P} \quad (3.6)$$

where  $P_1$  and  $P_2$  are the pressures at the inlet and outlet of the cylinder,  $u_2$  is the velocity at the outlet,  $P_m$  is the mean pressure,  $\Delta P$  is the pressure difference,  $\mu_{air}$  is the air viscosity at experiment temperature,  $L$  is the length of the media. The permeability of the packing material was also estimated from the particle size diameter using the Carman-Kozeny equation.

$$K_{CK} = \frac{\phi^3 \times D_p^2}{180(1 - \phi^3)} \quad (3.7)$$

where ( $K$ ) is the permeability ( $\phi$ ) and ( $D_p$ ) are porosity of the medium and diameter of the particle, respectively. Table 3.4 shows values of estimated sample permeability as well as the measured permeability measurement for four different permeabilities. A sample of the glass beads permeability calculations are presented in Appendix A.

**Table 3.4** Permeability of the glass beads

<b>Glass beads type</b>	<b>Average diameter (mm)</b>	<b>Porosity</b>	<b>Experimental <math>K</math> (Darcy)</b>	<b>Estimated (<math>K_{CK}</math>)</b>
<b>BT 3</b>	0.717	0.385	439.2	427
<b>BT 4</b>	0.506	0.38	220.0	204
<b>BT 5</b>	0.334	0.378	97.4	87
<b>BT 6</b>	0.229	0.376	44.4	40

### 3.9 Experimental Errors

Table 3.5 shows the specifications for the instrument used during this study and the instrument's range of operation and their accuracy.

**Table 3.5** Instrument specifications used during Vapex study

<b>Name of Instrument</b>	<b>Used in</b>	<b>Range</b>	<b>Accuracy (Error %)</b>
Resistance Temp Detectors	Vessel, and Flash Separation Tank	0–230 °C 0–2500 (psig)	0.1% (full scale)
Pressure Transducer	Pressure Vessel	0–200 (psig)	0.5%
Differential Pressure Transducer	Viscosity Measurement	0–30 (psig) 0–200 (psig)	0.5%
Flow Meter	Butane Supply Rate	-10 to 50 °C 125 psig (max)	0.1%
Load Cell	Physical Model weight measurement	0 – 4500 (g) -54 to 93 °C	0.025% (of full load)



# 4

## Optimal Control of Vapex

This chapter presents the optimal control of Vapex to maximize oil production, which is the primary objective of this study. To influence oil production, the interfacial solvent concentration versus time is employed as a control function in the optimal control problem. The optimal control function is then determined. This function corresponds to the optimal solvent injection pressure versus time policy, which maximizes oil production in Vapex.

The optimal control of Vapex is based on a detailed mass transfer model, which comprises continuity equation of solvent diffusion into heavy oil. The model has the control function — the time-varying, interfacial solvent concentration — as a boundary condition. Using the principles of Optimal Control, the necessary conditions are derived for maximum oil production in Vapex. These conditions determine the optimal control function, or equivalently the optimal solvent injection pressure versus time policy, which would provide maximum oil production. A numerical algorithm is developed to compute the optimal policies.

## 4.1 Mass Transfer Model

In this section, a mass transfer model of Vapex is presented to describe the process of solvent gas absorption and subsequent live oil drainage in our experiments. Following are the details of the mathematical model and the basic assumptions of the model.

1. Constant temperature

Experiments were carried out at constant temperature with a standard deviation of 0.01 °C

2. The flow of the live oil along the vertical direction is governed by Darcy's law in a porous medium.
3. The diffusion of the solvent gas takes place along the radial direction only. Diffusion in the vertical direction is neglected.
4. The porous medium has uniform porosity and permeability.
5. Due to very low density of the solvent gas, it was assumed that density of the live oil remains constant throughout the recovery process. Abukhalifeh et al., (2009) study, show that there is a small variations in the live oil density measured experimentally and the sensitivity study conducted shows that the effect of the density variation on the dispersion values is insignificant.
6. The heavy oil is non-volatile.
7. There were no chemical reactions as the absorption of the solvent gas in heavy oil is purely a physical phenomenon.

The optimal control technique was used in this work based on the unsteady state mass balance for solvent gas in a cylindrical differential element Figure (4.1). The unsteady-state mathematical model is given by the following differential equations:

$$\frac{d}{dt}(\Delta V \phi \rho \omega) = [v \Delta A \rho \omega]_{z+\Delta z} - [v \Delta A \rho \omega]_z + [J \Delta S]_{r+\Delta r} - [J \Delta S]_r \quad (4.1)$$

where  $\Delta V = 2\pi r \Delta r \Delta z$  is the volume of the element,  $\phi$  is the medium porosity,  $\rho$  is the live oil density,  $\omega$  is the mass fraction of propane in the medium,  $\Delta A = 2\pi r \Delta r$  is the area transverse to

the live oil velocity  $v$  in the downward direction, and  $\Delta S = 2\pi r \Delta z$  is the area transverse to the dispersive flux  $J$  in the radial direction as shown in the figure. The diffusive flux along the vertical direction is assumed insignificant in comparison with the gravity-generated flux. Assuming constant temperature, pressure and live oil density, the radial flux can be written as

$$J = -D\rho \frac{d\omega}{dr} \quad (4.2)$$

where  $D$  is the undetermined concentration-dependent dispersion coefficient of propane in the porous medium. Taking the limits of  $\Delta r$  and  $\Delta z$  to zero, the above equations yield the following mass transfer model:

$$\frac{\partial \omega}{\partial t} = \frac{\partial D}{\partial \omega} \left( \frac{\partial \omega}{\partial r} \right)^2 + D \left[ \frac{1}{r} \frac{\partial \omega}{\partial r} + \frac{\partial^2 \omega}{\partial r^2} \right] - \frac{1}{\phi} \left[ \omega \frac{\partial v}{\partial \omega} \frac{\partial \omega}{\partial z} + v \frac{\partial \omega}{\partial z} \right] \quad (4.3)$$

$v$  in the above expression is assumed to be Darcy Velocity and is replaced by:

$$v = \frac{K_r K \rho g}{\mu} \quad (4.4)$$

where  $K_r$  is relative permeability of the medium,  $K$  is its permeability,  $\rho$  is the density of live oil,  $g$  is gravity, and  $\mu = \mu_0 \omega^{-2}$  is the concentration-dependent live oil viscosity. The drainage

reduces the height ( $Z$ ) of the bitumen in the packed medium. The change in the height with time at any radial location is given by the negative of Darcy velocity at the bottom of the media as

$$\frac{\partial Z}{\partial t} = -v_0(r) \quad (4.5)$$

where  $v_0(r)$  the negative of the Darcy velocity of live oil at a given  $r$ , and averaged over the differential volume  $2\pi r dr dz$  at the medium bottom, i.e. at  $Z=0$ .

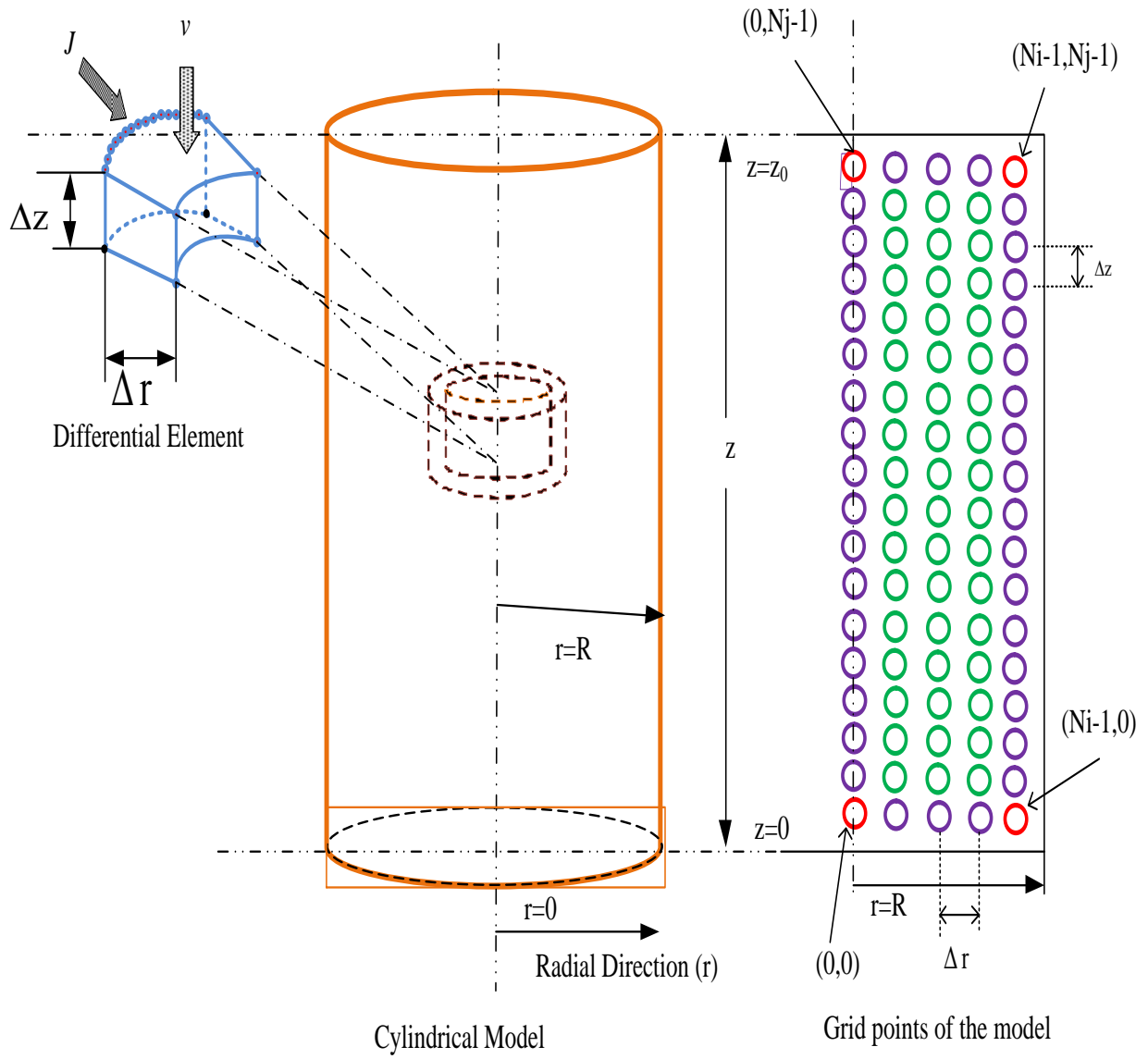


**Figure 4.1** Packed cylindrical medium with its differential element and the arrangement of grid points



## 4.2 Initial and Boundary Conditions

Initially, the height of the bitumen is  $Z_0$  with no propane inside the medium. However, its surface has the equilibrium concentration of propane at all times. Thus the initial conditions at  $t = 0$  are as follows:

$$\omega = \begin{cases} 0 & \forall 0 < z < Z_0 \text{ and } 0 \leq r < R \\ \omega_{\text{sat}} & \text{at } z = 0, Z_0 \text{ and } 0 \leq r \leq R; \text{ and at } r = R \text{ and } 0 \leq z \leq Z_0 \end{cases} \quad (4.6)$$

The boundary conditions at  $t \geq 0$  are

$$\omega = \omega_{\text{sat}} \text{ at } z = 0, Z(r, t) \text{ and } 0 \leq r \leq R; \text{ and at } r = R \text{ and } 0 \leq z \leq Z(r, t) \quad (4.7)$$

where  $Z(r, t)$  is the height of the bitumen in the porous medium at a given  $r$  and  $t$ . Furthermore, because of symmetry, at all times

$$\frac{\partial \omega}{\partial r} = 0 \quad \forall 0 \leq z \leq Z \text{ and } r = 0$$

The cumulative mass of produced live oil at any time was calculated by integrating from 0 to  $R$  for a calculated change in height of the physical sample and is given by

$$m_{\text{cal}} = 2\pi\rho\phi \int_0^R (Z_0 - z) r \, dr \quad (4.8)$$

### 4.3 Optimal Control Analysis

The objective is to maximize oil production in Vapex by using solvent pressure versus time as a control function. The latter translates to  $\omega_{\text{int}}$  versus time in the optimal control problem as follows.

Mathematically, the problem is to maximize objective functional  $I$  which is written as:

$$I = \int_0^T m dt \quad (4.9)$$

where  $m$  is the mass of the dead oil produced. With the help of Equation (4.8), the objective functional becomes

$$I = \beta \int_0^T \int_0^R (Z_0 - z) r dr dt \quad (4.10)$$

where  $\beta = 2\pi\rho\phi$ . The maximum of  $I$  is subject to Equation (4.3), which can be expressed as

$$\frac{\partial \omega}{\partial t} - f_1 = G(t, r, z) = 0 \quad (4.11)$$

where

$$f_1 = \left( \frac{\partial D}{\partial \omega} \right) \cdot \left( \frac{\partial \omega}{\partial r} \right)^2 + \frac{D}{r} \left( \frac{\partial \omega}{\partial r} \right) + D \left( \frac{\partial^2 \omega}{\partial r^2} \right) - 3\alpha \frac{\omega^2}{\phi} \left( \frac{\partial \omega}{\partial z} \right) \quad (4.12)$$

and subjected to Equation (4.5), which in turn can be written as

$$\frac{\partial z}{\partial t} - f_2 = H(t, r) = 0 \quad (4.13)$$

where

$$f_2 = -v(t, r, 0) = -\alpha[\omega(t, r, 0)]^2 \quad (4.14)$$

Equation (4.11) and Equation (4.13) are the constraints for the objective functional  $I$ . These constraints are highly non-linear partial differential equations. Therefore, to solve the optimal control problem, two undetermined adjoint variables  $\lambda_1(t, r, z)$  and  $\lambda_2(t, r)$  are introduced into Equation (4.10) to obtain the following augmented objective functional:

$$J = I + \underbrace{\int_0^T \int_0^R \int_0^Z \lambda_1(t, r, z) G(t, r, z) dz dr dt}_{I_2} + \underbrace{\int_0^T \int_0^R \lambda_2(t, r) H(t, r) dr dt}_{I_3} \quad (4.15)$$

By substituting Equations (4.10), (4.11), and (4.13) into Equation (4.15), we obtain

$$J = \beta \int_0^T \int_0^R (Z_0 - z) r dr dt + \int_0^T \int_0^R \int_0^Z \lambda_1 \left[ \left( \frac{\partial D}{\partial \omega} \right) \cdot \left( \frac{\partial \omega}{\partial r} \right)^2 + \frac{D}{r} \left( \frac{\partial \omega}{\partial r} \right) + D \left( \frac{\partial^2 \omega}{\partial r^2} \right) - 3\alpha \frac{\omega^2}{\phi} \left( \frac{\partial \omega}{\partial z} \right) \right] dz dr dt + \int_0^T \int_0^R \lambda_2 \left( \frac{\partial z}{\partial t} - f_2 \right) dr dt \quad (4.16)$$

where  $\lambda_1(t, z, r)$  and  $\lambda_2(t, r)$  are the adjoint variables. The maximization of  $I$  subject to constraints is equivalent to the maximization of  $J$ .

## 4.4 Necessary Conditions for the Optimum

The necessary condition for the optimum of  $J$  stem from  $\delta J = 0$ . We proceed by deriving  $\delta J$  as follows:

$$\begin{aligned} \delta J = & -\beta \int_0^T \int_0^R r \delta z dr dt + \int_0^T \int_0^R \int_0^Z \lambda_1 \frac{\partial(\delta \omega)}{\partial t} dz dr dt - \int_0^T \int_0^R \int_0^Z \lambda_1 \frac{\partial f_1}{\partial \omega} \delta \omega dz dr dt - \int_0^T \int_0^R \int_0^Z \lambda_1 \frac{\partial f_1}{\partial \omega_z} \delta \omega_z dz dr dt \\ & - \int_0^T \int_0^R \int_0^Z \lambda_1 \frac{\partial f_1}{\partial \omega_r} \delta \omega_r dz dr dt - \int_0^T \int_0^R \int_0^Z \lambda_1 \frac{\partial f_1}{\partial \omega_{rr}} \delta \omega_{rr} dz dr dt + \int_0^T \int_0^R \lambda_2 \frac{\partial(\delta z)}{\partial t} dr dt - \\ & \int_0^T \int_0^R \lambda_2 \delta f_2 dr dt = 0 \end{aligned}$$

(4.17)

Applying integration by parts of the second integral of the Equation (4.17) we obtain

$$\int_0^T \int_0^R \int_0^Z \lambda_1 \frac{\partial(\delta \omega)}{\partial t} dz dr dt = \int_0^T \int_0^R \lambda_1 \delta \omega \Big|_0^T dz dr - \int_0^T \int_0^R \int_0^Z \frac{\partial \lambda_1}{\partial t} \delta \omega dz dr dt \quad (4.18)$$

By applying the initial conditions into first integral on right hand side in Equation(4.18). This integral is eliminated based on the fact that the solvent mass fraction is known at  $t=0$ , so that its variation is ruled out, i.e.

$$(\lambda_1 \delta \omega|_T - \lambda_1 \delta \omega|_0) dz dr \quad (4.19)$$

at  $t=0$

$$\delta \omega(0, r, z) = 0 \quad \forall r: 0 \leq r \leq R \quad \text{and} \quad \forall z: 0 \leq z \leq Z_0$$

The final mass fraction of solvent in bitumen,  $\omega(T, r, z)$ , is not specified. Variation due to  $\omega(T, r, z)$  is eliminated if its multiplicative term.

$$\lambda_1(T, r, z) = 0 \quad (4.20)$$

$$\forall \quad 0 \leq r \leq R \text{ and } \forall \quad 0 \leq z \leq Z_0$$

Therefore Equation (18) becomes

$$\int_0^T \int_0^R \int_0^Z \lambda_1 \frac{\partial(\delta\omega)}{\partial t} dz dr dt = - \int_0^T \int_0^R \int_0^Z \frac{\partial \lambda_1}{\partial t} \delta\omega dz dr dt \quad (4.21)$$

Applying integration by parts of the fourth integral of the Equation (4.17) we obtain

$$\int_0^T \int_0^R \int_0^Z -\lambda_1 \frac{\partial f_1}{\partial \omega_z} \delta\omega_z dz dr dt = - \int_0^T \int_0^R \lambda_1 \frac{\partial f_1}{\partial \omega_z} \delta\omega \Big|_0^Z dr dt + \int_0^T \int_0^R \int_0^Z \frac{\partial}{\partial z} \left( \lambda_1 \frac{\partial f_1}{\partial \omega_z} \right) \delta\omega dz dr dt \quad (4.22)$$

By applying the boundary conditions into the first integral of Equation (4.22) we obtain the following equation:

$$\left( -\lambda_1 \frac{\partial f_1}{\partial \omega_z} \delta\omega \Big|_Z + \lambda_1 \frac{\partial f_1}{\partial \omega_z} \delta\omega \Big|_0 \right) dz dr \quad (4.23)$$

$$\omega = \omega_{\text{int}} \quad \text{at} \quad z = 0, \quad \text{and} \quad z = Z(r, t) \quad \forall \quad 0 \leq r < R \quad (4.24)$$

Therefore Equation (4.22) becomes

$$\int_0^T \int_0^R \int_0^Z -\lambda_1 \frac{\partial f_1}{\partial \omega_z} \delta\omega_z dz dr dt = \int_0^T \int_0^R -\lambda_1 \frac{\partial f_1}{\partial \omega_z} \delta\omega(t, r, Z) dr dt + \int_0^T \int_0^R \lambda_1 \frac{\partial f_1}{\partial \omega_z} \delta\omega(t, r, 0) dr dt + \int_0^T \int_0^R \int_0^Z \frac{\partial}{\partial z} \left( \lambda_1 \frac{\partial f_1}{\partial \omega_z} \right) \delta\omega dz dr dt \quad (4.25)$$

Applying integration by parts of the fifth integral of the Equation (4.17) we obtain the following equation:

$$\int_0^T \int_0^R \int_0^Z -\lambda_1 \left( \frac{\partial f_1}{\partial \omega_r} \delta \omega_r \right) dz dr dt = - \int_0^T \int_0^Z \lambda_1 \frac{\partial f_1}{\partial \omega_r} \delta \omega \Big|_0^R dz dt + \int_0^T \int_0^R \int_0^Z \frac{\partial}{\partial r} \left( \lambda_1 \frac{\partial f_1}{\partial \omega_r} \right) \delta \omega dz dr dt \quad (4.26)$$

By applying the boundary conditions into the first integral of Equation (4.26) we obtain the following equation:

$$\left( -\lambda_1 \frac{\partial f_1}{\partial \omega_r} \delta \omega \Big|_R + \lambda_1 \frac{\partial f_1}{\partial \omega_r} \delta \omega \Big|_0 \right) dz dt \quad (4.27)$$

Since the solvent mass fraction in heavy oil  $\omega(t, R, z)$  in Equation (4.27) for all  $z$  and  $t$ , the  $\omega(t, R, z) = \omega_{\text{int}}$ , therefore the variation  $\delta \omega(t, R, z) = \delta \omega_{\text{int}}$

The variation due to  $\omega(t, 0, z)$  is eliminated if its multiplicative term is equal to zero which is natural condition  $\delta \omega(t, 0, z) \neq 0$ , i.e.

$$\begin{aligned} \lambda_1(t, 0, z) &= 0 \quad \forall t: 0 \leq t \leq T \text{ and } \forall z: 0 \leq z \leq Z \\ \omega(t, R, z) &= \omega_{\text{int}}, \end{aligned} \quad (4.28)$$

Therefore Equation (4.25) becomes

$$\int_0^T \int_0^R \int_0^Z -\lambda_1 \left( \frac{\partial f_1}{\partial \omega_r} \delta \omega_r \right) dz dr dt = \int_0^T \int_0^Z -\lambda_1 \frac{\partial f_1}{\partial \omega_r} \delta \omega(t, R, z) dz dt + \int_0^T \int_0^R \int_0^Z \frac{\partial}{\partial r} \left( \lambda_1 \frac{\partial f_1}{\partial \omega_r} \right) \delta \omega dz dr dt \quad (4.29)$$

Applying integration by parts to the sixth integral of Equation (4.17), we obtain the following equation:

$$\int_0^T \int_0^R \int_0^Z -\lambda_1 \left( \frac{\partial f_1}{\partial \omega_{rr}} \delta \omega_{rr} \right) dz dr dt = - \int_0^T \int_0^Z \lambda_1 \frac{\partial f_1}{\partial \omega_{rr}} \delta \omega_r \Big|_0^R dz dt + \int_0^T \int_0^R \int_0^Z \frac{\partial}{\partial r} \left( \lambda_1 \frac{\partial f_1}{\partial \omega_{rr}} \right) \delta \omega_r dz dr dt \quad (4.30)$$

Applying integration by parts to the second integral of Equation (4.30),

$$\begin{aligned} \int_0^T \int_0^R \int_0^Z -\lambda_1 \left( \frac{\partial f_1}{\partial \omega_{rr}} \delta \omega_r \right) dz dr dt &= - \int_0^T \int_0^Z \lambda_1 \frac{\partial f_1}{\partial \omega_{rr}} \delta \omega_r \Big|_0^R dz dt + \int_0^T \int_0^Z \frac{\partial}{\partial r} \left( \lambda_1 \frac{\partial f_1}{\partial \omega_{rr}} \right) \delta \omega \Big|_0^R dz dt \\ &\quad - \int_0^T \int_0^R \int_0^Z \frac{\partial^2}{\partial r^2} \left( \lambda_1 \frac{\partial f_1}{\partial \omega_{rr}} \right) \delta \omega dz dr dt \end{aligned} \quad (4.31)$$

By applying the boundary conditions of the first integral in Equation (4.31), as a result the first term in same equation is eliminated by the multiplicative term is equal to zero, i.e.

$$\lambda_1(t, R, z) = 0 \quad (4.32)$$

Application of boundary conditions in Equations (4.28) into the Equation second integral of Equation (4.31), we obtain

$$\int_0^T \int_0^Z \frac{\partial}{\partial r} \left( \lambda_1 \frac{\partial f_1}{\partial \omega_{rr}} \right) \delta \omega \Big|_0^R dz dt = \int_0^T \int_0^Z \frac{\partial}{\partial r} \left( \lambda_1 \frac{\partial f_1}{\partial \omega_{rr}} \right) \delta \omega(t, R, z) dz dt \quad (4.33)$$

As a result Equation (4.31) becomes

$$\int_0^T \int_0^R \int_0^Z -\lambda_1 \left( \frac{\partial f_1}{\partial \omega_{rr}} \delta \omega_{rr} \right) dz dr dt = \int_0^T \int_0^Z \frac{\partial}{\partial r} \left( \lambda_1 \frac{\partial f_1}{\partial \omega_{rr}} \right) \delta \omega(t, R, z) dz dt - \int_0^T \int_0^R \int_0^Z \frac{\partial^2}{\partial r^2} \left( \lambda_1 \frac{\partial f_1}{\partial \omega_{rr}} \right) \delta \omega dz dr dt \quad (4.34)$$

Applying integration by parts to the seventh integral of Equation (4.17), we obtain

$$\int_0^T \int_0^R \lambda_2 \left( \frac{\partial(\delta z)}{\partial t} \right) dr dt = \int_0^R \lambda_2 \delta z \Big|_0^T dr - \int_0^T \int_0^R \frac{\partial \lambda_2}{\partial t} \delta z dr dt \quad (4.35)$$

By applying the initial conditions into the first integral of Equation (4.35). The initial height of heavy oil,  $Z(0, r)$ , is known, then the variation of  $Z(0, r)$  is ruled out, i.e.

$$\delta Z(0, r) = 0 \quad \forall \quad 0 \leq r \leq R \quad (4.36)$$

The final height of model,  $Z(T, r)$ , is not specified. Variation due to  $Z(T, r)$  is eliminated if its multiplicative term,  $\lambda_2(t, r)$ , is forced to zero, i.e.,

$$\lambda_2(T, r) = 0 \quad \forall \quad 0 \leq r \leq R \quad (4.37)$$

As a result Equation (4.35) becomes

$$\int_0^T \int_0^R \lambda_2 \left( \frac{\partial(\delta z)}{\partial t} \right) dr dt = - \int_0^T \int_0^R \frac{\partial \lambda_2}{\partial t} \delta z dr dt \quad (4.38)$$

The last integral of the Equation (4.17) becomes

$$- \int_0^T \int_0^R \lambda_2 \delta f_2 dr dt = - \int_0^T \int_0^R \lambda_2 \frac{\partial f_2}{\partial \omega(t, r, 0)} \delta \omega(t, r, 0) dr dt \quad (4.39)$$

Substituting of the Equations (4.25), (4.29), (4.34), (4.38) and (4.39) into Equation (4.17) and rearrange, we obtain the final equation of variation of  $J$ , which is written as

$$\begin{aligned} \delta J = & \int_0^T \int_0^R \left[ -\beta r - \frac{\partial \lambda_2}{\partial t} \right] \delta z dr dt + \\ & \int_0^T \int_0^R \int_0^Z \left[ -\frac{\partial \lambda_1}{\partial t} - \lambda_1 \frac{\partial f_1}{\partial \omega} + \frac{\partial}{\partial z} \left( \lambda_1 \frac{\partial f_1}{\partial \omega_z} \right) + \frac{\partial}{\partial r} \left( \lambda_1 \frac{\partial f_1}{\partial \omega_r} \right) - \frac{\partial^2}{\partial r^2} \left( \lambda_1 \frac{\partial f_1}{\partial \omega_{rr}} \right) \right] \delta \omega dz dr dt - \\ & \int_0^T \int_0^R \lambda_1 \frac{\partial f_1}{\partial \omega_z} \delta \omega(t, r, Z) dr dt + \int_0^T \int_0^R \left[ \lambda_1 \frac{\partial f_1}{\partial \omega_z} - \lambda_2 \frac{\partial f_2}{\partial \omega} \right] \delta \omega(t, r, 0) dr dt + \\ & \int_0^T \int_0^Z \left[ -\lambda_1 \frac{\partial f_1}{\partial \omega_r} + \frac{\partial}{\partial r} \left( \lambda_1 \frac{\partial f_1}{\partial \omega_{rr}} \right) \right] \delta \omega(t, R, z) dz dt = 0 \end{aligned} \quad (4.40)$$



By applying the boundaries in Equation (4.7) into Equation (4.40) for  $\delta\omega(t, R, z)$  ,  $\delta\omega(t, r, 0)$  and  $\delta\omega(t, r, Z)$ , we obtain the following equations:

$$\delta\omega(t, R, z) = \delta\omega(t, r, 0) = \delta\omega(t, r, Z) = \delta\omega_{\text{int}} \quad (4.41)$$

Therefore Equation (4.40) becomes

$$\begin{aligned} \delta J = & \underbrace{\int_0^T \int_0^R \left[ -\beta r - \frac{\partial \lambda_2}{\partial t} \right] \delta z \, dr \, dt}_{\delta J_1} + \\ & \underbrace{\int_0^T \int_0^R \int_0^Z \left[ -\frac{\partial \lambda_1}{\partial t} - \lambda_1 \frac{\partial f_1}{\partial \omega} + \frac{\partial}{\partial z} \left( \lambda_1 \frac{\partial f_1}{\partial \omega_z} \right) + \frac{\partial}{\partial r} \left( \lambda_1 \frac{\partial f_1}{\partial \omega_r} \right) - \frac{\partial^2}{\partial r^2} \left( \lambda_1 \frac{\partial f_1}{\partial \omega_{rr}} \right) \right] \delta \omega \, dz \, dr \, dt}_{\delta J_2} - \\ & \underbrace{\int_0^T \int_0^R \lambda_1 \frac{\partial f_1}{\partial \omega_z} \delta \omega_{\text{int}}(t, r, Z) \, dr \, dt}_{\delta J_3} + \underbrace{\int_0^T \int_0^R \left[ \lambda_1 \frac{\partial f_1}{\partial \omega_z} - \lambda_2 \frac{\partial f_2}{\partial \omega} \right] \delta \omega_{\text{int}}(t, r, 0) \, dr \, dt}_{\delta J_4} + \\ & \underbrace{\int_0^T \int_0^Z \left[ -\lambda_1 \frac{\partial f_1}{\partial \omega_r} + \frac{\partial}{\partial r} \left( \lambda_1 \frac{\partial f_1}{\partial \omega_{rr}} \right) \right] \delta \omega_{\text{int}}(t, R, z) \, dz \, dt}_{\delta J_5} = 0 \end{aligned} \quad (4.42)$$

Assuming that the involved function are sufficiently differentiable,  $\delta J$  is zero if all the additive term in Equation (4.42) are individually zero. Thus,

Eliminating the terms  $\delta J_1$  and  $\delta J_2$  by defining the following adjoint equations:

$$\frac{\partial \lambda_1}{\partial t} = -\lambda_1 \left( \frac{\partial f_1}{\partial \omega} \right) + \frac{\partial}{\partial z} \left( \lambda_1 \frac{\partial f_1}{\partial \omega_z} \right) + \frac{\partial}{\partial r} \left( \lambda_1 \frac{\partial f_1}{\partial \omega_r} \right) - \frac{\partial^2}{\partial r^2} \left( \lambda_1 \frac{\partial f_1}{\partial \omega_{rr}} \right) \quad (4.43)$$

$$\frac{\partial \lambda_2}{\partial t} = -\beta r \quad (4.44)$$

Eliminate the terms  $\delta J_3$  to  $\delta J_5$  by defining the variational derivative with respect to  $\omega_{\text{int}}$  is

$$\begin{aligned} \frac{\partial J}{\partial \omega_{\text{int}}} = J\omega_{\text{int}} = & \int_0^T \int_0^R \left\{ \lambda_1 \frac{\partial f_1}{\partial \omega_z} \Big|_{(t,r,Z)} + \lambda_1 \frac{\partial f_1}{\partial \omega_z} \Big|_{(t,r,0)} - \lambda_2 \frac{\partial f_2}{\partial \omega} \Big|_{(t,r,0)} \right\} dr dt + \\ & \int_0^T \int_0^Z \left[ -\lambda_1 \frac{\partial f_1}{\partial \omega_r} + \frac{\partial}{\partial r} \left( \lambda_1 \frac{\partial f_1}{\partial \omega_{rr}} \right) \right]_{(t,R,z)} dz dt = 0 \end{aligned} \quad (4.45)$$

From Equations (4.12) and (4.45), we obtain

$$\begin{aligned} \frac{\partial J}{\partial \omega_{\text{int}}} = J\omega_{\text{int}} = & \int_0^T \int_0^R \left( -3\lambda_1 \frac{\alpha \omega^2}{\phi} \Big|_{z=Z} - \left[ 3\lambda_1 \frac{\alpha \omega^2}{\phi} - 2\lambda_2 \alpha \omega \right]_{z=0} \right) dr + \\ & \int_0^Z \left( -\lambda_1 \frac{\partial D}{\partial \omega} \cdot \frac{\partial \omega}{\partial r} - \lambda_1 \frac{D}{r} + \frac{\partial \lambda_1}{\partial r} D \right)_{(t,R,z)} dz dt \end{aligned} \quad (4.46)$$

See Appendix D for the derivations of Equation (4.46)

Equation (4.46) is the necessary condition for the maximization of  $J$  when the continuity as well as adjoint equations are satisfied. The boundary conditions of adjoint Equation (4.43) are

$$\lambda_1(T, r, z) = 0; \quad 0 \leq r \leq R, 0 \leq z \leq Z \quad (4.47)$$

$$\lambda_1(t, 0, z) = \lambda_1(t, R, z) = 0; \quad 0 \leq t \leq T, 0 \leq z \leq Z \quad (4.48)$$

The boundary conditions of adjoint Equation (4.44) is given by

$$\lambda_2(T, r) = 0 \quad ; \quad 0 \leq r \leq R \quad (4.49)$$

## 4.5 Adjoint Equations

From Equation (4.12), (4.14), and (4.43) and (4.44), the final adjoint equations are

$$\frac{\partial \lambda_1}{\partial t} = -\frac{3\alpha}{\phi} \omega^2 \frac{\partial \lambda_1}{\partial z} + \frac{\partial \lambda_1}{\partial r} \frac{D}{r} - \lambda_1 \frac{D}{r^2} - \frac{\partial^2 \lambda_1}{\partial r^2} D \quad (4.50)$$

$$\frac{\partial \lambda_2}{\partial t} = -\beta r = -2\pi\rho\phi r \quad (4.51)$$

(See all the derivations of Equations (4.50) and (4.51) in Appendix E)

The boundary conditions for Equation (4.50) are

$$\lambda_1(T, r, z) = 0 \quad (4.52)$$

$$\lambda_1(t, 0, z) = \lambda_1(t, R, z) = 0 \quad (4.53)$$

The boundary condition for Equation (4.51) is

$$\lambda_2(T, r) = 0 \quad (4.54)$$

## 4.6 Optimal Control Algorithm

Due to the presence of highly non-linear partial differential equations with split boundaries, the analytical solution of this optimization problem is not possible. Therefore, the optimal control problem has to be solved numerically. The Optimal Control algorithm developed to determine the variation of propane concentration functional. To start the solution of the problem, the following computational algorithm is applied to maximize  $J$ , and determines the solvent concentration of solvent-oil interface versus time:

1. Initial guess for interface concentration function  $\omega_{\text{int}}(t)$  was provided.
2. Integrate the continuity equations forward i.e., Equations (4.3) and (4.5) using the initial, and the control function, to obtain the values of state variables  $\omega(t, r, z)$  and  $\omega(z, t)$  at each node. Save the values of state variables at the discretized points.
3. Evaluate the objective functional using the values of control functions, and state variables. Save the objective functional value.
4. Integrate adjoint equations backward i.e., Equation (4.50) and Equation (4.51) using final condition, the control function, and saved values of state variables. Save the values of adjoint variables at the discretized point. Equations (4.3), (4.5), (4.46), (4.50) and (4.51) were expressed in a finite difference form to be utilized in the simulation.
5. Improve  $\omega_{\text{int}}(t)$  using the gradient correction  $J\omega_{\text{int}}(t)$  given by Equation (4.46).
6. Repeat computations, go to step 2 until there is no further improvement in the objective functional value. When the improvement in is negligible the control functions are optimal.

#### 4.6.1 The Gradient Improvement Method

A gradient method was adapted for iterative solution of this optimal control problem. The greatest local rate of increase in the value of a function with respect to its variables is in the direction of its gradient. This direction is called the steepest ascent direction. The negative of the variational derivative for  $J$  gives its steepest ascent direction at  $r$  and  $z$  and time  $t$ . Equation (4.45) is used to set the search direction to find the maximum of  $J$ .

Quasi-Newton methods (or called variable metric methods) are the most favored of the methods that use gradient of a function. These methods compute a search direction utilizing first order gradient information. Newton's methods make use of the second order information (Hessian matrix) of a function. Hessian matrix is calculated numerically, which involve a large amount of computations. Quasi-Newton methods avoid the calculation of exact Hessian by generating approximate Hessian matrix using an appropriate updating technique. A large number of Hessian updating methods have been developed. However, the formula derived by Broyden, Fletcher,

Goldfarb, and Shanno, 1970 (BFGS) is one of the most effective method. It utilizes first order gradient information to generate the Hessian.

#### 4.6.2 Implementation of the Improvement Method

The search direction was set by the variational derivative  $J_{\omega_{\text{int}}}$  given by

$$\begin{aligned} \frac{\partial J}{\partial \omega_{\text{int}}} = J_{\omega_{\text{int}}} = & \int_0^T \left[ \int_0^R \left( -3\lambda_1 \frac{\alpha \omega^2}{\phi} \Big|_{z=Z} - \left[ 3\lambda_1 \frac{\alpha \omega^2}{\phi} - 2\lambda_2 \alpha \omega \right]_{z=0} \right) dr + \right. \\ & \left. \int_0^Z \left( -\lambda_1 \frac{\partial D}{\partial \omega} \cdot \frac{\partial \omega}{\partial r} - \lambda_1 \frac{D}{r} + \frac{\partial \lambda_1}{\partial r} D \right)_{(t,R,z)} dz \right] dt \end{aligned} \quad (4.46)$$

The gradient correction  $J_{\omega_{\text{int}}}$  was expressed in a finite-difference form along  $r$  direction to be utilized in the simulation. Differential changes are averaged at any concentration, which has multiple existences in the height domain. The values of differential changes are time-averaged before their usage for the gradient correction in  $(\omega_{\text{int}})$  by the BFGS method. The iterative improvement in the value of  $(\omega_{\text{int}})$  was given by

$$\omega_{\text{int}i+1} = \omega_{\text{int}i} - \beta_i J_{\omega_{\text{int}}} \quad (4.55)$$

where  $\beta_i$  is the optimal step length along the search direction in the  $i$  th iteration determined by BFGS algorithm (Press et al., 2007).

#### 4.7 Integration of Continuity and Adjoint Equations

These partial differential equations (PDEs) were integrated as follows. The cylindrical model was divided into equal-spaced grid points in  $r$  and  $z$  directions denoted by  $N_r$  and  $N_z$  respectively as shown in Figure 4.2. This transformed each of them into a set of simultaneous ordinary differential equations. The ordinary differential equations are stiff equations since there are

different scales of the independent variable on which the dependent variables change. The numerical method used to solve the stiff equations is semi-implicit extrapolation method (Press et al., 2007). It is robust and an excellent method for stiff problems. An adaptive step size control method was used in the algorithm to achieve the accuracy in the solution with minimum computational effort.

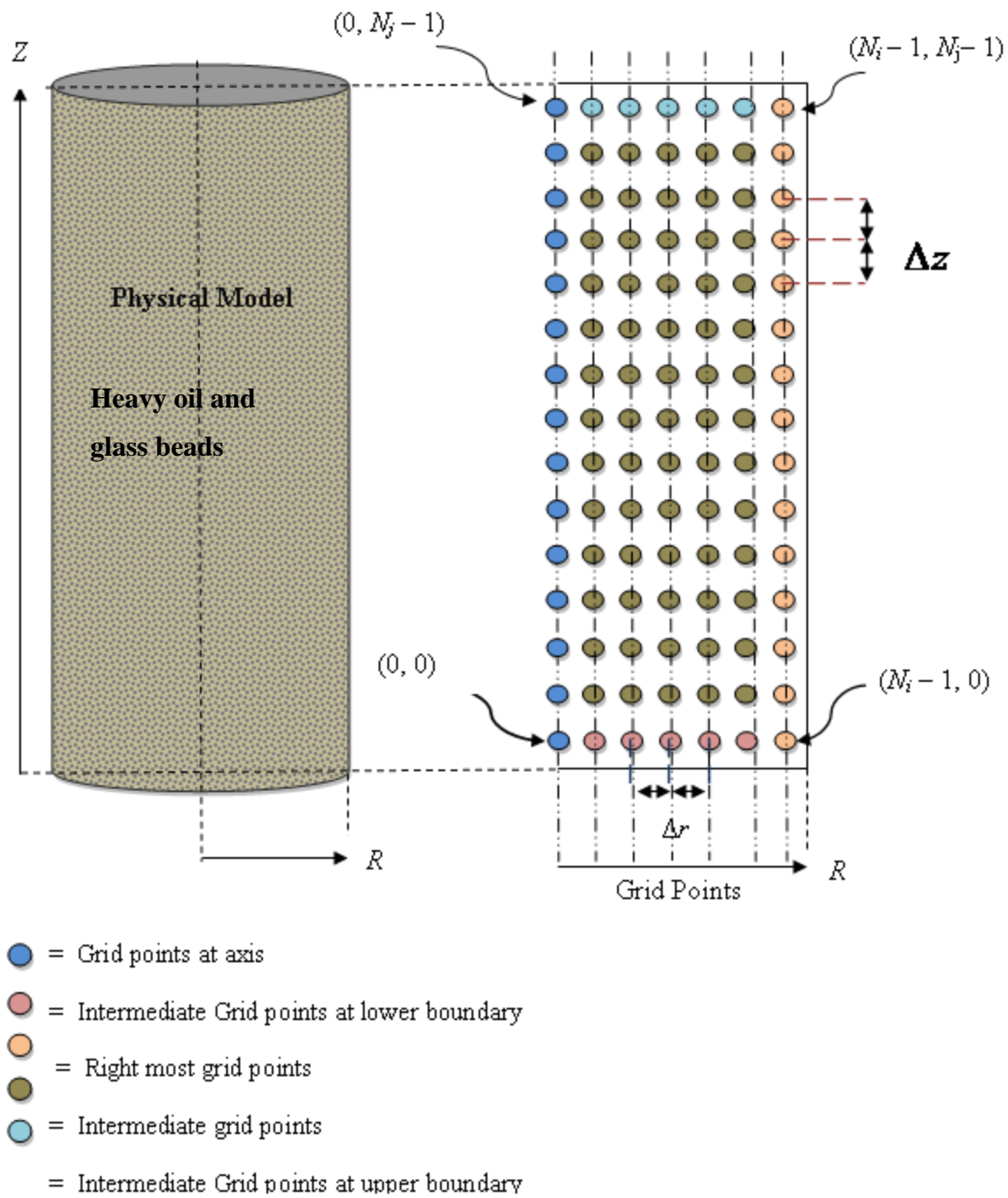


**Figure 4.2** Cylindrical model and node distribution

### 4.7.1 Discretized Mathematical Model

The PDEs given by Equations (4.3) and (4.5) were finite-differenced along  $r$  and  $z$  directions to obtain a set of ordinary differential equations (ODEs). The second order finite difference formulas were used. The ODEs are as follows.

#### For intermediate Grid points

For  $0 < i < (N_i - 1)$  and  $0 < j < (N_j - 1)$

$$\begin{aligned} \frac{d\omega_{i,j}}{dt} = D \left[ \frac{1}{r_i} \frac{\omega_{i+1,j} - \omega_{i-1,j}}{2\Delta r} + \frac{\omega_{i+1,j} - 2\omega_{i,j} + \omega_{i-1,j}}{\Delta r^2} \right] + \\ \frac{\partial D}{\partial \omega} \left[ \frac{\omega_{i+1,j} - \omega_{i-1,j}}{2\Delta r} \right]^2 - \frac{K_r K \rho g \cos \theta}{\mu_0 \phi} 3\omega_{i,j}^2 \left[ \frac{\omega_{i,j+1} - \omega_{i,j-1}}{2\Delta z_i} \right] \end{aligned} \quad (4.56)$$

#### For Axis Grid Points

When  $i = 0$  for  $0 < j < (N_j - 1)$

$$\frac{d\omega_{0,j}}{dt} = - \frac{K_r K \rho g \cos \theta}{\mu_0 \phi} 3\omega_{0,j}^2 \left[ \frac{\omega_{0,j+1} - \omega_{0,j-1}}{2\Delta z_i} \right] \quad (4.57)$$

When  $i = 0$  and  $j = 0$

$$\frac{d\omega_{0,0}}{dt} = - \frac{K_r K \rho g \cos \theta}{\mu_0 \phi} 3\omega_{0,0}^2 \left[ \frac{\omega_{0,1} - \omega_{\text{int}}}{2\Delta z_0} \right] \quad (4.58)$$

When  $i = 0$  and  $j = (N_j - 1)$



$$\frac{d\omega_{0,N_j-1}}{dt} = -\frac{K_r K \rho g \cos \theta}{\mu_0 \phi} 3\omega_{0,N_j-1}^2 \left[ \frac{\omega_{\text{int}} - \omega_{0,N_i-2}}{2\Delta z_0} \right] \quad (4.59)$$

### For Right most Grid Points

When  $i = (N_i - 1)$  and  $j = 0$

$$\begin{aligned} \frac{d\omega_{Ni-1,0}}{dt} = D \left[ \frac{1}{r_{Ni-1}} \frac{\omega_{\text{int}} - \omega_{Ni-2,0}}{2\Delta r} + \frac{\omega_{\text{int}} - 2\omega_{Ni-1,0} + \omega_{Ni-2,0}}{\Delta r^2} \right] + \\ \frac{\partial D}{\partial \omega} \left[ \frac{\omega_{\text{int}} - \omega_{Ni-2,0}}{2\Delta r} \right]^2 - \frac{K_r K \rho g \cos \theta}{\mu_0 \phi} 3\omega_{Ni-1,0}^2 \left[ \frac{\omega_{Ni-1,1} - \omega_{\text{int}}}{2\Delta z_{Ni-1}} \right] \end{aligned} \quad (4.60)$$

When  $i = (N_i - 1)$

$$\begin{aligned} \frac{d\omega_{Ni-1,j}}{dt} = D \left[ \frac{1}{r_{Ni-1}} \frac{\omega_{\text{int}} - \omega_{Ni-2,j}}{2\Delta r} + \frac{\omega_{\text{int}} - 2\omega_{Ni-1,j} + \omega_{Ni-2,j}}{\Delta r^2} \right] + \\ \frac{\partial D}{\partial \omega} \left[ \frac{\omega_{\text{int}} - \omega_{Ni-2,j}}{2\Delta r} \right]^2 - \frac{K_r K \rho g \cos \theta}{\mu_0 \phi} 3\omega_{Ni-1,j}^2 \left[ \frac{\omega_{Ni-1,j+1} - \omega_{Ni-1,j-1}}{2\Delta z_{Ni-1}} \right] \end{aligned} \quad (4.61)$$

when  $i = (N_i - 1)$  and  $j = (N_j - 1)$

$$\begin{aligned} \frac{d\omega_{Ni-1,N_j-1}}{dt} = D \left[ \frac{1}{r_{Ni-1}} \frac{\omega_{\text{int}} - \omega_{Ni-2,N_j-1}}{2\Delta r} + \frac{\omega_{\text{int}} - 2\omega_{Ni-1,N_j-1} + \omega_{Ni-2,N_j-1}}{\Delta r^2} \right] + \\ \frac{\partial D}{\partial \omega} \left[ \frac{\omega_{\text{sat}} - \omega_{Ni-2,N_j-1}}{2\Delta r} \right]^2 - \frac{K_r K \rho g \cos \theta}{\mu_0 \phi} 3\omega_{Ni-1,N_j-1}^2 \left[ \frac{\omega_{\text{it}} - \omega_{Ni-1,N_j-2}}{2\Delta z_{Ni-1}} \right] \end{aligned} \quad (4.62)$$

### For Lower most Intermediate Grid Points

When  $0 < i < (N_i - 1)$  and  $j = 0$

$$\begin{aligned} \frac{d\omega_{i,0}}{dt} = D \left[ \frac{1}{r_i} \frac{\omega_{i+1,0} - \omega_{i-1,0}}{2\Delta r} + \frac{\omega_{i+1,0} - 2\omega_{i,0} + \omega_{i-1,0}}{\Delta r^2} \right] + \\ \frac{\partial D}{\partial \omega} \left[ \frac{\omega_{i+1,0} - \omega_{i-1,0}}{2\Delta r} \right]^2 - \frac{K_r K \rho g \cos \theta}{\mu_0 \phi} 3\omega_{i,0}^2 \left[ \frac{\omega_{i,1} - \omega_{\text{int}}}{2\Delta z_i} \right] \end{aligned} \quad (4.63)$$

### For Upper most Intermediate Grid Points

When  $0 < i < (N_r - 1)$  and  $j = (N_z - 1)$

$$\begin{aligned} \frac{d\omega_{i,N_j-1}}{dt} = D \left[ \frac{1}{r_i} \frac{\omega_{i+1,N_j-1} - \omega_{i-1,N_j-1}}{2\Delta r} + \frac{\omega_{i+1,N_j-1} - 2\omega_{i,N_j-1} + \omega_{i-1,N_j-1}}{\Delta r^2} \right] + \\ \frac{\partial D}{\partial \omega} \left[ \frac{\omega_{i+1,N_j-1} - \omega_{i-1,N_j-1}}{2\Delta r} \right]^2 - \frac{K_r K \rho g \cos \theta}{\mu_0 \phi} 3\omega_{i,N_j-1}^2 \left[ \frac{\omega_{\text{int}} - \omega_{i,N_j-2}}{2\Delta z_i} \right] \end{aligned} \quad (4.64)$$

where  $\omega_{i,j}$  is the mass fraction of the solvent at the node,  $(i, j)$  corresponding to the coordinate,  $r$  and  $z$ . The distances between grid points are  $\Delta r$  and  $\Delta z_i$  respectively along  $r$  and  $z$  directions.  $\Delta r$  is constant and given by

$$\Delta r = \frac{R}{N_r} \quad (4.65)$$

but  $\Delta z_i$  varies with time along  $r$  direction, and is given by

$$\Delta z_i = \frac{z_i}{N_z + 1} \quad (4.66)$$

### Change in the Height of Physical Model

The change of the bitumen height at any time is given by the following equations:

The change in height for  $0 \leq i < (N_r - 1)$  is given by

$$\frac{dz_i}{dt} = -v_{i,0} = -3 \frac{K_r K \rho g \cos \theta}{\mu_0} \left[ \frac{\omega_{i,0} + \omega_{i+1,0} + 2\omega_{\text{int}}}{4} \right]^2 \quad (4.67)$$

and for  $i = N_r - 1$

$$\frac{dz_{N_r-1}}{dt} = -v_{N_r-1,0} = -3 \frac{K_r K \rho g \cos \theta}{\mu_0} \left[ \frac{\omega_{N_r-1,0} + 3\omega_{\text{int}}}{4} \right]^2 \quad (4.68)$$

### 4.7.2 The Adjoint Equations

The ordinary differential equations of adjoint equations written for corresponding grid points are as follows:

For intermediate grid points, i.e. for  $0 < i < (N_r - 1)$  and  $0 < j < (N_z - 1)$

$$\begin{aligned} \frac{d\lambda_{i,j}}{dt} = & D \left[ \frac{1}{r_{i_r}} \frac{\lambda_{i+1,j} - \lambda_{i-1,j}}{2\Delta r} - \frac{\lambda_{i+1,j} - 2\lambda_{i,j} + \lambda_{i-1,j}}{\Delta r^2} \right] - \\ & D \left[ \frac{\lambda_{i,j}}{r_i^2} \right] - 3 \frac{K_r K \rho g \cos \theta}{\mu_o \phi} \omega_{i,j}^2 \left[ \frac{\lambda_{i,j+1} - \lambda_{i,j-1}}{2\Delta z_i} \right] \end{aligned} \quad (4.69)$$

For axial grid points, i.e.  $i = 0$  and  $0 < j < (N_z - 1)$

$$\frac{d\lambda_{0,0}}{dt} = \frac{d\lambda_{0,j}}{dt} = \frac{d\lambda_{0,N_z-1}}{dt} = 0 \quad (4.70)$$

For the right most grid points, i.e.

**a)** for  $i = (N_r - 1)$  and  $j = 0$

$$\begin{aligned} \frac{d\lambda_{N_r-1,0}}{dt} = & D \left[ \frac{1}{r_{N_r-1}} \frac{-\lambda_{N_r-2,0}}{2\Delta r} - \frac{-2\lambda_{N_r-1,0} + \lambda_{N_r-2,0}}{\Delta r^2} \right] - \\ & D \left[ \frac{\lambda_{N_r-1,0}}{r_{N_r-1}^2} \right] - 3 \frac{K_r K \rho g \cos \theta}{\mu_o \varphi} \omega_{N_r-1,0}^2 \left[ \frac{\lambda_{N_r-1,1}}{2\Delta z_{N_r-1}} \right] \end{aligned} \quad (4.71)$$

**b)** for  $i = (N_r - 1)$  and  $0 < j < (N_z - 1)$

$$\begin{aligned} \frac{d\lambda_{N_r-1,j}}{dt} = & D \left[ \frac{1}{r_{N_r-1}} \frac{-\lambda_{N_r-2,j}}{2\Delta r} - \frac{-2\lambda_{N_r-1,j} + \lambda_{N_r-2,j}}{\Delta r^2} \right] - \\ & D \left[ \frac{\lambda_{N_r-1,j}}{r_{N_r-1}^2} \right] - 3 \frac{K_r K \rho g \cos \theta}{\mu_o \varphi} \omega_{N_r-1,j}^2 \left[ \frac{\lambda_{N_r-1,j} - \lambda_{N_r-1,j-1}}{2\Delta z_{N_r-1}} \right] \end{aligned} \quad (4.72)$$

**c)** for  $i = (N_r - 1)$  and  $j = (N_z - 1)$

$$\begin{aligned} \frac{d\lambda_{N_r-1,N_z-1}}{dt} = & D \left[ \frac{1}{r_{N_r-1}} \frac{-\lambda_{N_r-2,N_z-1}}{2\Delta r} - \frac{-2\lambda_{N_r-1,N_z-1} + \lambda_{N_r-2,N_z-1}}{\Delta r^2} \right] - \\ & D \left[ \frac{\lambda_{N_r-1,N_z-1}}{r_{N_r-1}^2} \right] - 3 \frac{K_r K \rho g \cos \theta}{\mu_o \varphi} \omega_{N_r-1,N_z-1}^2 \left[ \frac{\lambda_{N_r-1,N_z-2}}{2\Delta z_{N_r-1}} \right] \end{aligned} \quad (4.73)$$

For the lower most intermediate grid points, i.e. for  $0 < i < (N_r - 1)$  and  $j = 0$

$$\begin{aligned} \frac{d\lambda_{i,0}}{dt} = & D \left[ \frac{1}{r_i} \frac{\lambda_{i+1,0} - \lambda_{i-1,0}}{2\Delta r} - \frac{\lambda_{i+1,0} - 2\lambda_{i,0} + \lambda_{i-1,0}}{\Delta r^2} \right] - \\ & D \left[ \frac{\lambda_{i,0}}{r_i^2} \right] - 3 \frac{K_r K \rho g \cos \theta}{\mu_o \phi} \omega_{i,0}^2 \left[ \frac{\lambda_{i,1}}{2\Delta z_i} \right] \end{aligned} \quad (4.74)$$

For the upper most intermediate grid points, i.e. for  $0 < i < (N_r - 1)$  and  $j = (N_z - 1)$

$$\begin{aligned} \frac{d\lambda_{i,N_z-1}}{dt} = & D \left[ \frac{1}{r_i} \frac{\lambda_{i+1,N_z-1} - \lambda_{i-1,N_z-1}}{2\Delta r} - \frac{\lambda_{i+1,N_z-1} - 2\lambda_{i,N_z-1} + \lambda_{i-1,N_z-1}}{\Delta r^2} \right] - \\ & D \left[ \frac{\lambda_{i,N_z-1}}{r_i^2} \right] - 3 \frac{K_r K \rho g \cos \theta}{\mu_o \phi} \omega_{i,N_z-1}^2 \left[ \frac{-\lambda_{i,N_z-2}}{2\Delta z_i} \right] \end{aligned} \quad (4.75)$$

The equation for the second adjoint variable is

For  $0 \leq i < (N_r - 1)$

$$\frac{d\lambda_i}{dt} = -2\pi \rho \phi r_{i+1} \quad (4.76)$$

Similarly, the gradient correction  $J_{\omega_{\text{int}}}$  was expressed in a finite-difference form along  $r$  direction. The equations written for corresponding grid points are as follows:

For intermediate grid points, i.e. for  $0 < i < (N_r - 1)$  and  $0 < j < (N_z - 1)$

$$\begin{aligned} \frac{\partial J}{\partial \omega_{\text{int}}} = & \int_0^T \left[ \int_0^R \left( -3\lambda_1 \frac{\alpha \omega^2}{\phi} \Big|_{z=Z} - \left[ 3\lambda_1 \frac{\alpha \omega^2}{\phi} - 2\lambda_2 \alpha \omega \right]_{z=0} \right) dr + \right. \\ & \left. \int_0^Z \left( -\lambda_1 \frac{\partial D}{\partial \omega} \cdot \frac{\partial \omega}{\partial r} - \lambda_1 \frac{D}{r} + \frac{\partial \lambda_1}{\partial r} D \right)_{(t,R,z)} dz \right] dt \end{aligned} \quad (4.77)$$

$$\frac{\partial J}{\partial \omega_{\text{int}}} = \int_0^T \left[ \int_0^R T_1 dr + \int_0^Z T_2 dz \right] dt \quad (4.78)$$

where

$$T_1 = -3\lambda_1 \frac{\alpha \omega^2}{\phi} \Big|_{z=Z} - \left[ 3\lambda_1 \frac{\alpha \omega^2}{\phi} - 2\lambda_2 \alpha \omega \right]_{z=0} \quad (4.79)$$

$$T_2 = -\lambda_1 \frac{\partial D}{\partial \omega} \cdot \frac{\partial \omega}{\partial r} - \lambda_1 \frac{D}{r} + \frac{\partial \lambda_1}{\partial r} D \quad (4.80)$$

At  $Z=Z_0$

For the upper most intermediate grid points, i.e. for  $0 < i < (N_r - 1)$  and  $j = (N_z - 1)$

At  $Z=0$

For the lower most intermediate grid points, i.e. for  $0 < i < (N_r - 1)$  and  $j = 0$

So Equation (4.79) becomes

$$(T_1) = -3[\lambda_1]_{i, N_z-1} \frac{\alpha [\omega_{i, N_z-1}]^2}{\phi} \Big|_{z=Z} - 3\lambda_{1,0} \frac{\alpha [\omega_{i,0}]^2}{\phi} \Big|_{z=0} + 2[\lambda_2]_{i,0} \alpha \omega_{i,0} \Big|_{z=0} \quad (4.81)$$

For the right most grid point at  $r=R$ , i.e.  $0 < j < (N_z - 1)$  and  $i = N_r - 1$

applying backward finite difference

$$(T_2)_{N_r-1,j} = -\lambda_{N_r-1,j} \frac{\partial D}{\partial \omega} \left[ \frac{\omega_{\text{int}} - \omega_{N_r-2,j}}{2\Delta r} \right] - \lambda_{N_r-1,j} \frac{D_{N_r-1,j}}{r_{N_r-1}} + D_{N_r-1,j} \left[ \frac{\lambda_{1\text{int}} - \lambda_{1N_r-2,j}}{2\Delta r} \right] \quad (4.82)$$

$$\left( \frac{\partial J}{\partial \omega_{\text{int}}} \right)_{i,j} = \sum_{t=0}^{t=T} \left[ \left( \sum_{i=0}^{N_i-1} T_1 \right) \Delta r + \left( \sum_{j=0}^{N_j-1} T_2 \right) \Delta z \right] \Delta t \quad (4.83)$$

The cumulative mass of produced live oil at any time becomes:

$$m_{\text{cal}} = 2\pi\rho\phi \sum_{i=0}^{N_{i-1}} (Z_0 - z_i) r_{i+1} \Delta r \quad (4.84)$$

The adjoint equations have to be solved backward in the time domain. Since they are dependent on concentration and height, they can be only solved after solving the equation of continuity forward in the time domain. With an accuracy of  $10^{-6}$  in the time domain, the equations were numerically integrated using semi-implicit Bader-Deuflhard algorithm, and adaptive step size control (Press et al., 2007). Analytical Jacobian of Equations (4.56-4.64), (4.67), (4.68), (4.69-4.75) was employed in the calculations, and the validity of the Jacobian equations was confirmed with the analytical solution to an error of  $10^{-4}$ . To fix the number of grid points along the  $r$  and  $z$  directions,  $N_r$  and  $N_z$ , the equations were integrated with increasing the number of grid points until the changes in the calculated oil production rates became negligible. The number of grid points along the  $r$  and  $z$  directions, were chosen to provide reasonable computation times.

## 4.8 The Optimal Control Algorithm

Figure 4.3 shows the optimal control algorithm developed to determine solvent concentration of solvent-oil interface versus time. Programmed in C++ language, the developed algorithm was implemented on Itanium 2/ Intel Itanium processor (64 bit, 1.5 GHz, 15.9 GB of RAM) with Intel C++ compiler. The above algorithm is computationally very intensive because a large number of finite-differenced ordinary differential equations and the associated Jacobian evaluations are needed to obtain reliable solutions. The optimal control algorithm took 1–3 weeks to execute.

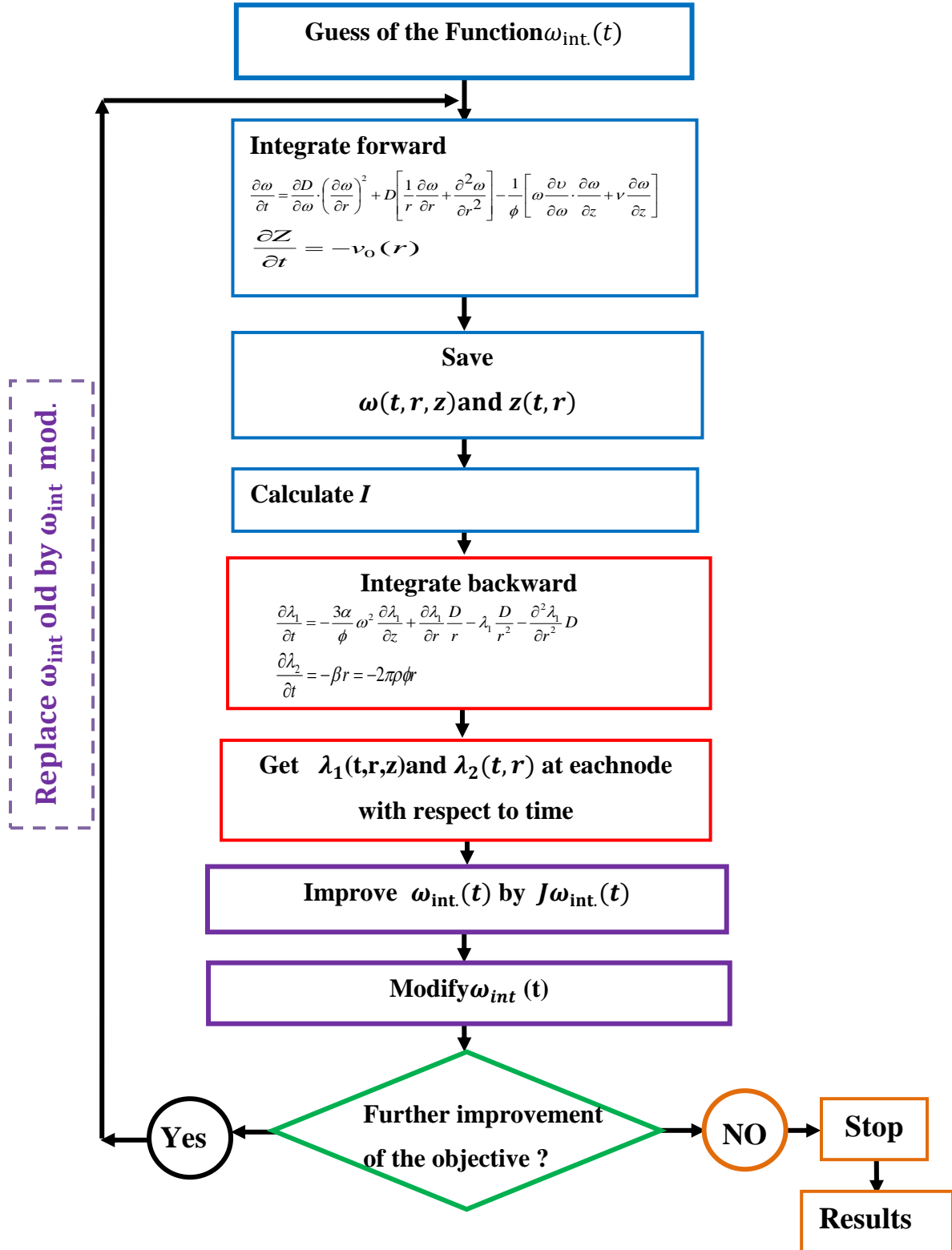


**Figure 4.3** The Optimal control algorithm





# 5

## Results and Discussion

This chapter experimentally examines the effect of permeability, physical model height, and uniform solvent injection pressure on oil production as well as live oil properties such as viscosity, density and solubility. Next, the results of proof-of-concept experiments are discussed. Finally, the results of the optimal control algorithm are presented. These results provide the optimal solvent injection pressure versus time policies. The associated enhanced oil production values are compared to those obtained from the validation experiments implementing the solvent injection versus time policies previously obtained from the optimal control algorithm.

As mentioned previously, all experiments were conducted using a laboratory scale physical model of heavy oil of 14,500 mPa·s viscosity at room temperature and pressure. To check the reproducibility of oil production, about half of the distinct Vapex experiments done in this study were randomly selected and repeated. The percentage errors between the oil production rates from the repeated experiments were found to be in the range of 1.5–2.0%.

## 5.1 Live Oil Production

To determine the effect of change in permeability, physical model height, and pressure on production rates, Vapex process was carried out using heavy oil with viscosity of 14,500 mPa·s and two models of different physical model lengths and varied permeabilities. The lengths of the models used were 25 and 45 cm. All physical models were packed with glass beads to create a homogeneous system with porosity of about 38% and different permeabilities. Propane and butane were individually used as pure solvents close to the dew point pressures (111.69 and 689.5 kPa, respectively) at the room temperature of 21°C.

Figure 5.1 shows the change in the weight of a physical model with time using butane in Vapex experiments for 204 Darcy permeability. Appendix G provides the graphs of recorded weight of the physical model versus time for the rest of the experiments.

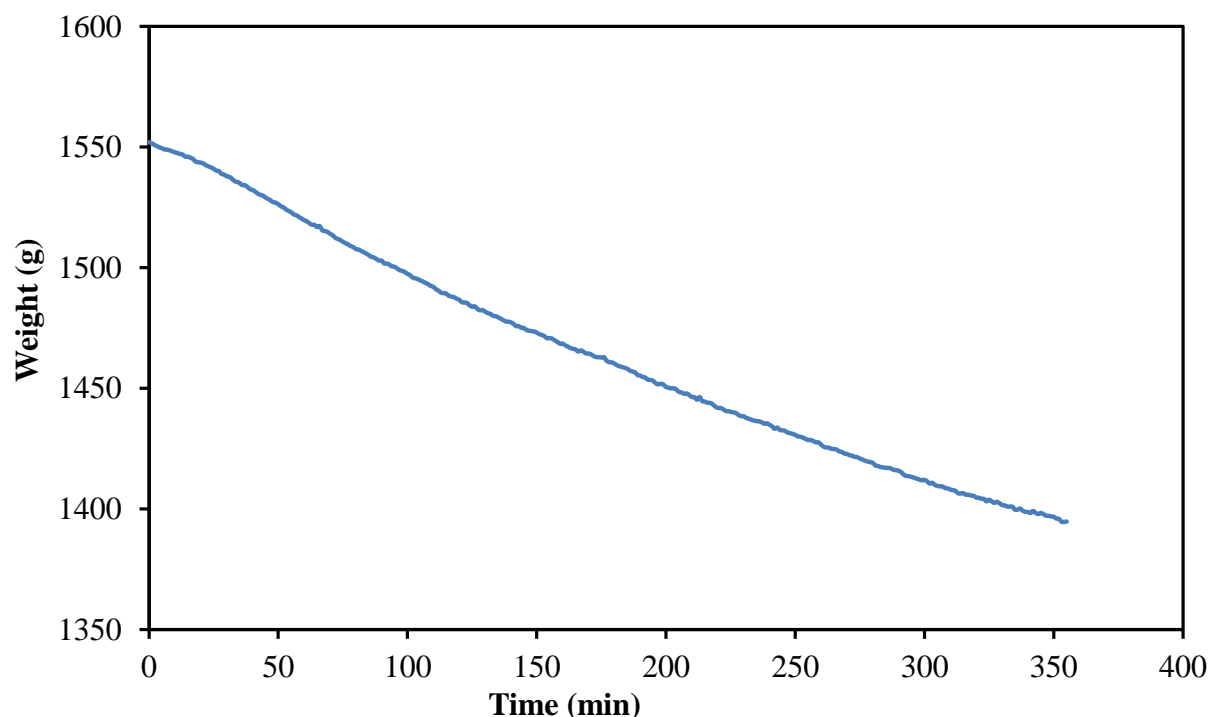


**Figure 5.1** Recorded weight of the physical model with time (model height: 25 cm, permeability: 204 Darcy, solvent: butane)

### 5.1.1 Oil Production Rate with Different Permeabilities

Figure 5.2 shows cumulative live oil production for different heights of the physical model. To determine production rate, the slope of the linear portion of cumulative production curve was taken for each model. The recorded production time starts at the time the first drop of oil gets into the collection tube and continues until production stops completely or slows down significantly.

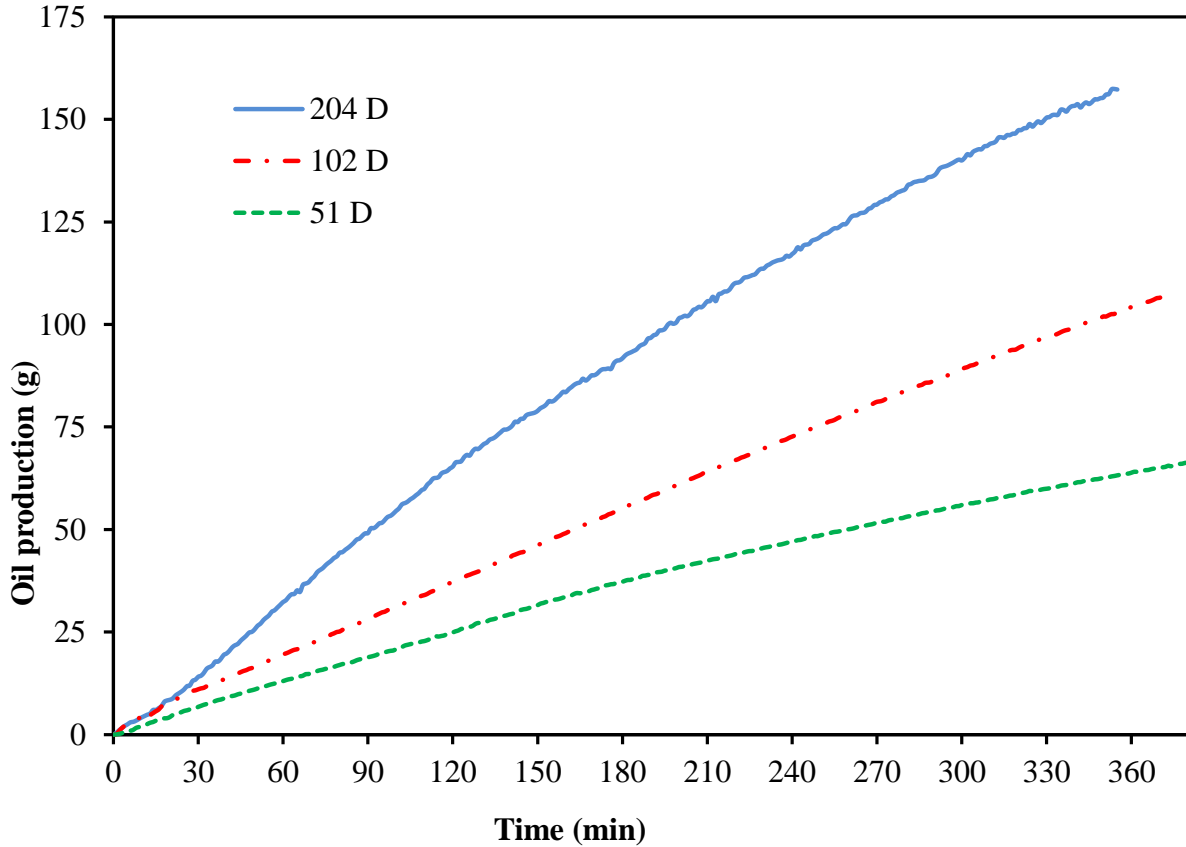


**Figure 5.2** Oil production versus time (model height: 25 cm, pressure: 111.69 kPa, solvent: butane)

Based on material balance, recovery of 85–92% of original oil in place (OOIP) was achieved in all experiments. The correlation between production rate  $m$  (g/min) and the permeability  $K$  (Darcy) is given by the following equation:

$$\dot{m} = 0.0122 K^{0.68} \quad (5.1)$$

with an  $r^2$  value of 0.9994. The above equation is a power function typically used to correlate live oil production through Vapex (Oduntan et al. 2001). The production rate does not increase linearly with the permeability of model ( $K$ ), but varies with almost the square root of the permeability.

Figure 5.3 presents the comparison of the cumulative live oil produced versus time for the physical model of 25 cm height with different permeabilities (427, 204, 87 and 40 Darcy) using propane as a solvent. It is observed that both the cumulative oil produced and the live oil production rate decreased with the model permeability. Higher permeability models resulted in higher % OOIP recovery and production rates.

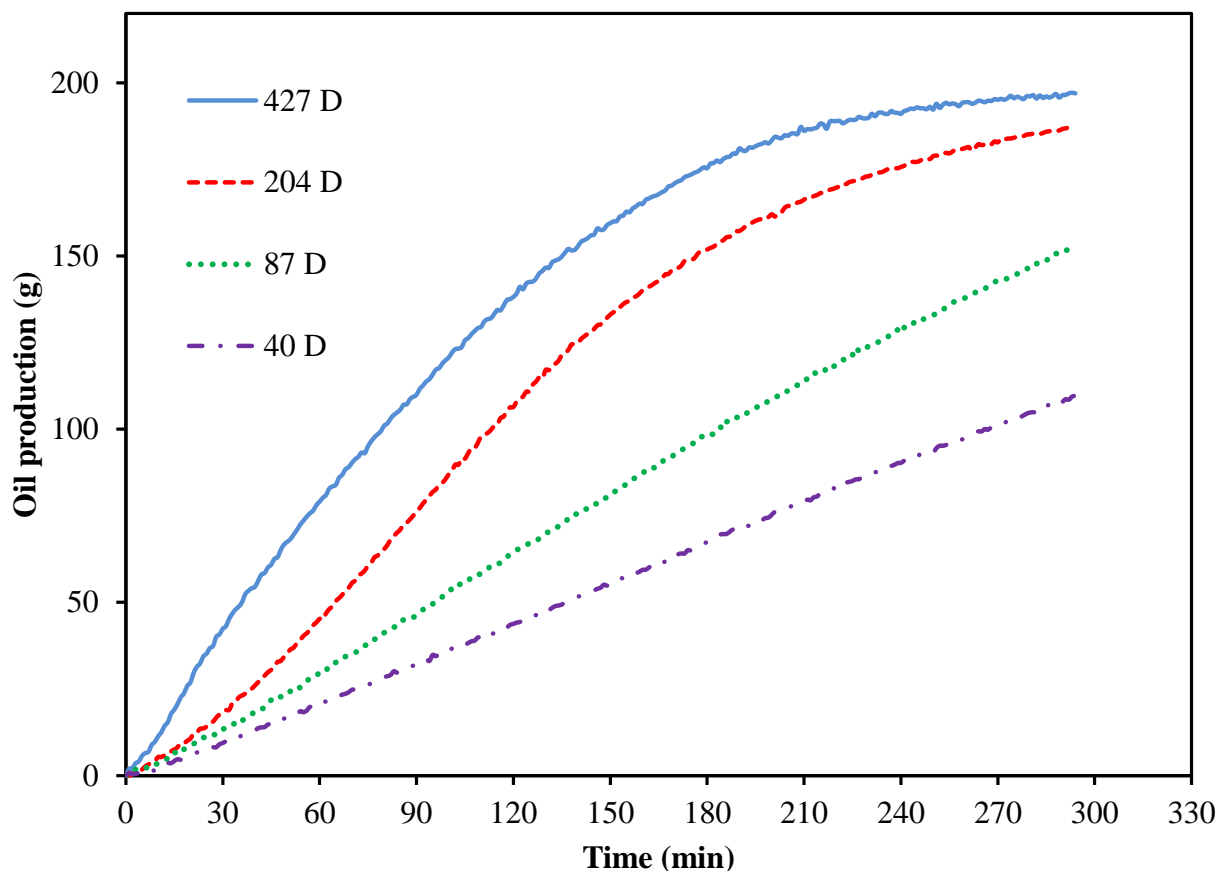


**Figure 5.3** Oil production versus time at different permeabilities, (model height: 25 cm, heavy pressure: 689.5 kPa, solvent: propane)

Figure 5.4 presents the relationship between the live oil production rate and model permeability. The production increases with permeability. The data points are fitted by a power function,

$$\dot{m} = 0.0594 K^{0.5061} \quad (5.2)$$

According to the above equation the oil production rate (g/min) in Vapex process is virtually square root function of the model permeability (Darcy).

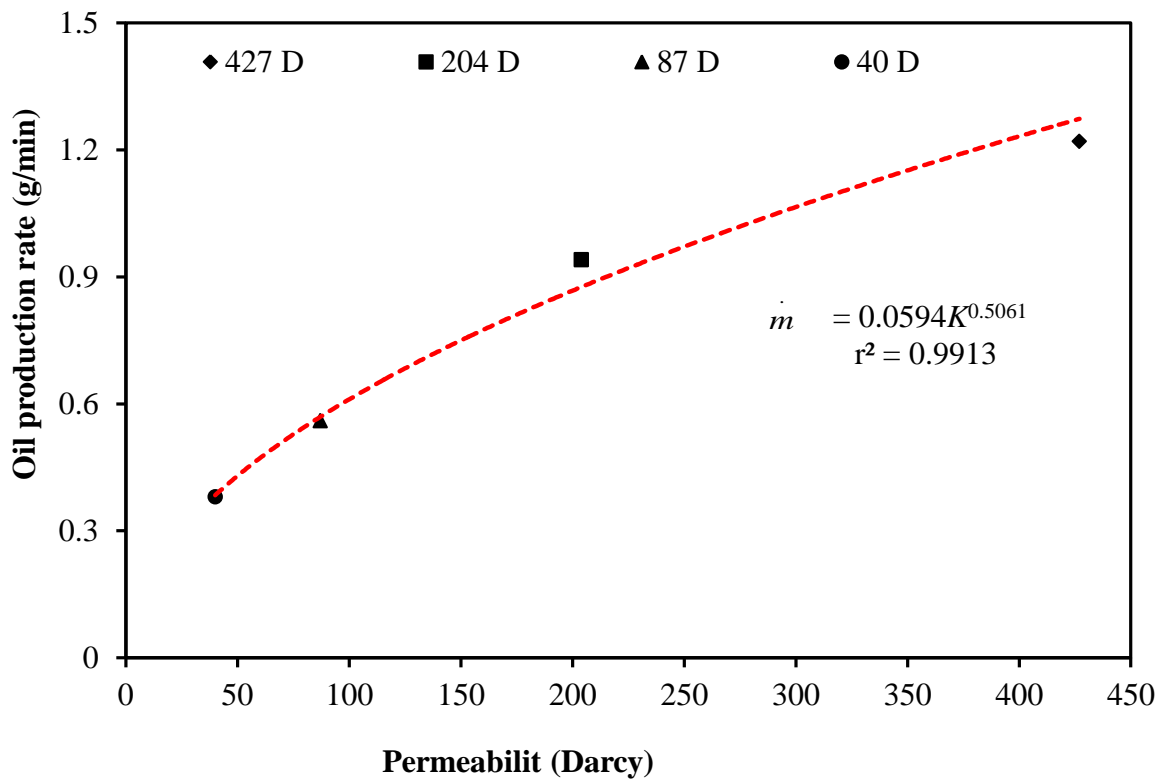


**Figure 5.4** Variation of production rate with model permeability (model height: 25 cm, pressure: 689.5 kPa, solvent: propane)

### 5.1.2 Oil Production Rate with Different Model Heights

Figure 5.5 shows a comparison of the oil production rates for different model heights (25 and 45 cm), and same permeability (204 Darcy) using butane as solvent. The average production

rates were calculated based on the cumulative live oil production divided by total production time during experiment. It was observed that production rate for 45 cm model height was 30% higher than 25 cm model. This percent increase indicates that live oil production from Vapex is strongly dependent on the height of the physical model.

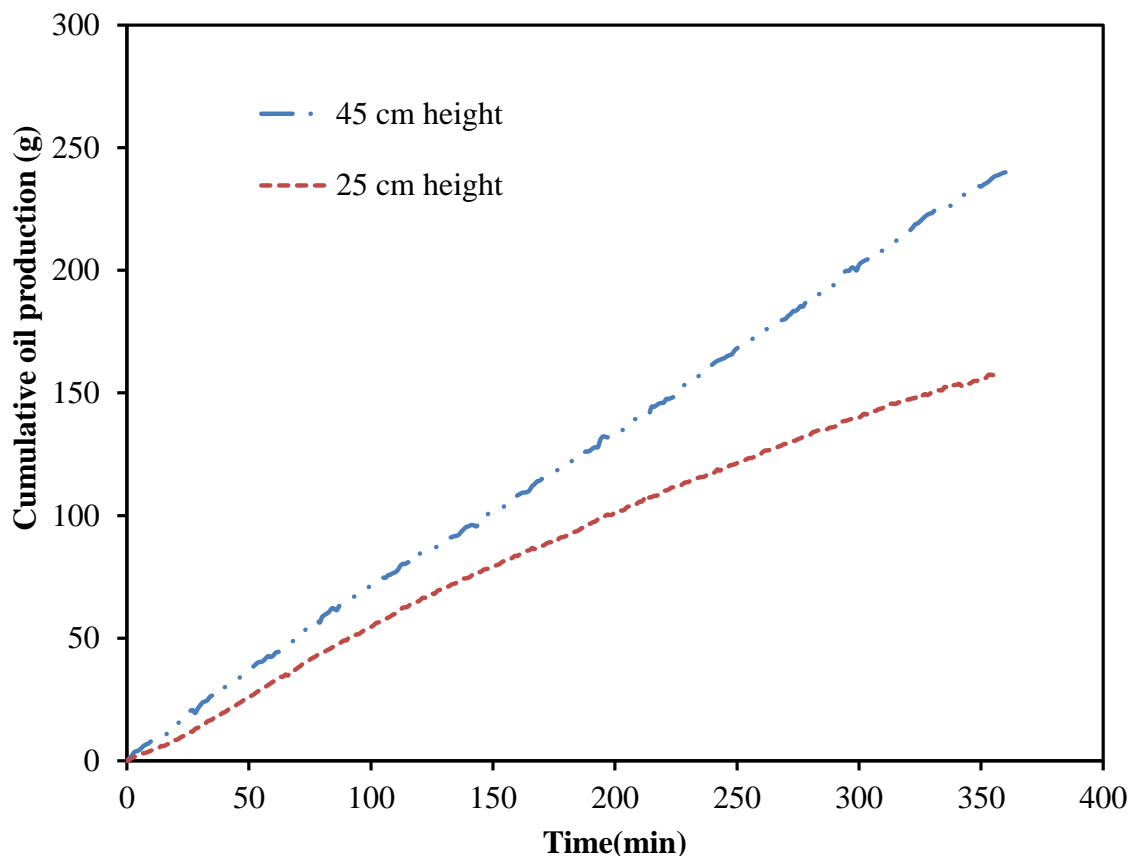


**Figure 5.5** Oil production versus experimental time for butane

### 5.1.3 Oil Production at Different Uniform Pressures

In order to study the effect of uniform pressure on heavy oil recovery by Vapex process, pure butane solvent at different injection pressures of 91.01, 97.90, 104.80, and 111.69 kPa was injected into the physical sample enclosure for 6 h using heavy oil with viscosity of 14,500 mPa·s. Figure 5.6 shows the cumulative live oil productions at varying pressures. It is clear from this figure that more oil was produced at higher pressures. Typically we found that by

increasing the pressure from 91.01 kPa to 111.69 kPa, the production rate of oil increased from 0.25 g/min to 0.45 g/min. This was due to the increase in the solubility of the solvent in heavy oil with pressure. In other words, use of vaporized solvent near its saturation conditions resulted in more oil recovery. As a result, the recovery process efficiency increased as the pressure approached the saturation pressure. We also injected the solvent gas at very close to the dew point. It was observed that at the pressure of 17.2 psi (118.58kPa), there was a sudden pressure drop and solvent condensation, which reduced oil production (see Figure 5.7). This reduction is due to a decrease in mass transfer in presence of liquid solvent.

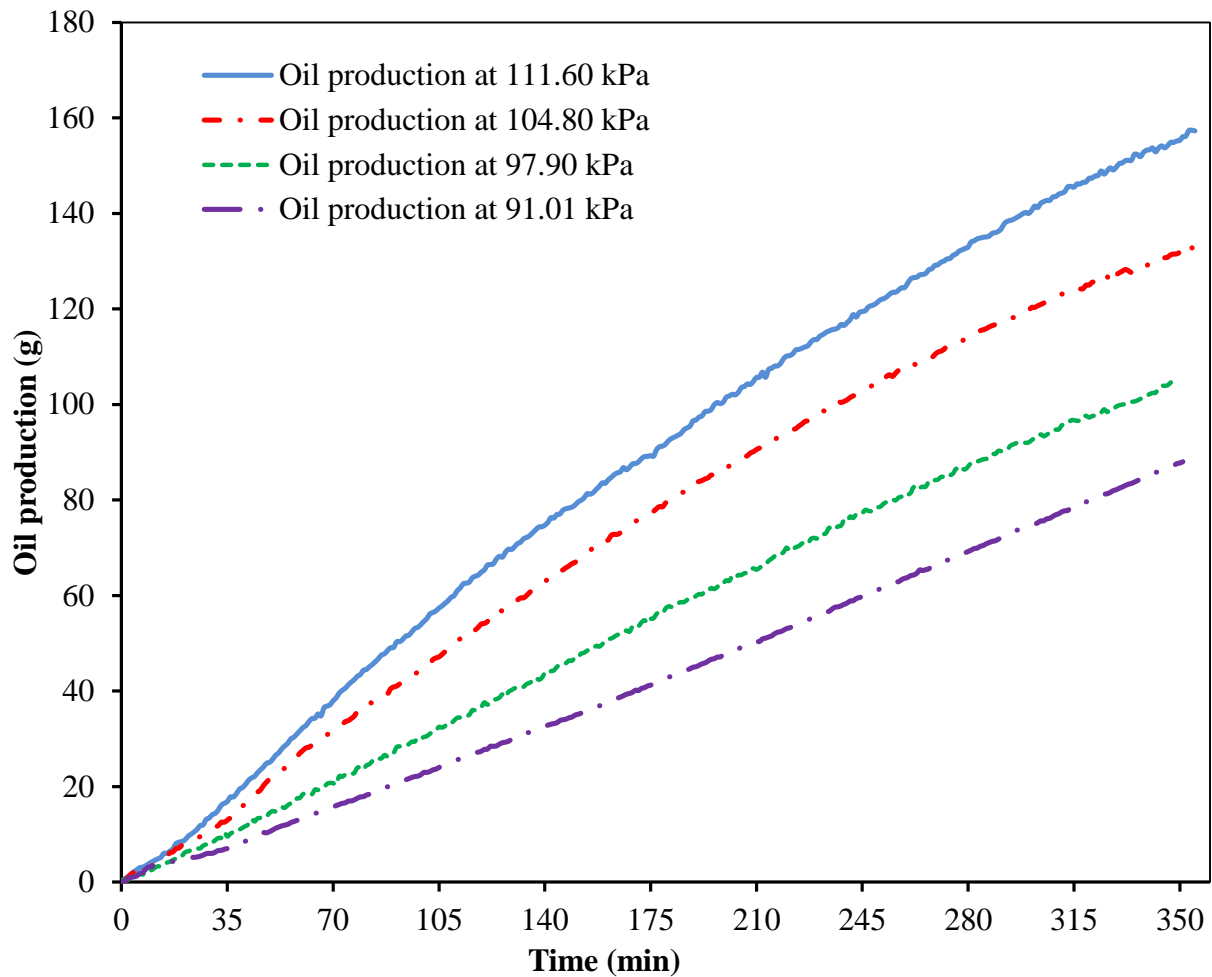


**Figure 5.6** Oil production versus time (204 Darcy, H=25 cm, butane, different pressure)



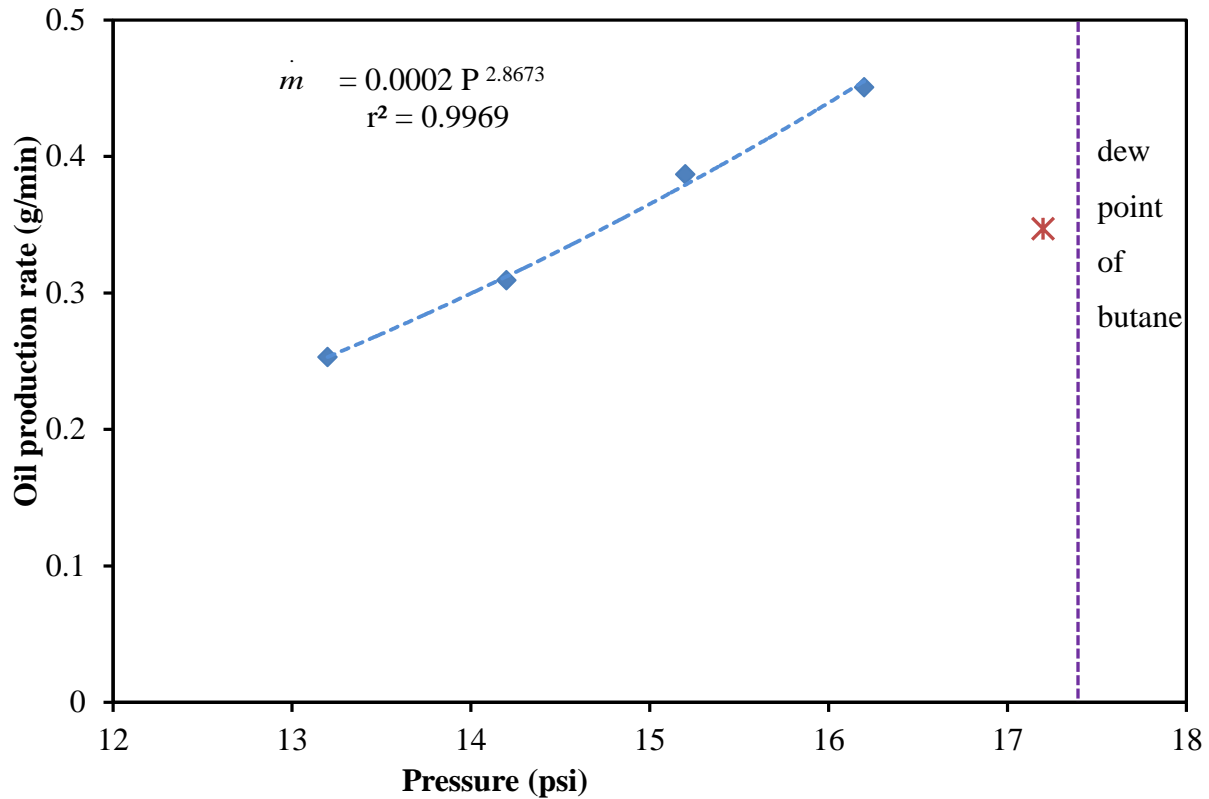


**Figure 5.7** Variation of production rate with model different pressure (204 Darcy, H=25 cm, butane)

The above experiments were performed for propane as well but not very close to the dew point. Four experiments were carried out at different uniform injection pressures of 482.6, 551.6, 620.5 and 689.5 kPa using the 25 cm high physical model of 14,500 mPa·s heavy oil of 204 Darcy permeability.

Figure 5.8 shows the cumulative live oil produced at the four injection pressures. As indicated in the figure, injecting propane close to its dew point pressure results in the highest oil production rate and recovery. A drop in propane pressure below the dew point pressure reduced the oil production rate as well as the overall oil recovery.

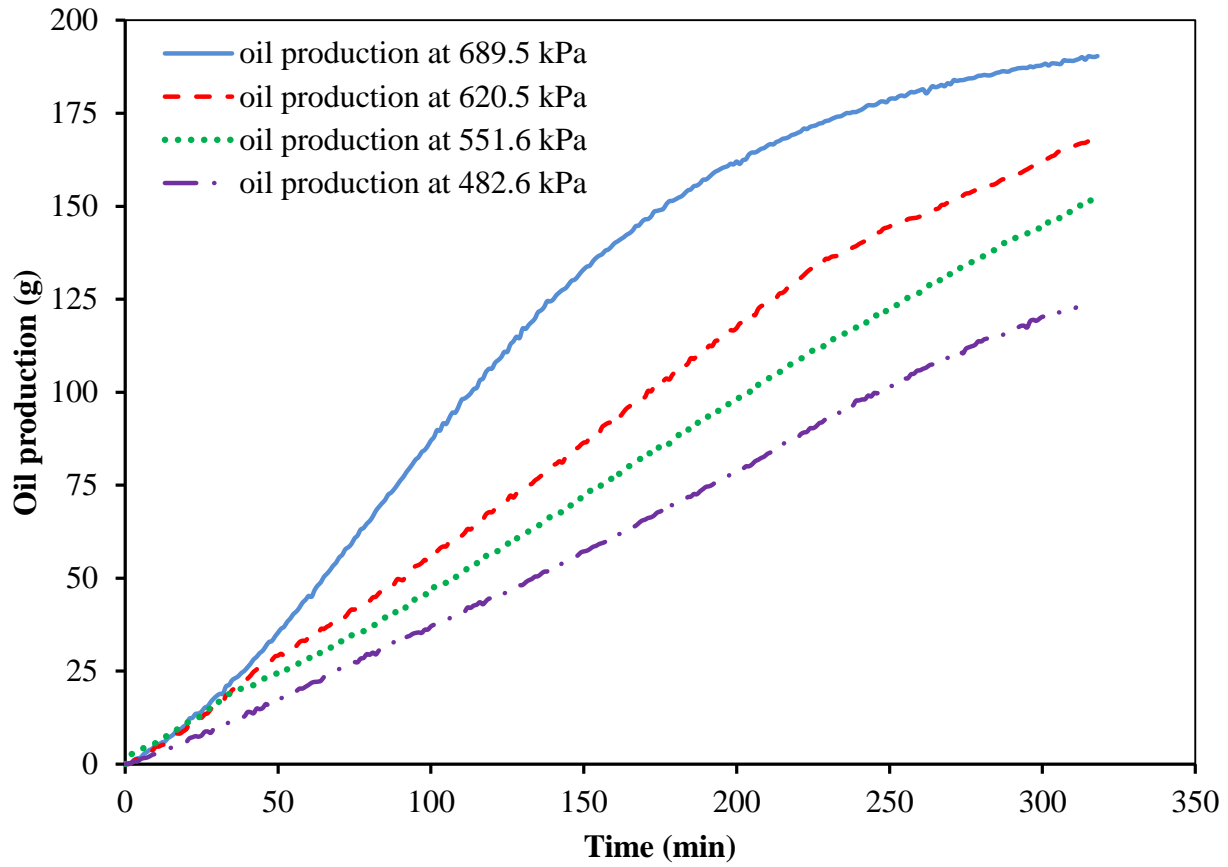


**Figure 5.8** Oil production versus time at different constant injection pressures (model height: 25 cm, heavy oil viscosity: 14,500 mPa·s, medium permeability: 204 Darcy)

## 5.2 Live Oil Properties

The experimental data generated in the Vapex experiments were used to calculate the live oil viscosity, density, cumulative production rate, and the solubility of solvent gas in heavy oil. These properties are needed to solve the mathematical mass transfer model of the experimental Vapex process.

### 5.2.1 Live Oil Density

Live oil density was measured at various times for each experiment as explained in Section 3.7. An average value for the live oil density was generated for each experiment. Table 5.2, shows average live oil density calculated from the data obtained from different physical model with almost the same temperature and pressure conditions for butane. It shows small variations in the measured density values. Table H.1 in Appendix H, shows average live oil density calculated from different properties of physical model.

**Table 5.1** Average live oil density for various physical models

Run (#)	Model Height (cm)	Permeability (Darcy)	Live oil Density (g/cm <sup>3</sup> )
1	25	204	0.8165
2	25	102	0.8138
3	25	51	0.8015
4	45	204	0.817

### 5.2.2 Live Oil Viscosity

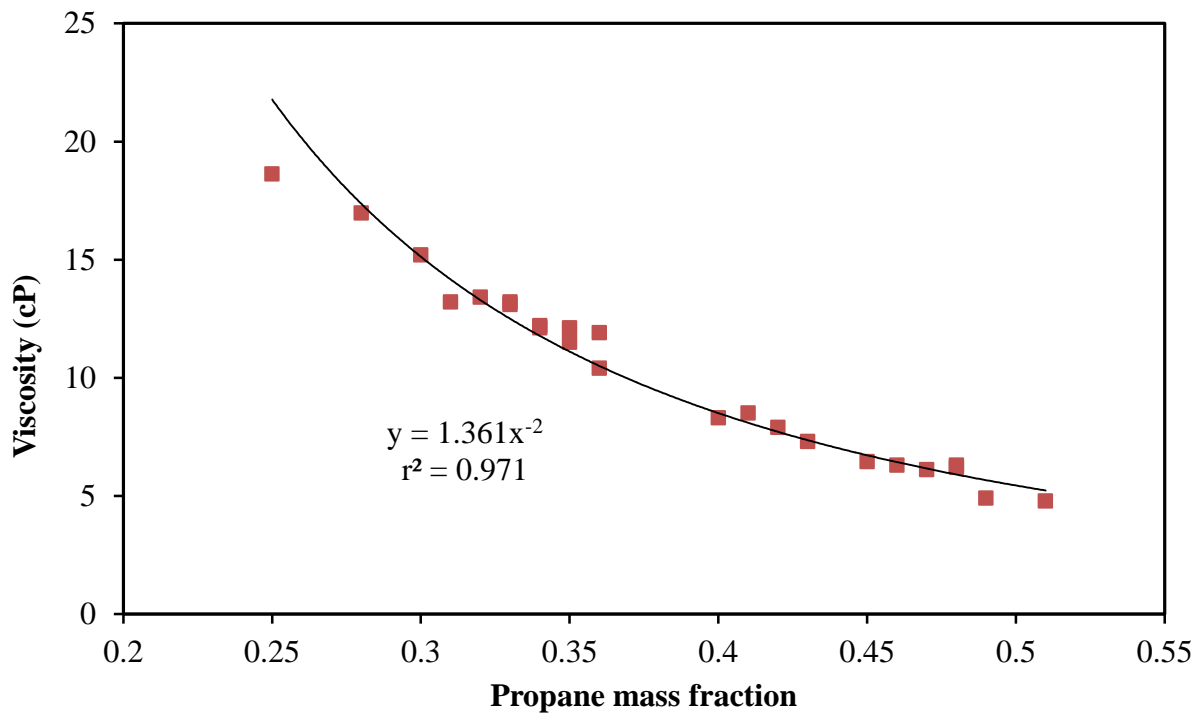
Reduced viscosity of heavy oil results from solvent concentration that augments as solvent penetrates and mixes with the heavy oil. Viscosity reduction of the mixture would affect the mobility and the fluid flow mechanism of the process. A viscosity model is crucial in Vapex since it governs the movement of live oil in the reservoir, and thus has a direct bearing on oil production. The viscosity of solvent-heavy oil system (live oil produced) was generated from the conducted experiments as explained in Section 3.6. Table 5.2 shows the experimentally measured live oil viscosity averaged for each experiment. The live oil viscosity is a strong function of propane mass fraction. It was reduced by four orders of magnitude and this would affect the mobility of the diluted oil.

**Table 5.2** Average live oil viscosity for physical models

Permeability (D)	Viscosity (cP)	
	25 cm model height	45 cm model height
204	8.3	6.91
102	5.49	4.3
51	4.12	3.01

Figure 5.9 is showing the viscosity as a function of propane mass fraction described by the power law relationship. The empirical correlation for the propane-heavy oil system during the process at the operating temperature and pressure is:

$$\mu = 1.361 \omega^{-2} \quad 0.25 \leq \omega \leq 0.51 \quad (5.3)$$

**Figure 5.9** Live oil viscosity versus propane mass fraction

### 5.2.3 Solubility of Solvent in Produced Oil

The amount of solvent gas dissolved in the produced heavy oil was determined by measuring the volume of the flashed gas and the weight of residual dead oil as explained in Section 3.6.3. Table 5.3 shows the averaged experimental values of propane mass fraction of Vapex experiments (10-12 live oil collections for each experiment). Propane mass fraction is found to increase with a decrease in permeability. Also seen in results of Das (1995), this dependence is justified by enhanced mass transfer, greater interfacial area, and larger residence time with lower permeability.

The dependence of solvent mass fraction on the height of the physical model height is apparent. The solvent mass fraction increases with the height of the physical model. The reason is that the time and path of exposure to the solvent increases with the height.

**Table 5.3** Solvent mass fractions in the produced oil for various physical models

Permeability (Darcy)	Propane mass fraction at 25 cm	Propane mass fraction at 45 cm
204	0.35	0.39
102	0.42	0.46
51	0.48	0.54

The average experimental amount of propane dissolved in the heavy oil falls in the range of observed propane solubility measured in the laboratory experiments by other investigators (Bademchi-Zadeh et al. 2009; Luo and Gu 2009; Freitag et al. 2005).

### 5.2.4 Correlation of Pressure with Solvent Interfacial Concentration

Experiments were performed to evaluate a functional relationship between the injection pressure of a solvent and its concentration at the solvent-heavy oil interface. This interfacial concentration is a boundary condition, which needs to be specified in order to solve the mathematical mass transfer model of the Vapex process.

Experiments with different injection pressures were conducted in the setup whose schematic is shown in Figure 3.3 and the maximum solvent concentration for each pressure was measured. Figure 5.10 presents the results obtained. According to the figure, the relationship between injection pressure and solvent concentration at the interface can be approximated with a power function with an  $r^2$  value of 0.998. This relationship was used to apply the injection pressure control policy to the Vapex process evaluated from simulations. The maximum propane mass fraction is 0.77 at 689.5 kPa, which agrees well with the previous study by Abukhalifeh (2009) for propane and the same heavy oil.

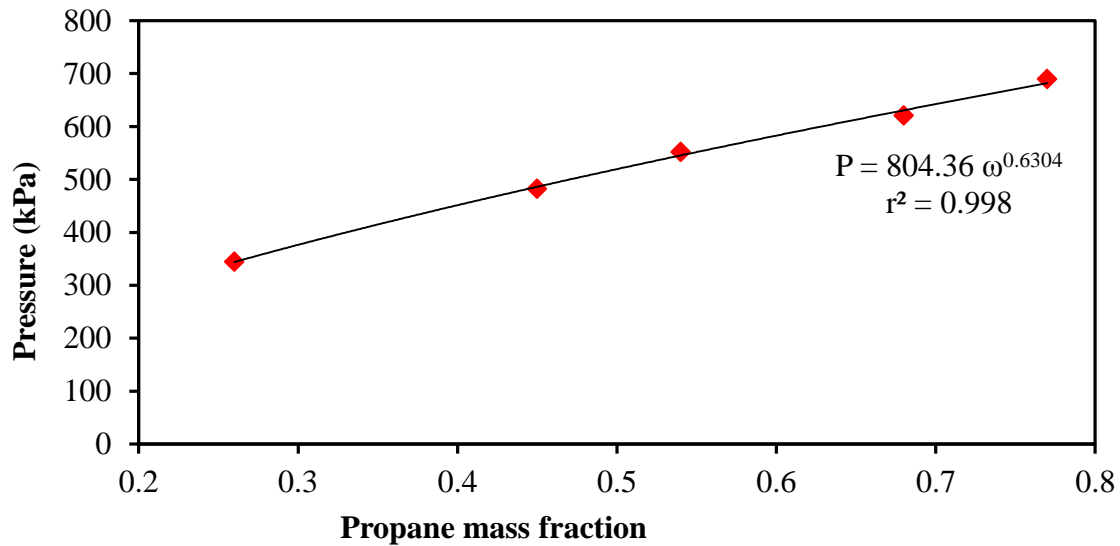


**Figure 5.10** Variation of propane mass fraction with different constant pressure

### 5.3 Proof of Concept for Vapex Enhancement by Variation of Solvent Injection Pressure

In this part of the study, we investigated the enhancement of oil recovery from Vapex by varying the solvent injection pressure with time. A heavy oil of 14,500 mPa·s viscosity was used in the experiments. Three different permeabilities, and two physical model heights of 25 and 45 cm were considered. The experiments were performed with varying solvent injection pressure versus time. Sharp pressure variations or pulses were introduced by sudden release and re-injection of the solvent gas (Muhamad, et. al., 2012).

It was found that the temporal variation of solvent injection pressure enhanced the extraction process significantly; resulting in an increase in live oil production. Pulse changes in pressure

were found to be more effective in increasing the production in comparison with other pressure versus time policies. These results serve to demonstrate that solvent pressure variations can enhance the oil recovery in Vapex.

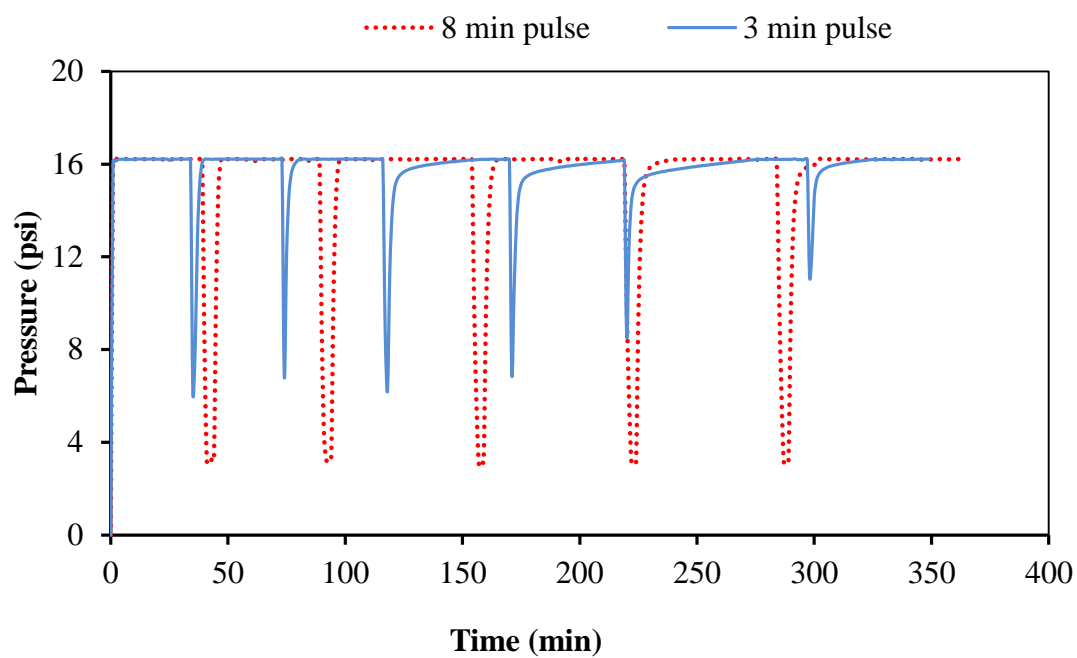
### 5.3.1 Effect of Pressure Variations

To examine this effect, the model height and permeability were fixed at 25 cm and 204 Darcy, respectively. Solvent injection pressure was varied to generate a temporal variation in pressure made of pressure pulses. The pressure was varied by releasing the solvent gas at once to vent and re-injecting the gas again with a specified time interval. The oil production history at two different re-injection times was studied and was compared with the production history from a constant injection pressure.

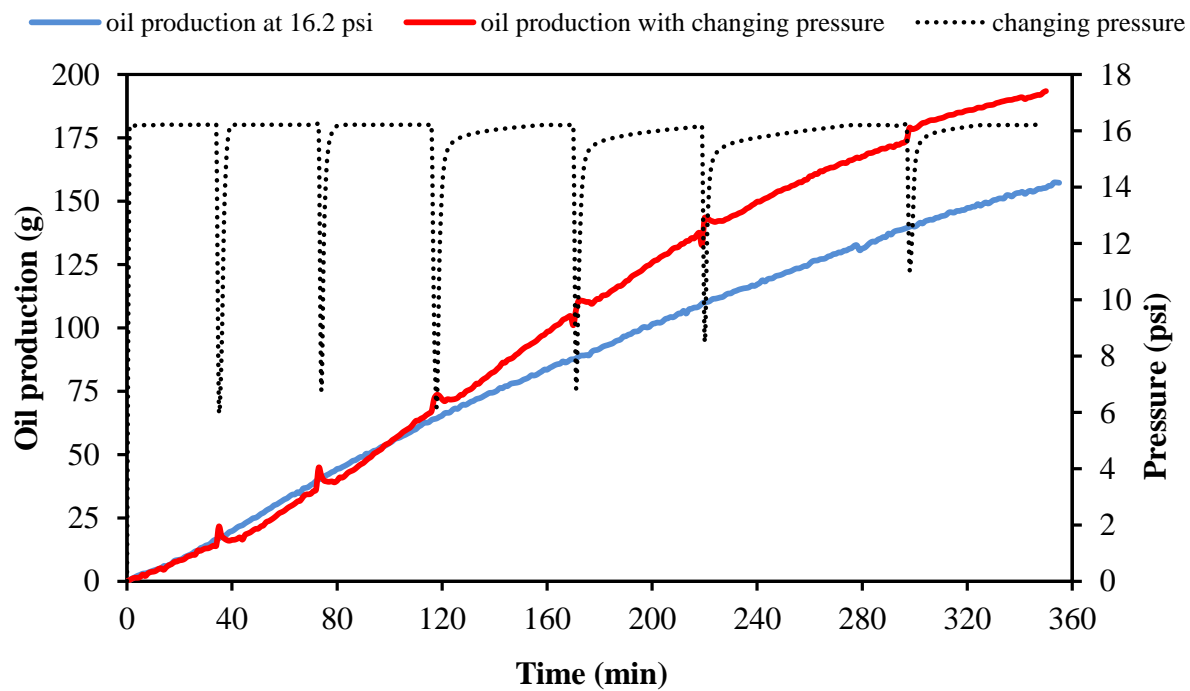
Figure 5.11 presents the solvent injection pressure versus time curves for two re-injection times. The solid black line shows the pressure curve when solvent was re-injected quickly to result in a *short pulse* of 3 minutes. The dotted black line shows the pressure when solvent was re-injected with a delay, thereby resulting in a *long pulse* of 8 minutes.

Figure 5.12 compares the cumulative oil production obtained from the constant pressure injection and pressure pulsing generated with short pulses. The pulse injection pressure is also presented on the same plot. Temporal variation in the injection pressure resulted in the recovery of 193 grams of oil in 350 minutes as compared to 155 grams of oil recovery over the same period for a constant injection pressure. This outcome indicates that a variation in the injection pressure pulsing resulted in 24% more recovery compared to constant injection pressure.

Figure 5.13 compares the cumulative oil production curves obtained from the constant pressure injection and pressure pulsing generated with long pulse. Similar to the previous case, temporal variation in injection pressure with long re-injection times resulted in ~19% more oil recovery compared to constant injection pressure. However, a short pulse showed more promising recovery and oil production rate. Moreover, the results also showed that there was an increase in production rate at the re-injection intervals, which indicates that some oil gets entrained along with solvent gas from the physical model



**Figure 5.11** Pressure versus time with long 8 min pulses, and short 3 min pulses



**Figure 5.12** Oil production versus time (204 Darcy, H=25 cm, butane, short pulse)



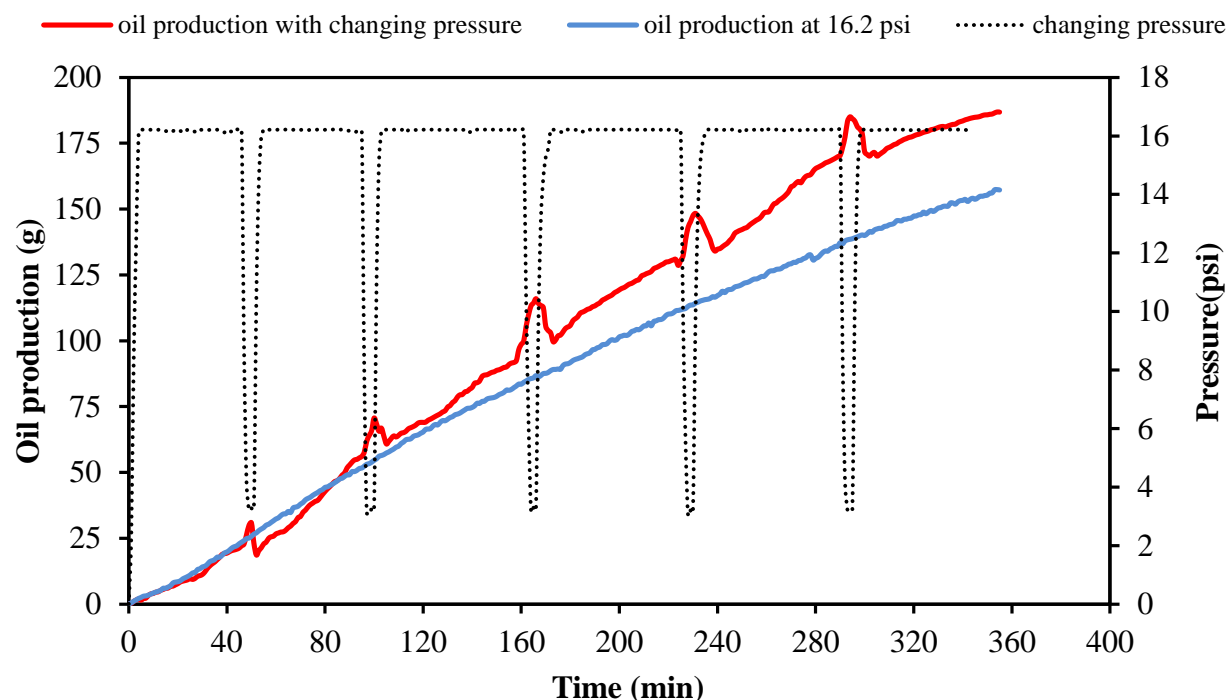


**Figure 5.13** Oil production versus time (204 Darcy, H=25 cm, butane, long pulse)

**NOTE** For the rest of the experiments, short pressure pulses were used, since they were found to be superior to the long pulses. Thus by pressure variation or pulsing we mean the use of short pulses.

### 5.3.2 Effect of Pressure Variation with Different Medium Permeabilities

The effect of pressure pulsing on oil recovery was examined for different permeability mediums specifically 102 and 51 Darcy with a model physical model height of 25 cm. Short pulses of solvent injection pressure were employed.

Figures 5.14 and 5.15 below compare oil production at constant pressure of 16.2 psi to that with varying pressure made of short pulses for 102 and 51 Darcy permeability. For both values of permeability, the cumulative oil production at the end of 350 minutes of solvent injection was slightly higher with temporal pressure variation. However, the oil production increased with pulsing pressure as compared to that with constant pressure. The fractional increase on an

average was higher with the low permeability than that with the higher permeability (1% more). For permeability of 102 Darcy, ~61% increase in produced live oil at the end of 350 min was observed (compared to constant pressure injection) while 51 Darcy permeability lead to ~60% increase in the produced oil.

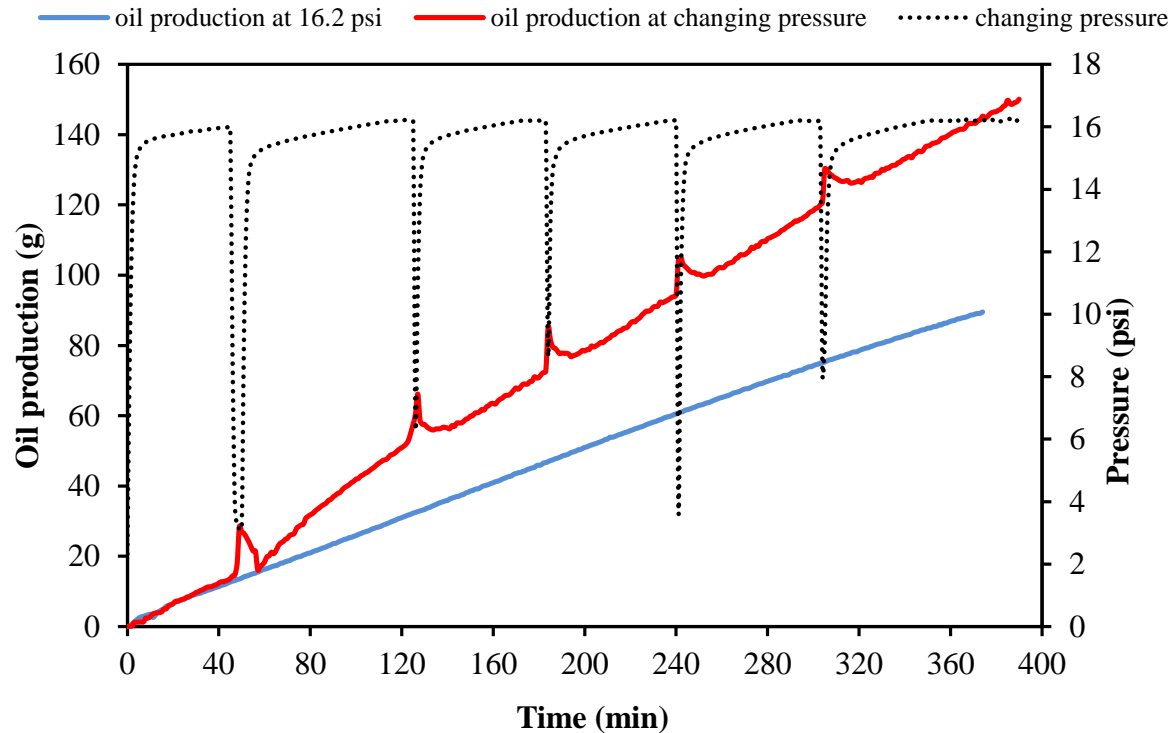


**Figure 5.14** Oil production versus time (102 Darcy, H=25 cm, butane gas, short pulse)

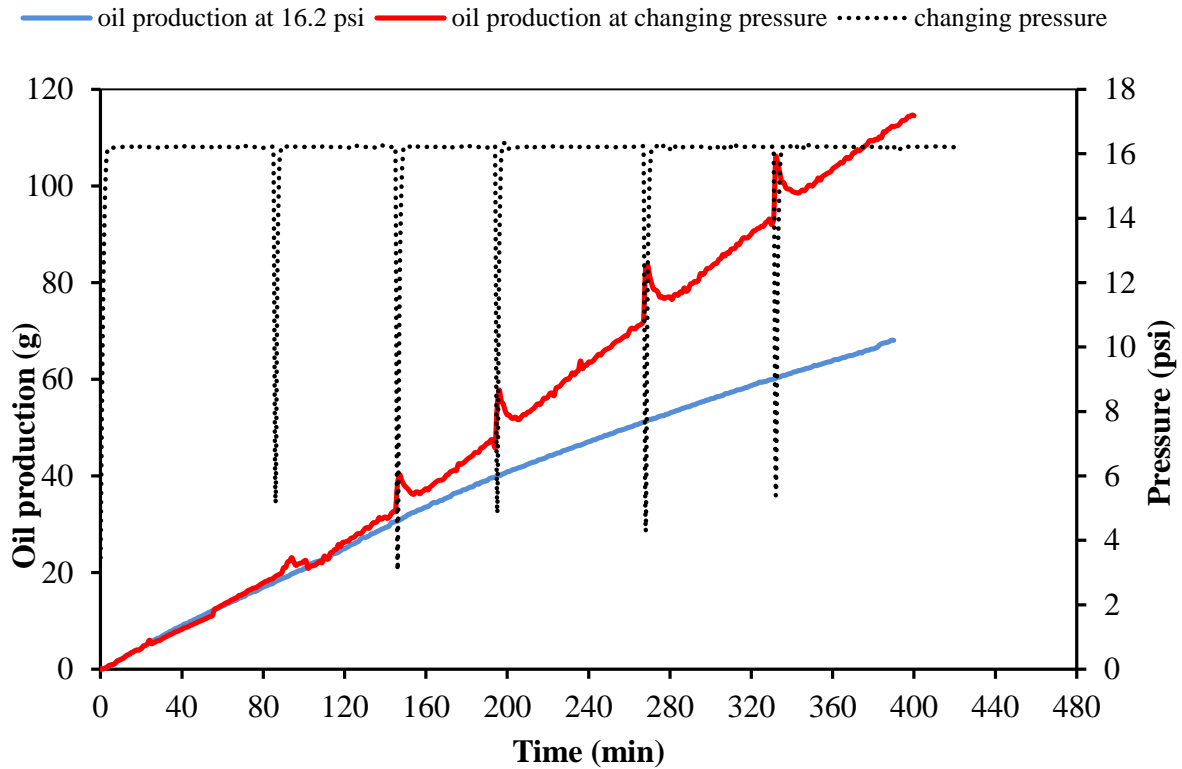


**Figure 5.15** Oil production versus time (51 Darcy, H=25 cm, butane gas, short pulse)

### 5.3.3 Effect of Pressure Variation with Different Physical Model Heights

To investigate the effect of pressure variation on oil recovery with different model heights, experiments were performed with physical model heights of 25 and 45 cm with a permeability of 204 Darcy, and varying solvent injection pressure.

Figures 5.16 and 5.17 present a comparison of the cumulative produced oil curves from constant injection pressure and from pressure pulsing for 25 and 45 cm model heights, respectively. Comparison of the produced oil curves from constant injection pressure for both the model heights showed that the 45 cm model produced 80% of original oil in place (OOIP) as compared to 77% of OOIP from the 25cm model. Comparison of the two figures below also reveals that effect of the pulses was more pronounced for the larger height model (45 cm).

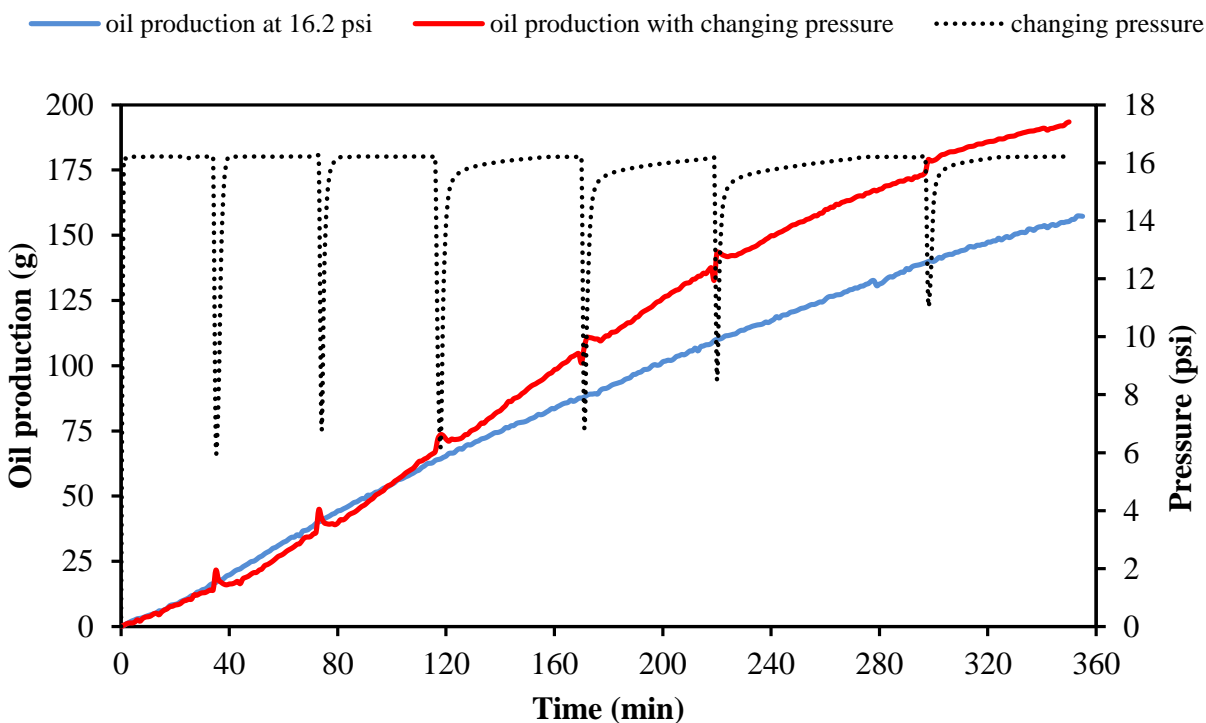


**Figure 5.16** Oil production versus time (204 Darcy, H=25 cm, butane, pulse pressure)

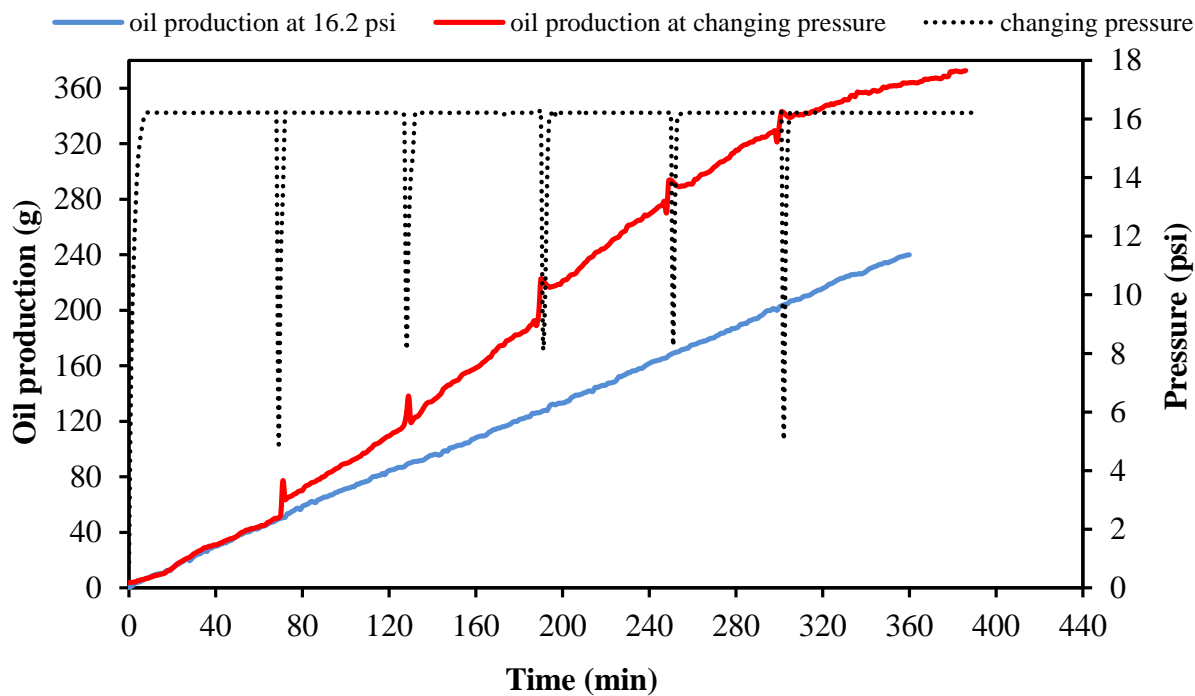


**Figure 5.17** Oil production versus time (204 Darcy, H=45 cm, butane, short pulse)

## **Proof of Concept**

The aforementioned experimental results prove the concept that the variation of solvent injection pressure can enhance oil production in Vapex. The results show that injection pressure parameter is directly related to the physical properties of the reservoir such as permeability, height and viscosity. In our experiments we observed that pressure pulsing enhances the oil recovery and increase with model height and oil viscosity but decrease with permeability. Actual field reservoirs have much higher height, lower permeability, and even orders of magnitude higher viscosities than what are used in the laboratory studies. These facts indicate that incorporating pressure pulsing in the field can significantly enhance oil recovery, and help eliminate economic barriers in the field implementation of Vapex.

A possible explanation of such a beneficial effect of pressure pulsing associated with model physical properties is as follows. The efficiency of Vapex depends upon the solvent mass transfer rate into the in-situ oil. The solvent dissolves into the oil, reduces its viscosity, and the reduced viscosity oil drains out of the model or reservoir by gravity. The reduction in oil viscosity depends upon the amount of dissolved gas present in it, and the rate of viscosity reduction depends upon the rate at which solvent gas dissolves into it. Hence the performance of Vapex can be improved by increasing the solvent mass transfer rate.

When a pressure pulse is introduced by reducing the system (solvent) pressure, the solvent concentration gradient begins to reverse starting from the solvent-oil interface where there is almost zero gas concentration in the bulk gas phase due to vacuum. This reversal then progresses inward to the core of the physical model as the dissolved solvent in the oil phase tends to move to the interface and out into the bulk gas phase. This phenomenon can also create more channels in the physical model, thereby providing larger areas for solvent mass transfer, enhancing solvent-oil mixing, and thus helping to further reduce the oil viscosity. As a consequence, when the solvent is re-injected by increasing the solvent pressure, the solvent penetration is easier and at a faster rate. The overall effect is better oil production relative to solvent injection at constant pressure. Finally, a larger height of the model provides more mass transfer area compared to smaller ones. With pressure variations, a large mass transfer areas results in a further increment in oil recovery.

## 5.4 Steps to Formalize the Concept

To formalize the concept that the variation of solvent injection pressure enhances oil production in Vapex, we needed to accomplish the following steps:

1. theoretically determine optimal policies for solvent injection pressure versus time, which maximize oil recovery in Vapex
2. experimentally validate the optimal policies

The first step requires the knowledge of concentration-dependent dispersion coefficient to be used in the mathematical mass transfer model of the Vapex experiments.

### 5.4.1 Determination of Concentration-Dependent Dispersion Coefficient

The mathematical model of Vapex describes the process of solvent absorption, and subsequent live oil drainage in the experiments. The gas dispersion coefficient is an important property used in the mathematical model utilized in the optimal control of Vapex.

In this study, the concentration-dependent dispersion coefficient of solvent gas was determined following the computational technique of Abukhalifeh et al. (2012), which minimizes the error between the predicted and experimental oil production. Figure 5.18 shows the dispersion coefficient of propane as a function of its concentration in the heavy oil in a Vapex experiment. Also shown is the initial guess used to initialize the technique. The figure shows that the optimally determined optimal  $D(\omega)$  rises to a maximum value, and then drops toward the end. This concentration dependent solvent dispersion dictates the mass transfer mechanism in Vapex process.

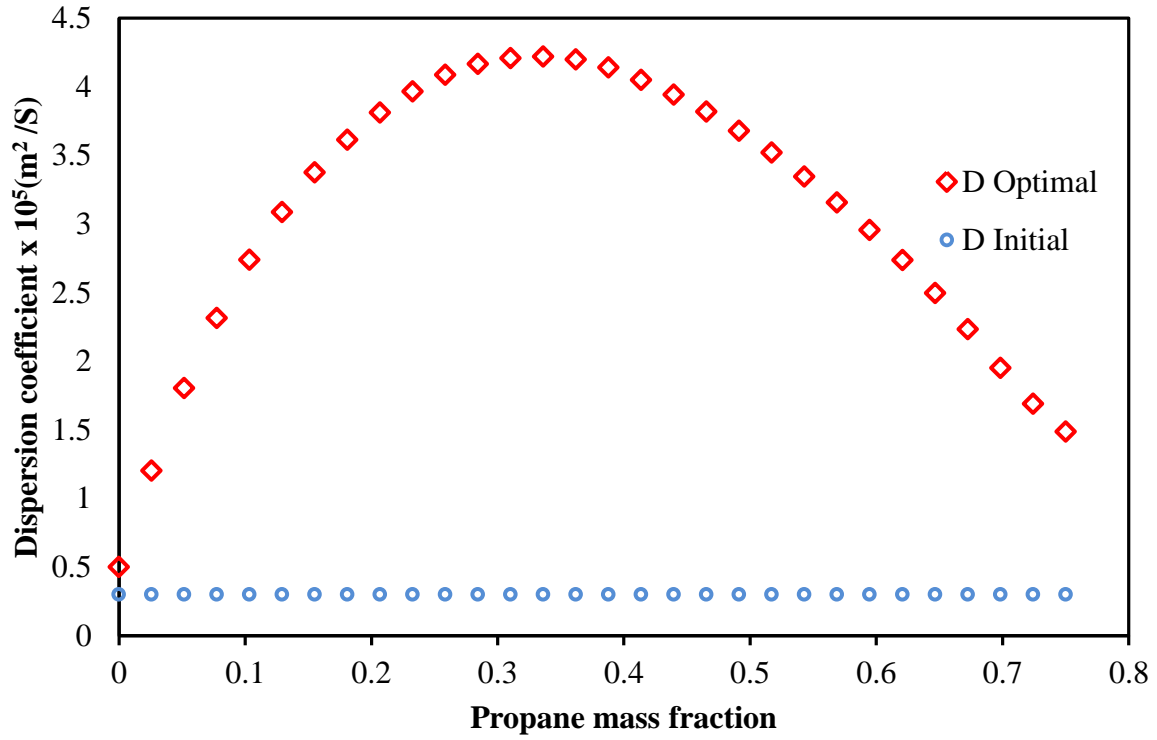


**Figure 5.18** Dispersion coefficient function of propane in heavy oil

The application of the algorithm resulted in an iterative reduction of the error accompanied by a corresponding improvement in  $D(\omega)$ . The error decreases to the minimum as shown in Figure 5.19 for 204 permeability, and 25 cm physical model height. The final optimal function  $D(\omega)$  was obtained after which no further improvement was observed.

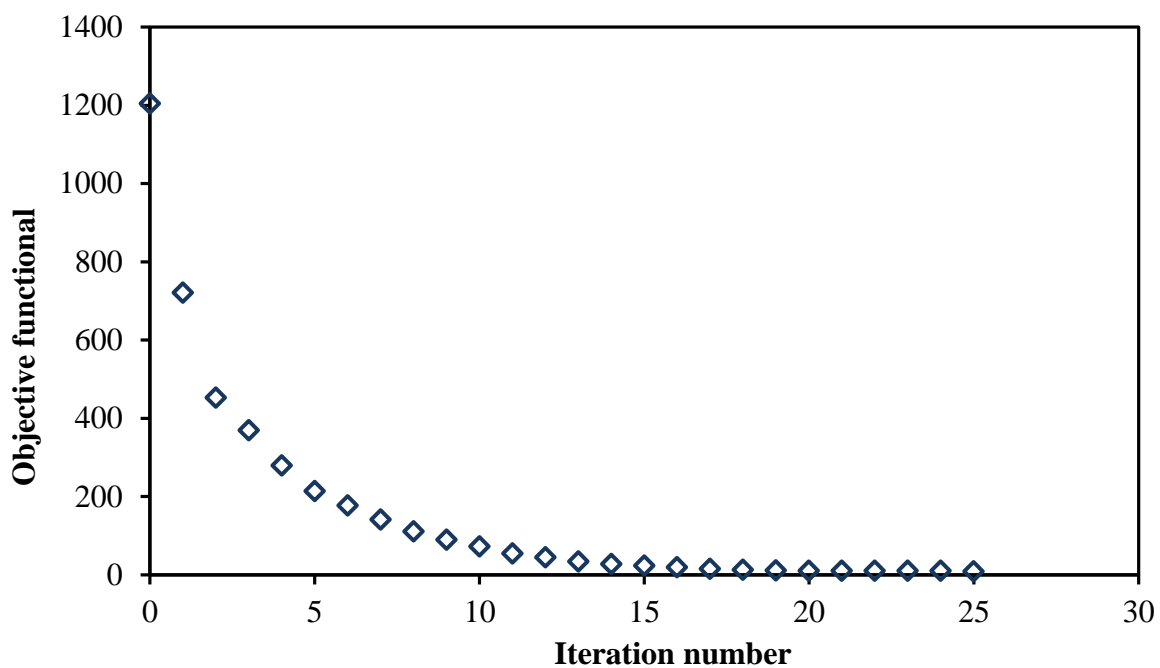


**Figure 5.19** Error versus iteration number (for 25 cm physical model height model, propane, 204 Darcy)

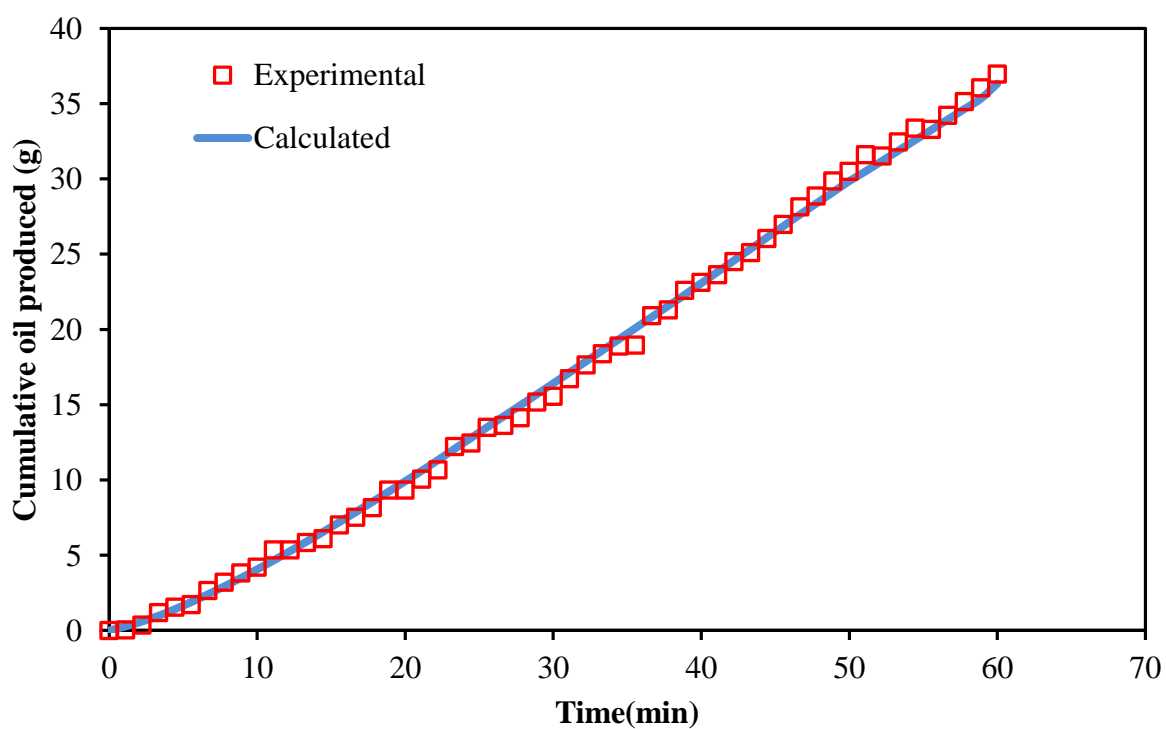


**Figure 5.20** Experimental and calculated mass of live oil produced with time (204 D, 25 cm, propane)



Figure 5.20 above compares the experimental live oil production to the calculated one with the optimally determined propane dispersion. The calculated production follows experimental production very closely during the operation time of about 60 minutes.

Appendix I, provides the optimally determined dispersion coefficient of solvent (propane and butane) as function of its concentration in the heavy oil for different physical models. These functions were used to compute the optimal control policies for solvent injection pressure versus time in Vapex.

## 5.5 Optimal Control Policies for Solvent Injection

These policies were obtained from the optimal control algorithm developed in the last chapter. It must be noted that the optimal control algorithm uses the interfacial solvent concentration versus time,  $\omega_{\text{int}}(t)$ , as a control function, and provides its optimal form. It is then converted to optimal solvent injection pressure versus time policy,  $p(t)$ , using the experimental correlation obtained in Section 5.2.4.

For a given set of operating conditions, the optimal solvent injection pressure policy is associated with maximum oil production *calculated* for the Vapex experiment. This policy is expected to yield enhanced *experimental* oil production in agreement with the *calculated* counterpart. This agreement is cross-checked in the experimental validation in the second step as laid out earlier in Section 5.5.

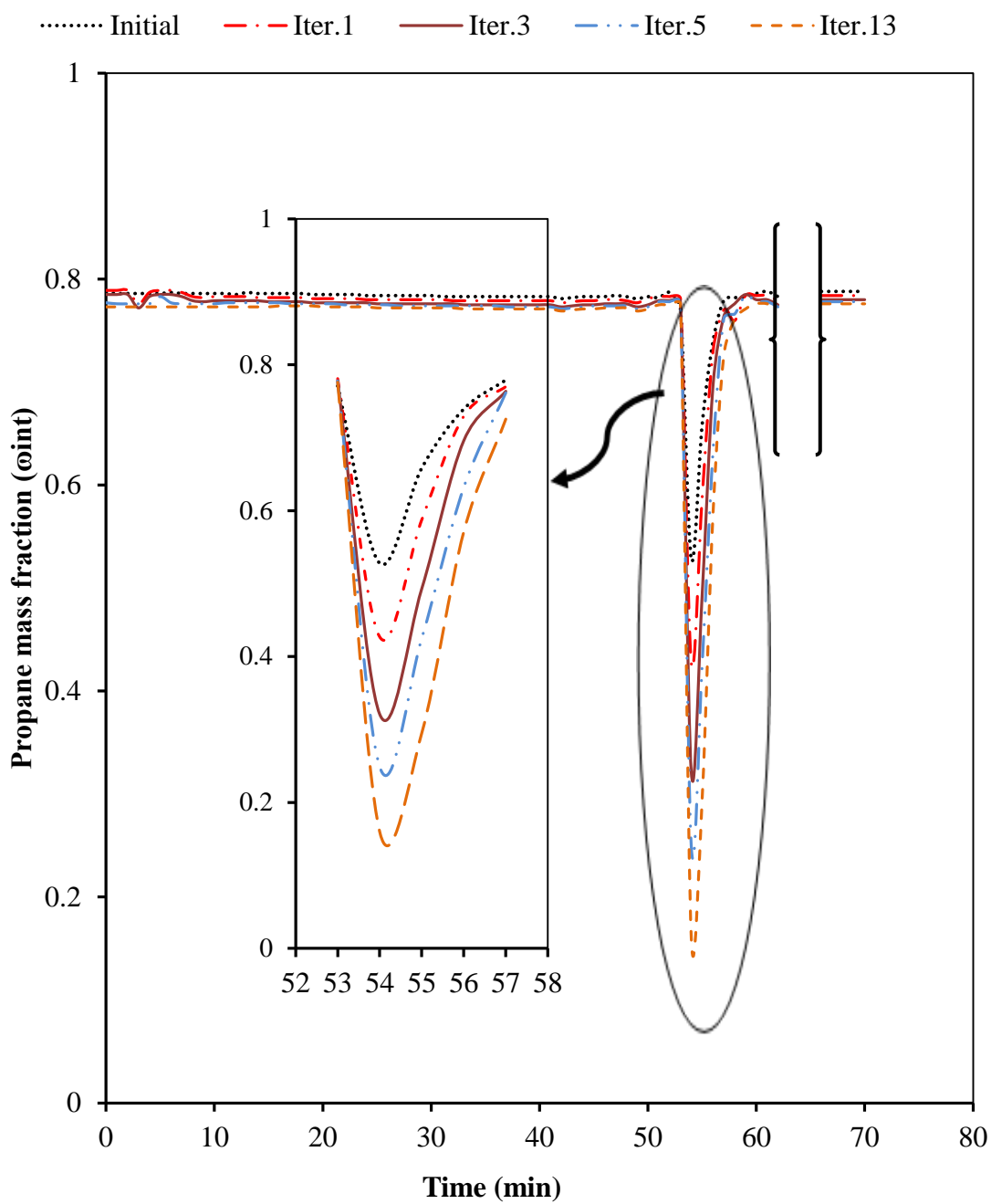
### 5.5.1 Optimal Control Policy for Solvent Concentration

Figure 5.21 shows the propane concentration versus time policy for different iterations of the optimal control algorithm. It resulted in an iterative increasing of the objective functional accompanied by a corresponding improvement in  $\omega_{\text{int}}(t)$ . The objective functional increased monotonically to the maximum as shown in Figure 5.22. The change was significant at the beginning, but the rate of improvement slowed down at final iterations. The maximum objective functional is that point when the gradient correction given by Equation (4.46) tends to zero. No further improvement is possible then. The final optimal function  $\omega_{\text{int}}(t)$  was obtained in 13

iterations after which no further improvement was observed. Table 5.4 lists the parameters used in the simulation of the mathematical model for physical model of 204 Darcy permeability and 25 cm physical model height.

**Table 5.4** Simulation model parameters (204 Darcy and 25 cm)

Codes	Parameters	Value
$N_r$	number of nodes in r direction	20
$N_z$	number of nodes in Z direction	10
$h_i$	initial step size	$10^{-10}$
$h_{\max}$	maximum step size	10
$eps$	accuracy of integration	$10^{-6}$
$K_r$	relative permeability	1
$K$	Permeability	$2.013 \times 10^{-6}$ (cm <sup>2</sup> )
$\rho$	live oil density	0.81 (g/cm <sup>3</sup> )
$g$	Gravity	3531600 (cm/min <sup>2</sup> )
$\varphi$	Porosity	0.38
$\mu_0$	live oil viscosity	0.695 (g/cm.min)
$R$	radius of physical model	3 (cm)
$Z$	height of physical model	25 (cm)



**Figure 5.21** The interfacial solvent concentration  $\omega_{\text{int}}(t)$  at different iterations of the optimal control algorithm

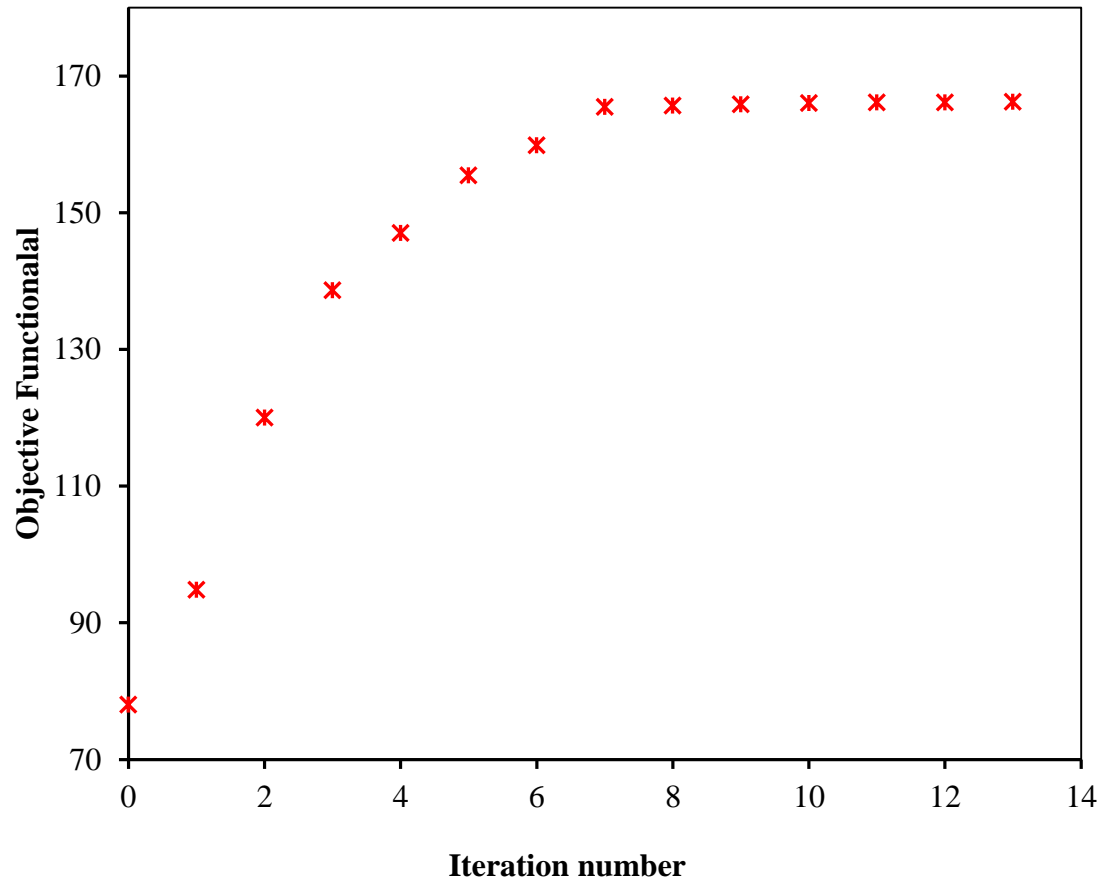


**Figure 5.22** Objective functional versus iteration number (204 Darcy and 25 cm).

### 5.5.2 Optimal Solvent Injection Pressure

Figure 5.23 presents the optimal interfacial propane concentration versus time obtained from the optimal control algorithm. According to this policy, to increase the oil production rate from Vapex, the propane concentration at the interface should be altered after certain time intervals. This policy, i.e.  $\omega_{\text{int}}(t)$ , is implemented through the corresponding propane injection pressure policy,  $P(t)$ , in Vapex experiments. The latter is derived using the experimental correlation between  $P(t)$  and  $\omega_{\text{int}}(t)$  as determined in Section 5.2.4. For example, Figure 5.24 shows the  $P(t)$  corresponding to  $\omega_{\text{int}}(t)$  in Figure 5.23.

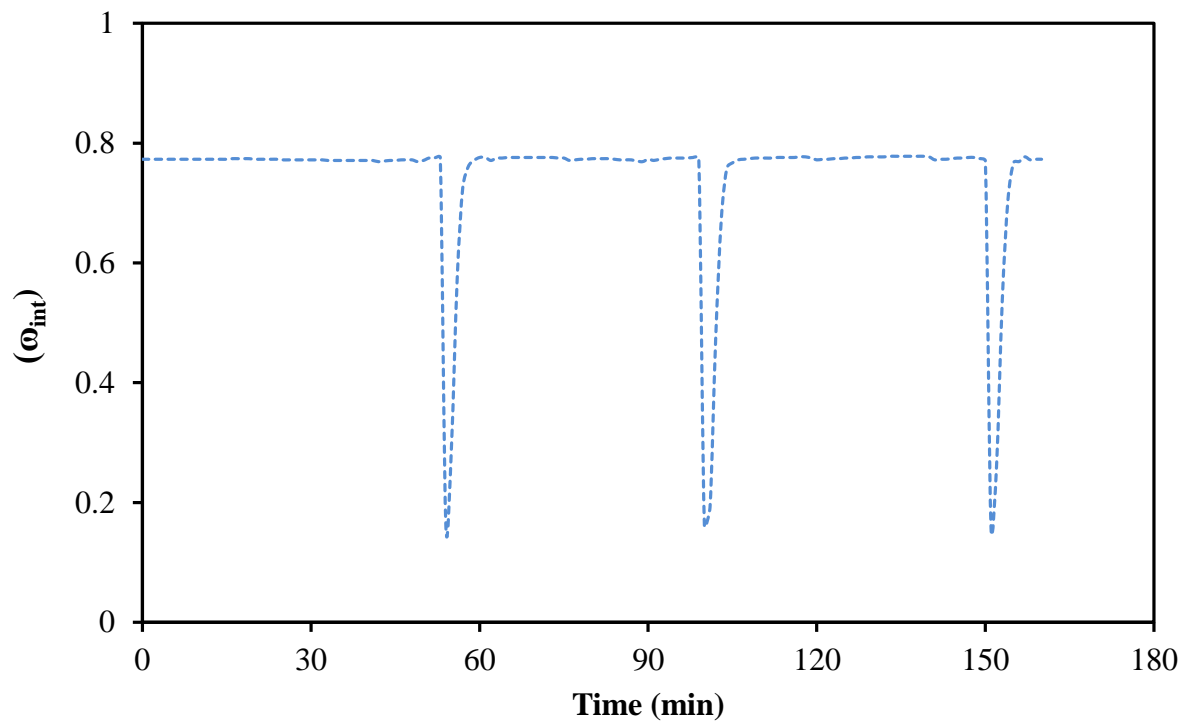


**Figure 5.23** Optimal interfacial propane concentration versus time (25 cm model height, 204 Darcy permeability)

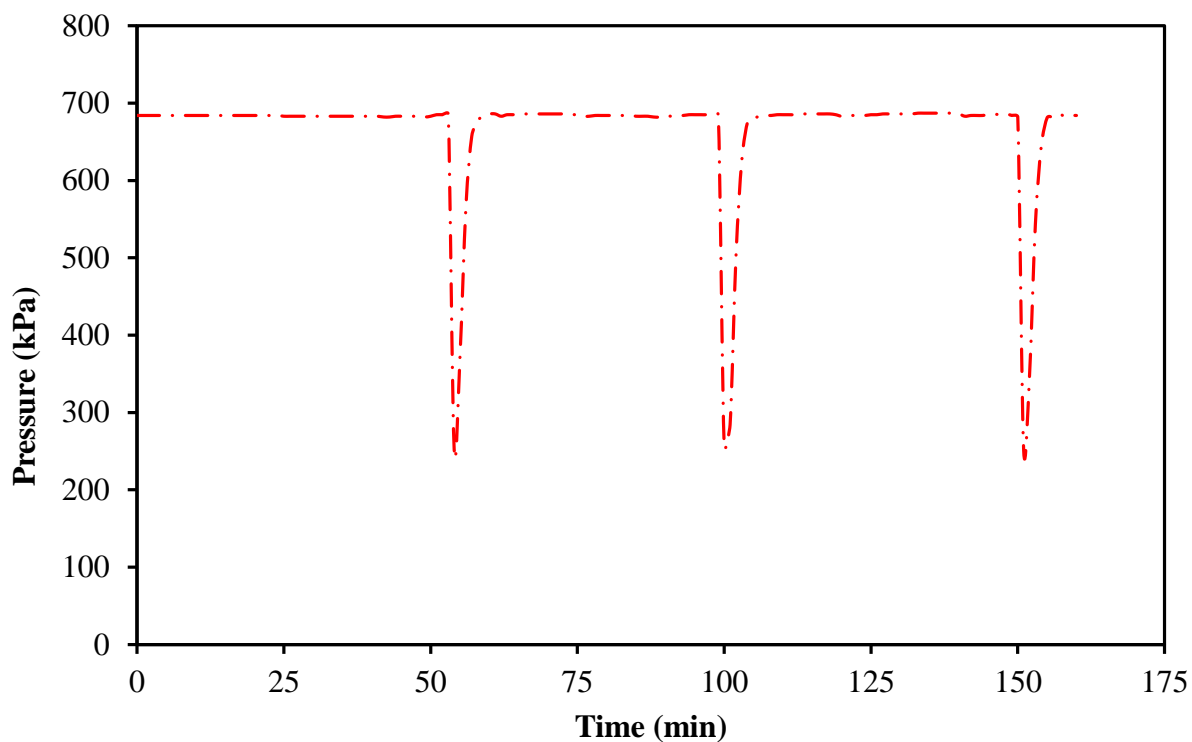


**Figure 5.24** Solvent injection pressure corresponding to the optimal  $\omega_{\text{int}}(t)$  in Figure 5.23

## 5.6 Validation of Optimal Control Policy

To validate that the optimal injection pressure policy enhances the oil production as expected, Vapex experiments were performed in which the optimal solvent injection pressure policy was implemented using Lab View version 7.1 software with a control valve.

The following were compared:

1. the *experimental* mass of oil produced in experiments using the optimal pressure policy  $P(t)$  obtained from the optimal control algorithm [after converting the optimal  $\omega_{\text{int}}(t)$  to optimal  $P(t)$ ]
2. the *predicted* mass of oil corresponding to the optimal pressure policy  $P(t)$  [i.e. the optimal  $\omega_{\text{int}}(t)$ ] based on the optimal control algorithm

### 5.6.1 Accuracy of Optimal Control

The aforementioned comparison of the experimental and predicted oil production showed the accuracy of Optimal Control of Vapex developed in this work. In the first validation experiment, the results showed that the predicted mass of oil produced was 166 grams, and the produced oil from the experimental work was 173. Thus, the percentage error in the mass of oil produced was less than 5%.

Figure 5.25 compares the cumulative produced oil curve obtained from experiments performed with optimal injection pressure policy to the one obtained with constant injection pressure. It is observed from the figure that optimal solvent injection pressure policy enhanced oil production by 24%.

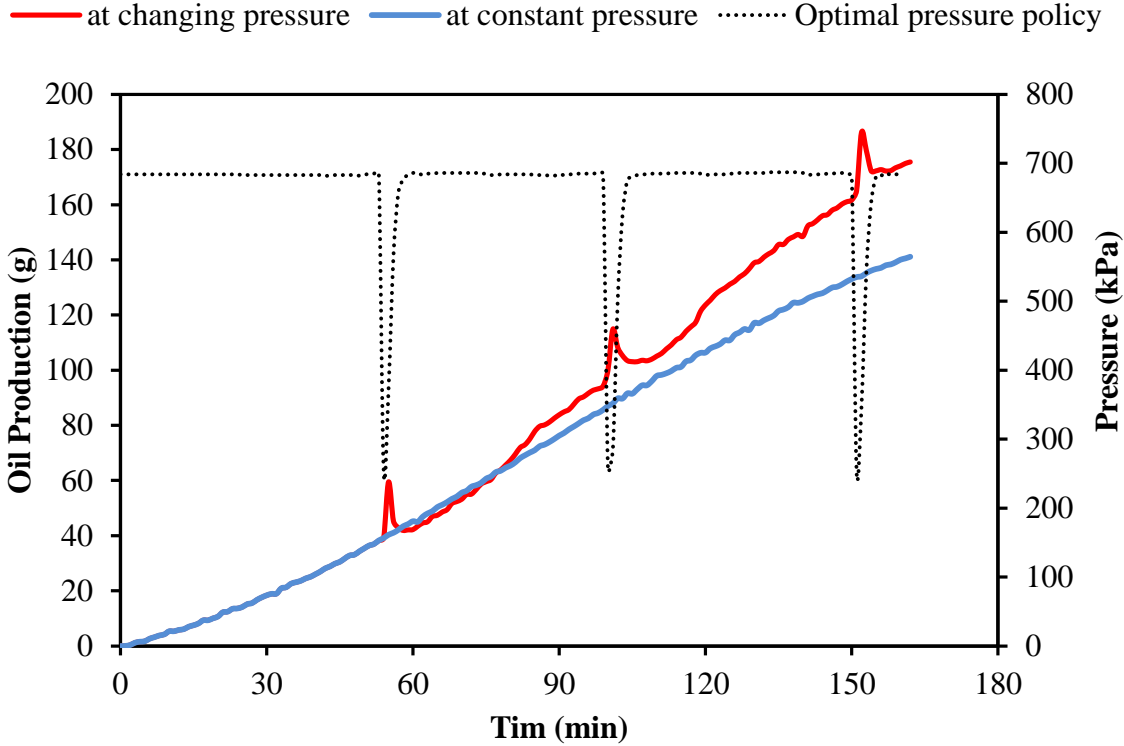


**Figure 5.25** Load cell reading of oil production versus time (propane, 25 cm model height, 204 Darcy)

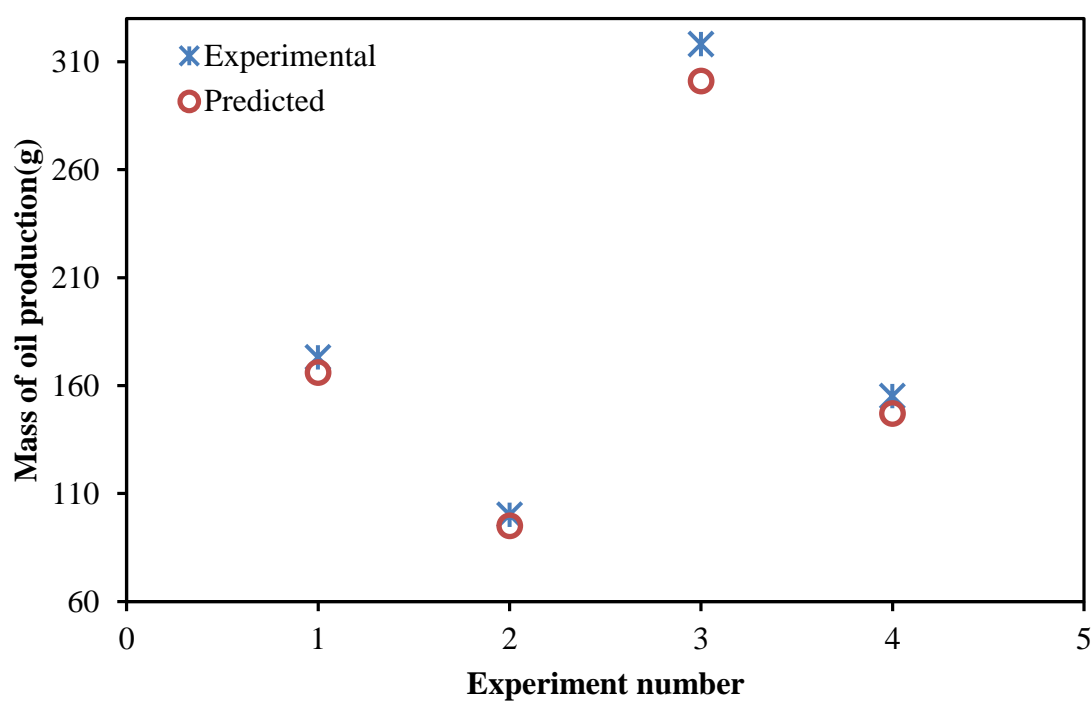
We did a total of four validation experiments. Table 5.5 provides the details. The experimental and the predicted masses of produced oil are compared in Figure 5.26. The percentage error in the mass of oil produced was found to be 5.6% or less. The low errors demonstrate that the Optimal Control of Vapex developed in this study can be confidently applied to enhance oil recovery, which we quantify next.

## 5.6.2 Enhanced Oil Recovery

The validation experiments also enable the comparison of the oil production with optimal solvent injection pressure policies to that with constant pressure. Figure 5.27 makes the comparison for one such case. It is found that the optimal pressure policy enhances the extraction process significantly; resulting in an increase in oil production by 20-35%.

**Table 5.5** Validation experiments for different physical models and solvent gas

Exp. No.	Solvent	Height (cm)	Permeability (Darcy)	experimental oil production (g)	Predicted oil production (g)	% error
1	propane	25	204	173	166	4.2
2	propane	25	51	100	95	5.2
3	propane	45	204	318	301	5.6
4	butane	45	204	155	146	5.4

**Figure 5.26** Experimental and the predicted masses of produced oil



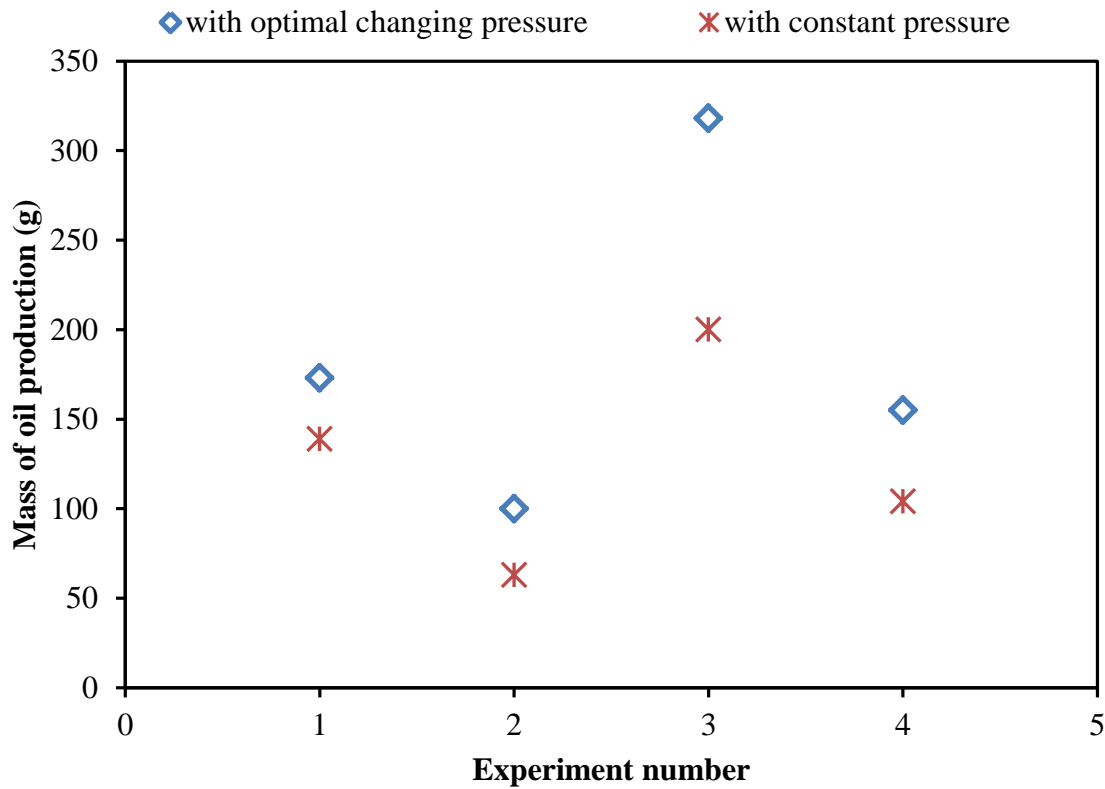


**Figure 5.27** Experimental mass of produced oil for different physical models

### 5.6.3 Summary

The validation results demonstrate that solvent injection pressure can be optimally varied to enhance oil production in Vapex. This enhancement may be attributed to the non-linearity of the complex solvent-to-heavy-oil penetration mechanism in conjunction with the concentration-dependent dispersion of the solvent. The whole process is captured by the mathematical model used in this work. The model utilizes concentration-dependent, solvent dispersion coefficient, which embodies the effect of several molecular-level phenomena not explicit as such in the model equations. The close proximity of the experimental and predicted oil production values underlines the reliability of the Optimal Control of Vapex developed in this work.

# 6

## Conclusions and Recommendations

### 6.1 Conclusions

In this study, two different experimental setups (Vapex setup, and interfacial solvent concentration setup) were designed, built and operated. The Vapex setup was employed

1. to produce oil from physical oil reservoir models of a cylindrical cross-section and different heights, and
2. to determine live oil viscosity, density, solvent mass fraction in the produced oil, and the concentration-dependent solvent dispersion coefficient in the heavy oil.

The second experimental setup was used to correlate the injection pressure of a solvent with its concentration at the solvent-heavy oil interface. Propane and butane were used as pure solvents in Vapex at room temperature.

The initial Vapex experiments provided the proof of the concept that oil production in Vapex can be enhanced by varying solvent injection pressure with time. This concept was formalized as follows:

The problem of Optimal Control of Vapex was formulated using solvent injection pressure versus time as a control function or pressure policy. The necessary conditions were derived to find the optimal policy that maximizes heavy oil production in Vapex. An optimal control algorithm was developed and programmed to yield the optimal pressure policies. These policies were experimentally validated, and enhanced oil production from Vapex was successfully realized. Following are the salient conclusions of this work:

1. The proof-of-concept experiments showed enhanced oil production from Vapex by varying solvent injection pressure with time. The enhancement was in the range 20 to 25% with pressure variation using short pulses (each of about 3 minute pressure drop) close to the dew point. Short pulses were found to be superior to long pulses of about 8 minute duration.
2. The Optimal Control of Vapex was successfully validated with high accuracy in four different experiments. The oil production with the optimal solvent injection pressure policy was found to be within 5.6% of that predicted by the optimal control algorithm.
3. Oil production with optimal solvent injection pressure policy was found to be 20 to 35% more than that with constant solvent injection pressure.

## 6.2 Recommendations

The optimal control of Vapex developed in this work may be used

1. to investigate its field applications, beginning with the study of large physical models with and without fractures.
2. to examine the effect of variation in the injection pressure of solvent mixtures on heavy oil recovery.
3. to use steam pressure versus time as a control function to enhance oil production in SAGD.



# Appendix A

Sample of porous medium permeability calculation

The permeability ( $K$ ) was calculated by applying the following equation (Dullien, 1992):

$$K = \frac{P_2 \times u_2 \times \mu_{air} \times L}{P_m \times \Delta P} \quad (3.2)$$

where  $P_1$  and  $P_2$  are the pressures at the inlet and outlet of the cylinder,  $u_2$  is the velocity at the outlet,  $P_m$  is the mean pressure,  $\Delta P$  is the pressure difference,  $\mu_{air}$  is the air viscosity at room temperature, and substituting for the parameters from Table A.

Table A Data for calculations

Parameter	Value
$P_1$ (atm)	1.153
$P_2$ (atm)	1.127
$Q_2$ (cm <sup>3</sup> /s)	61.96
$L$ (cm)	26
$D$ (cm)	4
$u_2$ (cm/s)	4.93
$\Delta P$ (atm)	0.026
$P_m$ (atm)	1.14
$\mu_{air}$ (cP)	0.0184
$K$ (Darcy)	222.438

## Sample of Calculations

$$K = \frac{P_2 \times u_2 \times \mu_{air} \times L}{P_m \times \Delta P}$$

$$K = \frac{1.127 \times 4.93 \times 0.0184 \times 26}{1.14 \times 0.0106} = 220.0 \text{ Darcy}$$



# Appendix B

## Sample of Live Oil Viscosity Calculations

The live oil viscosity was calculated by rearranging Equation (3.4), and substituting for all of the parameters from Table (B.1) to Equation (B.1).

$$\mu(\text{cp}) = \frac{\pi d^4 \Delta p 68948 \times 100}{128 Q L} \left[ \frac{\text{cm}^4 \text{ psi}}{\text{cm}^3 / \text{sec cm}} \right] \left[ \frac{\text{dyne/cm}^2}{\text{psi}} \right] \left[ \frac{\text{cp}}{\text{dyne/cm}^2 \text{s}} \right] \quad (\text{B.1})$$

Table B.1 Data for live oil viscosity calculations

<b>Volumetric Flow Rate (cm<sup>3</sup>/s)</b>	<b>Pressure Drop Across Capillary Tube (<math>\Delta p</math>)</b>	<b>Live Oil Viscosity (dyne.s/cm<sup>2</sup>)</b>	<b>Live Oil Viscosity (mPa.s)</b>
0.35	4.5	0.04634	4.634
0.125	3.3	0.0951	9.51
0.139	3.95	0.1078	10.78
0.134	4.8	0.1291	12.91





# Appendix C

Sample of solvent gas solubility and live oil density calculations.

To calculate the butane solubility and live oil density, substitute in equation (3.5) and (3.6) for all the parameters from Table (C.1).

**Table C. 1:** Data for Butane Solubility and Live Oil Density Calculations

$$C_4H_{10} \text{ Dissolved weight fraction} = \frac{6.68 \text{ g}}{7.46 \text{ g} + 6.68 \text{ g}} \quad (C.1)$$

$$\text{Live Oil Density} = \frac{6.68 \text{ g} + 7.46 \text{ g}}{16.74 \text{ cm}^3} \quad (C.2)$$

Dead Oil Mass (g)	Librated Butane Mass (g)	Live Oil Volume (cm3)	Live Oil Density (g/cm3)	Dissolved Butane Fraction
7.4	4.2	14.33	0.809490579	0.362
9.3	5.53	18.2	0.814835165	0.372
7.6	6.8	17.4	0.827586207	0.472
6.7	5.9	15.1	0.834437086	0.468
9.34	5.37	18.055	0.815	0.365



# Appendix D

## Derivations of Necessary Conditions

We need to find the terms of  $\left(\frac{\partial f_1}{\partial \omega_z}\right)$ ,  $\left(\frac{\partial f_2}{\partial \omega}\right)$ ,  $\left(\frac{\partial f_1}{\partial \omega_r}\right)$  and  $\left(\frac{\partial f_1}{\partial \omega_{rr}}\right)$  in Equation (4.45) which is

$$\begin{aligned} \frac{\partial J}{\partial \omega_{\text{int}}} = J\omega_{\text{int}} = & \int_0^T \int_0^R \left\{ \lambda_1 \frac{\partial f_1}{\partial \omega_z} \Big|_{(t,r,Z)} + \lambda_1 \frac{\partial f_1}{\partial \omega_z} \Big|_{(t,r,0)} - \lambda_2 \frac{\partial f_2}{\partial \omega} \Big|_{(t,r,0)} \right\} dr dt + \\ & \int_0^T \int_0^Z \left[ -\lambda_1 \frac{\partial f_1}{\partial \omega_r} + \frac{\partial}{\partial r} \left( \lambda_1 \frac{\partial f_1}{\partial \omega_{rr}} \right) \right]_{(t,R,z)} dz dt = 0 \end{aligned} \quad (4.45)$$

We have Equation (4.12) which is

$$f_1 = \left( \frac{\partial D}{\partial \omega} \right) \left( \frac{\partial \omega}{\partial r} \right)^2 + \frac{D}{r} \left( \frac{\partial \omega}{\partial r} \right) + D \left( \frac{\partial^2 \omega}{\partial r^2} \right) - 3\alpha \frac{\omega^2}{\phi} \left( \frac{\partial \omega}{\partial z} \right) \quad (4.12)$$

To find the derivative of the first and second terms of Equation (4.45)  $\left(\frac{\partial f_1}{\partial \omega_z}\right)$

From Equation (4.12) and (4.45) we obtain

$$\frac{\partial f_1}{\partial \omega_z} = \frac{\partial}{\partial \omega_z} [f_1] = -3\alpha \frac{\omega^2}{\phi}$$

(D.1)

To find the derivative of the third term of Equation (4.45)  $\left(\frac{\partial f_2}{\partial \omega}\right)$

We have Equations (4.14) which is

$$f_2 = -v(t, r, 0) = -\alpha[\omega(t, r, 0)]^2 \quad (4.14)$$

We get

$$\frac{\partial f_2}{\partial \omega} = -2\alpha\omega \quad (D.2)$$

To find the derivative of the fourth term of Equation (4.45)  $\left(\frac{\partial f_1}{\partial \omega_r}\right)$

From Equation (4.12), we obtain

$$\frac{\partial f_1}{\partial \omega_r} = \frac{\partial}{\partial \omega_r} [f_1] = 2 \frac{\partial D}{\partial \omega} \left( \frac{\partial \omega}{\partial r} \right) + \frac{D}{r} \quad (D.3)$$

To find the derivative of the last term of Equation (4.45)  $\left(\frac{\partial f_1}{\partial \omega_{rr}}\right)$

From Equation (4.12), we obtain

$$\frac{\partial f_1}{\partial \omega_{rr}} = \frac{\partial}{\partial \omega_{rr}} [f_1] = D \quad (D.4)$$

From Equations (D.1) and (D.2) the first integral of Equation (4.45) becomes

$$\int_0^T \int_0^R \left\{ \lambda_1 \frac{\partial f_1}{\partial \omega_z} \Big|_{(t,r,Z)} + \lambda_1 \frac{\partial f_1}{\partial \omega_z} \Big|_{(t,r,0)} - \lambda_2 \frac{\partial f_2}{\partial \omega} \Big|_{(t,r,0)} \right\} dr dt = \int_0^T \int_0^R \left\{ -3\lambda_1 \frac{\alpha \omega^2}{\phi} \Big|_{z=Z} - \left[ 3\lambda_1 \frac{\alpha \omega^2}{\phi} - 2\lambda_2 \alpha \omega \right]_{z=0} \right\} dr dt \quad (D.5)$$

From Equations (D.3) and (D.4) the second integral in Equation (4.45) becomes

$$\int_0^T \int_0^Z \left[ -\lambda_1 \frac{\partial f_1}{\partial \omega_r} + \frac{\partial}{\partial r} \left( \lambda_1 \frac{\partial f_1}{\partial \omega_{rr}} \right) \right]_{(t,R,z)} dz dt = \int_0^T \int_0^Z \left[ -2\lambda_1 \frac{\partial D}{\partial \omega} \cdot \frac{\partial \omega}{\partial r} - \lambda_1 \frac{D}{r} + \frac{\partial}{\partial r} (\lambda_1 D) \right]_{(t,R,z)} dz dt \quad (D.6)$$

or

$$= \int_0^T \int_0^Z \left[ -2\lambda_1 \frac{\partial D}{\partial \omega} \cdot \frac{\partial \omega}{\partial r} - \lambda_1 \frac{D}{r} + \frac{\partial \lambda_1}{\partial r} D + \lambda_1 \frac{\partial D}{\partial \omega} \cdot \frac{\partial \omega}{\partial r} \right]_{(t,R,z)} dz dt \quad (D.7)$$

or

$$\int_0^T \int_0^Z \left[ -\lambda_1 \frac{\partial f_1}{\partial \omega_r} + \frac{\partial}{\partial r} \left( \lambda_1 \frac{\partial f_1}{\partial \omega_{rr}} \right) \right] dz dt = \int_0^T \int_0^Z \left[ -\lambda_1 \frac{\partial D}{\partial \omega} \cdot \frac{\partial \omega}{\partial r} - \lambda_1 \frac{D}{r} + \frac{\partial \lambda_1}{\partial r} D \right]_{(t,R,z)} dz dt \quad (D.8)$$

By combining equations (D.5) and (D.8), Equation (4.45) becomes

$$\begin{aligned} \frac{\partial J}{\partial \omega_{\text{int}}} = & \int_0^T \int_0^R \left\{ -3\lambda_1 \frac{\alpha \omega^2}{\phi} \Big|_{z=Z} - \left[ 3\lambda_1 \frac{\alpha \omega^2}{\phi} - 2\lambda_2 \alpha \omega \right]_{z=0} \right\} dr dt + \\ & \int_0^T \int_0^Z \left[ -\lambda_1 \frac{\partial D}{\partial \omega} \cdot \frac{\partial \omega}{\partial r} - \lambda_1 \frac{D}{r} + \frac{\partial \lambda_1}{\partial r} D \right]_{(t,R,z)} dz dt \end{aligned} \quad (D.9)$$

Rearranging Equation (D.9), we obtain

$$\begin{aligned} \frac{\partial J}{\partial \omega_{\text{int}}} = & \int_0^T \left[ \int_0^R \left( -3\lambda_1 \frac{\alpha \omega^2}{\phi} \Big|_{z=Z} - \left[ 3\lambda_1 \frac{\alpha \omega^2}{\phi} - 2\lambda_2 \alpha \omega \right]_{z=0} \right) dr + \right. \\ & \left. \int_0^Z \left( -\lambda_1 \frac{\partial D}{\partial \omega} \cdot \frac{\partial \omega}{\partial r} - \lambda_1 \frac{D}{r} + \frac{\partial \lambda_1}{\partial r} D \right)_{(t,R,z)} dz \right] dt \end{aligned} \quad (D.10)$$

$$\frac{\partial J}{\partial \omega_{\text{int}}} = \int_0^T \left[ \int_0^R T_1 dr + \int_0^Z T_2 dz \right] dt \quad (\text{D.11})$$

where

$$T_1 = -3\lambda_1 \frac{\alpha \omega^2}{\phi} \Big|_{z=Z} - \left[ 3\lambda_1 \frac{\alpha \omega^2}{\phi} - 2\lambda_2 \alpha \omega \right]_{z=0} \quad (\text{D.12})$$

$$T_2 = -\lambda_1 \frac{\partial D}{\partial \omega} \frac{\partial \omega}{\partial r} - \lambda_1 \frac{D}{r} + \frac{\partial \lambda_1}{\partial r} D \quad (\text{D.13})$$

# Appendix E

## E.1 Finding Adjoint Equations

From Equations (4.12) and (4.45) we need to find  $\left(\frac{\partial f_1}{\partial \omega}\right), \left(\frac{\partial f_1}{\partial \omega_z}\right), \left(\frac{\partial f_1}{\partial \omega_r}\right)$  and  $\left(\frac{\partial f_1}{\partial \omega_{rr}}\right)$

$$f_1 = \left(\frac{\partial D}{\partial \omega}\right) \left(\frac{\partial \omega}{\partial r}\right)^2 + \frac{D}{r} \left(\frac{\partial \omega}{\partial r}\right) + D \left(\frac{\partial^2 \omega}{\partial r^2}\right) - 3\alpha \frac{\omega^2}{\phi} \left(\frac{\partial \omega}{\partial z}\right) \quad (4.12)$$

$$\frac{\partial \lambda_1}{\partial t} = -\lambda_1 \left(\frac{\partial f_1}{\partial \omega}\right) + \frac{\partial}{\partial z} \left(\lambda_1 \frac{\partial f_1}{\partial \omega_z}\right) + \frac{\partial}{\partial r} \left(\lambda_1 \frac{\partial f_1}{\partial \omega_r}\right) - \frac{\partial^2}{\partial r^2} \left(\lambda_1 \frac{\partial f_1}{\partial \omega_{rr}}\right) \quad (4.45)$$

To find the derivatives of the first term of Equation (4.45)

$$\frac{\partial f_1}{\partial \omega} = \frac{\partial}{\partial \omega} \left( \left(\frac{\partial D}{\partial \omega}\right) \left(\frac{\partial \omega}{\partial r}\right)^2 + \frac{D}{r} \left(\frac{\partial \omega}{\partial r}\right) + D \left(\frac{\partial^2 \omega}{\partial r^2}\right) - 3\alpha \frac{\omega^2}{\phi} \left(\frac{\partial \omega}{\partial z}\right) \right) \quad (E.1)$$

First term of Equation (E.1)

$$\frac{\partial}{\partial \omega} \left[ \left(\frac{\partial D}{\partial \omega}\right) \left(\frac{\partial \omega}{\partial r}\right)^2 \right] = \frac{\partial^2 D}{\partial \omega^2} \left(\frac{\partial \omega}{\partial r}\right)^2 \quad (E.2)$$

Second term of Equation (E.1)



$$\frac{\partial}{\partial \omega} \left[ \left( \frac{D}{r} \frac{\partial \omega}{\partial r} \right) \right] = \frac{1}{r} \frac{\partial D}{\partial \omega} \frac{\partial \omega}{\partial r} \quad (\text{E.3})$$

Third term of Equation (E.1)

$$\frac{\partial}{\partial \omega} \left[ D \frac{\partial^2 \omega}{\partial r^2} \right] = \frac{\partial D}{\partial \omega} \frac{\partial^2 \omega}{\partial r^2} \quad (\text{E.4})$$

Fourth term of Equation (E.1)

$$\frac{\partial}{\partial \omega} \left[ -3\alpha \frac{\omega^2}{\phi} \left( \frac{\partial \omega}{\partial z} \right) \right] = -6\alpha \frac{\omega}{\phi} \left( \frac{\partial \omega}{\partial z} \right) \quad (\text{E.5})$$

By combining Equations (E.2-E.5), we obtain the final equation of  $\frac{\partial f_1}{\partial \omega}$ , which is written as

$$\frac{\partial f_1}{\partial \omega} = \frac{\partial}{\partial \omega} [f_1] = \frac{\partial^2 D}{\partial \omega^2} \cdot \left( \frac{\partial \omega}{\partial r} \right)^2 + \frac{1}{r} \frac{\partial D}{\partial \omega} \cdot \frac{\partial \omega}{\partial r} + \frac{\partial D}{\partial \omega} \cdot \frac{\partial^2 \omega}{\partial r^2} - 6\alpha \frac{\omega}{\phi} \left( \frac{\partial \omega}{\partial z} \right) \quad (\text{E.6})$$

$$\frac{\partial f_1}{\partial \omega_z} = \frac{\partial}{\partial \omega_z} [f_1] = -3\alpha \frac{\omega^2}{\phi} \quad (\text{E.7})$$

$$\frac{\partial f_1}{\partial \omega_r} = \frac{\partial}{\partial \omega_r} [f_1] = 2 \frac{\partial D}{\partial \omega} \left( \frac{\partial \omega}{\partial r} \right) + \frac{D}{r} \quad (\text{E.8})$$

$$\frac{\partial f_1}{\partial \omega_{rr}} = \frac{\partial}{\partial \omega_{rr}} [f_1] = D \quad (\text{E.9})$$

Substituted of the Equations (E.6), (E.7), (E.8) and (D.9) into Equation (4.45), we obtain the following equation:

$$\begin{aligned} \frac{\partial \lambda_1}{\partial t} = & -\lambda_1 \frac{\partial^2 D}{\partial \omega^2} \left( \frac{\partial \omega}{\partial r} \right)^2 - \frac{\lambda_1}{r} \frac{\partial D}{\partial \omega} \frac{\partial \omega}{\partial r} - \lambda_1 \frac{\partial D}{\partial \omega} \frac{\partial^2 \omega}{\partial r^2} + \frac{6\alpha \omega}{\phi} \lambda_1 \left( \frac{\partial \omega}{\partial z} \right) - \\ & \frac{3\alpha}{\phi} \frac{\partial}{\partial z} \left( \lambda_1 \omega^2 \right) + \frac{\partial}{\partial r} \left( 2\lambda_1 \frac{\partial D}{\partial \omega} \frac{\partial \omega}{\partial r} + \lambda_1 \frac{D}{r} \right) - \frac{\partial^2}{\partial r^2} \left( \lambda_1 D \right) \end{aligned} \quad (\text{E.10})$$

Fifth term of Equation (E.10)

$$-\frac{3\alpha}{\phi} \frac{\partial}{\partial z} \left( \lambda_1 \omega^2 \right) = -\frac{6\alpha}{\phi} \lambda_1 \omega \left( \frac{\partial \omega}{\partial z} \right) - \frac{3\alpha}{\phi} \omega^2 \frac{\partial \lambda_1}{\partial z} \quad (\text{E.11})$$

Sixth term of Equation (E.10)

$$\begin{aligned} \frac{\partial}{\partial r} \left( 2\lambda_1 \frac{\partial D}{\partial \omega} \cdot \frac{\partial \omega}{\partial r} + \lambda_1 \frac{D}{r} \right) = & 2 \frac{\partial \lambda_1}{\partial r} \frac{\partial D}{\partial \omega} \cdot \frac{\partial \omega}{\partial r} + 2\lambda_1 \frac{\partial D}{\partial \omega} \cdot \frac{\partial^2 \omega}{\partial r^2} + \left( 2\lambda_1 \frac{\partial^2 D}{\partial \omega^2} \cdot \left( \frac{\partial \omega}{\partial r} \right)^2 \right) + \\ & \frac{\partial \lambda_1}{\partial r} \frac{D}{r} + \frac{\lambda_1}{r} \frac{\partial D}{\partial \omega} \frac{\partial \omega}{\partial r} - \lambda_1 \frac{D}{r^2} \end{aligned} \quad (\text{E.12})$$

where

$$\frac{\partial}{\partial r} \left( \frac{\partial D}{\partial \omega} \right) = \frac{\partial}{\partial \omega} \left( \frac{\partial D}{\partial r} \right) = \frac{\partial}{\partial \omega} \left( \frac{\partial D}{\partial \omega} \frac{\partial \omega}{\partial r} \right) = \frac{\partial^2 D}{\partial \omega^2} \frac{\partial \omega}{\partial r} \quad (\text{E.13})$$

Last term of Equation (E.10)

$$\begin{aligned}
-\frac{\partial^2}{\partial r^2}(\lambda_1 D) &= \frac{\partial}{\partial r} \left( \lambda_1 \frac{\partial D}{\partial \omega} \frac{\partial \omega}{\partial r} + \frac{\partial \lambda_1}{\partial r} D \right) = -\frac{\partial \lambda_1}{\partial r} \frac{\partial D}{\partial \omega} \frac{\partial \omega}{\partial r} - \lambda_1 \frac{\partial^2 \omega}{\partial r^2} \frac{\partial D}{\partial \omega} - \\
&\quad \lambda_1 \left( \frac{\partial \omega}{\partial r} \right)^2 \frac{\partial^2 D}{\partial \omega^2} - \frac{\partial^2 \lambda_1}{\partial r^2} D - \frac{\partial \lambda_1}{\partial r} \frac{\partial D}{\partial \omega} \frac{\partial \omega}{\partial r}
\end{aligned} \tag{E.14}$$

where

$$\frac{\partial}{\partial r} \left( \frac{\partial D}{\partial \omega} \right) = \frac{\partial}{\partial \omega} \left( \frac{\partial D}{\partial r} \right) = \frac{\partial}{\partial \omega} \left( \frac{\partial D}{\partial \omega} \frac{\partial \omega}{\partial r} \right) = \frac{\partial^2 D}{\partial \omega^2} \frac{\partial \omega}{\partial r}$$

So Equation (E.14) becomes

$$\boxed{\frac{\partial^2}{\partial r^2}(\lambda_1 D) = \frac{\partial \lambda_1}{\partial r} \frac{\partial D}{\partial \omega} \frac{\partial \omega}{\partial r} + \lambda_1 \frac{\partial^2 \omega}{\partial r^2} \frac{\partial D}{\partial \omega} + \lambda_1 \left( \frac{\partial \omega}{\partial r} \right)^2 \frac{\partial^2 D}{\partial \omega^2} + \frac{\partial^2 \lambda_1}{\partial r^2} D + \frac{\partial \lambda_1}{\partial r} \frac{\partial D}{\partial \omega} \frac{\partial \omega}{\partial r}} \tag{E.15}$$

Substitution of the Equations (E.12) and (E.15) into Equation (E.10), we obtain the following equation:

$$\begin{aligned}
\frac{\partial \lambda_1}{\partial t} &= -\lambda_1 \frac{\partial^2 D}{\partial \omega^2} \left( \frac{\partial \omega}{\partial r} \right)^2 - \frac{\lambda_1}{r} \frac{\partial D}{\partial \omega} \frac{\partial \omega}{\partial r} - \lambda_1 \frac{\partial D}{\partial \omega} \frac{\partial^2 \omega}{\partial r^2} + \frac{6\alpha\omega}{\phi} \lambda_1 \left( \frac{\partial \omega}{\partial z} \right) - \frac{6\alpha}{\phi} \lambda_1 \omega \left( \frac{\partial \omega}{\partial z} \right) - \frac{3\alpha}{\phi} \omega^2 \frac{\partial \lambda_1}{\partial z} + \\
&\quad 2 \frac{\partial \lambda_1}{\partial r} \frac{\partial D}{\partial \omega} \frac{\partial \omega}{\partial r} + 2 \lambda_1 \frac{\partial D}{\partial \omega} \cdot \frac{\partial^2 \omega}{\partial r^2} + 2 \lambda_1 \frac{\partial^2 D}{\partial \omega^2} \left( \frac{\partial \omega}{\partial r} \right)^2 + \frac{\partial \lambda_1}{\partial r} \frac{D}{r} + \frac{\lambda_1}{r} \frac{\partial D}{\partial \omega} \frac{\partial \omega}{\partial r} - \lambda_1 \frac{D}{r^2} - \\
&\quad \frac{\partial \lambda_1}{\partial r} \frac{\partial D}{\partial \omega} \frac{\partial \omega}{\partial r} - \lambda_1 \frac{\partial^2 \omega}{\partial r^2} \frac{\partial D}{\partial \omega} - \lambda_1 \left( \frac{\partial \omega}{\partial r} \right)^2 \frac{\partial^2 D}{\partial \omega^2} - \frac{\partial^2 \lambda_1}{\partial r^2} D - \frac{\partial \lambda_1}{\partial r} \frac{\partial D}{\partial \omega} \frac{\partial \omega}{\partial r}
\end{aligned} \tag{E.16}$$

Rearrange Equation (E.16) we obtain the following equation:

$$\begin{aligned}
\frac{\partial \lambda_1}{\partial t} = & -\lambda_1 \frac{\partial^2 D}{\partial \omega^2} \cdot \left( \frac{\partial \omega}{\partial r} \right)^2 - \lambda_1 \left( \frac{\partial \omega}{\partial r} \right)^2 \frac{\partial^2 D}{\partial \omega^2} + 2\lambda_1 \frac{\partial^2 D}{\partial \omega^2} \cdot \left( \frac{\partial \omega}{\partial r} \right)^2 - \frac{\lambda_1}{r} \frac{\partial D}{\partial \omega} \cdot \frac{\partial \omega}{\partial r} + \frac{\lambda_1}{r} \frac{\partial D}{\partial \omega} \frac{\partial \omega}{\partial r} - \\
& \lambda_1 \frac{\partial D}{\partial \omega} \cdot \frac{\partial^2 \omega}{\partial r^2} - \lambda_1 \frac{\partial^2 \omega}{\partial r^2} \cdot \frac{\partial D}{\partial \omega} + 2\lambda_1 \frac{\partial D}{\partial \omega} \cdot \frac{\partial^2 \omega}{\partial r^2} + \frac{6\alpha\omega}{\phi} \lambda_1 \left( \frac{\partial \omega}{\partial z} \right) - \frac{6\alpha}{\phi} \lambda_1 \omega \left( \frac{\partial \omega}{\partial z} \right) + \\
& 2 \frac{\partial \lambda_1}{\partial r} \frac{\partial D}{\partial \omega} \cdot \frac{\partial \omega}{\partial r} - \frac{\partial \lambda_1}{\partial r} \frac{\partial D}{\partial \omega} \cdot \frac{\partial \omega}{\partial r} - \frac{\partial \lambda_1}{\partial r} \frac{\partial D}{\partial \omega} \cdot \frac{\partial \omega}{\partial r} \\
& - \frac{3\alpha}{\phi} \omega^2 \frac{\partial \lambda_1}{\partial z} + \frac{\partial \lambda_1}{\partial r} \frac{D}{r} - \lambda_1 \frac{D}{r^2} - \frac{\partial^2 \lambda_1}{\partial r^2} D
\end{aligned} \tag{E.17}$$

Rearrange Equation (E.17), the final adjoint equations are

$$\frac{\partial \lambda_1}{\partial t} = -\frac{3\alpha}{\phi} \omega^2 \frac{\partial \lambda_1}{\partial z} + \frac{\partial \lambda_1}{\partial r} \frac{D}{r} - \lambda_1 \frac{D}{r^2} - \frac{\partial^2 \lambda_1}{\partial r^2} D \tag{4.50}$$

And from Equation (4.46), we obtain

$$\frac{\partial \lambda_2}{\partial t} = -\beta r = -2\pi\rho\phi r \tag{4.51}$$



# Appendix F

Finding the Jacobians for the state and co-state equations.

F.1 Following are the set of Jacobian equations employed to integrate the ODEs (Equations [4.56]–[4.68]):

**For intermediate grid points**

**For  $0 < i < (N_i - 1)$  and  $0 < j < (N_j - 1)$**

$$\begin{aligned} \varpi_{i,j} = & \frac{\partial D}{\partial \omega} \frac{1}{r_i} \left[ \frac{\omega_{i+1,j} - \omega_{i-1,j}}{2\Delta r} \right] + \frac{\partial D}{\partial \omega} \left[ \frac{\omega_{i+1,j} - 2\omega_{i,j} + \omega_{i-1,j}}{\Delta r^2} \right] D \left[ \frac{-2}{\Delta r^2} \right] + \\ & \frac{\partial^2 D}{\partial \omega^2} \left[ \frac{\omega_{i+1,j} - \omega_{i-1,j}}{2\Delta r} \right]^2 - \frac{K_r K \rho g \cos \theta}{\mu_o \phi} 3\omega_{i,j} \left[ \frac{\omega_{i,j+1} - \omega_{i,j-1}}{\Delta z_i} \right] \end{aligned} \quad (\text{F.1})$$

$$\varpi_{i+1,j} = D \left[ \frac{1}{2r_i \Delta r} \right] + \frac{D}{\Delta r^2} + \frac{\partial D}{\partial \omega} 2 \left[ \frac{\omega_{i+1,j} - \omega_{i-1,j}}{\Delta r} \right] \frac{1}{2\Delta r} \quad (\text{F.2})$$

$$\varpi_{i-1,j} = -D \left[ \frac{1}{2r_i \Delta r} \right] + \frac{D}{\Delta r^2} - \frac{\partial D}{\partial \omega} 2 \left[ \frac{\omega_{i+1,j} - \omega_{i-1,j}}{\Delta r} \right] \frac{1}{2\Delta r} \quad (\text{F.3})$$

$$\varpi_{i,j+1} = -\frac{K_r K \rho g \cos \theta}{\mu_o \phi} 3\omega_{i,j}^2 \left[ \frac{1}{2\Delta z_i} \right] \quad (\text{F.4})$$

$$\varpi_{i,j+1} = \frac{K_r K \rho g \cos \theta}{\mu_o \phi} 3\omega_{i,j}^2 \left[ \frac{1}{2\Delta z_i} \right] \quad (\text{F.5})$$

$$\varpi_z = \frac{K_r K \rho g \cos \theta}{\mu_o \phi} 3\omega_{i,j}^2 \left[ \frac{\omega_{i,j+1} - \omega_{i,j-1}}{2\Delta z_i^2} \right] \quad (\text{F.6})$$

### For Axis Grid Points

When  $i = 0$  for  $0 < j < (N_j - 1)$

$$\varpi_{o,j} = -\frac{K_r K \rho g \cos \theta}{\mu_o \phi} 3\omega_{0,j} \left[ \frac{\omega_{0,j+1} - \omega_{0,j-1}}{\Delta z_i} \right] \quad (\text{F.7})$$

$$\varpi_{0,j+1} = -\frac{K_r K \rho g \cos \theta}{\mu_o \phi} 3\omega_{0,j}^2 \left[ \frac{1}{2\Delta z_i} \right] \quad (\text{F.8})$$

$$\varpi_{0,j-1} = \frac{K_r K \rho g \cos \theta}{\mu_o \phi} 3\omega_{0,j}^2 \left[ \frac{1}{2\Delta z_i} \right] \quad (\text{F.9})$$

$$\varpi_z = \frac{K_r K \rho g \cos \theta}{\mu_o \phi} 3\omega_{0,j}^2 \left[ \frac{\omega_{0,j+1} - \omega_{0,j-1}}{2\Delta z_i^2} \right] \quad (\text{F.10})$$

When  $i = 0$  and  $j = 0$

$$\varpi_{0,0} = -\frac{K_r K \rho g \cos \theta}{\mu_o \phi} 3\omega_{0,0} \left[ \frac{\omega_{0,1} - \omega_{\text{int}}}{\Delta z_0} \right] \quad (\text{F.11})$$

$$\varpi_{0,1} = -\frac{K_r K \rho g \cos \theta}{\mu_o \phi} 3\omega_{0,0}^2 \left[ \frac{1}{2\Delta z_0} \right] \quad (\text{F.12})$$

$$\varpi_z = \frac{K_r K \rho g \cos \theta}{\mu_o \phi} 3\omega_{0,0}^2 \left[ \frac{\omega_{0,1} - \omega_{\text{int}}}{2\Delta z_0^2} \right] \quad (\text{F.13})$$

**When  $i = 0$  and  $j = (N_j - 1)$**

$$\varpi_{o,Nj-1} = -\frac{K_r K \rho g \cos \theta}{\mu_o \phi} 3\omega_{0,Nj-1} \left[ \frac{\omega_{\text{int}} - \omega_{0,Nj-2}}{\Delta z_0} \right] \quad (\text{F.14})$$

$$\varpi_{0,Nj-2} = \frac{K_r K \rho g \cos \theta}{\mu_o \phi} 3\omega_{0,Nj-1}^2 \left[ \frac{1}{2\Delta z_0} \right] \quad (\text{F.15})$$

$$\varpi_z = \frac{K_r K \rho g \cos \theta}{\mu_o \phi} 3\omega_{0,Nj-1}^2 \left[ \frac{\omega_{\text{int}} - \omega_{0,Nj-2}}{2\Delta z_0^2} \right] \quad (\text{F.16})$$

**For Right Most Grid Points**

**When  $i = (N_i - 1)$  and  $j = 0$**

$$\begin{aligned} \varpi_{N_i-1,0} = & \frac{\partial D}{\partial \omega} \frac{1}{r_{N_i-1}} \left[ \frac{\omega_{\text{int}} - \omega_{N_i-2,0}}{2\Delta r} \right] + \frac{\partial D}{\partial \omega} \left[ \frac{\omega_{\text{int}} - 2\omega_{N_i-2,0} + \omega_{N_i-1,0}}{\Delta r^2} \right] - \\ & D \left[ \frac{2}{\Delta r^2} \right] + \frac{\partial^2 D}{\partial \omega^2} \left[ \frac{\omega_{\text{int}} - \omega_{N_i-2,0}}{2\Delta r} \right]^2 - \\ & \frac{K_r K \rho g \cos \theta}{\mu_o \phi} 3\omega_{N_i-1,0} \left[ \frac{\omega_{N_i-1,1} - \omega_{\text{int}}}{\Delta z_i} \right] \end{aligned} \quad (\text{F.17})$$



$$\varpi_{N_i-2,0} = -D \left[ \frac{1}{2r_{N_i-1}\Delta r} \right] + \frac{D}{\Delta r^2} - \frac{\partial D}{\partial \omega} 2 \left[ \frac{\omega_{\text{int}} - \omega_{N_i-2,0}}{2\Delta r} \right] \frac{1}{2\Delta r} \quad (\text{F.18})$$

$$\varpi_{N_i-1,1} = -\frac{K_r K \rho g \cos \theta}{\mu_o \phi} 3\omega_{N_i-1,0}^2 \left[ \frac{1}{2\Delta z_{N_i-1}} \right] \quad (\text{F.19})$$

$$\varpi_z = \frac{K_r K \rho g \cos \theta}{\mu_o \phi} 3\omega_{N_i-1,0}^2 \left[ \frac{\omega_{N_i-1,1} - \omega_{\text{int}}}{2\Delta z_0^2} \right] \quad (\text{F.20})$$

**For  $i = (N_i - 1)$  and  $0 \leq j < (N_j - 1)$**

$$\begin{aligned} \varpi_{N_i-1,j} = & \frac{\partial D}{\partial \omega} \frac{1}{r_{N_i-1}} \left[ \frac{\omega_{\text{int}} - \omega_{N_i-2,j}}{2\Delta r} \right] + \frac{\partial D}{\partial \omega} \left[ \frac{\omega_{\text{int}} - 2\omega_{N_i-1,j} + \omega_{N_i-2,j}}{\Delta r^2} \right] - \\ & D \left[ \frac{2}{\Delta r^2} \right] + \frac{\partial^2 D}{\partial \omega^2} \left[ \frac{\omega_{\text{int}} - \omega_{N_i-2,j}}{2\Delta r} \right]^2 - \frac{K_r K \rho g \cos \theta}{\mu_o \phi} 3\omega_{N_i-1,j} \\ & \left[ \frac{\omega_{N_i-1,j+1} - \omega_{N_i-1,j-1}}{\Delta z_{N_i-1}} \right] \end{aligned} \quad (\text{F.21})$$

$$\varpi_{N_i-2,j} = -D \left[ \frac{1}{2r_{N_i-1}\Delta r} \right] + \frac{D}{\Delta r^2} - \frac{\partial D}{\partial \omega} 2 \left[ \frac{\omega_{\text{int}} - \omega_{N_i-2,j}}{2\Delta r} \right] \frac{1}{2\Delta r} \quad (\text{F.22})$$

$$\varpi_{N_{i-1},j+1} = -\frac{K_r K \rho g \cos \theta}{\mu_o \phi} 3\omega_{N_{i-1},j}^2 \left[ \frac{1}{2\Delta z_{N_{i-1}}} \right] \quad (\text{F.23})$$

$$\varpi_{N_{i-1},j-1} = \frac{K_r K \rho g \cos \theta}{\mu_o \phi} 3\omega_{N_{i-1},j}^2 \left[ \frac{1}{2\Delta z_{N_{i-1}}} \right] \quad (\text{F.24})$$

$$\varpi_z = \frac{K_r K \rho g \cos \theta}{\mu_o \phi} 3\omega_{N_{i-1},j}^2 \left[ \frac{\omega_{N_{i-1},j+1} - \omega_{N_{i-1},j-1}}{2\Delta z_{N_{i-1}}^2} \right] \quad (\text{F.25})$$

when  $i = (N_i - 1)$  and  $j = (N_j - 1)$

$$\begin{aligned} \varpi_{N_{i-1},N_{j-1}} &= \frac{\partial D}{\partial \omega} \frac{1}{r_{N_{i-1}}} \left[ \frac{\omega_{\text{int}} - \omega_{N_{i-2},N_{j-1}}}{2\Delta r} \right] + \frac{\partial D}{\partial \omega} \left[ \frac{\omega_{\text{int}} - 2\omega_{N_{i-1},N_{j-1}} + \omega_{N_{i-2},N_{j-1}}}{\Delta r^2} \right] \\ &\quad - D \left[ \frac{2}{\Delta r^2} \right] + \frac{\partial^2 D}{\partial \omega^2} \left[ \frac{\omega_{\text{int}} - \omega_{N_{i-2},N_{j-1}}}{2\Delta r} \right]^2 - \frac{K_r K \rho g \cos \theta}{\mu_o \phi} 3\omega_{N_{i-1},N_{j-1}} \\ &\quad \left[ \frac{\omega_{\text{int}} - \omega_{N_{i-1},N_{j-2}}}{\Delta z_{N_{i-1}}} \right] \end{aligned} \quad (\text{F.26})$$

$$\varpi_{N_{i-2},N_{j-1}} = -D \left[ \frac{1}{2r_{N_{i-1}}\Delta r} \right] + \frac{D}{\Delta r^2} - \frac{\partial D}{\partial \omega} 2 \left[ \frac{\omega_{\text{int}} - \omega_{N_{i-2},N_{j-1}}}{2\Delta r} \right] \frac{1}{2\Delta r} \quad (\text{F.27})$$

$$\varpi_{N_{i-1},N_{j-2}} = \frac{K_r K \rho g \cos \theta}{\mu_o \phi} 3\omega_{N_{i-1},N_{j-1}}^2 \left[ \frac{1}{2\Delta z_{N_{i-1}}} \right] \quad (\text{F.28})$$

$$\varpi_z = \frac{K_r K \rho g \cos \theta}{\mu_o \phi} 3\omega_{N_{i-1}, N_{j-1}}^2 \left[ \frac{\omega_{\text{int}} - \omega_{N_{i-1}, j-2}}{2\Delta z_{N_{i-1}}^2} \right] \quad (\text{F.29})$$

### For Lower most Intermediate Grid Points

When  $0 < i < (N_r - 1)$  and  $j = 0$

$$\begin{aligned} \varpi_{i,0} = & \frac{\partial D}{\partial \omega} \frac{1}{r_i} \left[ \frac{\omega_{i+1,0} - \omega_{i-1,0}}{2\Delta r} \right] + \frac{\partial D}{\partial \omega} \left[ \frac{\omega_{i+1,0} - 2\omega_{i,0} + \omega_{i-1,0}}{\Delta r^2} \right] - D \left[ \frac{2}{\Delta r^2} \right] + \\ & \frac{\partial^2 D}{\partial \omega^2} \left[ \frac{\omega_{i+1,0} - \omega_{i-1,0}}{2\Delta r} \right]^2 - \frac{K_r K \rho g \cos \theta}{\mu_o \phi} 3\omega_{i,0} \left[ \frac{\omega_{i,1} - \omega_{\text{int}}}{\Delta z_i} \right] \end{aligned} \quad (\text{F.30})$$

$$\varpi_{i+1,0} = \left[ \frac{D}{2r_i \Delta r} \right] + \frac{D}{\Delta r^2} + \frac{\partial D}{\partial \omega} 2 \left[ \frac{\omega_{i+1,0} - \omega_{i-1,0}}{2\Delta r} \right] \frac{1}{2\Delta r} \quad (\text{F.31})$$

$$\varpi_{i-1,0} = \left[ \frac{-D}{2r_i \Delta r} \right] + \frac{D}{\Delta r^2} - \frac{\partial D}{\partial \omega} 2 \left[ \frac{\omega_{i+1,0} - \omega_{i-1,0}}{2\Delta r} \right] \frac{1}{2\Delta r} \quad (\text{F.32})$$

$$\varpi_{i,1} = -\frac{K_r K \rho g \cos \theta}{\mu_o \phi} 3\omega_{i,0}^2 \left[ \frac{1}{2\Delta z_{N_{i-1}}} \right] \quad (\text{F.33})$$

$$\varpi_z = \frac{K_r K \rho g \cos \theta}{\mu_o \phi} 3\omega_{i,0}^2 \left[ \frac{\omega_{i,1} - \omega_{\text{int}}}{2\Delta z_i^2} \right] \quad (\text{F.34})$$

## For the upper most intermediate grid points

When  $0 < i < (N_r - 1)$  and  $j = (N_z - 1)$

$$\begin{aligned} \varpi_{i,Nj-1} = & \frac{\partial D}{\partial \omega} \frac{1}{r_i} \left[ \frac{\omega_{i+1,Nj-1} - \omega_{i-1,Nj-1}}{2\Delta r} \right] + \frac{\partial D}{\partial \omega} \left[ \frac{\omega_{i+1,Nj-1} - 2\omega_{i,Nj-1} + \omega_{i-1,Nj-1}}{\Delta r^2} \right] \\ & - D \left[ \frac{2}{\Delta r^2} \right] + \frac{\partial^2 D}{\partial \omega^2} \left[ \frac{\omega_{i+1,Nj-1} - \omega_{i-1,Nj-1}}{2\Delta r} \right]^2 - \\ & \frac{K_r K \rho g \cos \theta}{\mu_o \phi} 3\omega_{i,Nj-1} \left[ \frac{\omega_{\text{int}} - \omega_{i,j-2}}{\Delta z_i} \right] \end{aligned} \quad (\text{F.35})$$

$$\varpi_{i+1,Nj-1} = \left[ \frac{D}{2r_i \Delta r} \right] + \frac{D}{\Delta r^2} + \frac{\partial D}{\partial \omega} 2 \left[ \frac{\omega_{i+1,Nj-1} - \omega_{i-1,Nj-1}}{2\Delta r} \right] \frac{1}{2\Delta r} \quad (\text{F.36})$$

$$\varpi_{i-1,Nj-1} = \left[ \frac{-D}{2r_i \Delta r} \right] + \frac{D}{\Delta r^2} - \frac{\partial D}{\partial \omega} 2 \left[ \frac{\omega_{i+1,Nj-1} - \omega_{i-1,Nj-1}}{2\Delta r} \right] \frac{1}{2\Delta r} \quad (\text{F.37})$$

$$\varpi_{i,Nj-2} = \frac{K_r K \rho g \cos \theta}{\mu_o \phi} 3\omega_{i,Nj-1}^2 \left[ \frac{1}{2\Delta z_i} \right] \quad (\text{F.38})$$

$$\varpi_z = \frac{K_r K \rho g \cos \theta}{\mu_o \phi} 3\omega_{i,Nj-1}^2 \left[ \frac{\omega_{\text{int}} - \omega_{i,Nj-2}}{2\Delta z_i^2} \right] \quad (\text{F.39})$$

### Change in Height of Physical Model

$$z_{i,0} = -\frac{K_r K \rho g \cos \theta}{\mu_o} \left[ \frac{\omega_{i,0} + \omega_{i+1,0} + 2\omega_{\text{int}}}{8} \right] \quad (\text{F.40})$$

$$z_{i+1,0} = z_{i,0} \quad (\text{F.41})$$

$$z_{N_i-1,0} = -\frac{K_r K \rho g \cos \theta}{\mu_o} \left[ \frac{\omega_{N_i-1,0} + 3\omega_{\text{int}}}{8} \right] \quad (\text{F.42})$$

Where  $\varpi$  and  $z$  shows the Jacobian expression for corresponding node for solvent concentration and model height respectively.

F.2 Following are the set of Jacobian equations employed to integrate the ODEs of adjoint equations (Equations [4.69]–[4.75]). The equations written for corresponding grid points are as follows:

**For intermediate grid points, i.e for  $0 < i < (N_r - 1)$  and  $0 < j < (N_z - 1)$**

$$\bar{\lambda}_{i,j} = -D \left[ \frac{1}{r_i^2} \right] + \left[ \frac{2D}{2\Delta r^2} \right] \quad (\text{F.43})$$

$$\bar{\lambda}_{i,j+1} = -3 \frac{K_r K \rho g \cos \theta}{\mu_o \varphi} \omega_{i,j}^2 \left[ \frac{1}{2\Delta z_i} \right] \quad (\text{F.44})$$

$$\bar{\lambda}_{i,j-1} = 3 \frac{K_r K \rho g \cos \theta}{\mu_o \varphi} \omega_{i,j}^2 \left[ \frac{1}{2\Delta z_i} \right] \quad (\text{F.45})$$

$$\bar{\lambda}_{i+1,j} = D \left[ \frac{1}{r_i \ 2\Delta r} \right] - \left[ \frac{D}{\Delta r^2} \right] \quad (\text{F.46})$$

$$\bar{\lambda}_{i-1,j} = -D \left[ \frac{1}{r_i \ 2\Delta r} \right] - \left[ \frac{D}{\Delta r^2} \right] \quad (\text{F.47})$$

**For**  $i = (N_r - 1)$  and  $0 < j < (N_z - 1)$

$$\bar{\lambda}_{N_i-1,j} = -D \left[ \frac{1}{r_{N_i-1}^2} \right] + \left[ \frac{2D}{2\Delta r^2} \right] \quad (\text{F.48})$$

$$\bar{\lambda}_{N_i-2,j} = -D \left[ \frac{1}{r_{N_i-1} 2\Delta r} \right] - \left[ \frac{D}{\Delta r^2} \right] \quad (\text{F.49})$$

$$\bar{\lambda}_{N_i-1,j+1} = -3 \frac{K_r K \rho g \cos \theta}{\mu_o \varphi} \omega_{N_i-1,j}^2 \left[ \frac{1}{2\Delta z_{N_i-1}} \right] \quad (\text{F.50})$$

$$\bar{\lambda}_{N_i-1,j+1} = 3 \frac{K_r K \rho g \cos \theta}{\mu_o \varphi} \omega_{N_i-1,j}^2 \left[ \frac{1}{2\Delta z_{N_i-1}} \right] \quad (\text{F.51})$$

**For**  $i = (N_r - 1)$  and  $j = 0$

$$\bar{\lambda}_{N_i-1,0} = -D \left[ \frac{1}{r_{N_i-1}} \right] - \left[ \frac{D}{\Delta r^2} \right] \quad (\text{F.52})$$

$$\bar{\lambda}_{N_i-2,0} = -D \left[ \frac{1}{r_{N_i-1} 2\Delta r} \right] - \left[ \frac{D}{\Delta r^2} \right] \quad (\text{F.53})$$

$$\bar{\lambda}_{N_i-1,1} = -3 \frac{K_r K \rho g \cos \theta}{\mu_o \varphi} \omega_{N_i-1}^2 \left[ \frac{1}{2\Delta z_{N_i-1}} \right] \quad (\text{F.54})$$

$$\bar{\lambda}_{N_i-1,1} = 3 \frac{K_r K \rho g \cos \theta}{\mu_o \varphi} \omega_{N_i-1}^2 \left[ \frac{1}{2\Delta z_{N_i-1}} \right] \quad (\text{F.55})$$

**For**  $i = (N_r - 1)$  and  $j = (N_z - 1)$

$$\bar{\lambda}_{N_i-1,N_i-1} = -D \left[ \frac{1}{r_{N_i-1}^2} \right] + \left[ \frac{2D}{\Delta r^2} \right] \quad (\text{F.56})$$

$$\bar{\lambda}_{N_i-2,N_i-1} = -D \left[ \frac{1}{r_{N_i-1} 2\Delta r} \right] - \left[ \frac{D}{\Delta r^2} \right] \quad (\text{F.57})$$

$$\bar{\lambda}_{N_i-1,N_{j-2}} = 3 \frac{K_r K \rho g \cos \theta}{\mu_o \varphi} \omega_{N_i-1,N_{j-1}}^2 \left[ \frac{1}{2\Delta z_{N_i-1}} \right] \quad (\text{F.58})$$

**For the upper most intermediate grid points, i.e. for**  $0 < i < (N_r - 1)$  and  $j = (N_z - 1)$

$$\bar{\lambda}_{i,N_{j-1}} = -D \left[ \frac{1}{r_i^2} \right] + \left[ \frac{2D}{\Delta r^2} \right] \quad (\text{F.59})$$

$$\bar{\lambda}_{i+1,Nj-1} = D \left[ \frac{1}{r_i} \right] - \left[ \frac{D}{\Delta r^2} \right] \quad (\text{F.60})$$

$$\bar{\lambda}_{i,Nj-2} = 3 \frac{K_r K \rho g \cos \theta}{\mu_o \varphi} \omega_{Ni,Nj-1}^2 \left[ \frac{1}{2\Delta z_i} \right] \quad (\text{F.61})$$

**For the lower most intermediate grid points, i.e. for  $0 < i < (N_r - 1)$  and  $j = 0$**

$$\begin{aligned} \frac{d\lambda_{i,0}}{dt} = D \left[ \frac{1}{r_i} \frac{\lambda_{i+1,0} - \lambda_{i-1,0}}{2\Delta r} - \frac{\lambda_{i+1,0} - 2\lambda_{i,0} + \lambda_{i-1,0}}{\Delta r^2} \right] - \\ D \left[ \frac{\lambda_{i,0}}{r_i^2} \right] - 3 \frac{K_r K \rho g \cos \theta}{\mu_o \varphi} \omega_{i,0}^2 \left[ \frac{\lambda_{i,1}}{2\Delta z_i} \right] \end{aligned} \quad (\text{F.62})$$

$$\bar{\lambda}_{i,0} = 3 \frac{K_r K \rho g \cos \theta}{\mu_o \varphi} \omega_{i,0}^2 \left[ \frac{1}{2\Delta z_i} \right] - D \left[ \frac{1}{r_i^2} \right] + \left[ \frac{2D}{\Delta r^2} \right] \quad (\text{F.63})$$

$$\bar{\lambda}_{i+1,0} = D \left[ \frac{1}{r_i} \frac{1}{2\Delta r} \right] - \left[ \frac{D}{\Delta r^2} \right] \quad (\text{F.64})$$

$$\bar{\lambda}_{i-1,0} = -D \left[ \frac{1}{r_i} \frac{1}{2\Delta r} \right] - \left[ \frac{D}{\Delta r^2} \right] \quad (\text{F.65})$$

$$\bar{\lambda}_{i,1} = -3 \frac{K_r K \rho g \cos \theta}{\mu_o \varphi} \omega_{i,1}^2 \left[ \frac{1}{2\Delta z_i} \right] \quad (\text{F.66})$$





# Appendix G

Recorded mass of the physical model versus time in an experiment

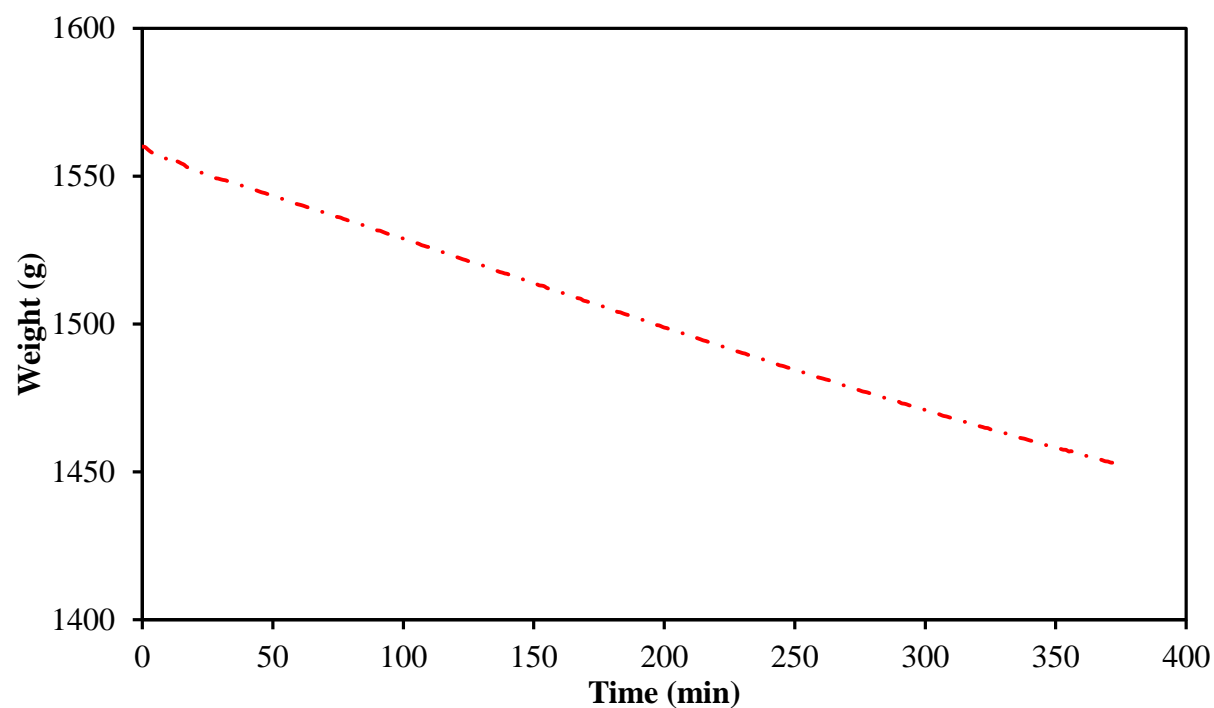


**Figure G.1** Recorded weight of the physical model with time (model height: 25 cm, permeability: 102 Darcy, solvent: butane)

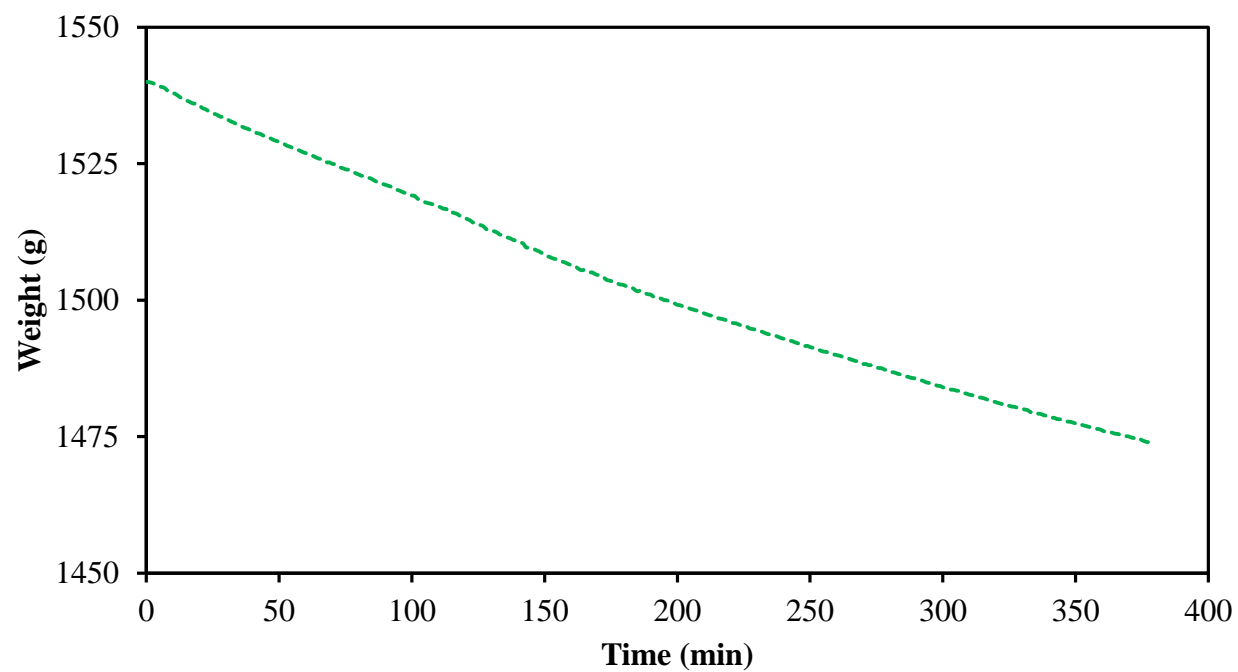


**Figure G.2** Recorded weight of the physical model with time (model height: 25 cm, permeability: 51 Darcy, solvent: butane)

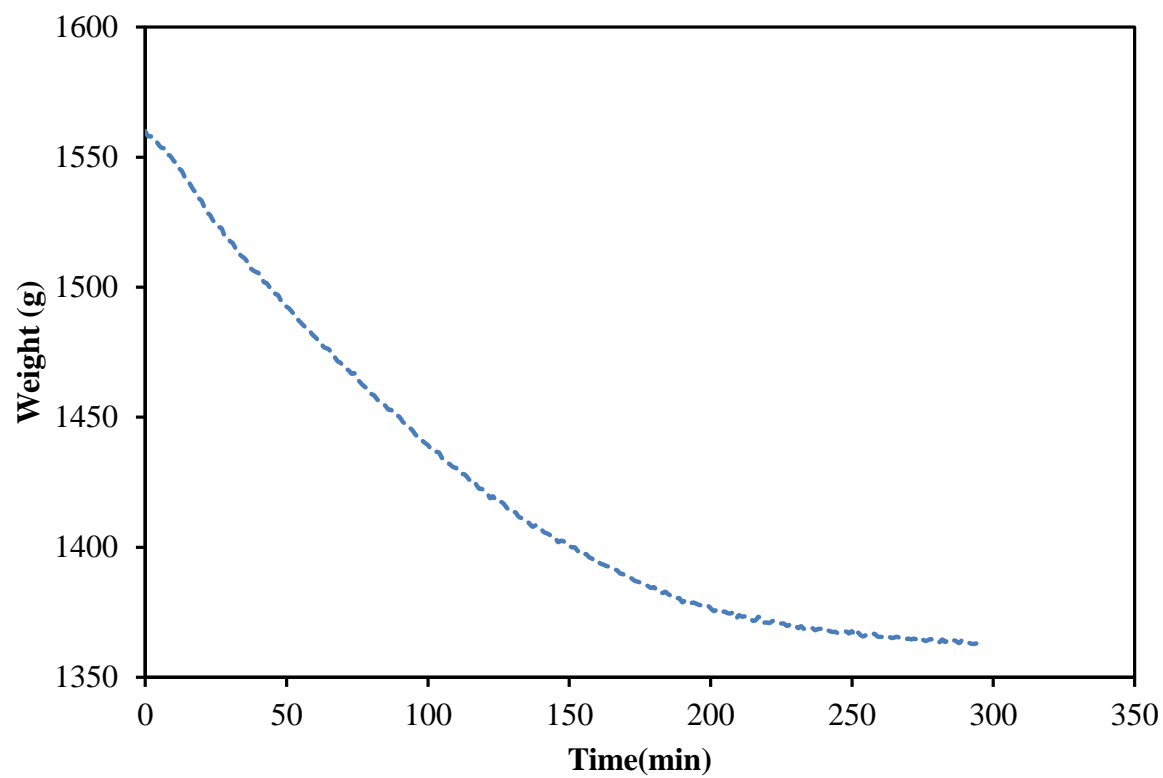


**Figure G.3** Recorded weight of the physical model with time (model height:25 cm, permeability:427 Darcy, solvent: propane)

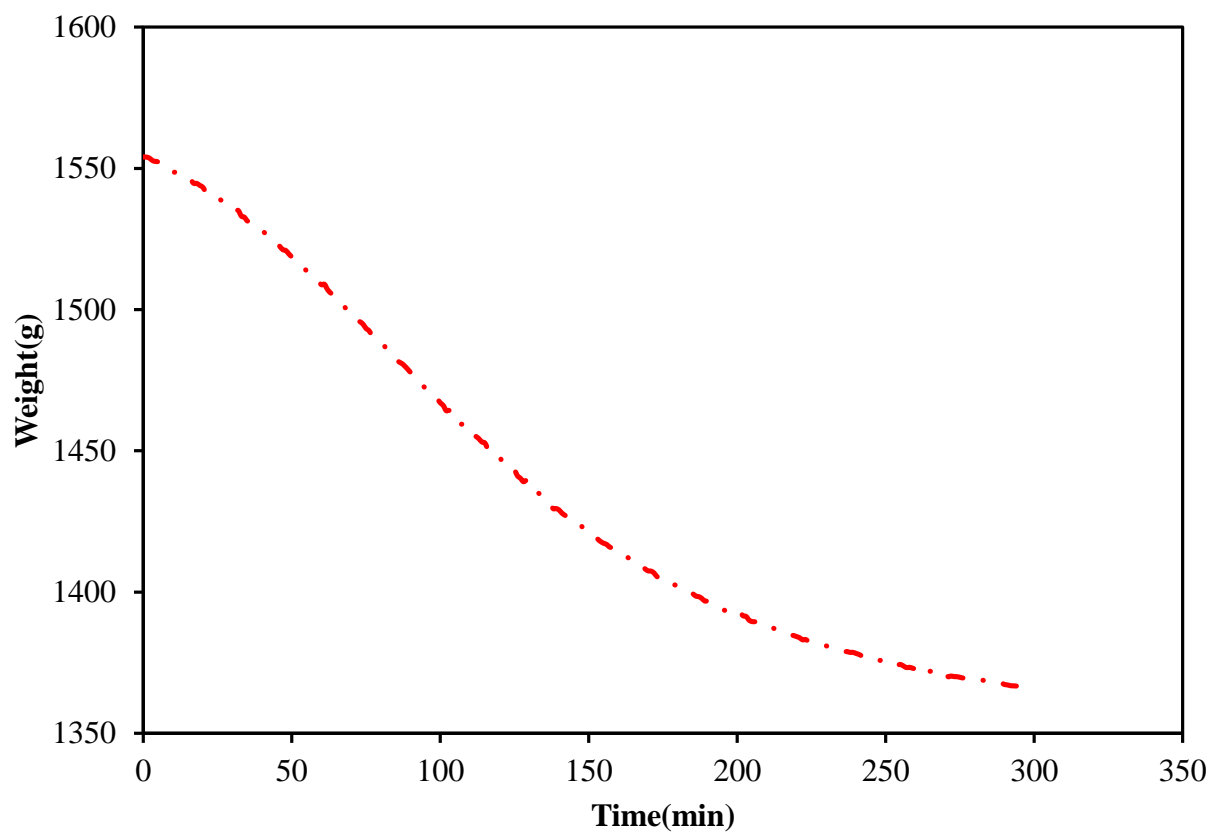


**Figure G.3** Recorded mass of the physical model with time (model height: 25 cm, permeability: 404 Darcy, solvent: propane)

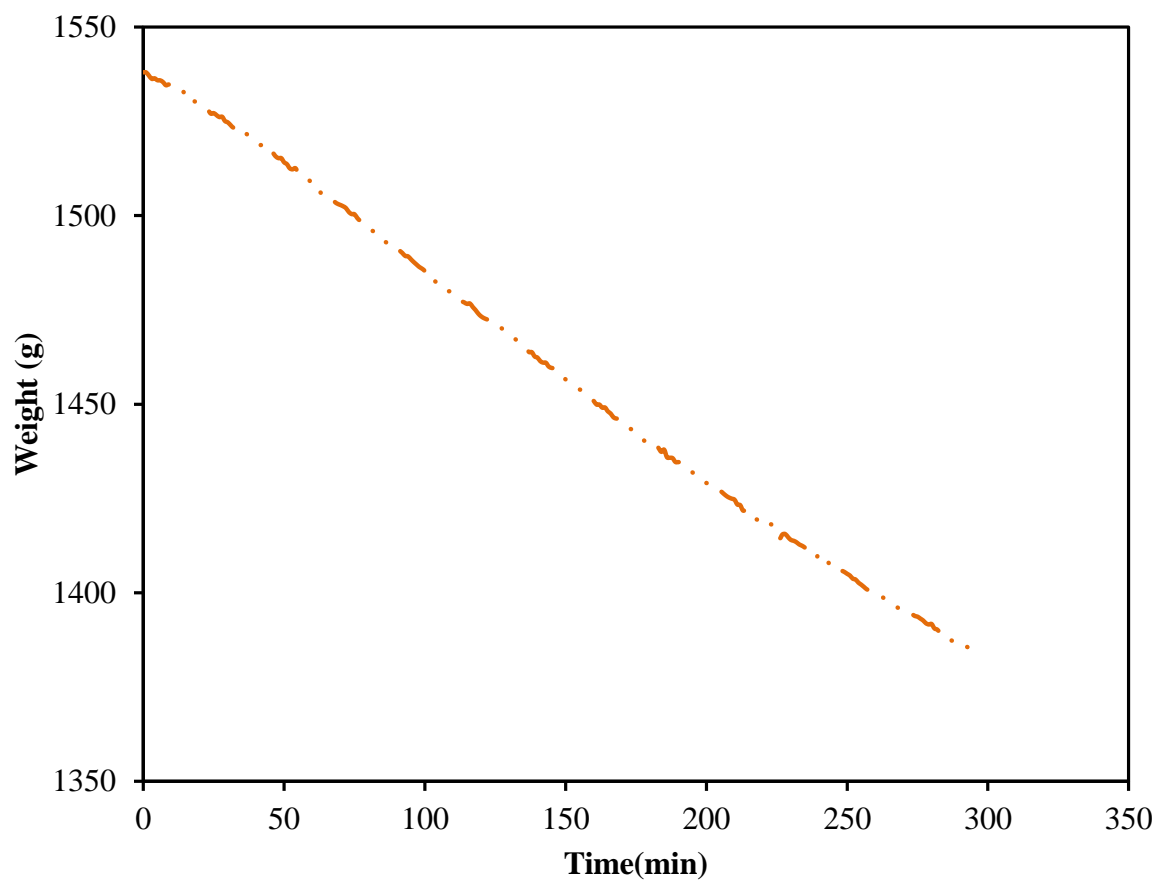


**Figure G.4** Recorded mass of the physical model with time (model height: 25 cm, permeability: 87 Darcy, solvent: propane)

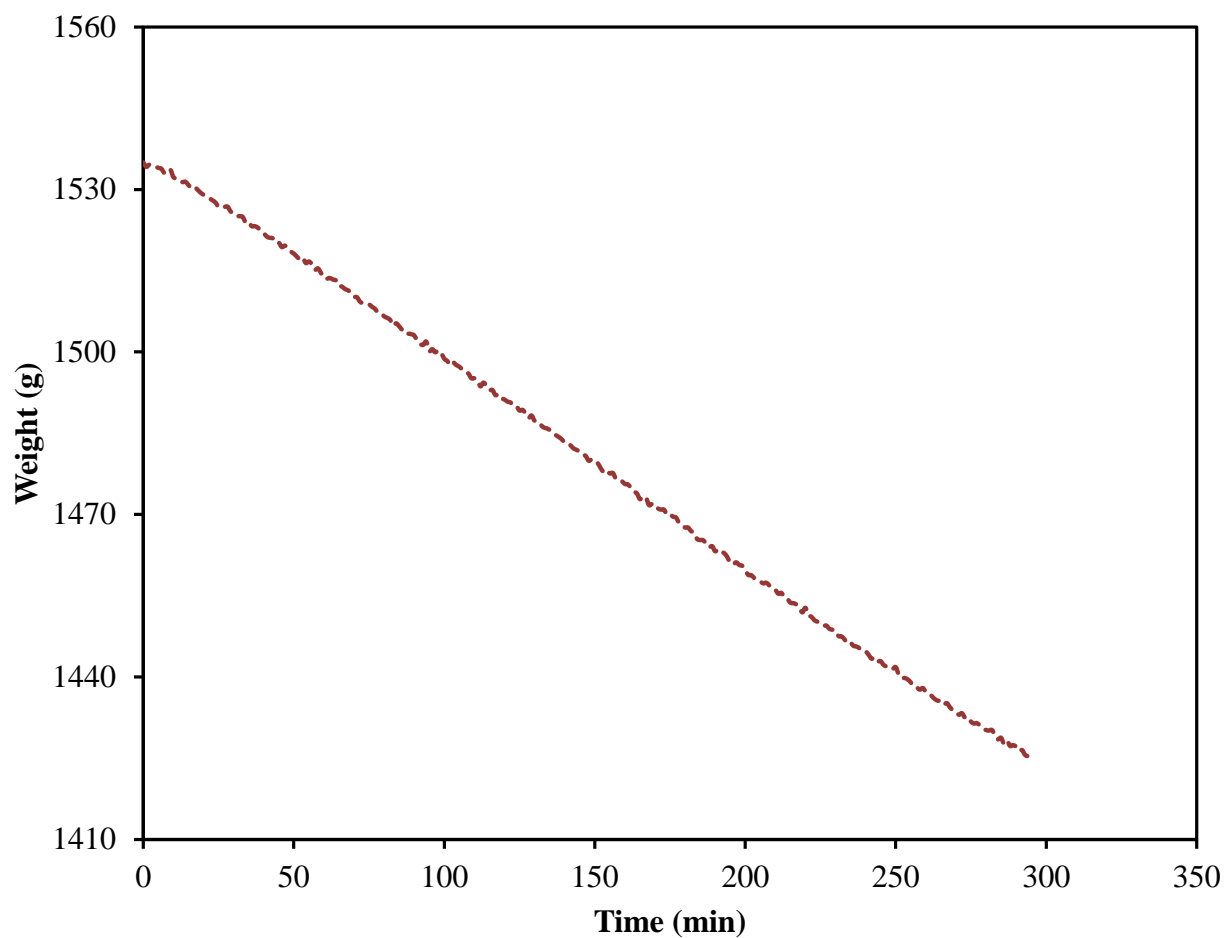


**Figure G.5** Recorded mass of the physical model with time (model height: 25 cm, permeability: 40 Darcy, solvent: propane)

# Appendix H

**Table H.1** Average live oil density (g/cm<sup>3</sup>) for various physical models

Run (#)	Model Height (cm)	Permeability (Darcy)	Solvent gas	Live oil Density (g/cm <sup>3</sup> )
1	25	204	Propane	0.831
2	25	87	Propane	0.829
3	25	40	Propane	0.825
4	45	204	Propane	0.827





# Appendix I

## Simulation Results for Determination of Concentration-Dependent Dispersion Coefficient

I.1 The simulation results for physical model of 25 cm physical model height, permeability of 204 Darcy, and butane gas.

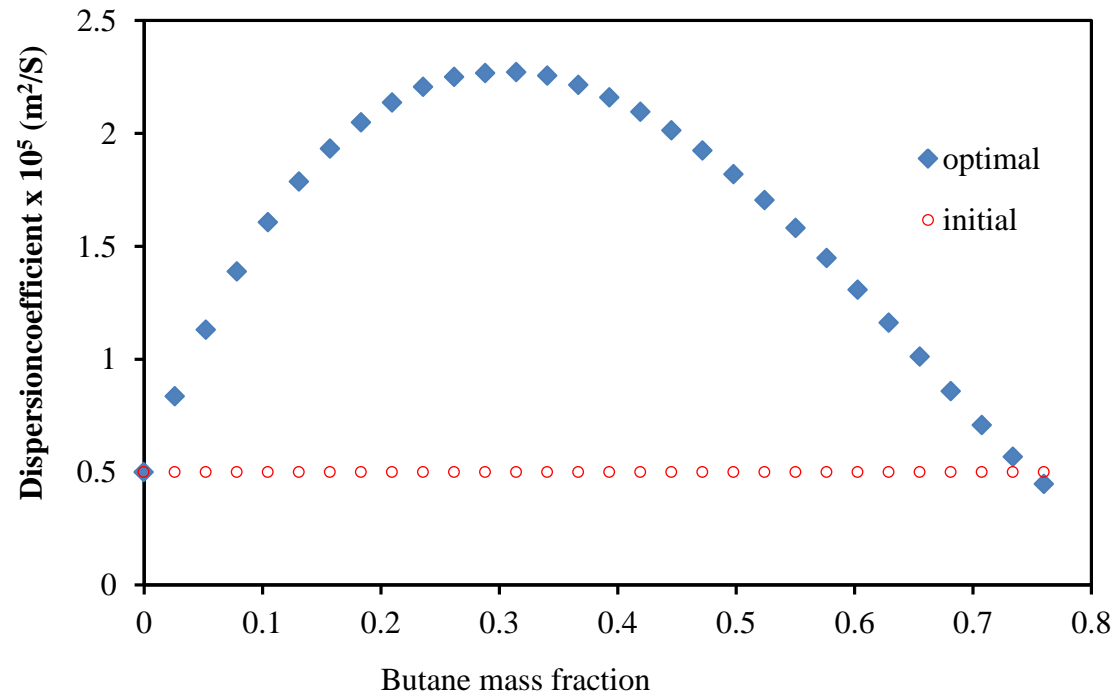


**Figure I.1** Dispersion coefficient function of propane in heavy oil for (butane, 25 cm model height, and 204 Darcy)

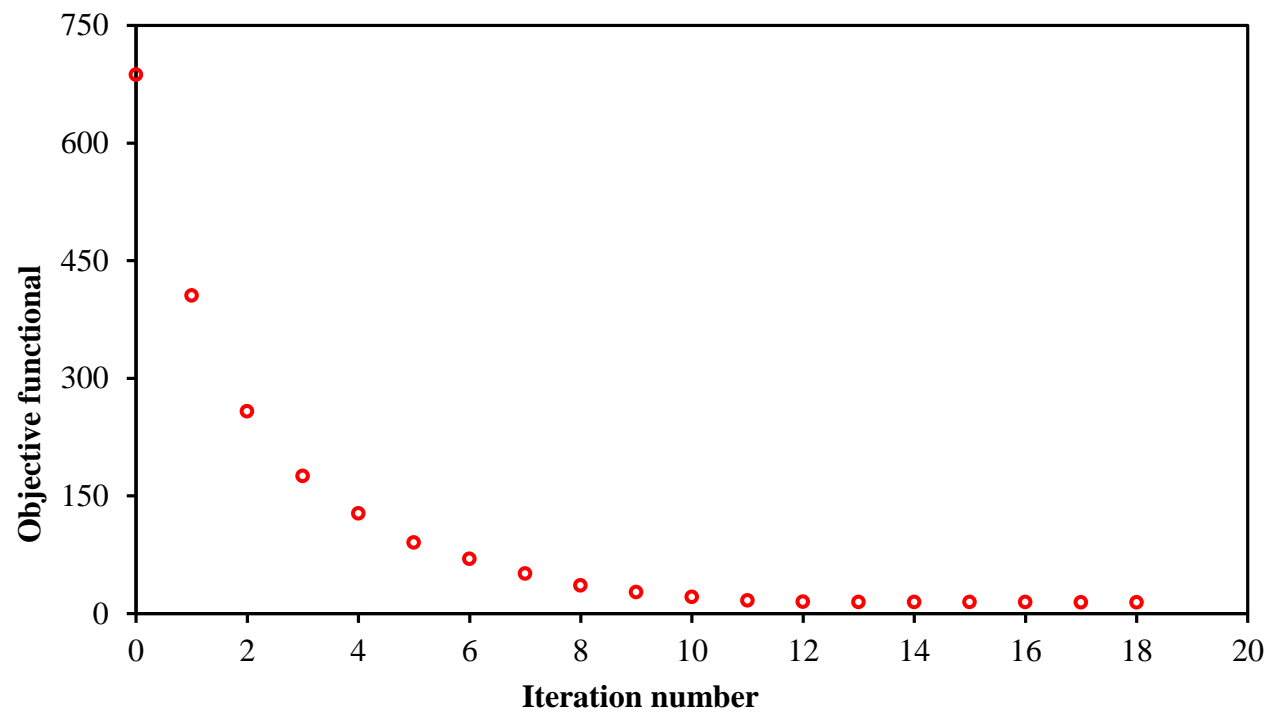


**Figure I.2** Error versus iteration number for (butane, 25 cm model height, and 204 Darcy)

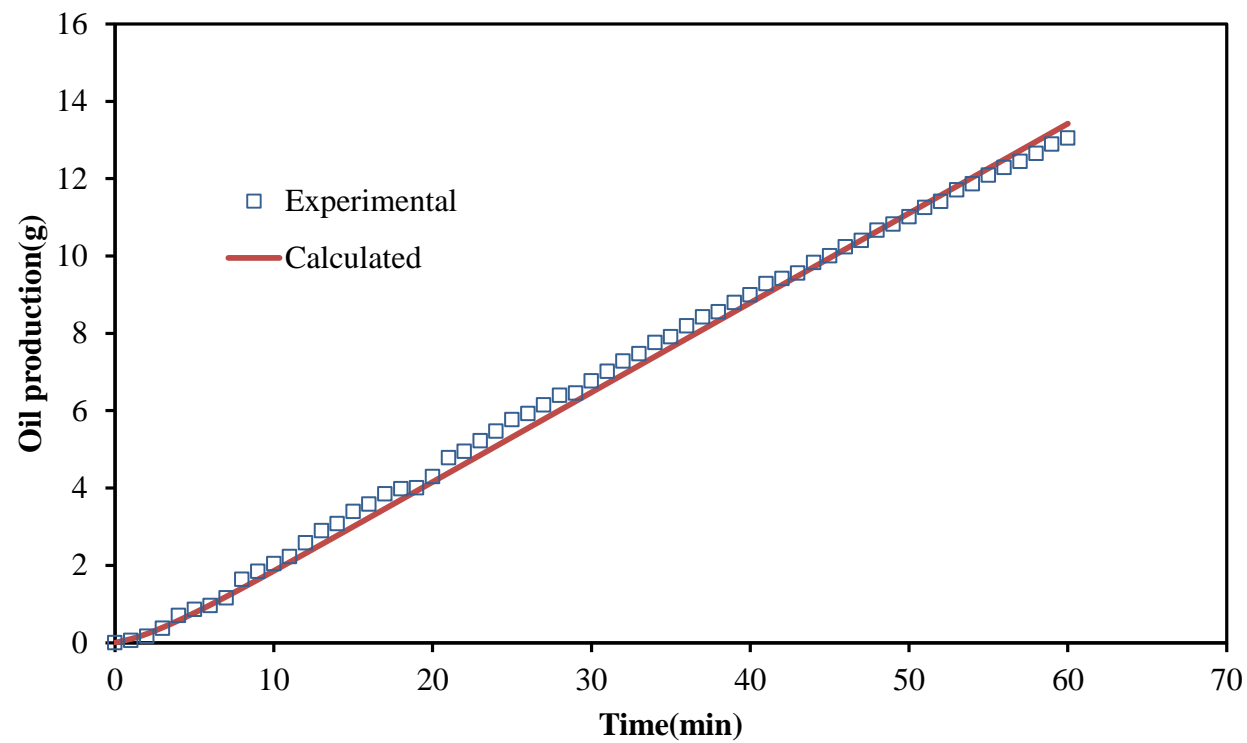


**Figure I.3** Experimental and calculated mass of oil produced with time (204 D, 25 cm model height, butane)

I.2 The simulation results for physical model of 45 cm physical model height, permeability of 204 Darcy, and butane gas.

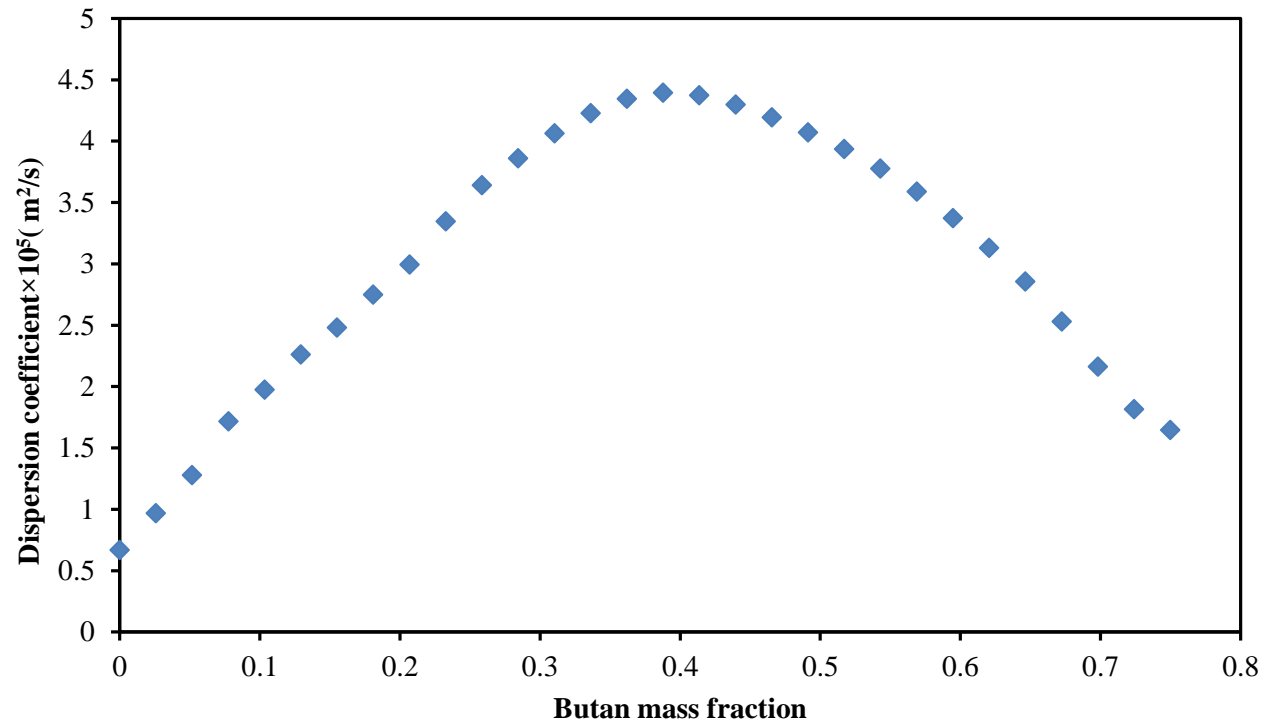


**Figure I.4** Dispersion coefficient function of propane in heavy oil for (butane, 45 cm model height, and 204 Darcy)

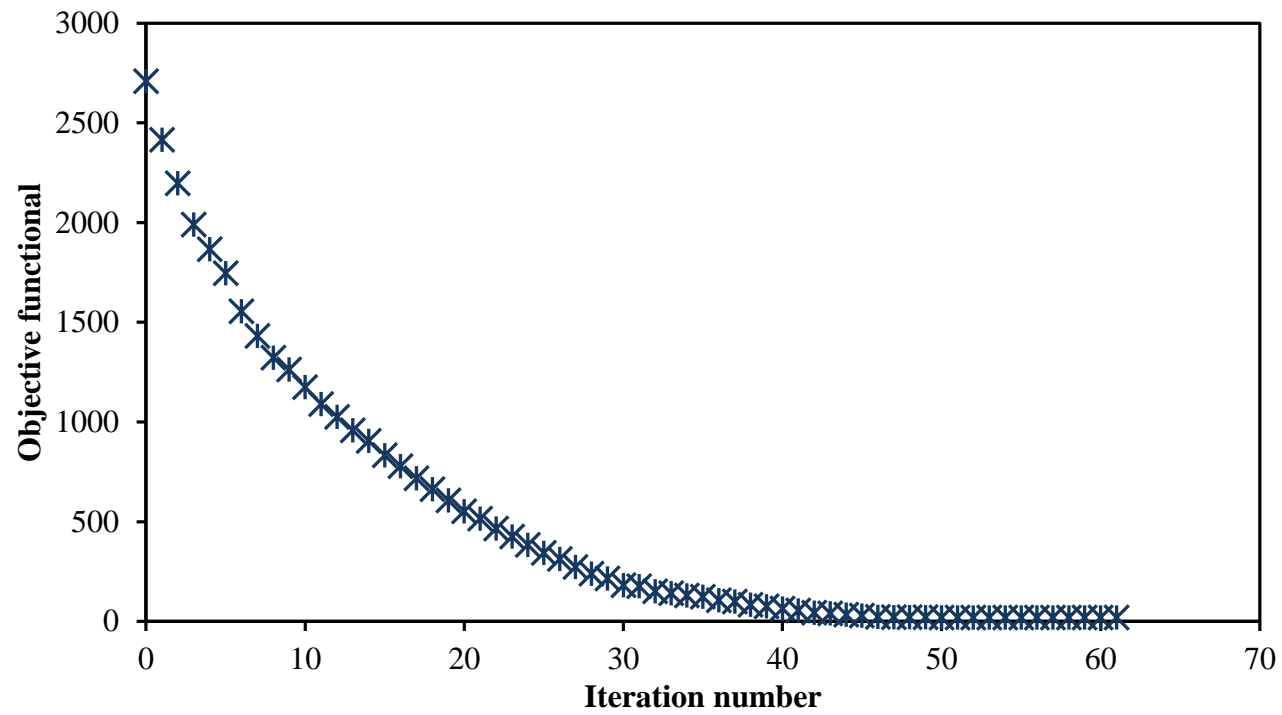


**Figure I.5** Error versus iteration number for (butane, 45 cm model height, and 204 Darcy)

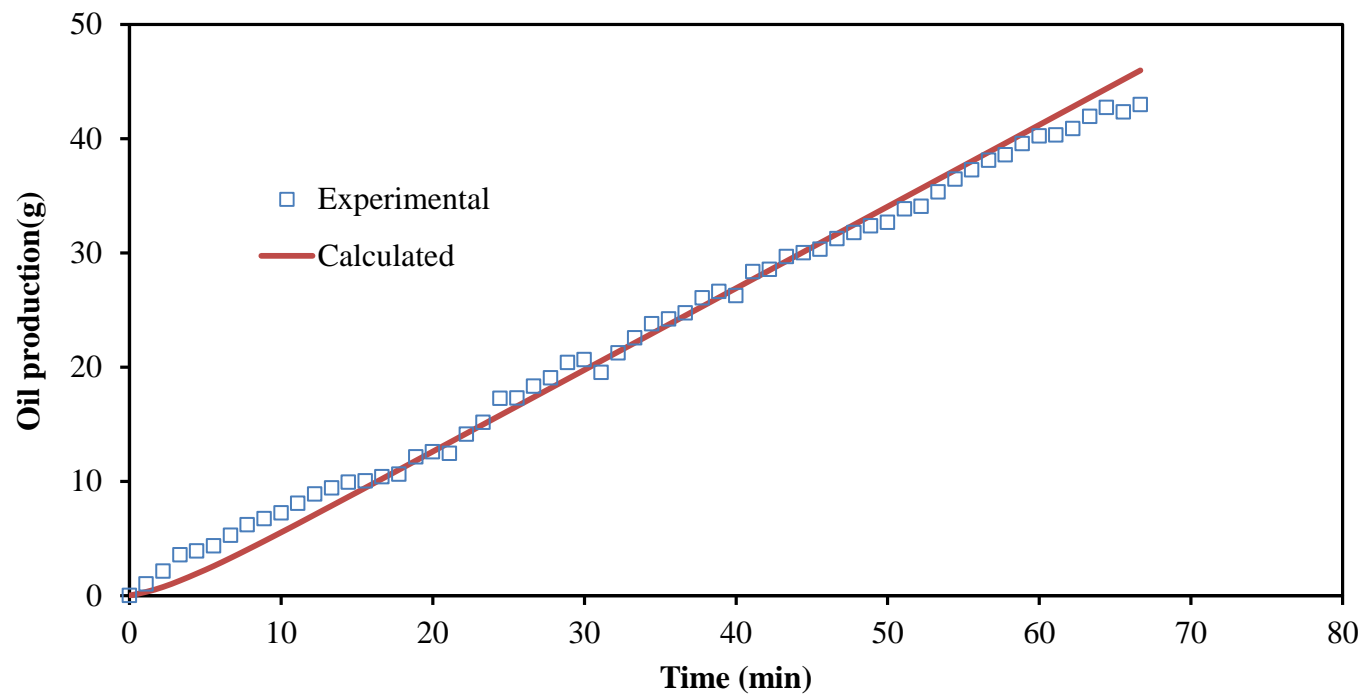


**Figure I.6** Experimental and calculated mass of oil produced with time (204 D, 45 cm model height, butane)

**I.3 The simulation results for physical model of 25 cm physical model height, permeability of 51 Darcy, and propane gas.**

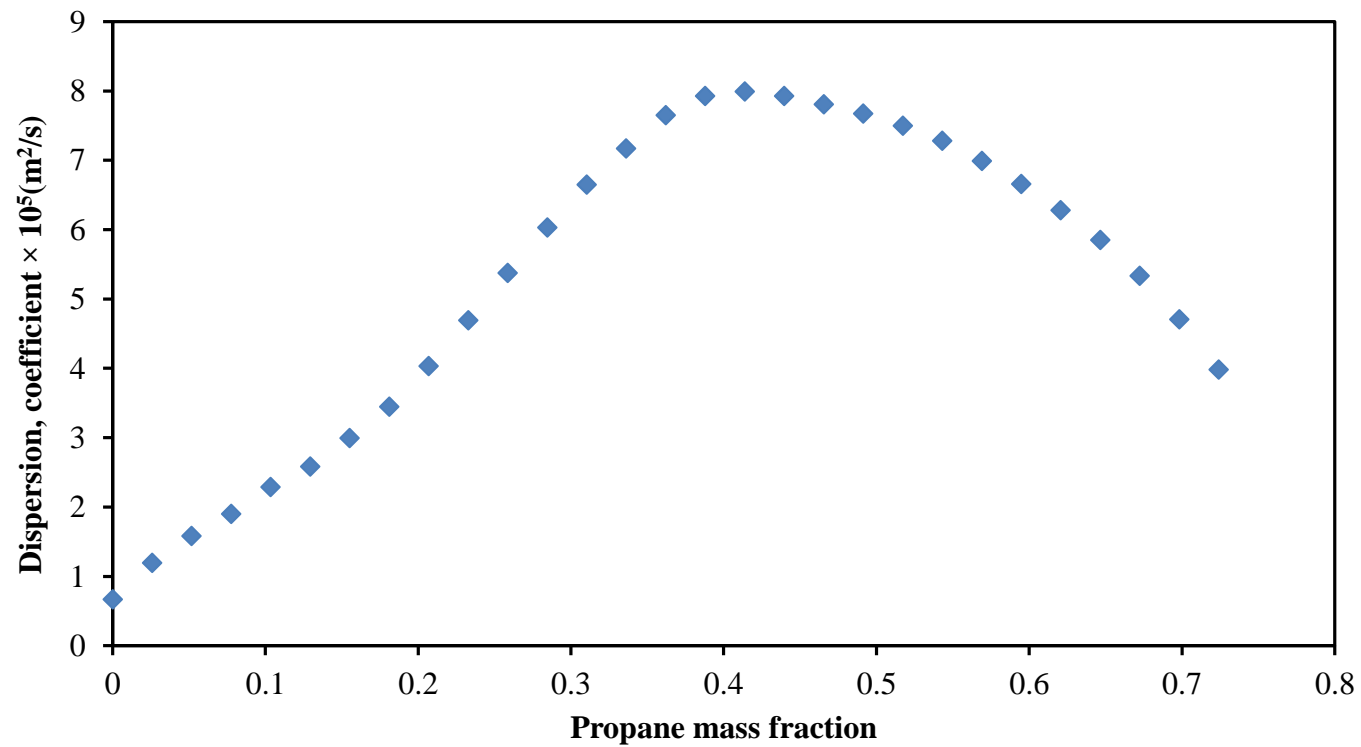


**Figure I.7** Dispersion coefficient function of propane in heavy oil for (propane, 25 cm model height, and 51 Darcy)



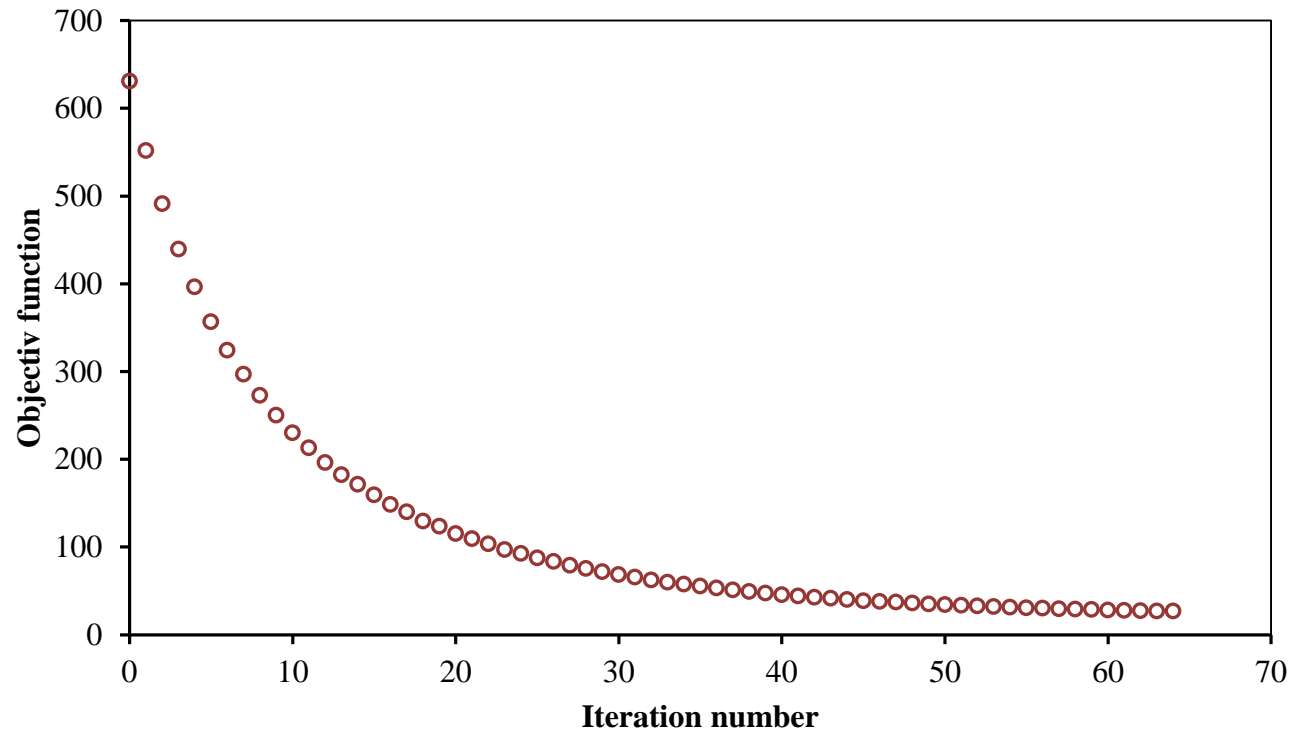


**Figure I.8** Error versus iteration number for (propane, 25 cm model height, and 51 Darcy)

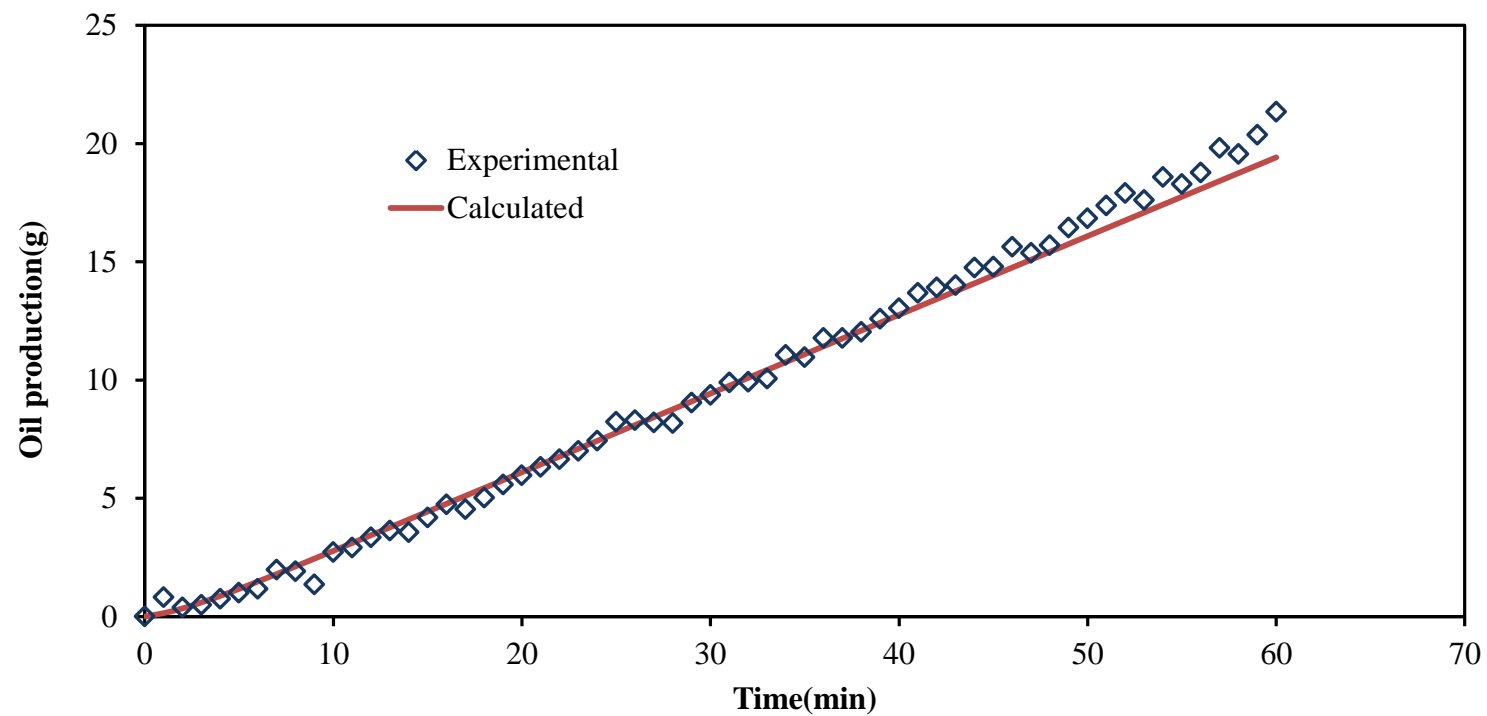


**Figure I.9** Experimental and calculated mass of oil produced with time (51 Darcy, 25 cm model height, Propane)

**I.4 The simulation results for physical model of 45 cm physical model height, permeability of 204 Darcy, and propane gas.**

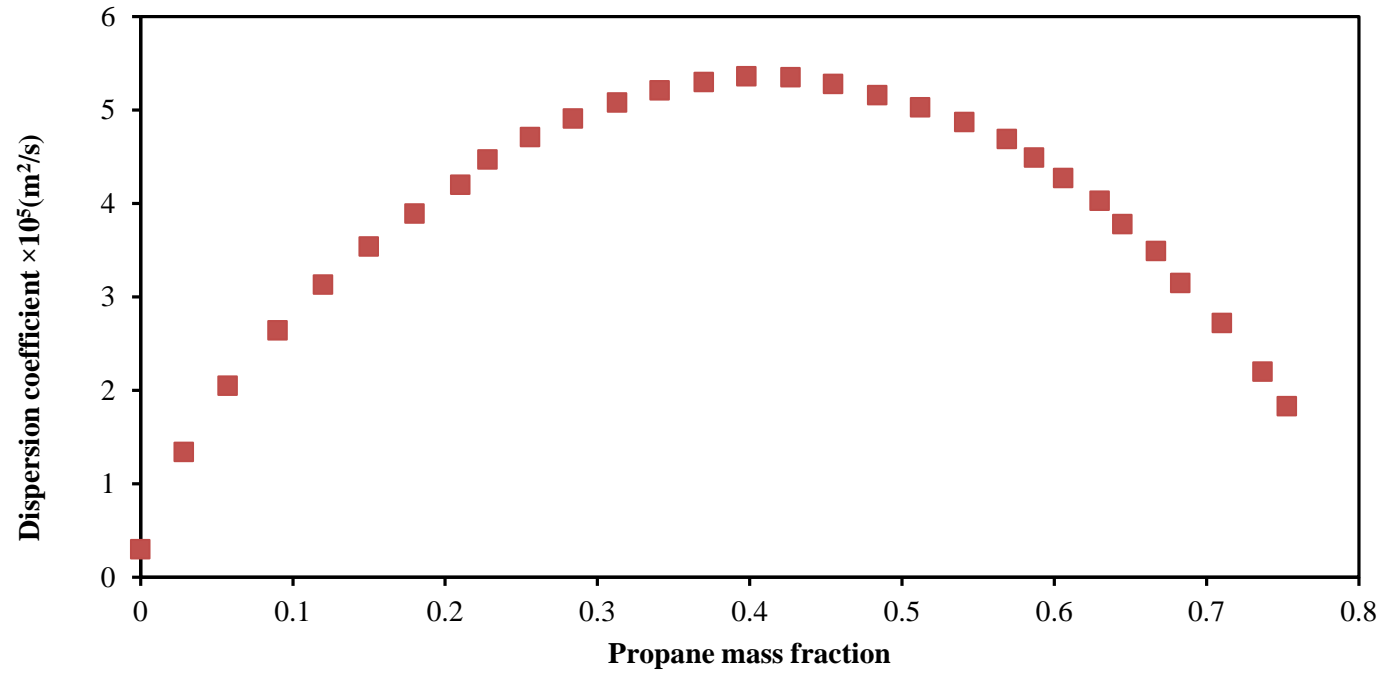


**Figure I.10** Dispersion coefficient function of propane in heavy oil for (propane, 45 cm model height, and 204 Darcy)

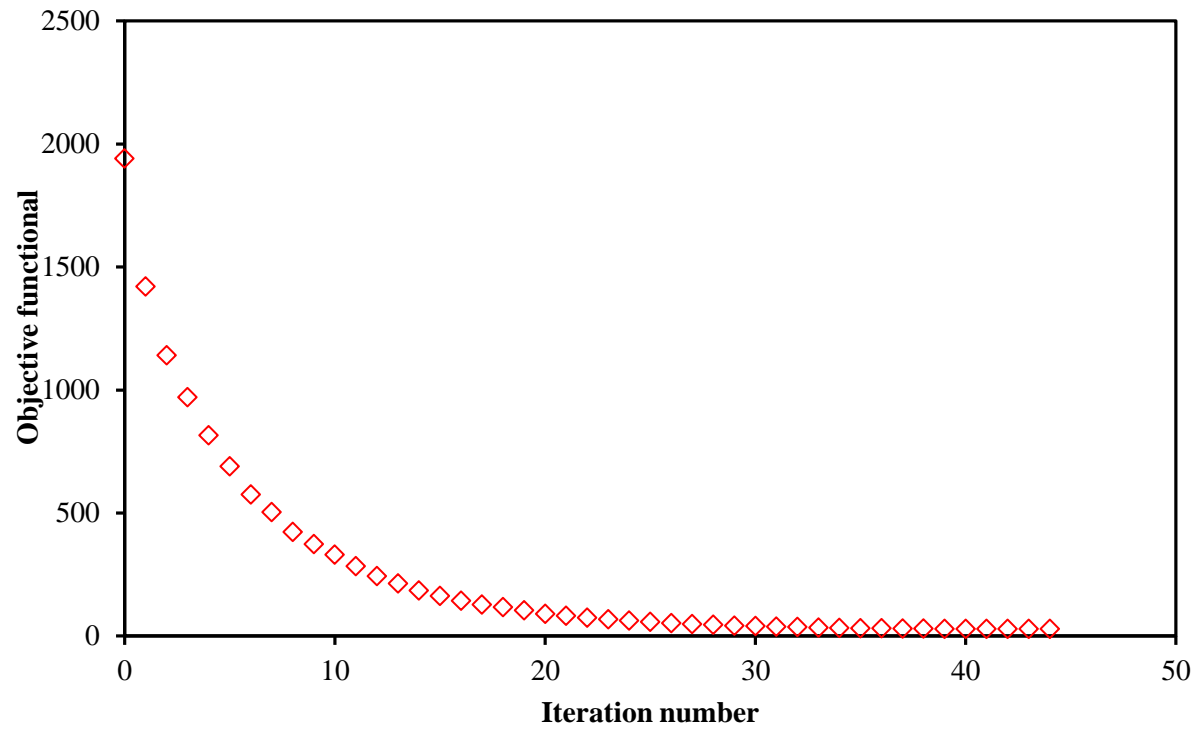


**Figure I.11** Error versus iteration number for (Propane, 45 cm model height, and 204 Darcy)

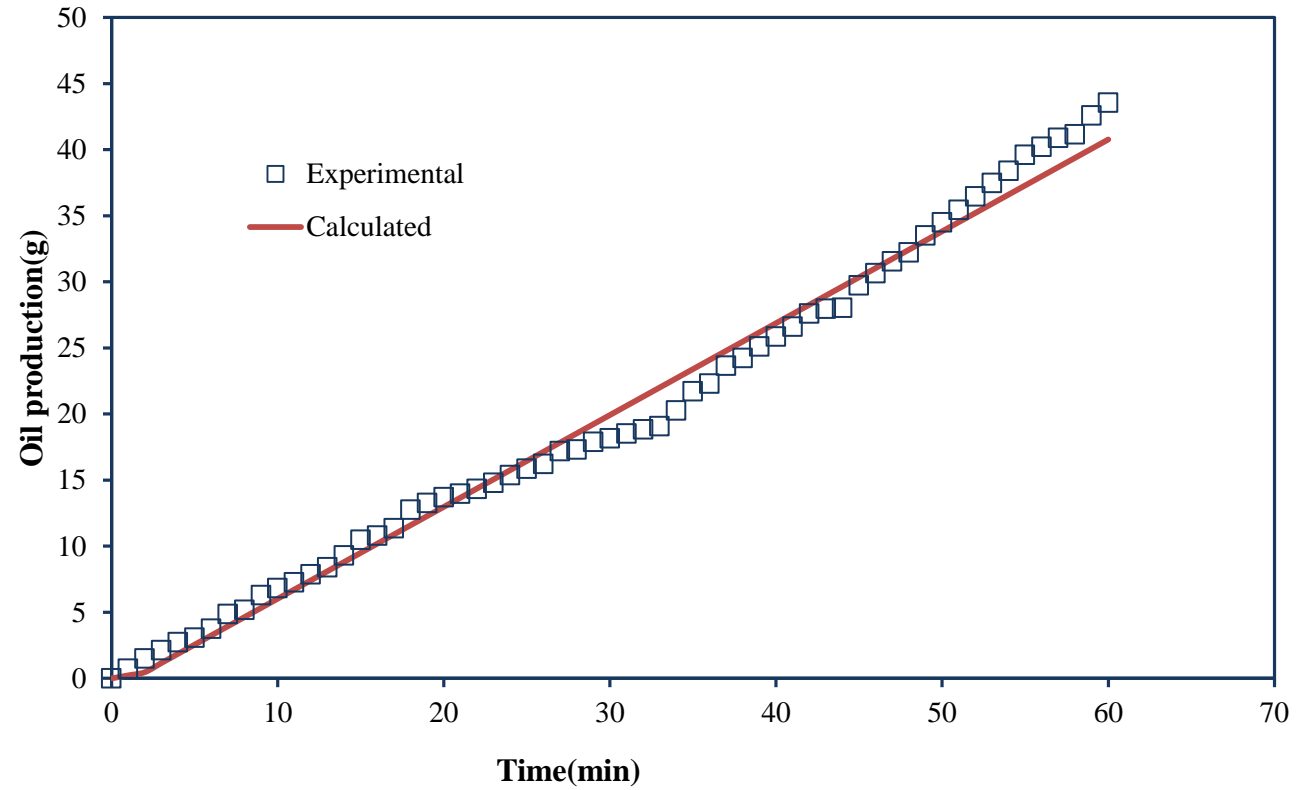


**Figure I.12** Experimental and calculated mass of oil produced with time (204 Darcy, 45 cm model height, propane)

# Appendix J

Simulation Results and Validation of Optimal Control Policy For Solvent Injection Pressure

**J.1 The simulation results of Optimal Control policy for physical model of 25 cm physical model height, permeability of 51 Darcy, and propane gas.**

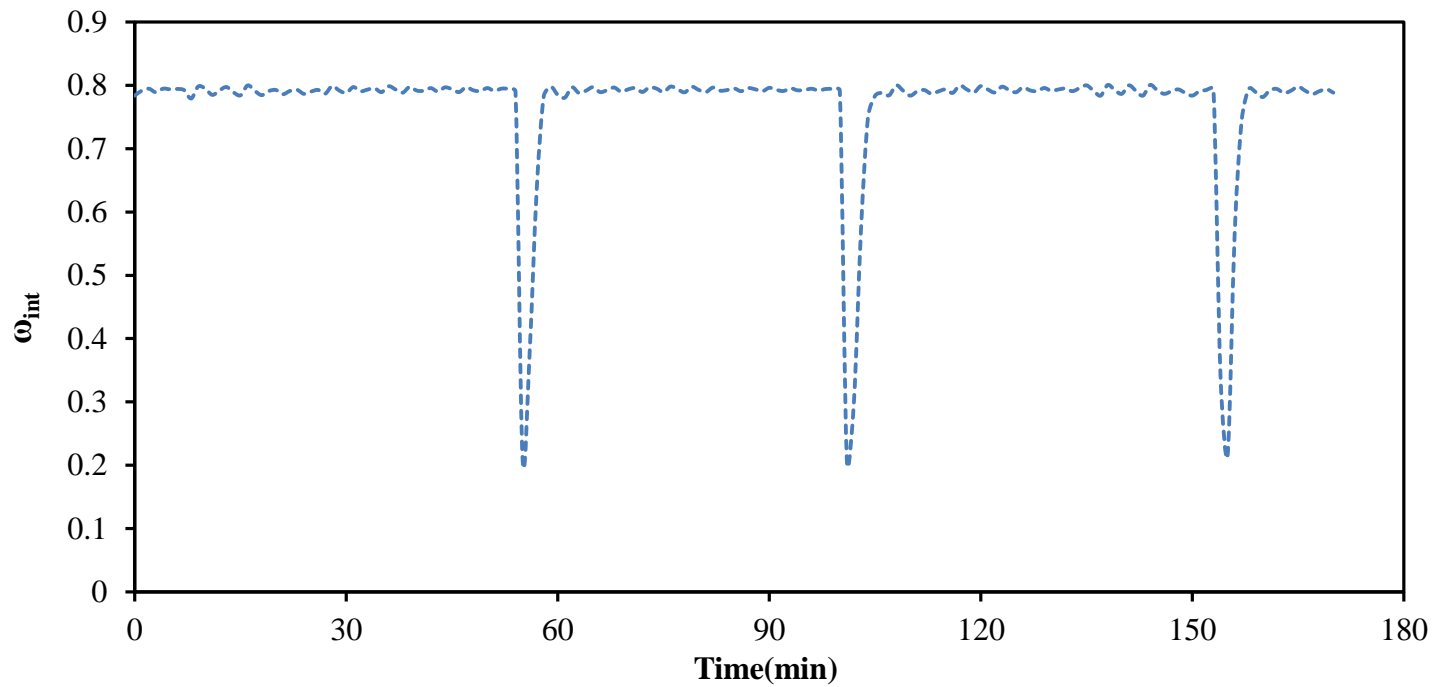


**Figure J.1** Simulation of variation interface concentration  $\omega_{int}$  function of time in heavy oil(propane, 25 cm model height, and 51 Darcy)

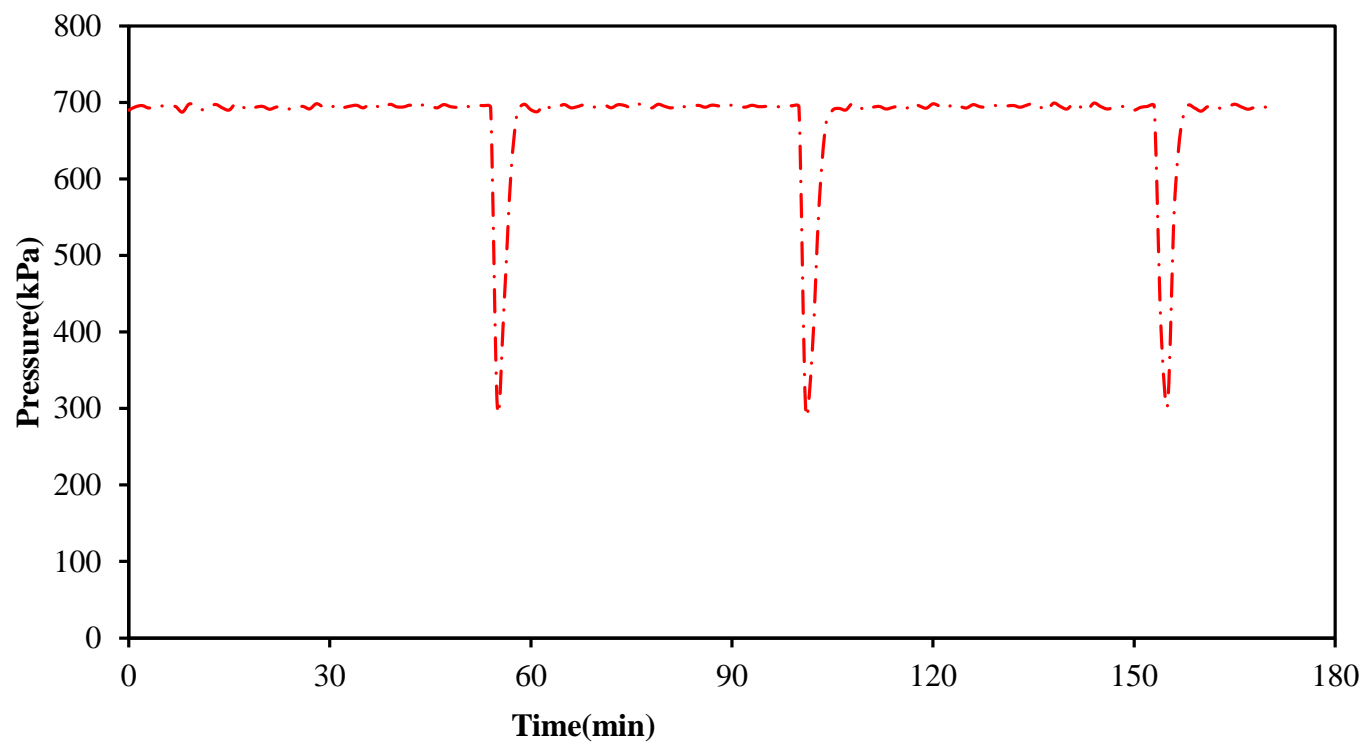


**Figure J.2** Solvent injection pressure corresponding to the optimal  $\omega_{\text{int}}(t)$  in Figure J.1

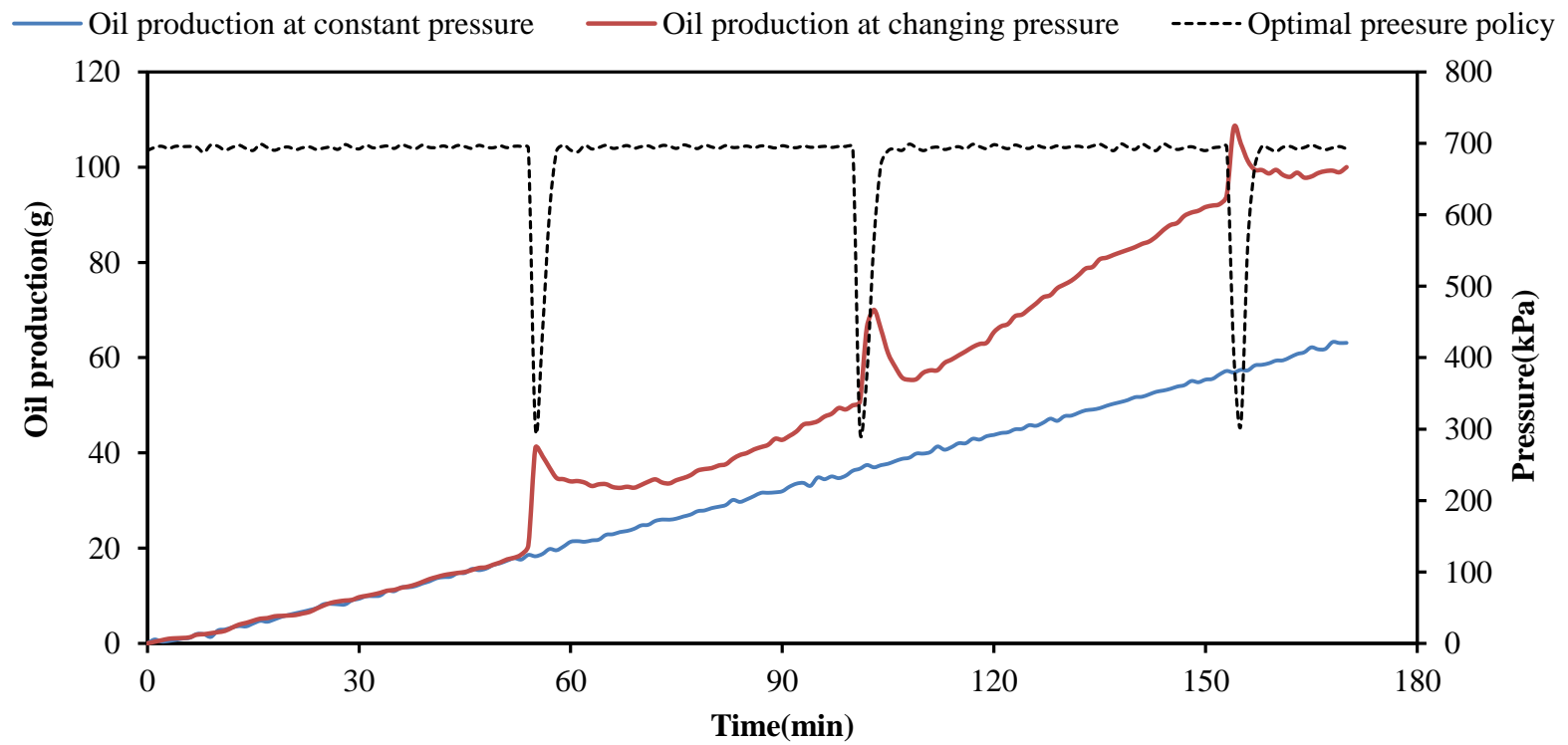


**Figure J.3:** Load cell reading of oil production versus time (Propane, 25 cm model height, 51 Darcy)



**J.2 The simulation results of Optimal Control policy for physical model of 45 cm physical model height, permeability of 204 Darcy, and propane gas.**

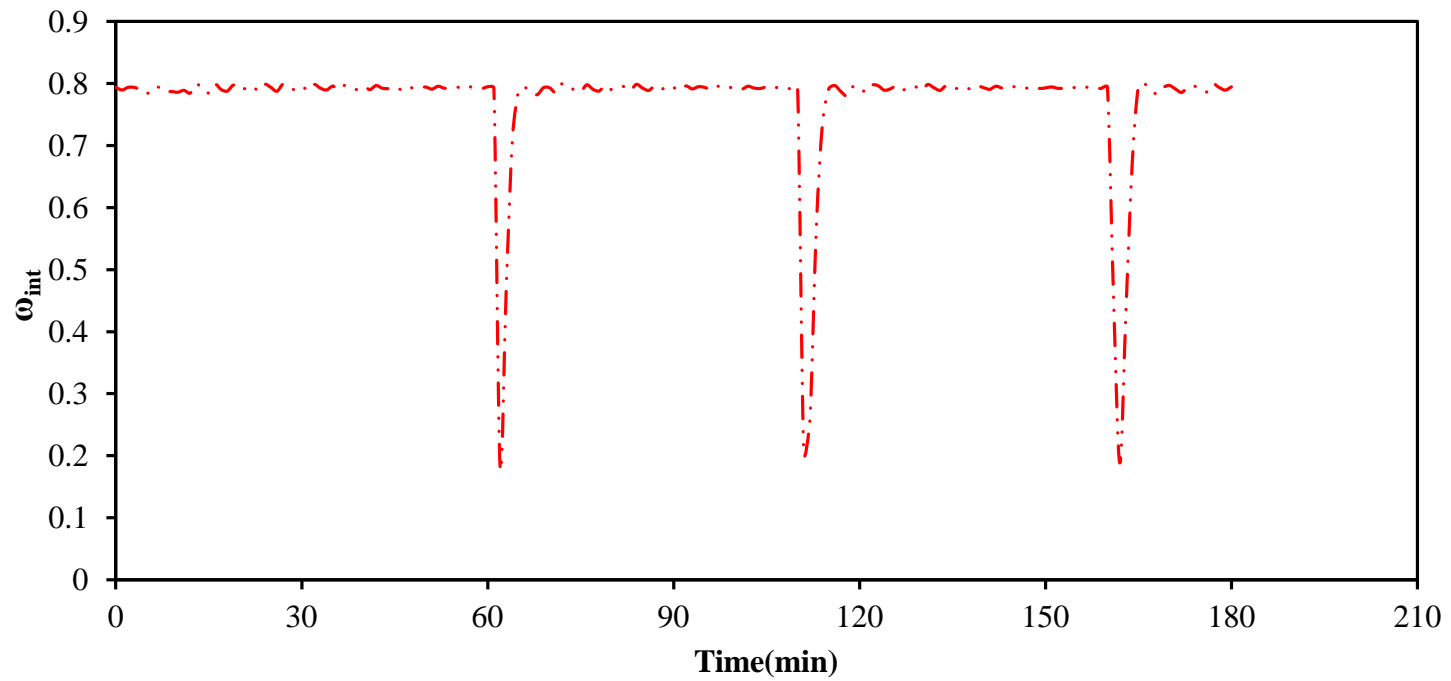


**Figure J.4** Simulation of variation interface concentration  $\omega_{int}$  function of time in heavy oil(Propane, 45 cm model height, 204 Darcy)

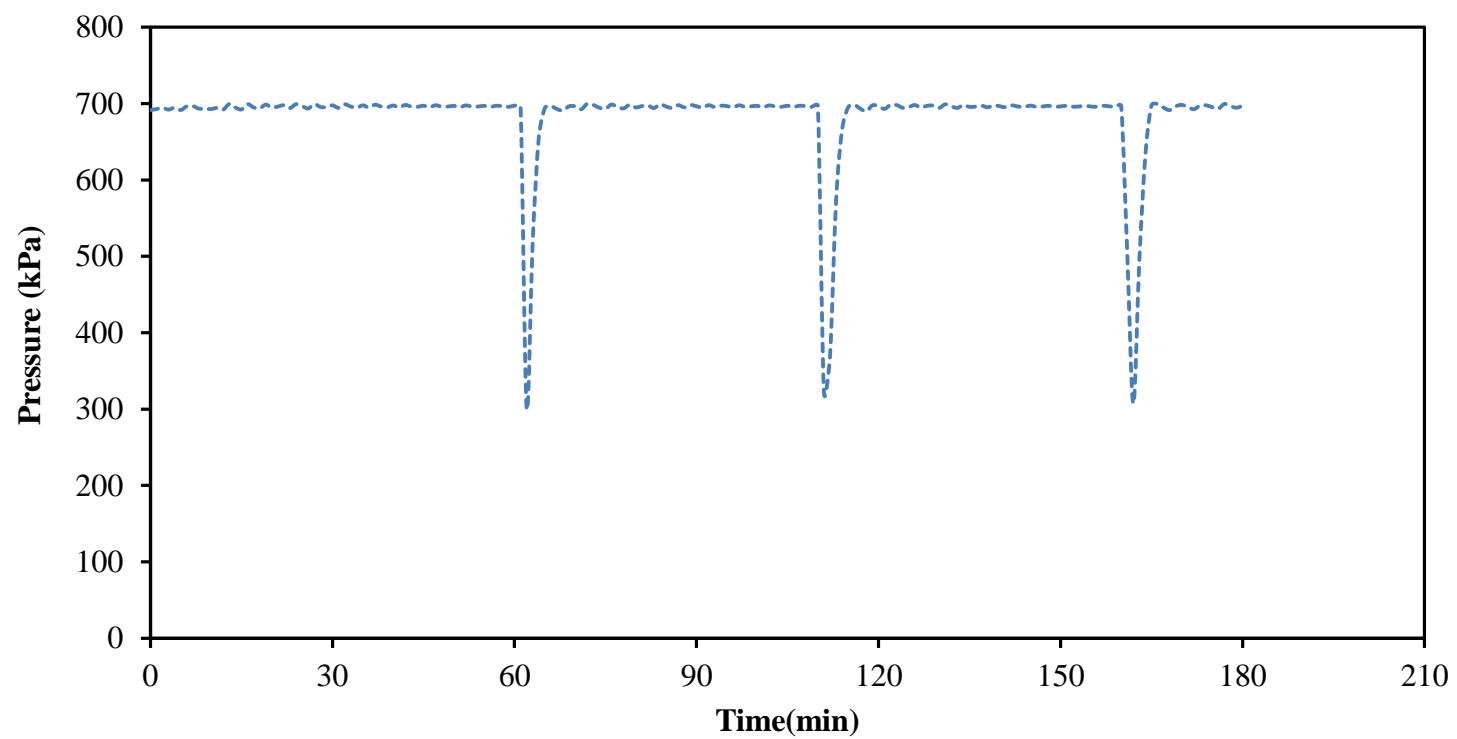


**Figure J.5** Solvent injection pressure corresponding to the optimal  $\omega_{\text{int}}(t)$  in Figure J.4

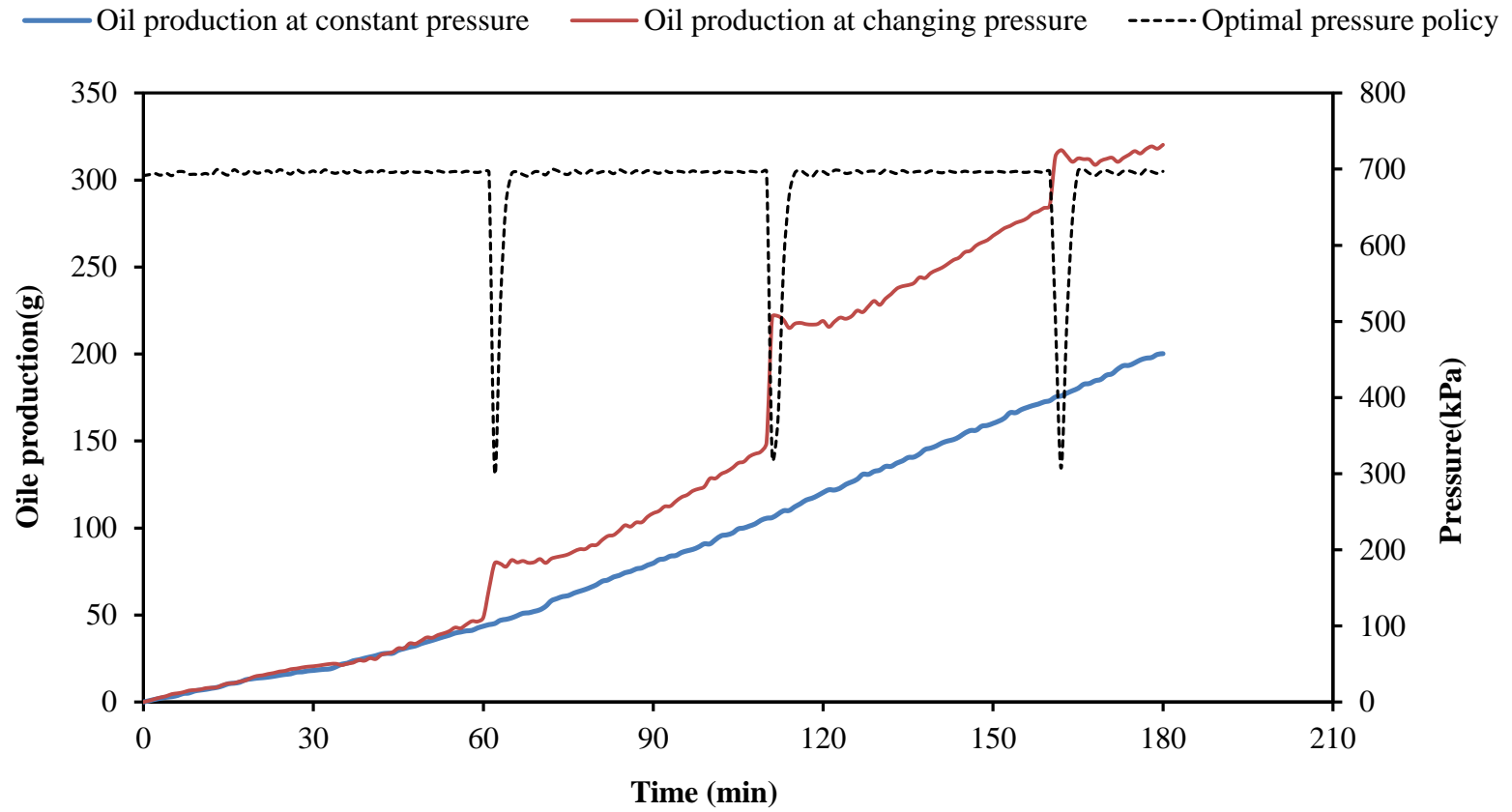


**Figure J.6** Load cell reading of oil production versus time (propane, 45 cm model height, 204 Darcy)

**J.3 The simulation results of Optimal Control policy for physical model of 45 cm physical model height, permeability of 204 Darcy, and butane gas.**

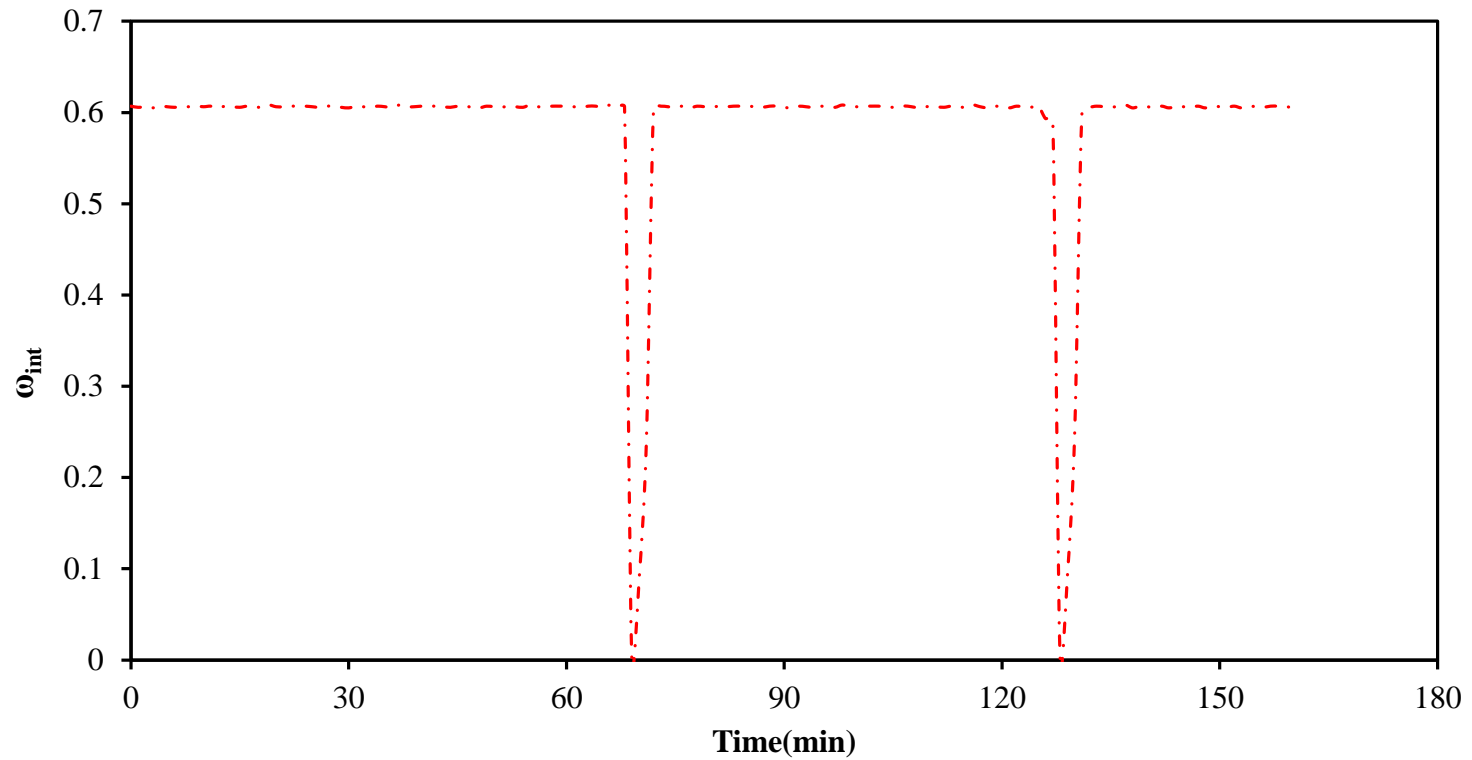


**Figure J.7** Simulation of variation interface concentration  $\omega_{int}$  function of time in heavy oil(butane, 45 cm model height, and 204 Darcy)

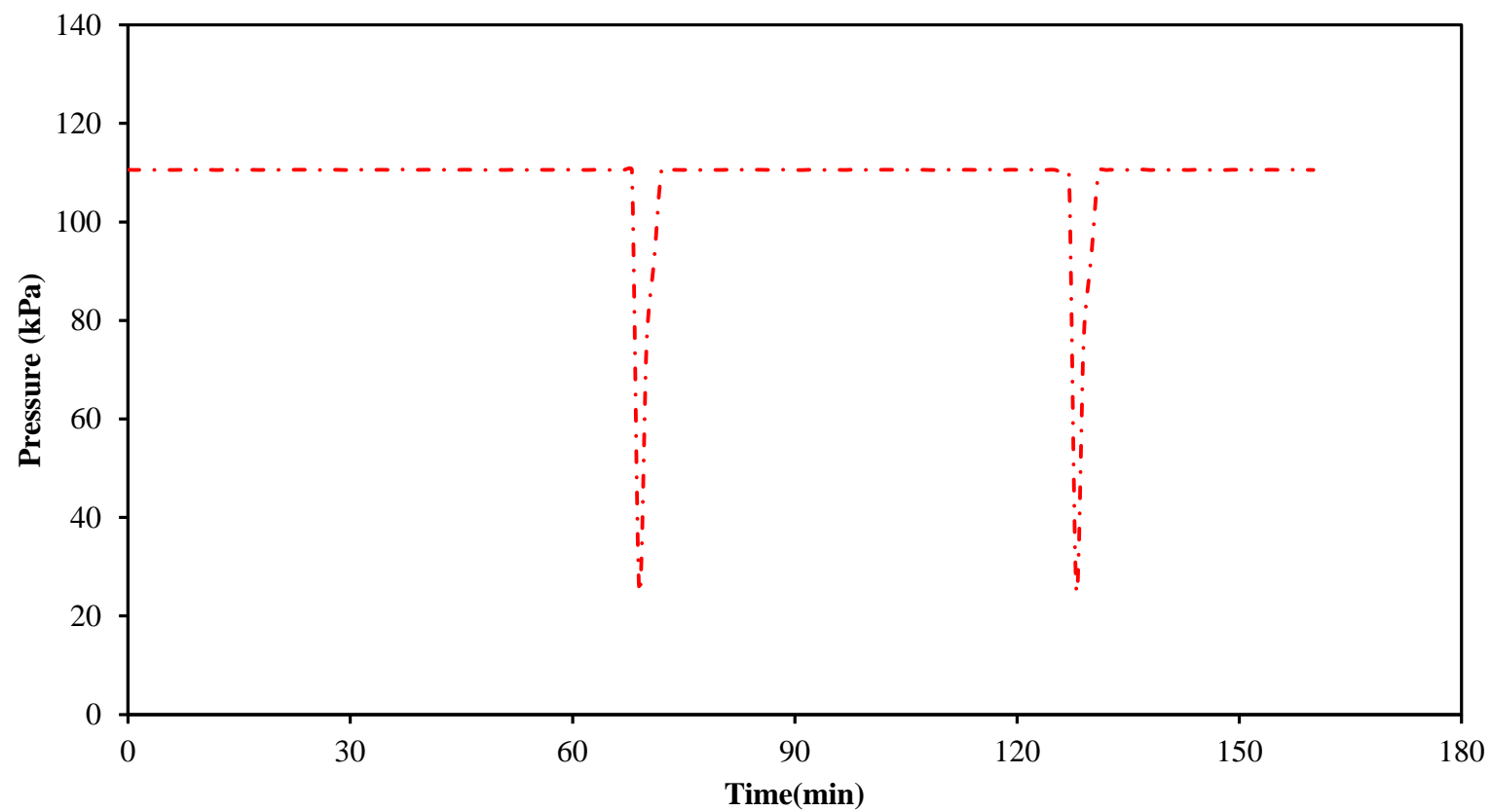


**Figure J.8** Solvent injection pressure corresponding to the optimal  $\omega_{\text{int}}(t)$  in Figure J.7

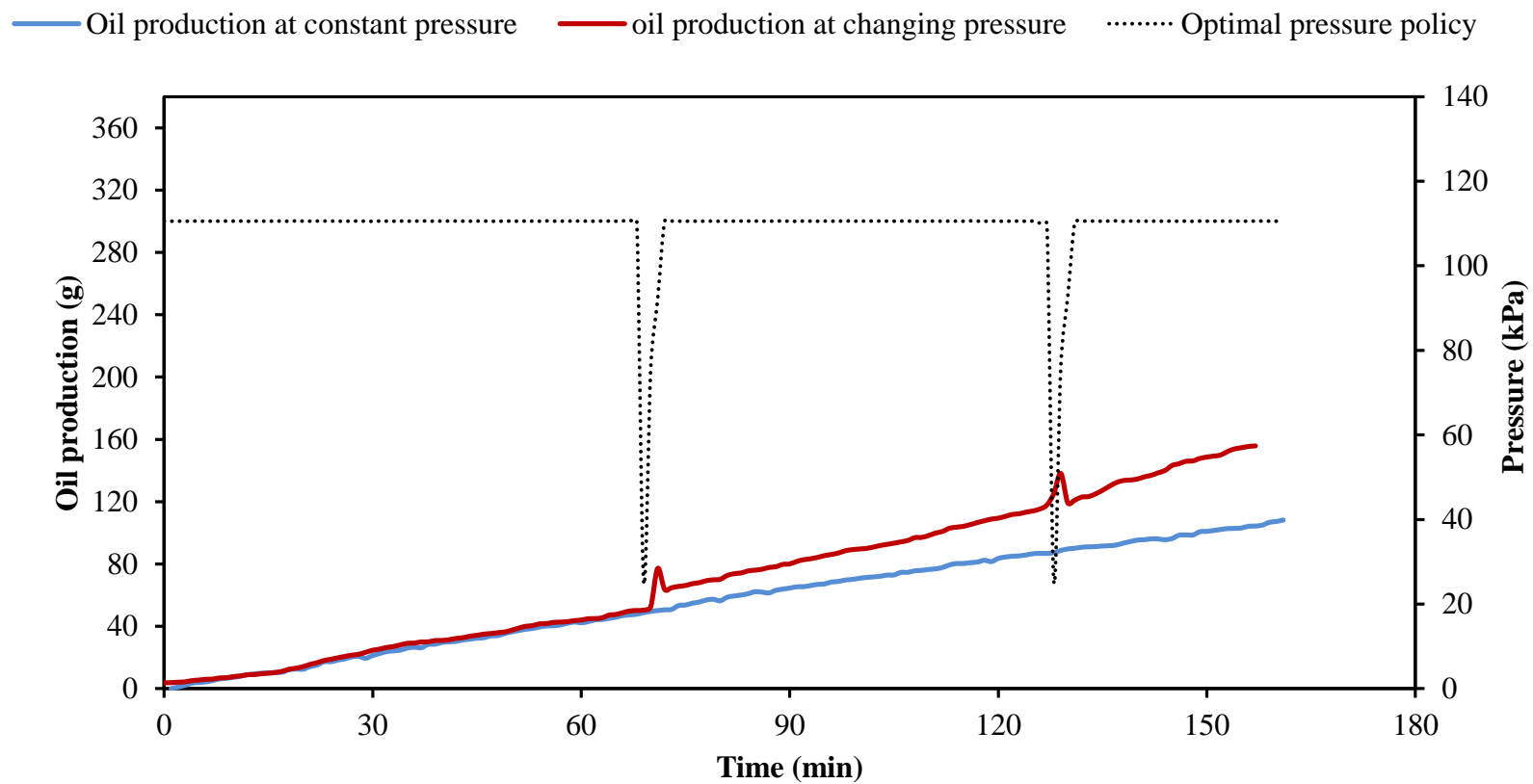


**Figure J.9** Load cell reading of oil production versus time (butane, 45 cm model height, 204 Darcy)



# References

**Abukhalifeh, H.; Lohi, A.; Upreti, S. R., 2009.** A Novel Technique to Determine Concentration-Dependent Solvent Dispersion in Vapex. *Energies*, 2, 851- 872.

**Abukhalifeh, H.; Upreti, S.R.; Lohi, A. 2011.** Permeability effect on the concentration dependent propane dispersion coefficient in Vapex. *Int. J. Oil, Gas and Coal Technology*, Vol. 4, No. 1.

**Alkindi, A.; Muggeridge, A.; Al-Wahaibi, Y., 2010.** Experimental Investigation into the Influence of Convective Dispersion and Model Height on Oil Drainage Rates during Vapex. In *SPE EOR Conference at Oil & Gas West Asia*, Muscat, Oman.

**Allen, J. C. 1974.** Gaseous solvent heavy oil recovery. Canadian Patent No. 1027851, 14 March 1974.

**Allen, J. C.; Woodward, C. D.; Brown, A.; and Wu C. H., 1976.** Multiple Solvent Heavy Oil Recovery Method, Assignee Texaco Inc., New York, N.Y. United States Patent 3954141, Appl. No. 546,580.

**Allen, J. C. 1977.** Carrier gas vaporized solvent oil recovery method, Assignee Texaco Inc., New York, N.Y. United States Patent 4008764, Appl. No. 594,983.

**Ardali, M.; Kharrat, R.; Rostami, B.; Derakhshanfar, M., 2009.** Partial Movement of Asphaltene in Presence of Connate Water in Vapex Process. In *EUROPEC/EAGE Conference and Exhibition*, Amsterdam, the Netherlands.

**Attanasi, E. D. and Meyer, R. F. 2010.** Natural Bitumen and Extra-Heavy Oil. Survey of energy resources (22 ed.). World Energy Council. pp. 123–140. ISBN0-946121-26-5.



**Azin, R.; Kharrat, R.; Ghotbi, C.; Vossoughi, S., 2007.** Improved heavy oil recovery by VAPEX process in the presence of vertical and horizontal fractures. *Journal of the Japan Petroleum Institute*, 50, (6), 340-348.

**Azin, R.; Kharrat, R.; Vossoughi, S.; Ghotbi, C., Study of the 2008.** Vapex Process in Fractured Physical Systems Using Different Solvent Mixtures. *Oil & Gas Science and Technology*, 63 (2), 219-227.

**Boustani, A., and Maini, B.B., 2001.** The Role of Diffusion and Convective Dispersion in Vapor Extraction Process. *Journal of Canadian Petroleum Technology*, 40, 68–77.

**Butler, R. M., and Yee, C. T., 2002.** Progress in the In-situ Recovery of Heavy Oils and Bitumens. *J. Can. Pet. Tech.*, 41(1):31-40

**Butler, R. M., and Jiang, Q., 2000.** Improved Recovery of Heavy Oil by Vapex with Widely Spaced Horizontal Injectors and Producers. *Journal of Canadian Petroleum Technology*, 39, (1), 48-56.

**Butler, R. M., and Mokrys, I. J., 1989.** Solvent Analog Model of Steam-Assisted Gravity Drainage. *AOSTRA Journal of Research*, 5, 17-32.

**Butler, R. M., and Mokrys, I. J., 1998.** Closed-loop extraction method for the recovery of heavy oils and bitumens underlain by aquifers: the Vapex process. *Journal of Canadian petroleum technology*, 37, (4), 41-50.

**Butler, R.M., and Jiang, Q., 2000.** Improved recovery of heavy oil by Vapex with widely spaced horizontal injection and producers. *Journal of Canadian Petroleum Technology*, 39(1):48-56.

**Butler, R.M., and Mokrys, I.J., 1991.** A New Process (Vapex) for Recovering Heavy Oils using Hot Water and Hydrocarbon Vapor. *Journal of Canadian Petroleum Technology*, 30(1), 97-106.

**Butler, R.M. and Mokrys, I.J., 1993.** Recovery of Heavy Oils Using Vaporized Hydrocarbon Solvents: Further Development of the Vapex Process. *Journal of Canadian Petroleum Technology*, 32(6):56-62.

**Canada's Oil Sands: Opportunities and Challenges to 2015 - Energy Market Assessment - May 2004** National Energy board, 2012. Website <http://www.neb-one.gc.ca>.

**Canadian Association Of Petroleum Producers (CAPP), 2008.** Canada's Oil sands overview and outlook, (2008), Available online:[http://www.cade.ca/files/2008\\_06\\_capp\\_overview\\_pryce.pdf](http://www.cade.ca/files/2008_06_capp_overview_pryce.pdf) (accessed October,02, 2009).

**Das, S. K., and Butler, R. M., 1994 a.** Effect of Asphaltene Deposition on the Vapex Process: A Preliminary Investigation using a Hele-Shaw Cell. *Journal of Canadian Petroleum Technology*, 33(6), 39–45.

**Das, S. K., and Butler, R. M., 1996.** Diffusion Coefficients of Propane and Butane in Peace River Bitumen. *Can. J. Chem. Eng.*, 74: 985–992.

**Das, S. K., 1995.** In Situ Recovery of Heavy Oil and Bitumen Using Vaporized Hydrocarbon Solvents, Ph.D. thesis, Department of Chemical and Petroleum Engineering, University of Calgary, Calgary.

**Das, S. K., and Butler, R. M., 1995.** Extraction of Heavy Oil and Bitumen Using Solvents at Reservoir Pressure. In *Technical Meeting / Petroleum Conference of The South Saskatchewan Section*, Regina, Canada.

**Das, S. K., and Butler, M. B., 1997.** Extraction of heavy oil and bitumen using vaporized hydrocarbon solvents. *Petroleum Science and Technology*, 15, (1&2), 51- 75.

**Das, S.K., and Butler, R.M., 1998.** Mechanism of the Vapor Extraction Process for Heavy Oil and Bitumen. *Journal of Petroleum Science and Engineering*, 21, 43–59.

**Das, S.K., 2002.** Vapex - A Unique Canadian Technology. *Journal of Canadian Petroleum Technology*, 41(8), 32-34.

**Das, S.K., 1998.** Vapex: An Effective Process for the Recovery of Heavy Oil and Bitumen. SPE50941, SPE Journal, 232-237.

**Dullien, F.A.L. 1992.** *Porous Media, Fluid Transport and Structure*, 2nd Edition, Academic Press, New York, USA.

**Dunn, S.G., Nenniger, E.H., Rajan, V.S.V., 1989.** A Study of Bitumen Recovery by Gravity Drainage using Low Temperature Soluble Gas Injection. *Canadian Journal of Chemical Engineering*, 67, 978–991.

**Dusseault, M.B., 2001.** Comparing Venezuelan and Canadian Heavy Oil and Tar Sands, Canadian International Petroleum Conference. Calgary, Canada (June 12–14).

**Dusseault, B. M., 2002.** Cold Heavy Oil Production with Sand in Canadian Heavy Oil Industry, Alberta Department of Energy

**El-Haj, R., 2007.** Experimental Determination of Solvent Gas Dispersion in Vapex Process. MAsc Thesis, Ryerson University, Chemical Engineering Department, Toronto, Ontario.

**El-Haj, R., Lohi, A., Upreti, S.R., 2009.** Experimental Determination of Butane Dispersion in Vapor extraction of Heavy Oil and Bitumen. *Journal of Petroleum Science and Engineering*.67, 41–47.

**Energy Information Administration, 2001.** "Venezuela Offers Full Market Value to Encourage Foreign Investment in Oil".

**Energy Technology Perspectives, 2006.** Scenarios and Strategies to 2050, International Energy Agency, p. 265-267.

**ERCB., 1989.** Energy Resources Conservation Board, Alberta's Reserves of Crude Oil, Oil Sands, Gas, Natural Gas Liquids and Sulphur, ST 95.

**Fatemi, S. M., and Bahonar, M., 2010.** Simulation Analysis of the Effects of Fractures Geometrical Properties on the Performance of Vapor Extraction (Vapex) Process. *Journal of Canadian Petroleum Technology*, 49, (7), 47-59.

**Fisher, D. B.; Singhal, A. K.; Das, S. K.; Goldman, J.; Jackson, C., 2000.** Use of Magnetic Resonance Imaging and Advanced Image Analysis as a Tool to Extract Mass Transfer Information from a 2D Physical Model of The Vapex Process. *SPE 59330*.

**Frauenfeld, T.; Jossy, C.; Rispler, K.; Kissel, G., 2004.** Evaluation of the Bottom Water Reservoir Vapex Process. In *5th Canadian International Petroleum Conference (55th Annual Technical Meeting)*, Calgary, Alberta, Canada.

**Guerrero-Aconcha, U.; Salama, D.; Kantzas, A., 2008.** Diffusion Coefficient of n alkanes in Heavy Oil. In *SPE Annual Technical Conference and Exhibition*, Denver, Colorado, USA.

**Haghighat, P., and Maini, B. B., 2008.** Role of Asphaltene Precipitation in Vapex Process. In *Canadian International Petroleum Conference/SPE Gas Technology Symposium 2008 Joint Conference (the Petroleum Society's 59th Annual Technical Meeting)*, Calgary, Alberta, Canada.

**Hayduk, M., and Minhas, B. S., 1982.** Correlations for Prediction of Molecular Diffusivities in Liquids. *Can. J. Chem. Eng.*, 60: 295–299.

**Hayduk, W., Castaneda, R., Bromfield, H. and Perras R.R., 1973.** Diffusivities of Propane in Normal Paraffin, Chlorobenzene, and Butanol Solvents; *AIChE Journal*, 19(4) 859-861.

**Hiss, T.G., and Cussler, E. L., 1973.** Diffusion in High Viscosity Liquids. *AIChE Journal*, 19: 698–703.

**Imran, M., Upreti, S. R., Lohi, A., 2008.** Optimal Oil Production from Vapex Potential Directions. *Petroleum Science Research Progress*, Nova Publishers, ISBN: 978-1-60456-012-1.

**James, L.A, 2009.** “Mass Transfer Mechanisms during the Solvent Recovery of Heavy Oil”, PhD. Thesis, the University of Waterloo, ON, Canada.

**Jiang, Q., 1997.** Recovery of heavy oil and bitumen using vapex process in homogeneous and heterogeneous reservoirs. University of Calgary, Calgary.

**Jiang, Q., and Butler, R.M., 1996.** Selection of Well Configurations in Vapex Process. *SPE* 37145.

**Jiang, Q., Butler, R.M., and Yee, C.T., 2000.** The Steam and Gas push (SAGP)-2: Mechanism Analysis and Physical Model Testing. *Journal of Canadian Petroleum Technology*. 39 (4),52-61.

**Jin, W., 1999.** Heavy Oil Recovery Using the Vapex Process, Master's Thesis, University of Waterloo, Waterloo, ON, Canada.

**Kapadia, R. A., 2004.** Dispersion determination in Vapex: Experimental design, modeling and simulation. *Masters Abstracts International*, 47, (1).

**Kapadia, R., Upreti, S.R., Lohi, A., Chatzis I., 2006.** Determination of Gas Dispersion in Vapor Extraction of Heavy Oil and Bitumen. *Journal of Petroleum Science and Engineering*, 51, 214–222.

**Karmaker, K., and Maini, B. B., 2003.** Experimental Investigation of Oil Drainage Rates in the Vapex Process for Heavy Oil and Bitumen Reservoirs, Paper *SPE* 84199 presented at the 2003 SPE Annual Technical Conference and Exhibition, Denver, October 5–8.

**Karmaker, K., and Maini, B. B., 2003.** Applicability of Vapor Extraction Process to Problematic Viscous Oil Reservoirs In *SPE Annual Technical Conference and Exhibition*, Denver, Colorado.

**Kok, M. V.; Yildirim, Y.; Akin, S., 2008.** Application of Vapex Process for Light Crude Oil. *Energy Sources, Part A*, 30, 20-26.

**Lim, G. B.; Kry, J. P. L.; Kwan, M. Y., 2004.** Cyclic solvent process for in-situ bitumen and heavy oil production.

**Luo, P., and Gu, Y., 2009.** Characterization of a Heavy Oil-Propane System in the Presence or Absence of Asphaltene Precipitation. *Fluid Phase Equilibria*, 277 (1), 1-8.

**Luo, H., and Kantzas, A., 2008.** Investigation of Diffusion Coefficients of Heavy Oil and Hydrocarbon Solvent Systems in Porous Media. *Proceedings: SPE Improved Oil Recovery Symposium*, 19-23 April 2008, Tulsa, Oklahoma, USA, paper SPE 113995.

**Luo, P., Yang C. and Gu, Y., 2007.** Enhanced Solvent Dissolution into In-Situ Upgraded Heavy Oil Under Different Pressures. *Fluid Phase Equilibria*, 252, 143-151.

**Luo, P., and Gu, Y., 2005.** Effects of Asphaltene Content and Solvent Concentration on Heavy-Oil Viscosity. In *SPE/PS-CIM/CHOA International Thermal Operations and Heavy Oil Symposium*, Calgary, Alberta, Canada.

**Moghadam, S.; Nobakht, M.; Gu, Y., 2009.** Theoretical and physical modeling of a solvent vapor extraction (Vapex) process for heavy oil recovery. *Journal of Petroleum Science and Engineering*, 65 93-104.

**Moghadam, S.; Nobakht, M.; Gu, Y., 2007.** Permeability Effects in a Vapor Extraction (Vapex) Heavy Oil Recovery Process. In *8th Canadian International Petroleum Conference (58th Annual Technical Meeting)*, Calgary, Alberta, Canada.

**Mokrys, I.J., and Butler, R.M., 1993.** In-Situ Upgrading of Heavy Oils and Bitumen by Propane Deasphalting: The Vapex Process. *SPE* 25452, March 21-23.

**Muhamad, H. Upreti, S. R., Lohi, A., and Doan, H. 2012,** “Performance Enhancement of Vapex by Varying the Propane Injection Pressure with Time”, *Energy and Fuels* 26 (6) , pp. 3514-3520.

**Muhamad, H. Upreti, S. R., Lohi, A., and Doan, H. 2012,**“Performance Enhancement of Vapex by Temporal Variation of Solvent Injection Pressure”, *Journal of Petroleum Science and Engineering*.

**Nasr T.N. and O.R. Ayodele, O.R., 2006.** New Hybrid Steam-Solvent Processes for the Recovery of Heavy Oil and Bitumen, *Society of Petroleum Engineers*, Abu Dhabi International Petroleum Exhibition and Conference, 5-8 November, Abu Dhabi, UAE

**Nghiem L. X., Sammon, P.H., Kohse B.F., 2001.** Modeling Asphaltene Precipitation and Dispersive Mixing in the Vapex Process. *SPE Reservoir Simulation Symposium Proceedings*.

**Nghiem, L. X.; Kohse, B. F.; Farouq Ali, S. M.; Doan, Q., 2000.** Asphaltene Precipitation: Phase Behaviour Modelling and Compositional Simulation. *SPE*59432.

**Oduntan, A.R. 2001.** Heavy Oil Recovery Using the Vapex Process: Scale Up and Mass Transfer Issues. Master’s Thesis, University of Waterloo, Waterloo, Canada.

**Oil Sands Technology Roadmap, 2004,** Chamber of Resources, Alberta, January 2004. Website <http://www.acr-alberta.com/>).

**Oil Sands Technology Roadmap**, Alberta Chamber of Resources , January 2004, 22.

**Perkins, T.K. and Johnston, O.C., 1963.** A Review of Diffusion and Dispersion in Porous Media. *SPE Journal*, 3, 70–84.

**Pourabdollah, K.; Zarringhalam Moghaddam, A.; Kharrat, R.; Mokhtari, B., 2010.** Study of Asphaltene and Metal Upgrading in Vapex Process. *Energy & Fuels*, 24, (8), 4396-4401. 121.

**Pourabdollah, K.; Zarringhalam Moghaddam, A.; Kharrat, R.; Mokhtari, B., 2010.** Experimental Feasibility Study of In-Situ Nano-Particles in Enhanced Oil Recovery and Heavy Oil Production. *Energy Sources, Part A*, Article in Press.

**Rahnema, H.; Ghaderi, S. M.; Farahani, S., 2007.** Simulation of Vapex process in problematic reservoirs: A promising tool along with experimental study. In *SPE/EAGE Reservoir Characterization and Simulation Conference*, Abu Dhabi, UAE.

**Ramakrishnan, V., 2003.** In situ Recovery of Heavy Oil by Vapex using Propane. Master's Thesis, University of Waterloo, Waterloo, Canada.

**Roopa, I., and Dawe, R. A., 2007.** Vapex-Gravity-assisted Film Drainage for Heavy Oil Recovery. *Petroleum Science and Technology*, 25, 645-658.

**Speight, J.G., 1999.** The desulfurization of heavy oils and residua, second edition, CRC Press P.(215-216).

**Talwani, M., 2002.** The Orinoco heavy oil belt in Venezuela (Or heavy oil to the rescue?), energy study, Schlumberger professor of earth science, Rice University.

**The Geological Society, 2012.** Website,  
<http://pgc.lyellcollection.org/content/7/1141/F4.expansion.html>



**Upreti, S. R., and Mehrotra, A. K., 2002.** Diffusivity of CO<sub>2</sub>, CH<sub>4</sub>, C<sub>2</sub>H<sub>6</sub> and N<sub>2</sub> in Athabasca Bitumen. *Can. J. Chem. Eng.*, 80: 116–125.

**Upreti, S. R., 2012.** Optimal Control for Chemical Engineers, Taylor and Francis Group, FL, USA, CRC Press; 1 edition.

**Wen, Y. W., and Kantzas, A., 2005.** Monitoring Bitumen–Solvent Interactions with Low- Field Nuclear Magnetic Resonance and X-ray Computer-Assisted Tomography. *Energy & Fuels*, 19 (4), 1319-1326.

**Yazdani, A, and Maini, B.B. 2005.** “Effect of Drainage Height and Grain Size on Production Rates in The Vapex Process: Experimental Study,” *SPE Reservoir Evaluation and Engineering*, 205-214.

**Yazdani, A. and B.B. Maini 2010.** “Measurement and Modeling of Phase Behaviour and Viscosity of a Heavy Oil/Butane System,” *Journal of Canadian Petroleum Technology*, Vol. 49, No. 2, 9-14

**Zeng, F.; Knorr, K. D.; Wilton, R. R., 2008.** Enhancing Oil Rate in Solvent Vapor Extraction Processes Through Tee-Well Pattern. In *International Thermal Operations and Heavy Oil Symposium*, Calgary, Alberta, Canada.